

JAERI-M
90-139

JAERI TANDEM, LINAC & V.D.G.
ANNUAL REPORT
1989

April 1, 1989—March 31, 1990

September 1990

Department of Physics

日本原子力研究所
Japan Atomic Energy Research Institute

JAERI-Mレポートは、日本原子力研究所が不定期に公刊している研究報告書です。

入手の問い合わせは、日本原子力研究所技術情報部情報資料課（〒319-11茨城県那珂郡東海村）
あて、お申しこしてください。なお、このほかに財団法人原子力弘済会資料センター（〒319-11茨城
県那珂郡東海村日本原子力研究所内）で複写による実費頒布をおこなっております。

JAERI-M reports are issued irregularly.

Inquiries about availability of the reports should be addressed to Information Division, Department
of Technical Information, Japan Atomic Energy Research Institute, Tokai-mura, Naka-gun,
Ibaraki-ken 319-11, Japan.

© Japan Atomic Energy Research Institute, 1990

編集兼発行 日本原子力研究所
印刷 日立高速印刷株式会社

JAERI TANDEM, LINAC & V.D.G.
Annual Report
1989

April 1, 1989 - March 31, 1990

Department of Physics
Tokai Research Establishment
Japan Atomic Energy Research Institute
Tokai-mura, Naka-gun, Ibaraki-ken

(Received August 1, 1990)

This annual report describes research activities which have been performed with the JAERI tandem accelerator, the electron linear accelerator and the Van de Graaff accelerator from April 1, 1989 to March 31, 1990. Summary reports of 49 papers, and list of publications, personnel and cooperative researches with universities are contained.

Keywords : JAERI TANDEM, e-LINAC, V.D.G., Atomic Physics, Radiation Chemistry, Solid State Physics, Material Science, Nuclear Chemistry, Nuclear Physics, Neutron Physics, Annual Report

Editors : Mitsuhiro Ishii
Chiaki Kobayashi
Akira Iwamoto
Yukio Kazumata
Yuuki Kawarasaki
Fujiyasu Nomura

原研タンデム，リニアック，バンデグラフ加速器
1989年度年次報告

日本原子力研究所東海研究所
物理部

(1990年8月1日受理)

本年次報告は，原研タンデム，リニアック及びバンデグラフ加速器で，1989年4月1日から1990年3月31日までの間に東海研で行われた研究活動を取りまとめたものである。

1) 加速器運転と開発研究 2) 化学と放射線生物物理 3) 原子物理，固体物理及び材料の放射線効果 4) 核化学 5) 核物理 6) 中性子物理の6部門にまたがる49編の研究報告，公表された文献，関与した職員及び大学等との協力研究のリストを収録している。

東海研究所：〒319-11 茨城県那珂郡東海村白方字白根2-4

(編集者) 石井三彦，小林千明，岩本 昭，数又幸生
河原崎雄紀，野村藤靖

PREFACE

This report covers activities of research and development which were carried out at accelerator facilities of Department of Physics during the period from April 1, 1989 through March 31, 1990. Accelerators Division of the Department maintains and operates three accelerators, i.e. the tandem accelerator, the electron linear accelerator and the Van de Graaff accelerator. All the accelerators were operated satisfactorily throughout the period.

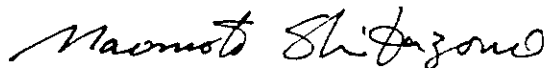
The tandem accelerator, with which a majority of the research activities has been performed, was stably operated and available beam time of over 5,600 hours was attained in this period.

The construction of superconducting booster is continued. Design studies of the machine control system, the helium refrigerator system and the new building for the booster have been worked out in this period. The budget for the construction of these all was already approved. The whole system of the post accelerator will be completed in 1992.

Considerable efforts were devoted to develop a compact electron storage ring 'JSR' which was installed in the electron linear accelerator. Electron beams of 150 MeV from the linac were injected into the JSR. Beams were accelerated up to 300 MeV by the JSR itself and stored. Stored beams of more than 100 mA were obtained for a mean storage time of 30 min.

Main subjects of our research activities are; 1) atomic physics and chemistry, 2) condensed matter physics and effects of irradiation of materials, 3) nuclear chemistry, 4) nuclear physics, and 5) neutron physics. During the period more than 60 staff members of JAERI have worked in these fields and about a hundred experiments were done in collaboration with universities and institutes outside JAERI.

A workshop was held at Tokai Research Establishment of JAERI on November 6-7, 1989 to study future experimental instrumentation for the post accelerator which will boost the energy of heavy ion beams four times as much as the presently available energy. Participants including 30 inside and 51 outside users discussed together and made suggestions and proposals for possible experiments which were considered to be important and should be promoted.



Naomoto SHIKAZONO
Director
Department of Physics

Since November 1, 1989
Deputy Director General
Tokai Establishment

Contents

I	ACCELERATOR OPERATION AND DEVELOPMENT	1
1.1	Tandem Accelerator Operation	3
1.2	Superconducting Booster	5
1.3	The Emittance Measurements of Injection Line Ion Beams for the JAERI Tandem Accelerator	9
1.4	Electron Linac Operation and Improvements	13
1.5	Operation of JSR	17
1.6	Brightness Enhanced Intense Slow Positron Beam Produced Using an Electron Linac	21
1.7	Design of the Control System for the JAERI Free Electron Laser	25
1.8	Optical Transition Radiation Beam Monitor for an FEL Experiment	29
II	CHEMISTRY AND RADIATION BIOLOGY	33
2.1	Chemical Behavior of Recoil ^{16}N Formed by Fast Neutron Irradiation on Various Aqueous Solutions	35
2.2	Heavy Ion Track Microfilter of Polyimide	39
2.3	Microdosimetry of High-energy Heavy Ions	43
2.4	Effect of Ion Beam Irradiation on Dry Cells of Radiation Resistant Bacterium, <i>Deinococcus Radiodurans</i>	47
III	ATOMIC PHYSICS, SOLID STATE PHYSICS AND RADIATION EFFECTS IN MATERIALS	51
3.1	High-Resolution Zero-Degree Electron Spectroscopy (II)	53
3.2	Response of Silicon Surface Barrier Detector to Heavy Ions	57
3.3	Perturbed Angular Correlation Measurement Using Pd-100/ Rh-100 Nuclear Probes II	61
3.4	X-Ray Diffraction on Carbon Ion-Irradiated Diamond	65
3.5	Effect of Electron-Excitation on Radiation Damage in Ion-Irradiated FCC Metals	69
3.6	Cascades and Their Kinetic Behavior in Ion-Irradiated Copper	72
3.7	Effects of He Ion Irradiation on Critical Current Behaviors of Bi-Sr-Ca-Cu-O Films	76
3.8	Effect of High Energy Ion Irradiation on Current-Voltage Characteristics in Oxide Superconductor $\text{YBa}_2\text{Cu}_3\text{O}_{7-x}$	80

3.9	Electrical and Structural Properties of Li-Ion Irradiated β -LiAl	84
3.10	Irradiation Behavior of Tritium-Breeding Ceramics	88
3.11	Ionic Conductivity of Al-Doped Li_4SiO_4 during and after Irradiation	92
3.12	A Study of Radiation Damage in Li_4SiO_4 by Electron Microscopic Observation	96
3.13	Microstructure and Mechanical Properties of α -Particle Irradiated Stainless Steels	99
3.14	Radiation Effect of Austenitic Stainless Steels	103
IV	NUCLEAR CHEMISTRY	107
4.1	Measurement of Beta-ray Maximum Energy with an HPG Detector	109
4.2	Measurement of Hold-Up Times of a Thermal Ion Source for Metallic and Monoxide Ions of La and Ce	113
4.3	Test of an Ion Guide Method for Isotope Separation on Line	119
4.4	A Research for the Production of Transuranium Elements	123
4.5	Fission Yields of Rare Earth Elements Produced in Proton- Induced Fission of ^{244}Pu	126
4.6	Mass and Energy Distribution in the Proton-Induced Fission of ^{232}Th	130
4.7	Ruthenium Isotopes Produced in the Proton-, ^{12}C -and ^{19}F -Induced Fissions of Actinides	134
4.8	Symmetric Mass Division of ^{105}Ag Formed in the Reactions $^{37}\text{Cl}+$ ^{68}Zn and $^{16}\text{O} + ^{89}\text{Y}$	136
V	NUCLEAR PHYSICS	141
5.1	Transfer Reactions for $^{16}\text{O} + ^{144,152}\text{Sm}$ near the Coulomb Barrier	143
5.2	Inelastic Scattering of ^{19}F on ^{28}Si	147
5.3	Measurement of $^8\text{Be}_{\text{g.s.}}$ - α Decays from ^{12}C Nuclei in the $^{16}\text{O} +$ ^{60}Ni Reaction at 90 MeV	149
5.4	Pre-Scission ^4He Multiplicity in the $^{19}\text{F} + ^{197}\text{Au}$ Reaction	151
5.5	Production Mechanism of Fission-like Fragments in the Reactions of $^{37}\text{Cl} + ^{64}\text{Ni}$, $E_{\text{lab}}=170, 186$ MeV	154
5.6	A Study of Fission-like Reactions with the System of $^{28}\text{Si} + ^{74}\text{Ge}$ at $E_{\text{lab}}=176$ MeV	156
5.7	Rotational Perturbation in the $K=3/2$ Band of ^{155}Gd	158
5.8	Lifetime Measurements of the First 2^+ States in $^{124,126}\text{Ba}$	161
5.9	Coulomb Excitation of the Unstable Nucleus ^{76}Kr	163

5.10	Search for a Double- γ Vibrational State in ^{164}Dy	166
5.11	Ns-Isomers in Neighbor Nuclei of ^{100}Sn	168
5.12	Evaporation of Charged Particles from Highly Deformed Nucleus	170
5.13	Shape Transition of Nuclei with Mass Around $A=100$	174
VI	NEUTRON PHYSICS	179
6.1	Neutron Cross Section Measurements in Several MeV Region Using $^1\text{H}(^{11}\text{B},n)^{11}\text{C}$ Neutron source	181
6.2	Scattering of 18.5 MeV Neutrons from ^{52}Cr	185
VII	PUBLICATIONS	189
VIII	PERSONNEL AND COMMITTEES	215
IX	CO-OPERATIVE RESEARCHES	227

I ACCELERATOR OPERATION AND DEVELOPMENT

1.1 TANDEM ACCELERATOR OPERATION

Tandem Accelerator Group

Department of physics, JAERI

Accelerator operation

During the year from April 1, 1989 to March 31, 1990, the tandem accelerator has been operated for many kinds of research programs. As the accelerator ran without troubles inside the pressure tank in this period, almost all of the experimental programs were performed under the arranged schedule. The following are summary of the operation and the maintenance. The running time was 5618 hours.

1) Time distribution by terminal voltage

>17 MV	1 days	0.5 %	:	11-12 MV	6 days	2.6 %
16-17	41	17.8	:	10-11	0	0.0
15-16	108	47.0	:	9-10	7	3.0
14-15	35	15.2	:	8- 9	11	4.8
13-14	14	6.1	:	< 8	1	0.5
12-13	6	2.6	:			

2) Time distribution by projectile

H	11 days	4.7 %	:	S	23 days	9.9 %
D	26	11.2	:	Cl	19	8.2
Li	9	3.9	:	Fe	8	3.4
B	8	3.4	:	Ni	27	11.6
C	22	9.4	:	Ge	10	4.3
O	39	16.7	:	Br	6	2.0
F	10	4.3	:	Ag	1	0.4
Si	6	2.6	:	I	7	3.0
			:	Au	1	0.4

3) Time distribution by activity

Operation for research	232 days
Atomic and solid state physics	(54 days)
Radiation effects in materials	(10)

Nuclear chemistry	(57)
Nuclear physics	(83)
Fast neutron physics	(28)
Voltage conditioning	2
Operation training	2
Scheduled maintenance	89
Unexpected repair	2
Holidays and vacation	38

Major troubles

1) August 19 - 20, 1989

The trouble of the control computer system.

Maintenance

1) The regular maintenance with the pressure tank opening were done twice. All of the corona points were renewed at the last tank opening.

2) Two SF₆ storage tanks were opened for regular inspection for the high pressure gas regulation, which is enforced once five year. Some scales and bath tab marks were found on the inside wall but no corrosion was found.

Improvement and development

1) For the efficient operation of the tandem accelerator and its convenient maintenance, we have built a second negative ion injector which was placed before the first injector. The second injector is equipped with a SNICS-II ion source purchased from National Electrostatics corporation. Main characteristics of the second injector are same as the first one except for number of ion source installed on it. The ion beams from the second injector are passing through the center port of the first injector's inflection magnet. Both injectors are used alternatively. Fig. 1 shows the layout of injectors.

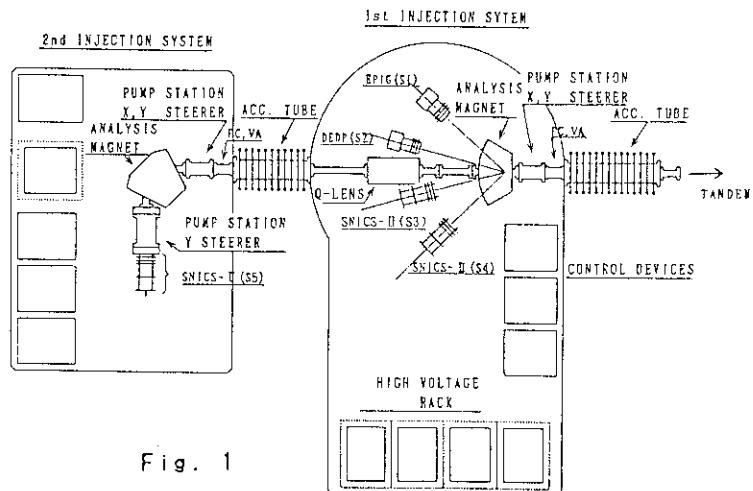


Fig. 1

1.2 SUPERCONDUCTING BOOSTER

BOOSTER PROJECT GROUP

Department of Physics

1. Introduction

The project of our superconducting tandem-booster is in progress as we planned. The year of 1989 was the second year of the fabrication of the linac. The fabrication of the front part (four of the ten linac units) has begun and the rear part (the rest six units) was contracted with the same manufacturer, Mitsubishi Electric. The four units shall be completed by the end of the fiscal year of 1990 and the rest six one year after. Two-years long budget for the building and the refrigerating system was approved by the Ministry of Finance. The design work for them has proceeded well. Main components of the booster will be assembled in the new building in the beginning of 1992.

2. Accelerating Structure

The front part of the linac is composed of 16 superconducting quarter wave resonators and four cryostats. The design of the resonators is the same as that of the resonators for the buncher and de-buncher previously made. The niobium materials prepared this time were found to have a thermal conductivity higher enough than our specification; the RRR (residual resistance ratio)s were mostly between 100 and 200, while the specified minimum value is 80. The fabrication procedure was improved further for the sake of making number of resonators. The machining tools for drift tubes and outer conductors were remarkably improved. The manufacture invested in an electron beam welder. After improvements of the equipments for electropolishing, we met a problem that a part of niobium surface of a center conductor was marked with small white spots in electropolishing. This was partly due to the fact that the electropolishing solution used there had not been mixed as we specified. Complete solution for the problem has not been found, yet.

For the cryostats, R&D work was made. In the buncher and debuncher

cryostats, the magnetic shield made of Parmarroy sheets could not shield the territorial magnetic field enough. As a result of various investigations with Parmarroy inter-shield models and iron vacuum chamber models, we decided to employ pure iron for the vacuum chambers and to add Parmarroy inter-shields inside the vacuum chambers. The magnetic field level can be suppressed well below 50 mG. The chambers are to be plated with nickel. The outgas from the nickel-plated iron surface was confirmed to be small enough with a model.

For the rear part of the linac, the contract was made at the very end of this fiscal year. The manufacturer can cope with the delay, because the designs of the resonators and the cryostats are the same as those of the front part.

On the other hand, the modification of the buncher cryostat was completed, which continued from the last fiscal year(see the annual report of 1988). Drying by vacuum pumping in the surface re-treatment was tried with the two resonators for the de-buncher. Their maximum accelerating field levels were improved to 8 and 9 MV/m from the previous values of 7 MV/m.

Reconsideration on the relative position of 260 MHz sub-buncher resonators to 130 MHz main buncher resonators was done with calculation of beam dynamics, because our idea that the sub-buncher resonators are in upstream of the main ones had been questioned by experts of beam dynamics. Whichever the sub-buncher resonators were put upstream or downstream of the main buncher resonators, no big difference was found in our calculation. As a result, we chose the downstream position for the sub-buncher from overall considerations.

3.Refrigerating system

We have decided to employ a dual closed loop refrigeration system for the booster. It shall be operated under the regulations for refrigerators in the high pressure gas law.

We worked for establishing its specification. From estimation of heat loads, following fundamental specification is proposed;

- a. The system is composed of 2 sets of refrigerators.
- b. The refrigerators are not assisted with liquid nitrogen for precool at all.

- c. Each refrigerator has two loops of liquid helium and 60-80K gaseous helium;
 The refrigeration power of liquid helium is 250 watts.
 The refrigeration power of 60-80 K gaseous helium is 1500 watts.
- d. Helium gas compressors work as a compressor for gas recovery as well as for main gas compression. The output of their motors is less than 360kW.
- e. External liquid helium dewars are not installed.

Refrigerators of several makes were investigated with their specification and by visiting other laboratories. A few of them are satisfactory. The work of establishing precise specification continues for a few months till the order of the system.

4. Building

The design of the building has been completed by the section of constructions. The ground was inspected also. The layout plan is shown in Fig. 1. The building is composed of a linac room of 8.6 m x 44 m, a target room of 24.5 x 13.6 m, an rf control room, 4 rooms for assembly and preparation and a separated room (10 m x 12 m) for helium gas compressors. The total area is 1230 m².

The linac room and the target room are surrounded by 2 m thick concrete walls for nuclear radiation shields. In these rooms, 2.8 ton and 5 ton cranes will be installed under the ceilings, respectively. The target room is to be equipped with a shield door with opening of 3 m x 3 m and a zigzag pass for an emergency escape. Two rooms are specified as a clean room for assembly and preparation of resonators. The installations of electric power and air conditioning are as same as those of the existing tandem building. The construction of the building will start in the mid of 1990 and finish in 1991.

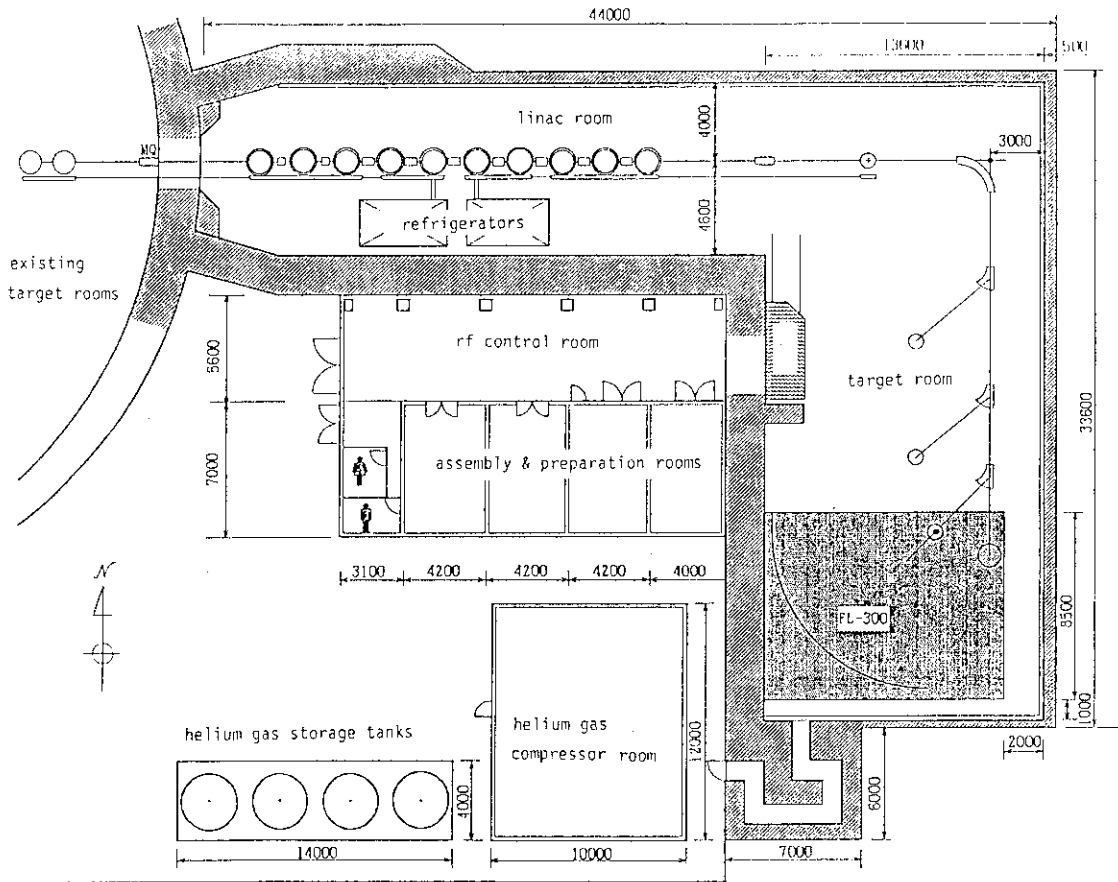


Fig. 1 Layout of the building

The slit can be slided in the X or Y direction across the beam, with the relative position to the faraday cup system unchanged, in order to measure the ion intensity distributions at 50 points within the beam. The faraday cup system is the 30 channels current detection system, 30 thin conductors and ceramic plates being piled up alternately, and is connected to the 30 channels current amplifier system. With this system, the intensity distributions of the ions passing through the slit can be measured with 30 fractions at each slit location within the beam. The control for driving whole system is performed with the HP-310C technical work station through the CAMAC system. Table 1 shows the basic specification for the emittance measurement device.

Table 1 Emittance measurement device

Distance slit-detector	500mm
Slit aperture opening	0.1 × 40mm
Maximum allowable current	100 μA
Minimum detectable current	10nA
Maximum ion beam energy	350KeV
Maximum ion beam angle	± 9mrad
Position resolution (detector)	0.1mm

3. Measurement of ion beam emittance

In October 1989, the emittance measurement devices was installed to the injection beam line when the test operation on the ion source test apparatus finished. The emittances were measured for the ion beams extracted from 4 types of ion source system²⁾. At the measurement, the ion beam handling were performed like as the normal operation as for the every experiments. That is, the intensity of the ion beam were handled to be maximized on the faraday cup after the injection magnet. Also beam intensity were kept constant more than 1 μA.

Figure 2 shows the whole devices along the injection beam line together with emittance measurement device. The ion beam from the sputter ion source, so called SNICS- II ion source, are sometimes out of the detector position, because of the large ion beam size and beam divergence. On this situation, the ion beams were readjusted using quadrupole lens and steering

devices to come into the detector but not to become impractical beam condition.

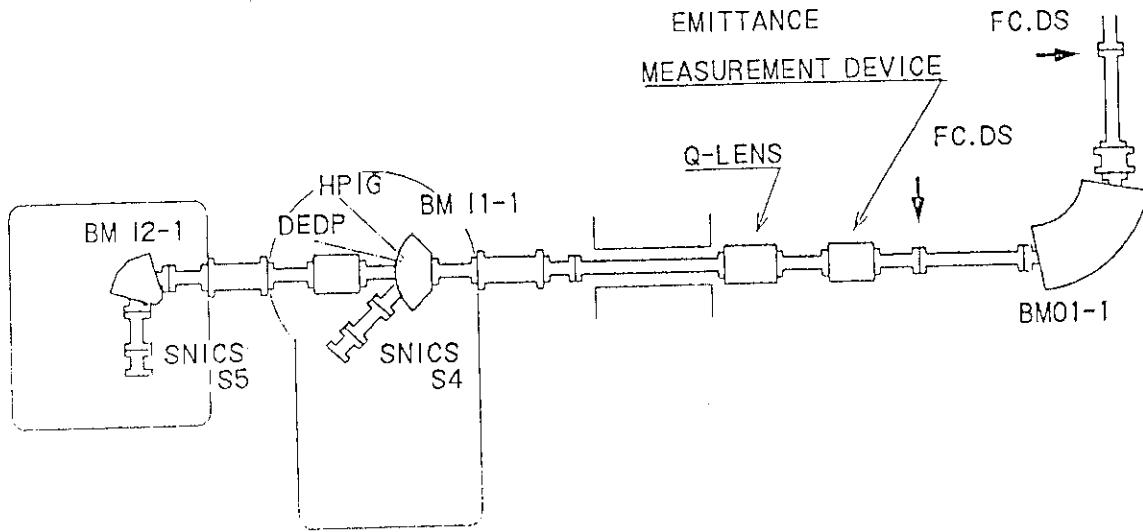


Fig.2 Emittance measurement device and ion injection line

Table 2 shows the results of measured emittance values obtained on the beam line and the ion source test apparatus. The test data show a little bit different values from those on the beam line. It is caused by different geometrical size of beam transport and optical elements. The emittance values for the various ion sources have been reported by some laboratories³⁾⁴⁾. But our emittance measurement device had to be installed behind some optical elements, so that a fraction of ion beam might be cut out by some limiter such as apertures. Therefore the emittance values of table 2 are not always in agreement with the results of others.

Table 2 Summary of emittance values

Ion source	Ion species	Normalized emittance(80%)	
		X / Y	π mm.mrad MeV ^{1/2}
SNICS	O	4.68/2.47	(4.95/2.58)
S4 (S5)	Cl	3.98/3.44	(4.03/4.03)
	Ni	3.49/3.39	(3.82/3.01)
	Ag	3.28/2.90	(3.17/2.90)
	Au	3.17/2.69	(3.60/3.44)

DEDP	D	0.76/0.82	(Table 2 cont.)
HPIG	Cl	1.03/1.41	

Results of ion source test apparatus

SNICS	C	5.32/4.55	
NISS	C	5.33/4.27	
(Sputter source)	O	5.46/4.43	
HPIG	F	1.55/1.22	
	Br	1.09/0.87	

4. Conclusion

We have got expected emittance values for various ion beams from several ion sources. And we have got some information other than the emittance values that can be used to diagnose the ion beam operation. Measured emittance data will be utilized to accelerator operation and adequate ion optics calculation. The measuring speed is an important factor when automated operation of the tandem accelerator is carried out. The present facility needs approximately 280 seconds to get data for both the X and Y directions, so we will have to develop higher speed measuring device.

References

- 1) S.Kikuchi and S.Takeuchi, JAERI-1308 (1987)
- 2) T.Yoshida, E.Minehara and S.Abe, JAERI Annual Report 12 (1988)
- 3) G.D.Alton, J.W.McConnell, S.Tajima and G.J.Nelson, Nucl. Instrum. & Methods. in phys. res., B24/25, 826(1987).
- 4) A.Nadji, F.Haas, G.Heng, Ch.Muller and R.Rebmeister, Nucl. Instrum. & Methods. in Phys. res., A287, 173(1990)

1.4 ELECTRON LINAC OPERATION AND IMPROVEMENTS

Katsuo MASHIKO, Tokio SHOJI, Nobuhiro ISHIZAKI
Hidekazu TAYAMA and Hideaki YOKOMIZO

Department of Physics, JAERI

1. Operation

The JAERI 120 MeV electron linear accelerator (linac) has been steadily operated with a repetition rate of less than 150 pps during a fiscal year 1989. A power-on time was totally summed up to 1,427 hours and a beam time was actual was 761 hours for experimental researches. A summary of the linac operating conditions from April, 1989 through March, 1990 is shown in Table 1 for each experimental program. The experiments of the beam injection for a compact electron storage ring (JSR) has started in this fiscal year. Around 55 % of the total beam time was for the JSR experiments.

Table 1 Machine Time and Output Beam for Research Program in 1989

Research Program	Time (h)	Ratio (%)	Energy (MeV)	Rate (pps)	Length (ns)	Current (μ A)
Neutron Cross Section, (Time of Flight Method) Neutron Radiography	220.8	29.0	120	150	25	12
Positron Experiment (Emission of monoenergetic Positron)	116.9	15.4	100	50	1000	10
JSR Injection	418.2	54.9	~150	0.5~1	1000	<1
Tuning and Test Operation	5.1	0.7	100~180	50~150	1000	~30
<u>Total</u>	<u>761.0</u>	<u>100.0</u>				

The period of no operation was dedicated to various improving and repairing works for the linac and experimental facilities.

(1) Replacement of the heat exchanger for the klystron cooling system (2 weeks)

(2) Installation of a JSR radiation shield, a profile monitor in the storage ring, a window viewer, remodeling of the linac beam transport system and replacement of the pump for JSR's klystron cooling system (3 weeks)

(3) Shut-down during a summer season (2 weeks)

(4) Repairing of the neutron target (1 week)

(5) Remodeling of the injection system to the JSR (BTK)(2.5 weeks)

2.The JSR experiment

The JSR has been constructed and connected to the linac in March, 1989. The experiments on electron beam accumulation in the JSR was started late in April, 1989 and the beam accumulation was first succeeded in July. Maximum stored beam current up to now is 160 mA.

The maximum stored beam current as a function of time of the operation for aging is shown in Fig. 1. The figure shows a distinct difference of the beam increase rate at the time of 300 hrs and also shows a time, ~450 hrs, at which the design value of stored beam current, 100 mA, has been achieved. Energy spectrum and peak pulse shape of the injected electron beam from the linac to the JSR are shown in Figs. 2 and 3, respectively. The characteristics of the beam are; Energy is 130 - 150 MeV \pm 0.5 %, current 30 - 40 mA, pulse width 0.3 μ s (FWHM) and beam radius 5 mm ϕ at the middle position of the transport system.

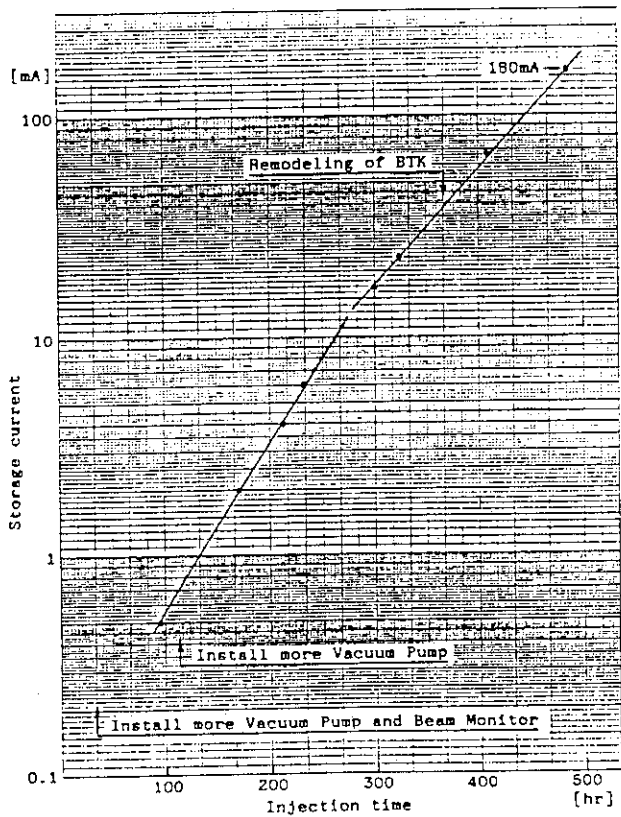


Fig. 1 JSR Storage Current

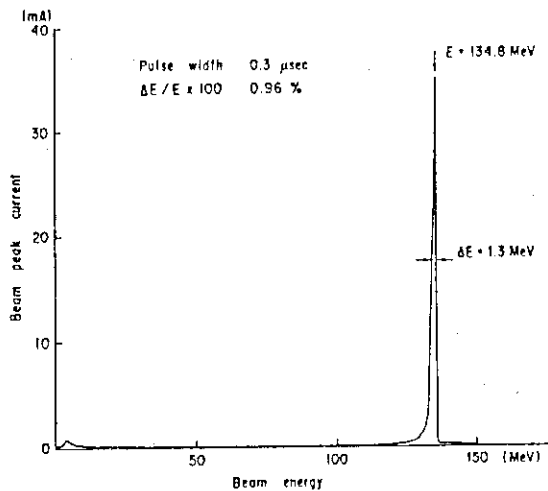
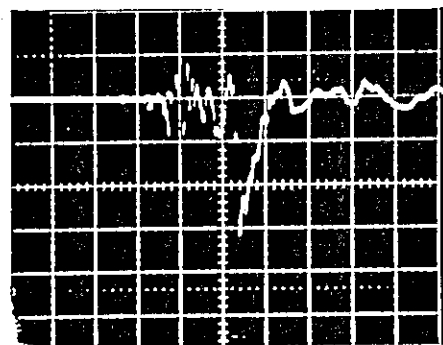


Fig. 2 Energy Resolution



X-Axis 1 μ s/div, Y-Axis 0.1 V/div

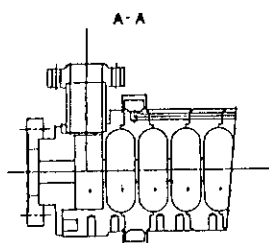
Fig. 3 Waveform of Beam Current

3. Maintenance

Unscheduled maintenances were due to the breakdown of a main klystron and the replacement of the heat exchanger assembly. The klystron damaged due to vacuum trouble was used for a total operation time of 6,850 hours. The heat exchanger was operated for about 4 years, which was broken by the electrolytic corrosion due to the bad quality of the water in the secondary circuit. The replacement of a vacuum chamber of stainless steel by an aluminum one in the beam transport tube and the remodeling for the JSR injection system were also carried out as the scheduled maintenance.

4. Improvement

(1) New accelerator structure



The new traveling wave type accelerator structure has been fabricated, the final adjustment being done at the factory, being accompanied with an RF-characteristic adjustment, in March, 1990 as an

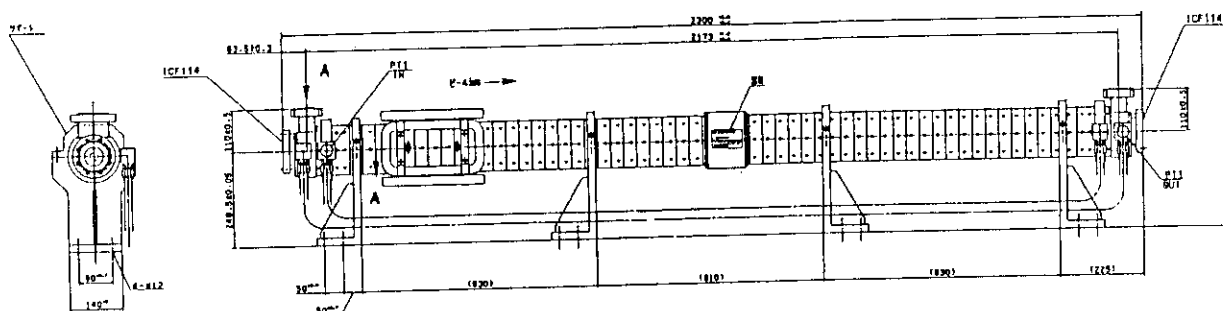


Fig. 4 Side View of New Accelerator Structure

alternate of the #1 accelerator structure (2 m long) of the linac.

A side view of the structure is shown in Fig. 4.

The new structure, which has semi-constant gradient field and U shaped cavities, is expected to have a gain of 1.33 times higher than the old conventional disk & cylinder type. A comparison of the microwave characteristics of the new one to the old one is shown in Table 2. After

	Old type	New type
Frequency	2856.75±0.05 MHz (40 °C Vac.)	2856.75±0.05 MHz (40 °C Vac.)
Mode	2/3π	2/3π
Power Rating	20 MW (20 kW Ave.)	20 MW (20 kW Ave.)
Phase Property	±3°	±2°
VSWR	f _o : 1.05 f _o ±1 MHz : 1.08	f _o : 1.05 f _o ±1 MHz : 1.08
Length	2.3 m (2.173 m eff.)	2.3 m (2.173 m eff.)
Q _o	13,300	14,900
γ	48 MΩ/m (2a=24~20)	67 MΩ/m (2a=24~20)
τ	0.118 N/m	0.146 N/m
E _o	15 MV/m	20 MV/m

Table 2 Accelerator structure characteristics

installation at the linac and aging with the high power RF field, this structure will be operated with the electron beam.

(2) Radiofrequency electron gun (RF gun)

An RF gun was newly fabricated in March, 1990 in order to obtain a low emittance and high brightness electron beam. This is expected to simplify linac injection system. A cross sectional view of the RF gun is shown in Fig. 5. The main characteristics is given in Table 3; the field strength being 100 MV/m and Q-factor 12,000. The resonator cavity of s-band (2856 MHz) contains lanthanum hexa borate (LaB₆) cathode. The microwave power of less than 6 MW is required to excite the cavity. The gun will be installed, aged with high RF field and tested to observe ion-bombardment effect before an actual beam test has been carried out.

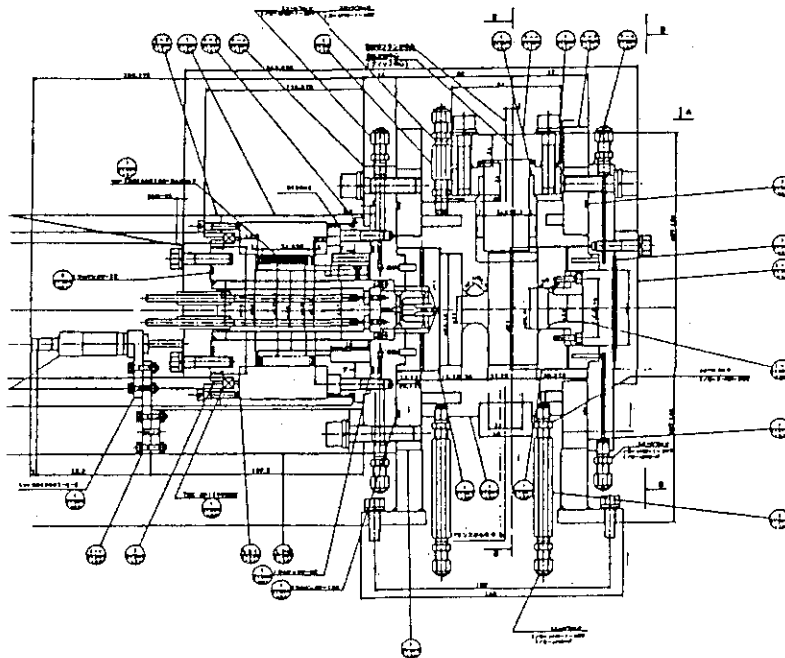


Fig. 5 Side View of RF Gun Structure

Table 3 RF Gun Characteristics

Frequency	2856±1.5 MHz	Q Value	>12,000
Cathode Cavity Length	26.25 mm	Output Beam Energy	>5 MeV
Acc. Cavity Length	57.25 mm	Cathode Material	LaB ₆
Acc. Cavity Diameter	83.18 mm	Cathode Diameter	5 mmφ
Aperture Diameter	20.0 mm	Input RF Pulse Width	1~2.5 μs
Nose Diameter	20.0 mm	Input RF Pulse Rate	<150 pps
Cathode Field	100 MV/m	Cathode Output Current	>35 A (at 10 ps)
Cavity Field	100 MV/m	Vacuum	<1×10 ⁻⁸ torr
Input RF Power	~ 6 MW	Vacuum Leakage	<5×10 ⁻⁹ torr/s

1.5 OPERATION OF JSR

Kenichi YANAGIDA, Hideaki YOKOMIZO, Shunji HARADA,
 Minoru YOKOYAMA, Takahisa NAGAI, Katuo MASHIKO*,
 Nobuhiro ISHIZAKI* and Hidekazu TAYAMA*

Office of Synchrotron Radiation Facility Project,
 *Department of Physics, JAERI

JSR(JAERI Storage Ring) has been in operation since April 1989. Some quantities were measured at injection energy of 150MeV. A maximum beam current is reached up to 160mA. A beam lifetime is measured to be 5.8min at the beam current of 100mA which is mainly determined by a collision with gas desorpted by synchrotron radiation.

INTRODUCTION

JSR is an electron acceleration/storage ring which is located in the linac building. Principle parameters of JSR is given in Table 1. The descriptions of design, construction and performance of components are given in previous papers¹⁾²⁾³⁾⁴⁾. This paper describes the operation modes and measurements.

Table 1 Principle parameters of JSR.

Storage energy	300MeV
Injection energy	150MeV or less
Circumference	20.546m
Bending radius	0.835m
Bending magnet field	1.2T at 300MeV
Tune	x 2.23
	y 0.83
Energy loss	0.86keV/turn at 300MeV
RF frequency	116.7MHz
Peak RF voltage	30kV

The linac is used for several kinds of experiments besides JSR. The machine time for JSR is dedicated one or two weeks a month. The total machine time was only 420hours for JSR in fiscal year of 1989. The major improvements are the installation of sputter ion pump(400l/sec) and titanium getter pump(800l/sec) on the RF cavity, the power up of RF-knock out electrode power supply,

the improvement of beam transport line and the use of button type electrode for ion clearing.

OPERATION MODE

JSR takes Chasman-Green type lattice with a superperiodicity of three. There are long straight sections of ~1.5m even in the small ring. Each cell is composed of two bending, single quadrupole and two pairs of doublet quadrupole magnets. The betatron and dispersion functions are variable by changing those quadrupole magnet. It is possible not only to suppress the dispersion but also to leave it on the long straight section. Fig.1, Fig.2 and Fig.3 are the betatron and the dispersion functions at the same operating point; around $V_x=2.23$ and $V_y=0.83$. These operating modes are named mode A, mode B and mode C.

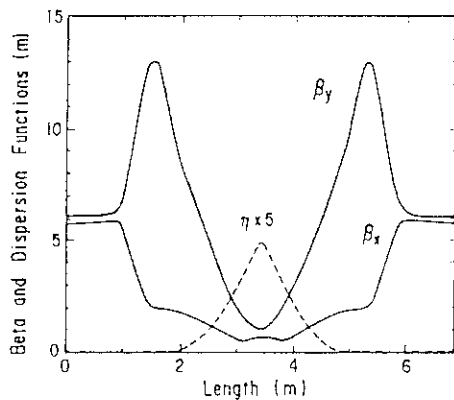


Fig.1 Beta and dispersion function at mode A.

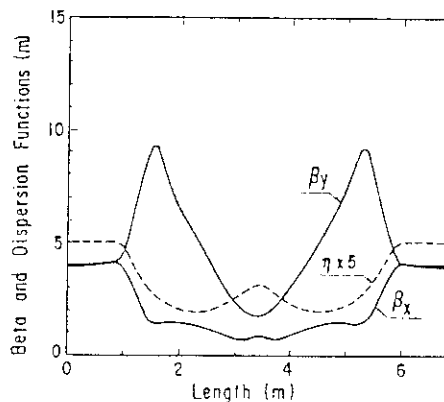


Fig.2 Beta and dispersion function at mode B.

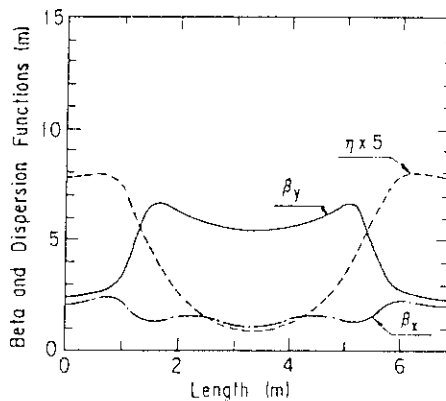


Fig.3 Beta and dispersion function at mode C.

MEASUREMENT

The experiments were mainly carried out at mode C. The beam current stored in JSR is measured by DCCT (D.C. Current Transformer). Fig.4 shows a time evolution of the beam current during injection and storage at 150MeV. It is possible to accumulate up to 100mA within 2min.

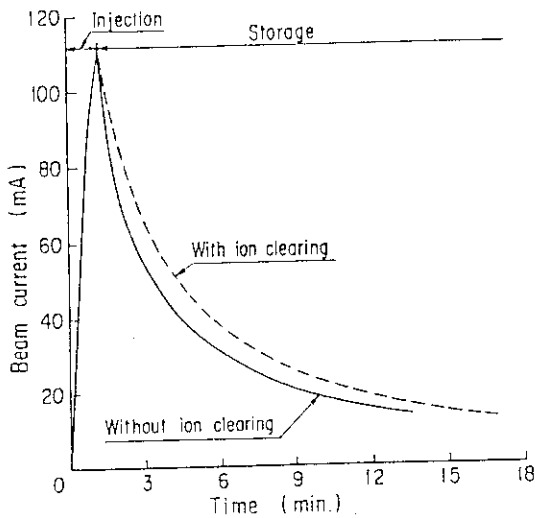


Fig. 4 Time evolution of beam current.

In order to remove the trapped ions on the orbit the ion clearing voltage is applied. The beam lifetime becomes longer when the ion clearing voltage is put on.

A relation of the beam current I and the decay rate $\frac{dI}{I dt}$ which is an inverse of the beam lifetime is given as $\frac{dI}{I dt} = aI + b$ in Fig. 5 where a and b are some constants.

On the other hand the vacuum pressure of the beam chamber also depends on the beam current. (see Fig. 6) The decay rate is enhanced due to outgassing from the chamber walls in the presence of high stored beam current. The time integration of stored beam current $IT = \int I dt$ is used as a quantity how the vacuum chamber has been aged. The chamber wall of $IT = 0.43A \cdot h$ is better aged comparing with one of $IT = 0.33A \cdot h$ by synchrotron radiations.

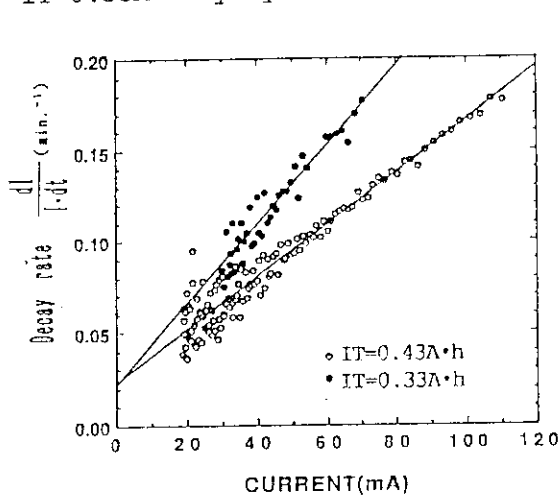


Fig. 5 Measured decay rate.

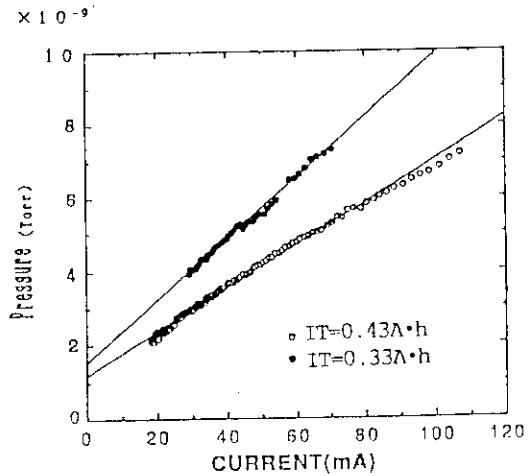


Fig. 6 Vacuum pressure of beam chamber.

Fig. 7 is the tune diagram around operating point. When the operating points are on resonance accumulation becomes difficult. In this figure case A and case B are the operating points where the beam is accumulated and is not accumulated respectively.

The chromaticity ξ is defined as the variation of betatron frequency ν with momentum P of stored electrons;

$$\xi_{x,y} = \Delta\nu_{x,y} / \frac{\Delta P}{P}$$

The chromaticity is measured by the corresponding tune shift as the RF frequency. The results of measurement are shown in fig.8 and the values are $\xi_x = -1.82$, $\xi_y = -1.28$. The chromaticity measurement was carried out at mode B.

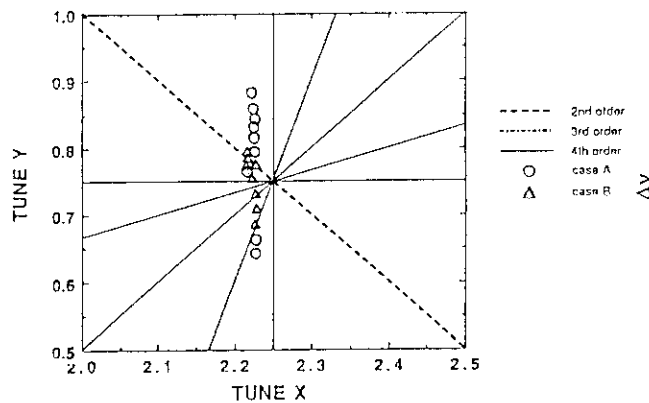


Fig.7 Tune diagram around operating point.

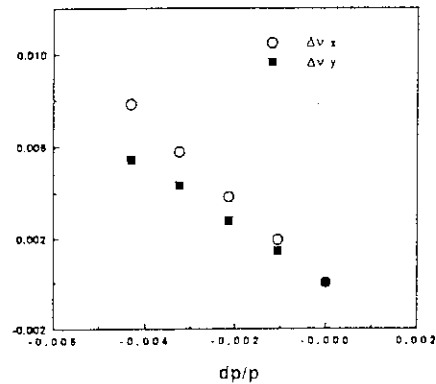


Fig.8 Measurement of chromaticity

CONCLUSION

Here is described the experiment around typical working point; $\nu_x=2.23$, $\nu_y=0.83$ and the dispersion function remains on the long straight section. A vacuum chamber is not sufficiently aged by synchrotron radiation. The lifetime is mainly determined by vacuum condition.

REFERENCES

- 1) H. Yokomizo, et al., Proc. European Particle Accelerator Conf., Vol.1, 445 (Rome, 1989)
- 2) H. Yokomizo, et al., Rev. Sci. Instrum., 60, 1724 (1989)
- 3) H. Yokomizo, et al., To be published Proc. 14th Int. Conf. on Synchrotron Radiation Instrument, SRI-89 Berkeley (1989)
- 4) S. Harada, et al., Particle Accelerators, Vol.33, 39, (1990)

1.6 BRIGHTNESS ENHANCED INTENSE SLOW POSITRON BEAM PRODUCED USING AN ELECTRON LINAC

*Yasuo ITO, Saburo TAKAMURA, *Masafumi HIROSE, **Osamu SUEOKA, ***Ikuzo KANAZAWA, and ****Sohei OKADA

*RCNST, University of Tokyo, Department of Physics, JAERI,
Faculty of Engineering, Yamaguchi University, *Tokyo Gakugei University, ****Takasaki Research Establishment, JAERI

Introduction

Intense pulsed slow positron beam was extracted from a 100 MeV electron Linac of JAERI-Tokai using solenoid transport tubes⁽¹⁾. The intensity of the slow positron beam was about 3×10^7 e⁺/s at 1/10 of full power operation (at 10 μ A average electron beam current).

In order to use the beam for various positron spectroscopies as positron scattering, positron diffraction, positron re-emission microscopy, and positron annihilation induced spectroscopies, the beam was transferred from the solenoid magnetic field to non-magnetic field, and then was brightness enhanced. The beam size was reduced from 10 mm ϕ (in the solenoid magnetic field) to 0.5 mm ϕ after two stages of re-moderation. The intensity of the brightness enhanced positrons has not yet been determined prevented by the pulsed mode, but the beam is probably the strongest of the brightness enhanced slow positrons at present. The details of the beam line construction and possible improvements are reported.

Beam Line Configuration

Slow positrons were produced by irradiating electron beam on water-cooled converter. The converter was made of several Ta plates, with the last plate serving as the wall of the vacuum chamber. The positron moderator, placed behind the last Ta plate, was W sheets either as the Venetian-blind type or as the transmission type geometry. The slow positrons were transported through solenoid tubes to the experimental sec-

tion.

In order to construct the brightness enhanced positrons, it is necessary to transfer the beam from the magnetic field to non-magnetic one. This was performed by accelerating the positrons before the end of the solenoid coil, and simultaneously suppressing the dispersion of the beam using static electric tube lens (Fig. 1). Since designing of this stage was difficult, the optimum configuration was determined experimentally. The fast component could be eliminated at this stage.

Positrons extracted from the solenoid magnetic field were focused on a reflection type re-emission moderator made of W(110) single crystal (W_1 of Fig. 1). The brightness enhancement was performed twice. The brightness enhanced positrons thus produced is to be introduced to a positron scattering chamber.

Brightness Enhancement

Positrons extracted from the solenoid magnetic field was focused on the re-emission moderator (W_1) with an energy between 2-5 keV. The re-emitted positrons were again accelerated and focused on a second re-emission moderator (W_2), and the final beam profile, measured by MCPA, was 0.5 mm in diameter.

Although the whole beam line and the brightness chamber could be evacuated to better than 10^{-9} Torr, most of the preliminary experiments were performed in a lower vacuum. We noticed that slow protons, with an intensity comparable to that of the slow positrons, are also transported through the solenoid tube. (This fact is interesting and important from a different viewpoint). They are most probably formed by desorption of H from the W surface on electron/positron bombardment. Since such protons accompany positrons all the way along the path of the positrons, a magnetic deflector was mounted instead of an electric field deflector to separate protons from positrons.

In brightness enhanced slow positron beams based on RI positron sources, it is customary to hold the positron source to a high positive electric potential so that the brightness enhanced positrons come at the ground potential. This was also done in our beam line, i.e. the whole solenoid transport tubes together with the associated components and the

optics up to W_1 were held at high positive potential. The main leak of the high potential resistivity occurred at the cooling water of the Ta converter, which became even more substantial during electron beam irradiation.

Conclusion and Improvements

Brightness enhanced intense slow positron beams has been obtained. The beam size is 0.5 mm in diameter at present, but it can be made much smaller by improvements of the optics of the brightness enhancement. Unfortunately the positron beam is not stable enough as compared to the RI slow positrons. A small difference in the condition of electron beam irradiation at the Ta converter results in a change in the spot position at W_1 , which affect all the optics thereafter. After further improvements on these points, the beam will be used for various experiments.

Brightness - Enhanced
Intense Slow Positron Beam

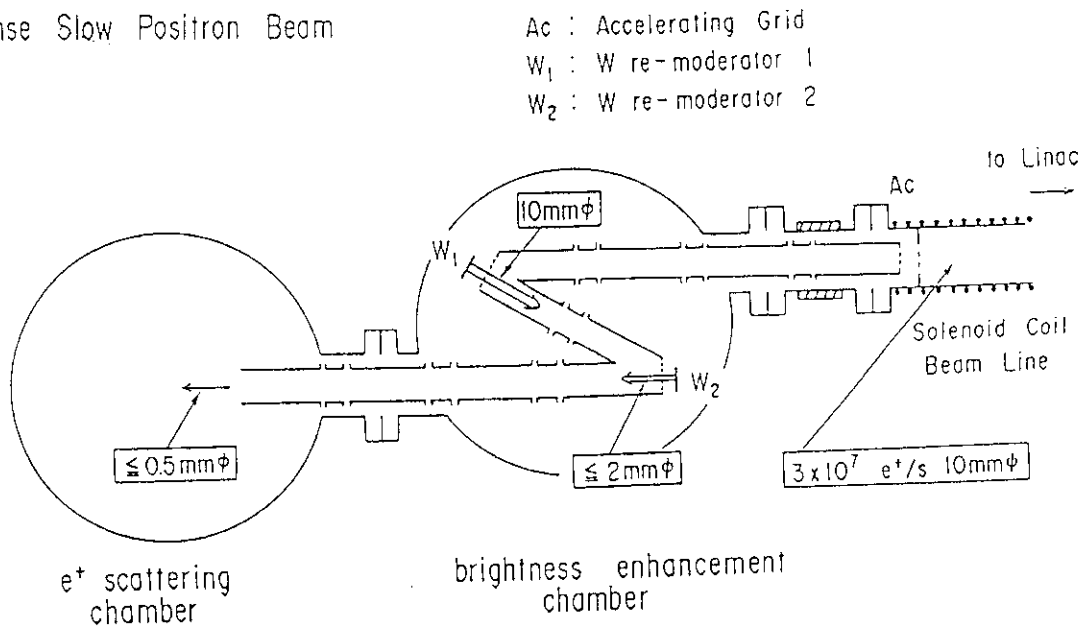


Fig.1 Configuration of the beam line around the brightness enhancement chamber. The slow positron beam enters the brightness enhancement chamber from the right.

Acknowledgment

This work has been carried out as one of the projects of the Universities-JAERI Collaborative Project Research Program. It is also supported financially in part by the Grant-in-Aid of the Ministry of Education, Science and Culture. Other contributors are Drs. Yoshitada Murata, Ayao Ichimiya, Masayuki Hasegawa, and Toshio Hyodo.

References

- 1) Y. Ito, O. Sueoka, M. Hirose, M. Hasegawa, S. Takamura, T. Hyodo and Y. Tabata, in Positron Annihilation, L.D.-Vanpraet, M.R. Dorikens and D. Segers, eds., (World Scientific, 1989), p.583
- 2) O. Sueoka, M. Yamazaki and Y. Ito, Jpn. J. Appl. Phys., 28, L1663 (1989)

1.7 DESIGN OF THE CONTROL SYSTEM FOR THE JAERI FREE ELECTRON LASER

Masayoshi SUGIMOTO

Department of Physics, JAERI

The JAERI Free Electron Laser requires a compact and flexible control system including the fast monitoring of the electrons and photons. The device control section consists of the standard i/o interfaces: GPIB and CAMAC. The stand-alone CAMAC crates controlled by personal computers, manage each part of the system: (1) injector, (2) accelerator and (3) undulator-optical resonator. Such units are linked by network to a main control unit. The control software is designed to adapt for frequent modifications of the hardware.

Introduction

The JAERI Free Electron Laser(FEL)¹⁾ has three major blocks of the components:

- (1) the injector which consists of electron-gun, sub-harmonic buncher(SHB), buncher, and analyzing magnet with associated injection beam line components.
- (2) the superconductive accelerator(SCA)s which consists of two pre-accelerators with single cell and a main accelerator with multi-cell configuration, and the cryogenic system and high power RF system to operate the SCAs.
- (3) the undulator and the optical resonator to generate an infrared laser and the photon measurement system.

The number of the devices to be controlled is not so large. However, many kinds of the control items exist and they would be changed along with the progress of the research and development. So, the primary requirement to the control system of the JAERI FEL is the flexibility. We employ a standard hardware to save the development time and cost for the hardware. But the control software should be developed as it can be adapted for the frequent modifications of the hardware and its configuration.²⁾

The another important issue is the realtimeness. The FEL system is operated in 10 Hz, 1 ms width of macro-pulse. It is desirable to detect the mismatched parameters occurred at the previous macro-pulse and remedy

them or inform to the other control units, before the next macro-pulse is coming.

The interlock system for emergency is prepared as the separated system, and communicates to the control system through the network.

Basic concept

Fig. 1 shows the block diagram of the control system for the JAERI FEL. In this case, the system is divided into three blocks as described above. Each block is controlled by a dedicated local control unit with the standard interfaces: CAMAC and GPIB. Since these local control units are identical to each other, the configuration can be changed easily. For instance, it is possible to install one more local control unit and to control all beam transport components, separately.

We are aware of the limitation of the data transfer rate of the CAMAC bus system which is matured but not up-to-date one. And it may be replaced by some other system, e.g. the VME bus system, in future. In this sense, the control software must be designed for a virtual bus system which may support several types of bus architecture.

Our system has no host computer, which controls all local control units as the slave computers, in a usual sense. The main control unit is the same one used in the local control units. The difference is that it has a lot of operator interfaces, such as large screen monitor, touch panel, dials and knobs, and a mass storage to serve and acquire the control data. In other words, any local control units may become a host and a backup machine, by moving the functions of the operator interface. From the view point of the control software, the computers have equivalent kernels and the processes can be migrated from one computer to the other through the network. There are two kinds of the communication in the network: (1) a short message fitted in a single packet, such as execution commands, and (2) a long text, such as downloaded program or retrieved data file. Ideally, two different networks based on the packet switching and the circuit switching, respectively, cooperate to avoid the deadlock due to the collision between short messages and long texts.

Another crucial point to be considered is the assistant system for the operators. The most primitive one is the help facility to conduct the machine start-up and shutdown processes. The next step is the semiautomatic operation using the control expert system. The final

objective is the full-automatic operation using the self-diagnosis and prediction capability of the advanced control system.

Actual control system and tools

The devices are directly controlled and monitored by CAMAC modules of digital i/o, analog i/o and GPIB interface. The CAMAC is controlled by a 32-bit personal computer(NEC PC-9801RA2, 20 MHz i80386 CPU). At least, a local control unit consists of the personal computer, its add-on boards for networking and crate controller interface, a CAMAC crate/crate-controller, a GPIB interface and some other CAMAC modules.

For the first stage, each local unit is developed as an isolated system and served for the installation check.

The kernel would be developed to work under the 80386's protect mode, and many application tools are executed using a VM mode. The kernel will be very small because most tasks of the monitor is separated as the independent processes. This may be done using a computer language, Forth³⁾, which is portable and flexible, but not popular. Other high-level languages are also necessary to develop the advanced control system with an assistance capability.

Operator console consists of a CRT and a keyboard of the personal computer, basically. This is due to that the operator would be a machine in some time at the advanced system. Optionally, the operator can communicate with the system using a mouse, a touch panel, etc. under the graphical user interface of the control system. There are more user interfaces, such as a spreadsheet style or a database style, as a choice of the operator.

To achieve the efficient control, it is necessary to develop some tools for the control system :

- (1) the database manager to supply the historical information about the control parameters, and acquire the new information,
- (2) the on-line beam transport program to diagnose the status of the beam condition, and
- (3) the performance analyzer to simulate and test the message transfer among the control units.

Conclusion

The JAERI FEL control system consists of the accelerator control and

the optical measurement, which are closely related to maintain the laser oscillation. Each component is controlled by a local control unit with no time delay, and is monitored by a main control unit through network. Though the standard hardware is employed, the software for the distributed control system must be developed. The associated software tools, control database manager, on-line beam transport program and message transfer simulator, are also need to be developed.

References

- 1) Y. Kawarasaki et al., Nucl. Instrum. & Methods A285 (1989) 338.
- 2) M. Sugimoto and Y. Kawarasaki, Proc. of the 14th Linear Accelerator Mtg. in Japan, Sep. 7-9, 1989, p.322.
- 3) Y. Kawarasaki and M. Sugimoto, Proc. of the 7th Symp. on Accelerator Science and Technology, Osaka, Japan, Dec. 12-14, 1989. p.262.

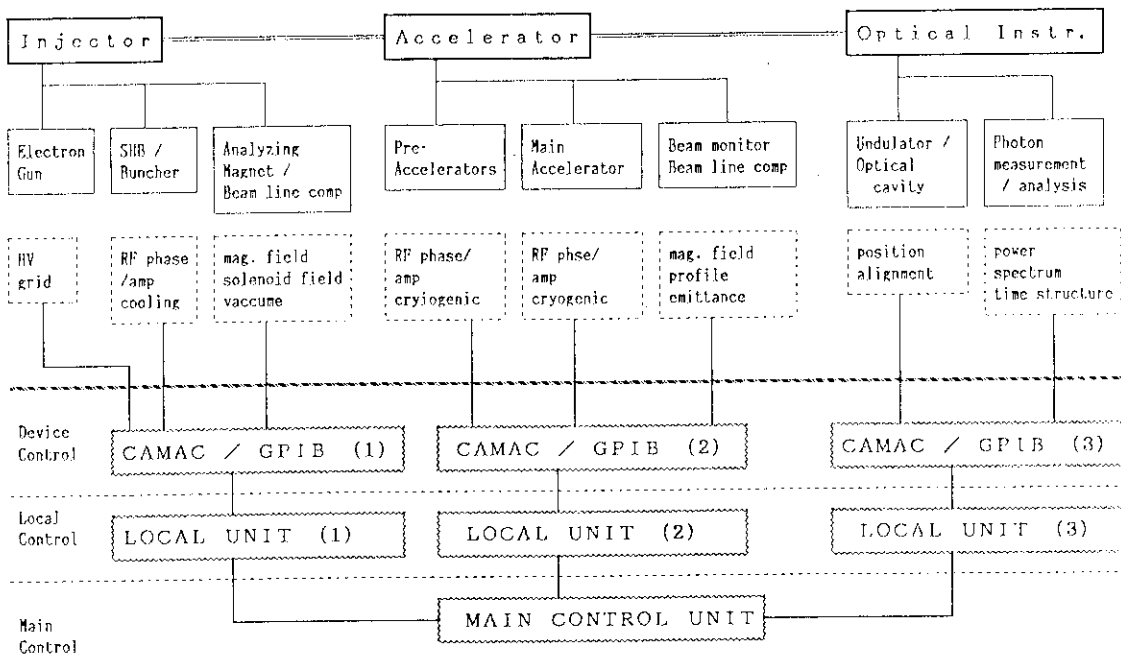


Fig.1 Block diagram of the JAERI Free Electron Laser control system

1.8 Optical Transition Radiation Beam Monitor for an FEL Experiment

Jun SASABE^{*}, Ryoichi HAJIMA^{**}, Toru UEDA^{**}, Yoichi YOSHIDA^{**}
^{*} Department of Physics, JAERI, ^{**} Nuclear Engineering Research Laboratory, Faculty of Engineering, University of Tokyo.

This report describes a preliminary experiment on Optical Transition Radiation(OTR) for preparation of a beam diagnostic system and discuss further improvement. The experiment has been carried out in viewing the OTR lights from a Kapton foil with an I-CCD camera under passage of the electron beam from a 14MeV linac at Tokyo University.

1. Introduction

Beam diagnostics play an important role to optimize beam characteristics (peak current, emittance, energy, beam radius et al.), especially in FEL accelerators. Precise information of the beam position, furthermore, is necessary to align the axes of a wiggler and an optical resonator with respect to the beam. Ceramic has been used as a beam position and profile monitor. Combination of such a monitor with a quadrupole magnet has been used to measure the beam emittance. However, this method has a drawback; it should intercept the beam destructively, and further which would cause intense X-ray emission and the damage of ceramic screen and optical window. In addition, the measured value of beam emittance is the average value among successive macropulses.

A new beam diagnostic method using unique OTR light has recently been proposed and studied¹⁾ for FEL experiments.²⁾⁻³⁾ Fig.1 shows behavior of the OTR light when charged particle beams pass through the boundaries of two materials of different dielectric constant(e.g., vacuum and a thinner metal foil) in the direction of normal (Fig.1,left) and oblique incidence(right). OTR light is generated at these boundaries and emitted linearly polarized in forward and backward direction with respect to passing beams in an angle of some degrees. Fig.2 shows theoretical angular-distribution for normal incidence and 14MeV beam energy calculated from formula in reference¹⁾. This distribution is called an OTR pattern. Angle of peak intensity θ_p presents the beam energy ($\theta_p \approx 1/\gamma$: γ is just the energy of the electron expressed in units of its rest energy) and width of the pattern presents beam emittance.

Therefore, the OTR light includes such valuable informations as energy, emittance, beam profile, and beam position. It should be further emphasized that this method can obtain temporal information by using a higher-speed I-CCD camera (CCD camera with an Image-Intensifier). A thinner foil affects less degradation; less X-ray emission, especially in comparison with a ceramic screen.

2. Experiment

Fig.3 shows schematically experimental set-up. Two chambers are located in behind of bending magnet section of the linac. The first chamber (Chamber-1) includes a ceramic screen (Desmarquest AF995R) which can be rotated from outside, hence, e^- beam can pass through to the next chamber. The second chamber (Chamber-2) includes ceramic screen and OTR foil (Kapton: $50\mu\text{m}$). These screens can be exchanged in position by rotating a knob. The ceramic screen was also used to record the e^- beam position. Since the OTR light is so weak (e.g., 1 photon per 100 electrons⁴), an Image-Intensifier (Hamamatsu C4273) with a zoom lens was used to get enough and short time resolution (beam pulse width: $6\mu\text{s}$). The synchronization among linac, I-I, video memory and CCD was secured by a triggering circuits. Both beam images on the foil were recorded in the video memory and these data were transferred to the image processor which analyzed a precise horizontal and vertical distributions.

Our experimental procedure was:

- 1) two beam positions on the Desmarquest were recorded (Mirror A and B are on the resettable plate),
- 2) the He-Ne laser was aligned to coincide with an axis between these positions,
- 3) the screen foil was exchanged to OTR foil in the Chamber-2,
- 4) I-CCD camera was aligned with the reflected He-Ne laser light from the OTR foil.

For the beam profile, the lens was focused on the OTR foil and for the OTR pattern, the lens was focused at infinity.

The linac was normally operated with beams of about a $6\mu\text{s}$ long macropulse, peak current 120mA (at the exit of Chamber-2), beam energy 14MeV.

3. Results and discussion

The I-CCD camera was found to have the sensitivity enough to detect weak OTR light. Fig.4 shows the OTR light on the Kapton foil. However, the light in the figure is mixture of the backward OTR light and the background lights. These background lights consist of a reflected forward OTR light from the Kapton foil and a backward OTR light from a titanium beam window, because the distance of the

OTR foil to the window is unfortunately too short ($\approx 20\text{cm}$). Furthermore, the thermal effect of the e^- beam deformed the surface of this foil. Because of the backward lights and the foil deformation, the OTR pattern could not be obtained. In our configuration, it was found that the foil which did not transit the scattering lights would be better. An aluminized ($\approx 1\mu\text{m}$) synthetic quartz is a second choice for an OTR foil. Before the OTR experiment using the foil above mentioned, the life time test on this material was done in air ($6\mu\text{s}$ pulse width, 160mA peak current, 12.5pps , 33minites) and no damage was obserbed.

In conclusion, as the OTR beam diagnostic method has a unique character, we will try again in the next experiment to obtain the OTR pattern and then to do so in double-foil system for getting more precise information of the beam divergence. And we will also perform the theoretical calculations of OTR.

* On leave from Hamamatsu Photonics Inc.

References

- 1) L. Wartski, et al., J. Appl. Phys. **46** 3644 (1975)
- 2) X.K. Maruyama, R.B. Fiorito and D.W. Rule, Proc. 9th Int. FEL Conf., Williamsburg, VA, 1987, Nucl. Instrum. & Methods A272 (1988) 237.
- 3) A.H. Lumpkin, et al., Nucl. Instrum. & Methods A285 (1989) 343.
- 4) R.B. Fiorito, et al., Proc. 6th Int. Conf. on High Power Beams, Kobe, Japan, 1986

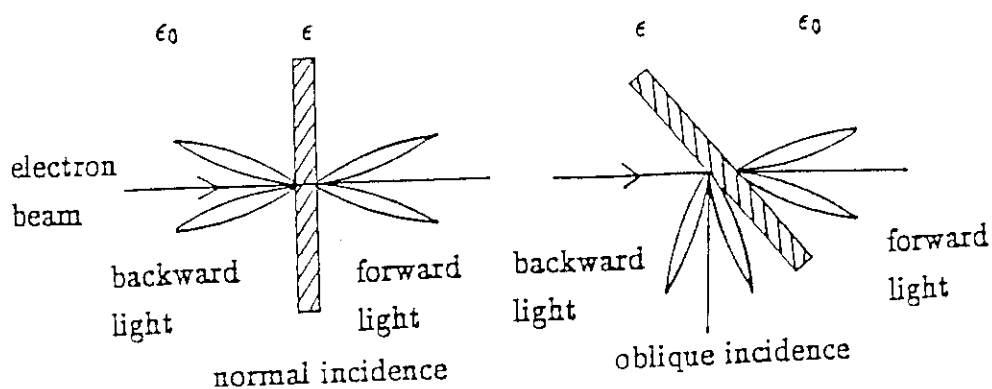


Fig.1 The Optical Transition Radiation

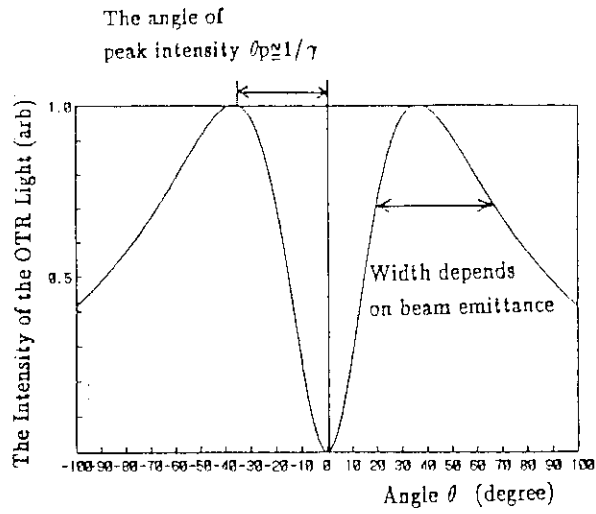


Fig.2 Theoretical angular distribution of OTR pattern(14MeV)

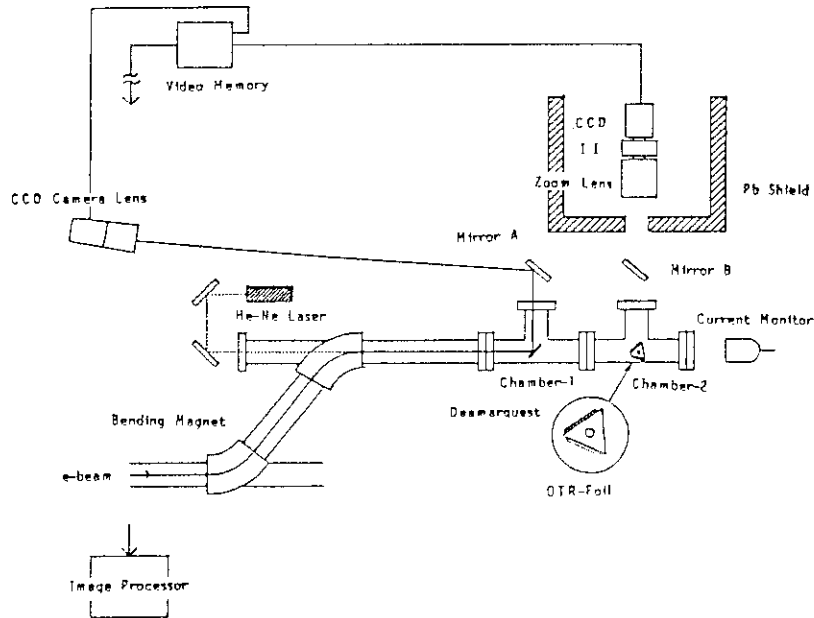


Fig.3 Schematics of the experimental set-up



Fig.4 OTR light on the Kapton foil

II CHEMISTRY AND RADIATION BIOLOGY

2.1 CHEMICAL BEHAVIOR OF RECOIL ^{16}N FORMED BY FAST NEUTRON IRRADIATION ON VARIOUS AQUEOUS SOLUTIONS

Enzo TACHIKAWA, Shin-ichi OHNO, Michio HOSHI, Masakatsu SAEKI, Yasuyuki ARATONO, Mikio NAKASHIMA, Shin-ichi ICHIKAWA, Nobuo SHINOHARA, Yoshimaro YAMANOUCHI^{*} Motoharu MIZUMOTO^{*}, Shunsuke UCHIDA^{**}, Eishi IBE^{**}, Teruo HARA^{**}, Osamu KURIYAMA^{**}, Masayoshi KONDO^{**} and Sadaharu SUZUKI^{**}

Department of Chemistry, ^{*}Department of Physics, JAERI

^{**}Energy Research Laboratory, Hitachi Ltd.,

1. Introduction

Nitrogen-16, which is produced through fast neutron absorption by ^{16}O in a water-cooled nuclear reactor, is a radioactive nuclide with half life of 7.1 seconds and decays to ^{16}O , emitting gamma ray of about 6 MeV. The movement of ^{16}N to a turbine system in a boiling water reactor causes an additional exposure of radiation to workers. Therefore, it is very important to clarify the mechanism for the formation of ^{16}N -labeled products and to establish the method to suppress the movement of ^{16}N to the turbine system. Some works have been performed from the view points of fundamental^{1,2)} and engineering³⁻⁶⁾ aspects, but the problem is still unsolved.

2. Experimental

All chemicals were JIS special grade and used without further purification. Ion-exchanged water(0.1 us/cm) was prepared by the purifier(Millipore Co., MILLI-Q). Nitrogen-16 was produced through the nuclear reaction of $^{16}\text{O}(n,p)^{16}\text{N}$, where the fast neutron was generated by the bombardment of D_2 with 14 MeV D^+ ion. The ion current of D^+ was between 0.6 and 1.5 μA . The estimated neutron flux was about $10^7/\text{cm}^2/\text{s}$ at the irradiation port. Figure 1 shows a schematic view of the experimental setup. The glass cell for irradiation (Pylex glass) was 40 mm in diameter and 120 mm in height and contained about 100 ml of aqueous solution. The radioactive gaseous and liquid products were transferred to counting cells through flow

lines (5 mm in diameter, 11 m long). Their radioactivity was measured by conventional gamma ray spectrometer equipped with 3" x 3" NaI(Tl) scintillator covered with Pb(35 cm) and B-containing(20 %) paraffin(30 cm) shields. The flow rates of the aqueous solution and gaseous phase were 0.6 l/min and 2.2 l/min, respectively. The measurement of radioactivity was started at about 10 min after the irradiation in order to allow the radioactivity to be equilibrium. The ratio of radioactivity of the gaseous ^{16}N -labeled product to total radioactivity, D, was calculated after the correction of decay for the difference of the flow rates between gaseous and liquidus phases.

3. Results and discussion

Gamma ray spectrum of aqueous solution was very similar to the reported one for ^{16}N . The same spectrum was obtained in the gaseous products, though the radioactivity was weaker than that in the aqueous solution. The half life was analyzed to be 7.0 seconds and agreed very well with the reported value of 7.13 seconds. Thus, the radioactivity in the aqueous and gaseous products was originated from the sole nuclide of ^{16}N . Figure 2 shows that the D values for pure water are between 2 and 3%. In the acidic solutions such as HNO_3 or H_2SO_4 , the values increase with the acidity, while the values decrease with increase of pH in the alkaline solutions such as NaOH , NH_4OH or LiOH . As for the neutral reagents, NaNO_2 and Na_2SO_3 , the values are different each other and those for the latter decrease to less than one-half for pure water. These results suggest that the movement of ^{16}N to gaseous phase can be suppressed by adjusting the cooling water to be alkaline, though the various technical difficulties must be conquered in the actual water-cooled reactors.

The addition of 10 vol% of NO to He carrier gas resulted in a striking effect on the D value, as shown in Fig. 2. In the present case, the solution was initially pure water. The experimental value was plotted at pH=3.4 based on the analytical results of the final solution, as is shown in Table 1. The D value is 30% higher than that for nitric acid solution. As is seen in the table, the concentration of NO_2^- for NO-added solution is very high compared to the other solutions. Though the consistent mechanism to explain the formation behavior of the gaseous products for each reagent has not been drawn from the present limited experimental results, the effect of NO-addition may imply that NO_2^- is the precursor of the gaseous

product. However, though the amount of NO_2^- is relatively large in the case of 10^{-4} mol/l NaNO_2 solution, the D value is lower than those in the nitric acid. Therefore, it is considered that the formation of the gaseous product is controlled by the synergetic effects invoked by the concentration of NO_2^- and acidity of the solutions and, thus, the final yield of gaseous product in each solution might be determined by the secondary reaction of NO_2^- with solute. The numerical model calculation on the formation mechanism of ^{16}N -labeled products is currently in progress.

References

- 1) J. J. Schleiffer and J. P. Adloff: *Radiochimica Acta* 3 (1964) 145.
- 2) E. Ibe, H. Karasawa, M. Nagase, M. Utamura and S. Uchida: *J. Nucl. Sci. Technol.* 26 (1989) 760.
- 3) R. L. Breden : Status of the Art Report vol 2, Water Chemistry and Corrosion, ANL-6562 (1963).
- 4) L. Hammer, S. Forsén, S. Hedlund and R. Lundqvist: " Water Chemistry Research at the Halden Boiling Water Reactor(HBWR)" OECD Halden Reactor Project Report No. HPR 55, Halden Norway (June 1967).
- 5) J. E. LeSurf and G. M. Allison: *Nucl. Technol.* 29 (1976) 160.
- 6) C. C. Lin: Proc. 1988 JAIF Int. Conf. on Water Chemistry in Nuclear Power Plants, vol. 2 (1988) 714.

Table 1 Analytical results of some of the final solutions.

Additives	Concn. (mol/l)	pH	NO(mg/l)	NO_2^- (mg/l)
HNO_3	10^{-6}	6.4	0.1	<0.02
	10^{-5}	5.3	0.86	<0.02
	10^{-4}	4.0	7.8	<0.02
NO	0.1(vol%)	3.4	2.1	18.9
NaNO_2	10^{-6}	6.1	0.02	0.04
	10^{-5}	6.2	0.02	0.53
	10^{-4}	6.1	0.02	5.10

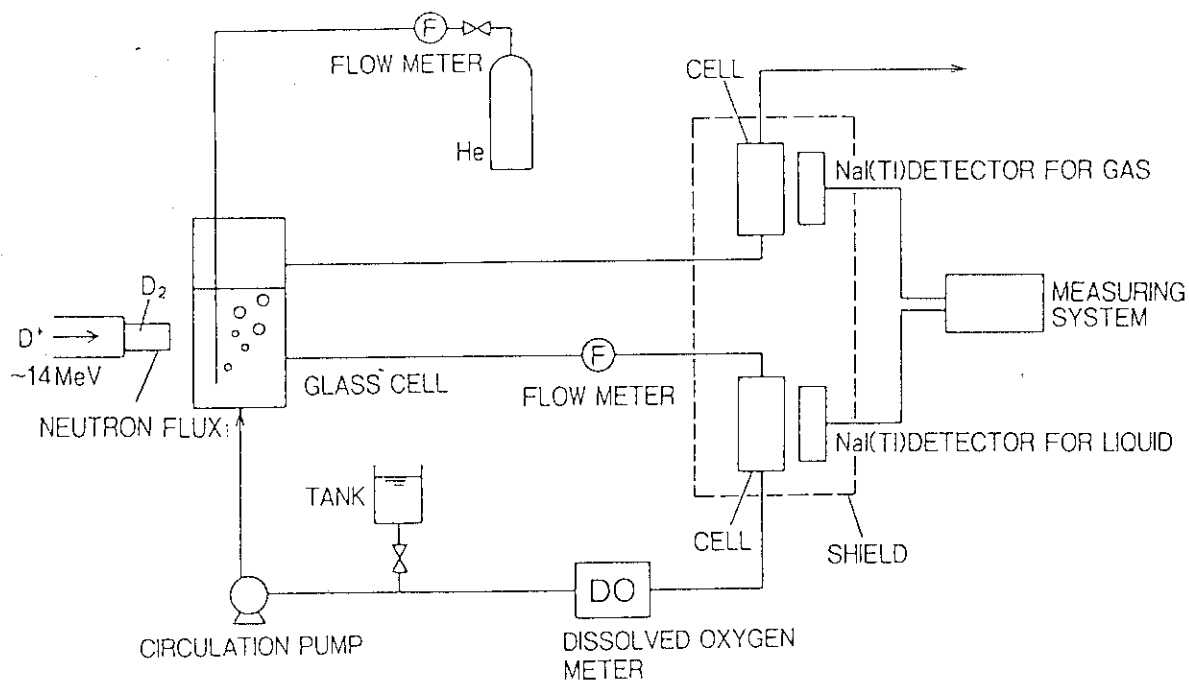


Fig. 1 Schematic view of the experimental setup.

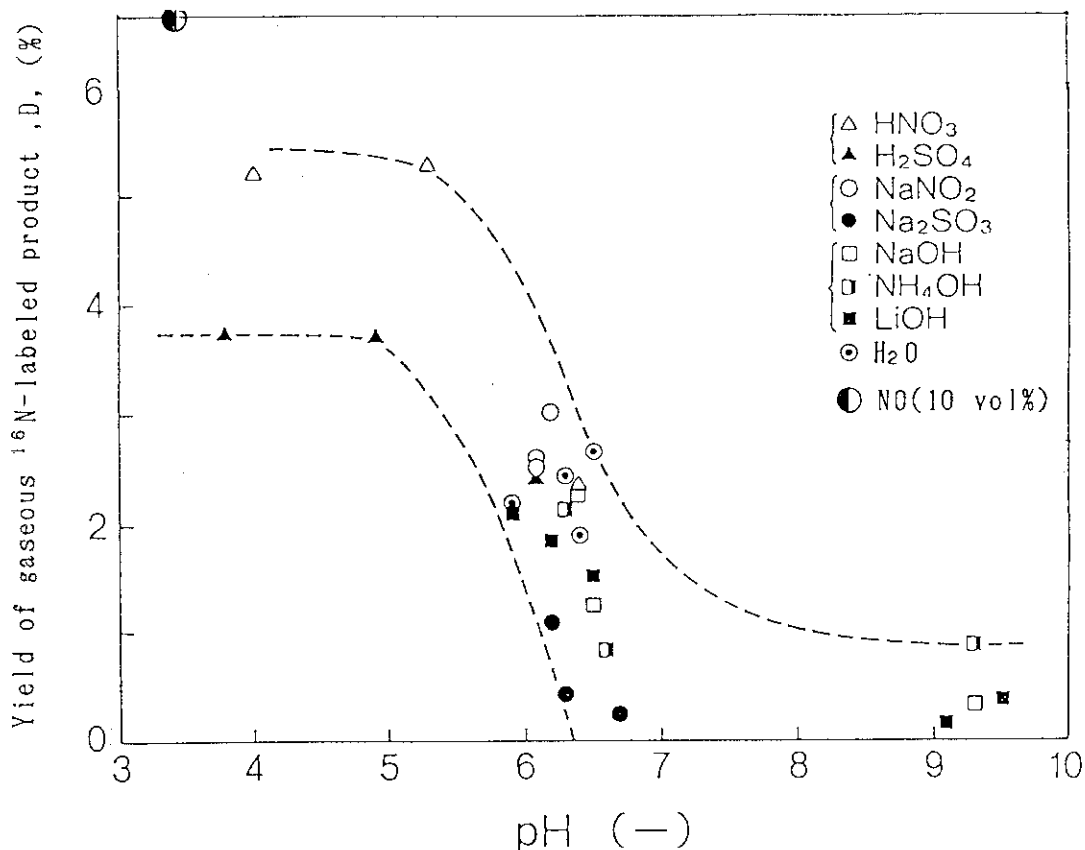


Fig. 2 Effects of pH on the yield of gaseous ^{16}N -labeled product.

2.2 HEAVY ION TRACK MICROFILTER OF POLYIMIDE

Yoshihide KOMAKI, Nirou ISHIKAWA, Tsutomu SAKURAI, Minoru KUMAKURA*, Katsutoshi FURUKAWA, Shinichi OHNO and Hideki NAMBA*

Department of Chemistry, JAERI, *Takasaki Radiation Research Establishment, JAERI.

1. Introduction

Heavy ion track microfilter of polyimide has been studied¹⁾, as the next experiment for polyvinylidene fluoride filter. Microfilter made of polymer by heavy ion irradiation and etching is based upon the selective large chemical etchability along the pass of heavy ion. But, any polymer is not etched whenever it is irradiated with heavy ions. Effective etching for a polymer is different with kinds of the ions(light or heavy ion), and for an ion with kinds of polymers. Each etchability for tracks in different polymers is influenced by the amount and the nature of degraded products along the track.

Resistivities to radiation and to heat of polyimide are the greatest in those of all of polymers. A microfilter produced from the polymer would be useful as heat-resistant separation membrane. This experiment was carried out from the interests how polyimide is etched after the heavy ion irradiations.

2. Experiments

$^{59}\text{Ni}^{13+}$ (200 MeV), $^{79}\text{Br}^{10+}$ (120 MeV), $^{108}\text{Ag}^{8+}$ (120 MeV), $^{32}\text{S}^{10+}$ (165 MeV) and $^{12}\text{C}^{7+}$ (110 MeV) from JAERI TANDEM accelerator were bombarded perpendicularly on a 12.5 μm thick polyimide film, "UPILEX", supplied by UBE Industry Co.Lmt. Each ion with enough kinetic energy perforates through entire film thickness. The film was irradiated with defocussed beam of particles of about 25 mm in diameter at a current of 2 nA for 10 seconds, leading to a density of track number of $3\text{-}6 \times 10^8/\text{cm}^2$. The films irradiated were etched in a solution of 5% and 25% KMnO_4 at 100°C and in solutions of 5%, 7% and 10% NaClO at 40°C, 55°C and 70°C, respectively. After washing and drying, the perforated hole diameter was determined by the Knudsen's formula for Ar transmittance through the pores in the films.

3. Results and discussion

Polyimide "UPILEX" has been developed in recent year and its resistivity to heat is superior to "Kapton" polyimide. Etchant for the track emergence in polyimide has been little known except KMnO_4 solution²⁾. Etching solutions of 5% and 25% KMnO_4 , $\text{K}_2\text{Cr}_2\text{O}_7$ in conc H_2SO_4 , 10M NaOH and 10% NaClO were examined. Etched track was detected only in the case of 25% KMnO_4 solution at 100°C and 10% NaClO solution at 70°C. The film was dissolved away in 10M NaOH solution and any track was not observed in $\text{K}_2\text{Cr}_2\text{O}_7\text{-H}_2\text{SO}_4$ solution.

Figure 1 shows the dissolution rates of polyimide exposed to Co-60 γ -rays to a dose of 1×10^2 MGy with the virgin film. No difference was found between two samples. Figure 2 shows a relation between hole diameter and etching time for "UPILEX" irradiated by $^{32}\text{S}^{10+}$ (165 MeV) and then etched for 8 hr in a solution of 25% KMnO_4 at 100°C.

The diameter of track hole in polyimide was found to be enhanced only under the severe etching condition. Figure 3 is an SEM image of etched tracks on the polyimide. The holes are not yet perforated and their diameter at surface is considerably enlarged. Large taper angle at the entrance of the hole is characteristic of track etching in the polyimide.

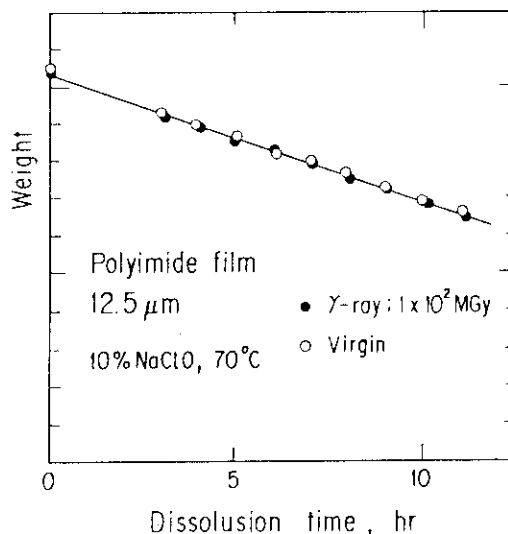


Fig. 1 Dissolution behaviors of polyimides exposed to γ -rays to a dose of 1 MGy in 10% NaClO solution.

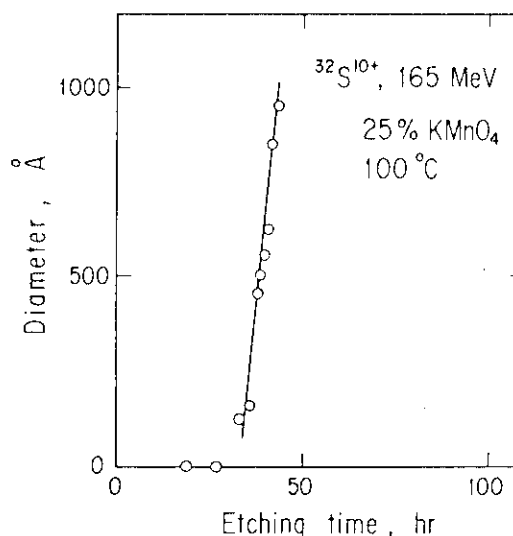


Fig. 2 Growth of perforated holes in polyimide irradiated with $^{32}\text{S}^{10+}$ ions. etching: 25% KMnO_4 solution.

It was found that the ratio of track etching rate, V_1 which was determined half of film thickness divided by the induction time and to bulk etching rate, V_2 which was obtained from the slope of curve in fig. 2, was about 5, then the taper angle θ is estimated to be 12 degree from a formula,

$$\theta = \sin^{-1}(V_2/V_1).$$

The $KMnO_4$ etching at $100^\circ C$ was successful. However, it is fairly dangerous in operation. Thus more mild conditions were searched³⁾. Figure 4 shows results of etching by the 10% $NaClO$ solution at $70^\circ C$. It is obvious that the diameter of holes in the film irradiated separately by $^{108}Ag^{11+}$, $^{79}Br^{11+}$ $^{59}Ni^{10+}$ increases with etching time.

Every perforated holes enhance linearly and quickly with the etching time after an induction time, as observed for the case of the $KMnO_4$ solution. The etching rate along the track becomes larger in order of $Ag > Br > Ni$ ions while the bulk etching rate is independent of the kinds of the incident ions. Figure 5 shows the track etching rate, V_1 , vs the concentration of etching $NaClO$ solution at $70^\circ C$. Generally, the higher the concentration of $NaClO$, the larger the V_1 becomes.

Table 1 shows etching rates, V_1 and V_2 against the various conditions of etching for the several kinds of ion irradiations. The track etching rates in the $NaClO$ solution are several times larger than that in the $KMnO_4$ solution,

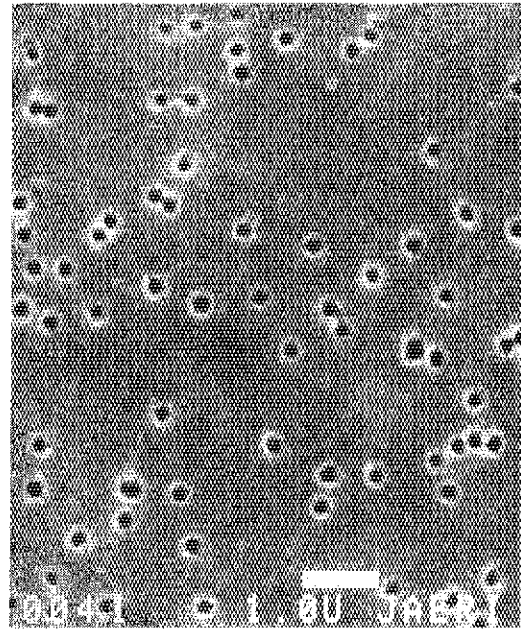


Fig. 3 SEM image of etched surface of polyimide irradiated with $^{32}S^{10+}$ ions of 165 MeV. etching :25% $KMnO_4$ solution at $100^\circ C$, 8hr.

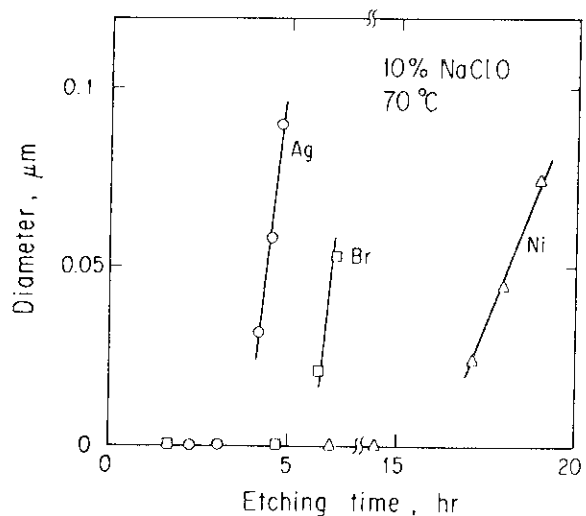


Fig. 4 Growth of perforated holes in polyimide irradiated with Ag, Br and Ni ions. etching: 10% $NaClO$ solution.

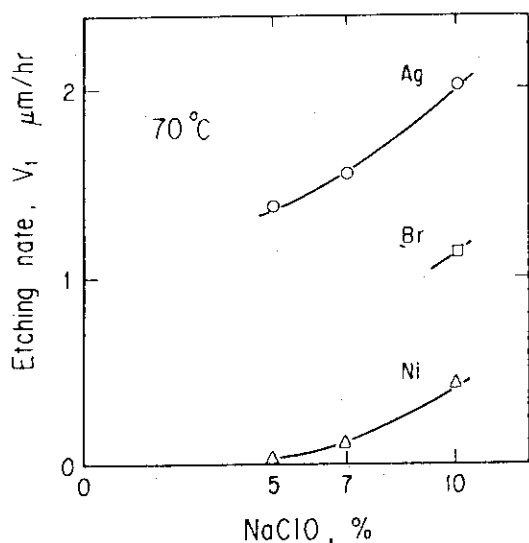


Fig. 5 Effect of the track etching rate of polyimide irradiated with Ag, Br and Ni ions on the concentration of NaClO.

Table 1 Etching rates, V_1 and V_2 , and V_1/V_2 for various etching conditions.

	KMnO ₄	NaClO			
	100 °C	(IONS)	70 °C		
	25 %		10 %	7 %	5 %
V_1	(S)	Ag	1.6	1.4	1.1
	0.2	Br	1.1		
		Ni	0.4	0.4	0.3
V_2	0.04	Ag	0.05	0.03	0.02
		Br	0.05		
		Ni	0.01	0.03	0.03
V_1/V_2	5	Ag	33	47	55
		Br	22		
		Ni	29	15	11

V_1, V_2 : (μm/hr)

though the bulk etching rate scarcely different in both of them. The ratio of the etching rate, V_1/V_2 is found to be larger in the Ag ion irradiation than the Ni ion irradiation.

References

- 1) Y.Komaki, Y.Matsumoto, N.Ishikawa and T.Sakurai:POLYMER COMMUNICATIONS., 30,(1989)43.
- 2) H.Besson, M.Monnin, and S.Sanzell:Compt.Rend.,Paris 264B(1967) 1751.
- 3) S.L. Koul, I.D. Campbell, D.C. McDonald, Lewis T. Chdderton, D. Fink, J.P. Biersack, and M. Muller: Nucl.Instrum & Methods in Phys.Res. B32(1988)186.

2.3 MICRODOSIMETRY OF HIGH-ENERGY HEAVY IONS

Katsutoshi FURUKAWA, Shinichi OHNO, Hideki NAMBA*,
Yoshihide KOMAKI, Yasuhiro YAMADA and Yhota NAKAI**

Department of Chemistry, * Department of
Research (Takasaki), **Department of Physics

1. Introduction

In microdosimetry of high-energy heavy ions, two kinds of information are of fundamental importance; (1) the ratio of the deposited energy going into kinetic energy of atoms to that going into electronic excitations or ionizations, and (2) the spatial distribution of the deposited energy around the track of an incident heavy ion.

The well-known fact that W-value, mean energy required to produce an ion-electron pair, has little dependence on energy at very high energies comes about because the amount of energy going into kinetic energy of gas atoms is negligible¹⁾. For heavy or low-energy incident particles, the fraction of the energy that goes into atomic kinetic energy due to "nuclear collision" becomes large, resulting in an increase of W. Thus, we aim at experimental determinations of W of Ar gas as a function of primary energy of the incident particle. Then we try to compare the results with those obtained from the estimation of how the initial energy is divided between electronic processes and the kinetic energy of gas atoms, using LSS theory²⁾.

As to information on the spatial distribution of the deposited energy, we employ the method which have been reported by Wingate and Baum³⁾ and which measures radial distribution of ionization current produced in a small wall-less ionization chamber.

A collimated beam of the heavy ion of the energy range 100-150 MeV from the JAERI Tandem accelerator is introduced in the vacuum vessel through a set of aperture (of the diameter of 0.5 and 0.5 mm) which serves also differential pumping system.

2. Experimental

A schematic view of the apparatus used in the present work is shown in Fig. 1. A large cylindrical ionization chamber (of diameter 180 mm, length 900 mm) made of Al (a) is for measurements of W. Details of this

chamber were reported previously.⁴⁾

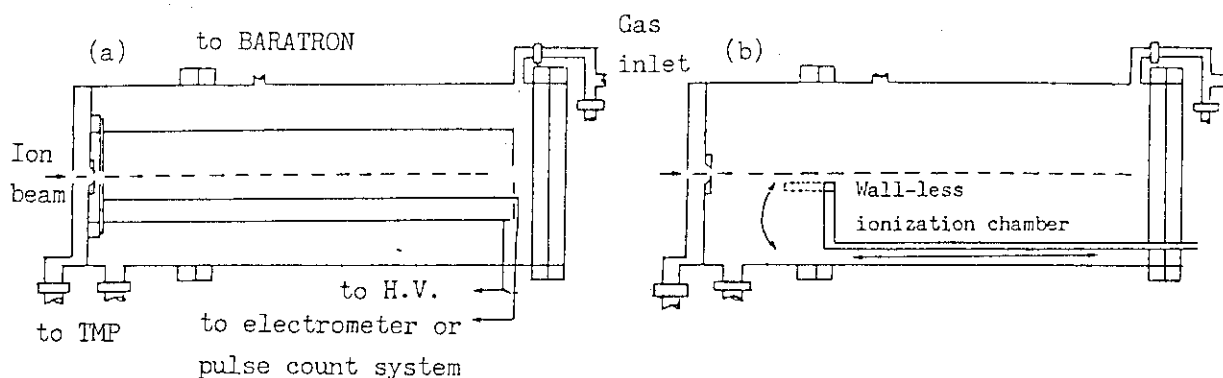


Fig. 1 A schematic view of the ionization chamber

The small wall-less ionization chamber (b) is for measurement of spatial distribution of the deposited energy. It is consisted of two cylindrical meshes and a central wire supported by Teflon insulator, respectively. The inner cylindrical mesh (of diameter 15 mm, length 85 mm) which acts as H.V. electrode is made of Ni of 0.005 mm wire diameter, 50 meshes. The outer mesh (of diameter 30 mm, length 90 mm) which acts as shield is made of SUS of 0.21 mm wire diameter, 30 meshes. The central wire which acts as the collecting electrode is made of 1 mm Cu wire.

The wall-less ionization chamber itself is placed in a large vacuum vessel filled with an Ar gas at variable pressure and it is movable by remote operation. The radial distance from the beam track in measurement of spatial distribution was adjusted by changing either the gas pressure or the radial position of the wall-less ionization chamber.

3. Results and Discussion

The saturation curves for the 23.1 and 86.7 MeV S^{10+} and 90.9 MeV I^{7+} ions entering the chamber containing Ar gas at the pressure ranging from 0.45 to 100 Torr were obtained. The saturation currents obtained at the pressure of 50 and 100 Torr are nearly the same, indicating that the incident ions are completely stopped within the ionization chamber. This has been confirmed by the expected ion-ranges calculated from mean ion depth data²⁾.

W value is the mean energy required to create an ion-electron pair when an incident ion is stopped in the gas. Thus if N ions of energy E

lose all their energy in the gas and produce ionization current I , then W is given by:

$$W = E N e / I$$

where e is the electronic charge. W values which have been determined in the present work are listed in Table 1.

Table 1 W -values determined in the present experiment

Ion	Energy	Rate of incident ions	Ionization current	Ion pair yield	W value
	MeV	/s	nA	10^6	eV
S^{10+}	23.1	110	0.016	0.91	25.4 ± 1.3
S^{10+}	86.7	1.5×10^4	8.64	3.6	24.1 ± 1.2
I^{7+}	90.9	70.6	0.0324	2.87	29.5 ± 1.5

In Fig. 2 are plotted the W values in the table and also the value in the literature as a function of the reduced energy. The results indicate that W value is clearly dependent on the energy of the incident ion. In

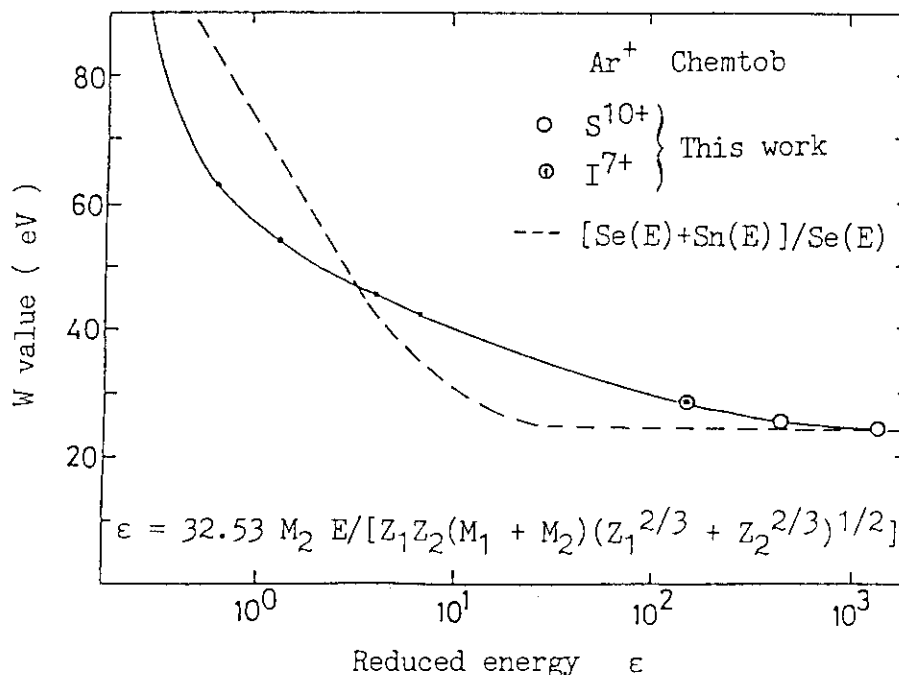


Fig. 2 W as a function of reduced energy for Ar gas

the figure is also shown the calculated curve which is :

$$[Se(E)+Sn(E)]/Se(E) \text{ vs. } E$$

where $Se(E)$ and $Sn(E)$ are electronic and nuclear stopping power, respectively, at the energy E . They were obtained according to the following equations:

$$S_e(E) = 8\pi e^2 N a_0 Z_1^{7/6} Z_2 (Z_1^{2/3} + Z_2^{2/3})^{-3/2} v/v_0$$

$$S_n(E) = s_n (8.462 Z_1 Z_2 M_1) / [(M_1 + M_2) (Z_1^{2/3} + Z_2^{2/3})^{1/2}]$$

$$s_n = 0.5 \ln(1 + \epsilon) / (\epsilon + 0.107^{0.375})$$

$$\epsilon = 32.53 M_2 E / [Z_1 Z_2 (M_1 + M_2) (Z_1^{2/3} + Z_2^{2/3})^{1/2}]$$

where the ion energy, E, is in keV; M1 and M2 are the ion and target masses in amu, respectively. a₀ is the Bohr radius of the H-atom; v₀ is the Bohr velocity; Z₁ and Z₂ are the atomic number of the ion and the target.

In Fig. 3 is shown the radial distribution of ionization currents obtained by a small wall-less ionization chamber at the various distance from the path of the incident ion. The ionization currents are normalized to deposited energy of the axial position (150 mm from the entrance aperture) of the wall-less chamber for various gas pressure, calculated from the data of stopping power. Also, the radial distance are all normalized to the constant density of 1 g/cm³. The results indicate that radial distribution of the normalized ionization current decreases nearly exponentially to the normalized radial distance.

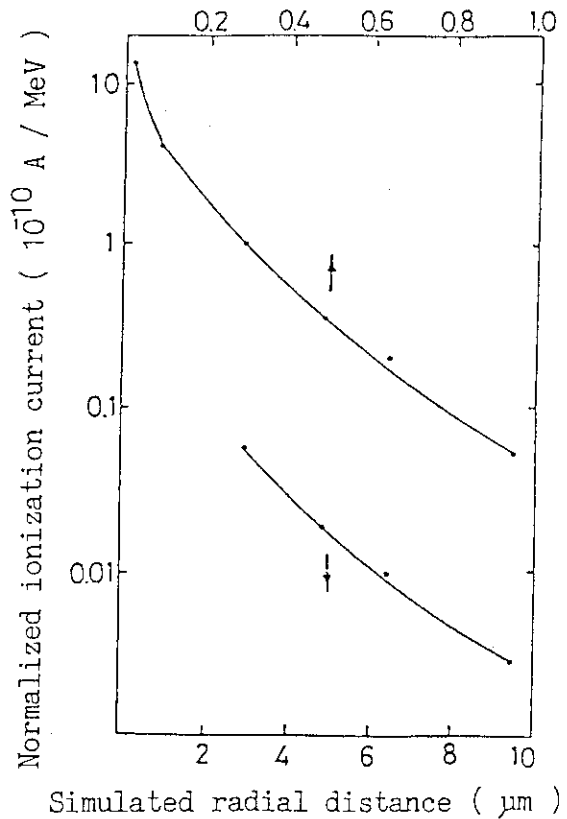


Fig. 3 The radial distribution of ionization currents

References

- 1). "Average Energy Required to Produce An Ion Pair, ICRU Report 31 (1979).
- 2). J. F. Ziegler: Handbook of Stopping Cross-Section for Energetic Ions of All Elements," Pergamon Press, N.Y., (1979).
- 3). C. L. Wingate and J. W. Baum: Radiat. Res., 65, 1 (1976).
- 4). K. Furukawa, S. Ohno, Y. Komaki, H. Namba, Y. Aoki and Y. Nakai: JAERI-M89-119 (1989) p.83-86.

2.4 EFFECT OF ION BEAM IRRADIATION ON DRY CELLS OF RADIATION RESISTANT BACTERIUM, Deinococcus radiodurans

Hiroshi WATANABE, Shigeru INABA**, Yasuhiko KOBAYASHI, Masahiro KIKUCHI, Ranko OBATA, Makoto IMAI*, Masao SATAKA* and Yohta NAKAI*

Department of Research, *Department of Physics, JAERI,
**Tokyo University of Agriculture

I. INTRODUCTION

Deinococcus radiodurans R₁ is a representative strain of the radiation resistant bacteria, which was first isolated from irradiated meat in 1956¹⁾. Survival of this bacterium does not decrease even after exposure with about 5 kGy. It has been demonstrated that the radiation resistance of R₁ strain is attributable to repair of all DNA damages including double strand breaks induced with doses up to 5 kGy²⁾. On the other hand, it is believed that high LET radiation takes place irreparable damage in DNA and subsequently most kinds of cells show exponential survival curve.

Dewey³⁾ and Kitayama et al.⁴⁾ examined the effect of high LET radiation on the wet cells of R₁ strain using He to Ar ions. Recently, Schafer et al.⁵⁾ also measured the radiosensitivity using Ti and U ions. From these studies it was clear that the survival curve was sigmoidal, indicating that the DNA damage induced by ion beams also can be repaired. The lethal effect of radiation in these experiments using wet cells involves indirect action from water. Therefore, we examined the survival of dry cells to clarify direct action of ion beams and observed the changes in cell structure by transmission electron microscope(TEM).

II. MATERIALS AND METHODS

(1) Strain and Cultivation

D. radiodurans R₁ strain was cultivated in TGY medium at 30°C with shaking. The cells at stationary phase were harvested by centrifugation, washed twice by 0.1 M phosphate buffer(pH 7.0), and resuspended in the same buffer. The cells were filtrated by membrane filter, and then lyophilized.

(2) Irradiation

The membrane filter with lyophilized cells was wound around a columnar

rod, and irradiated in vacuum (10^{-6} Torr) by 0.5 MeV He^+ or 0.45 MeV C^+ ions with 1 to 30 nA using Van de Graaff accelerator (JAERI, Tokai Establishment). The columnar rod was rotated at 60 rpm throughout irradiation. The beam current was measured by Faraday cup. In the case of electron beam, the membrane filter was irradiated in glass vessel in vacuo with 2 MeV using electron accelerator (JAERI, Takasaki Establishment). The fluences were calculated from the measurement of Sunaga et al.⁶⁾.

III. RESULTS AND DISCUSSION

(i) Radiosensitivity

In order to irradiate the cells in vacuo, it is necessary to keep the cells stable under dry condition. D. radiodurans was stable after lyophilization in 0.1M phosphate buffer (pH 7). Figure 1 shows survival curves of D. radiodurans R_1 irradiated with C^+ ions and electrons.

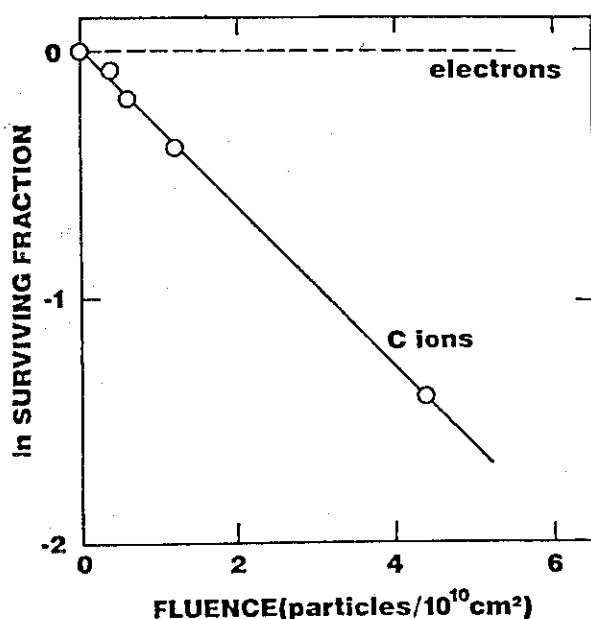


Fig.1 Survival Curves of D. radiodurans R_1 Irradiated with 0.45 MeV C^+ Ions and 2 MeV Electrons

When the dry cells were irradiated with 0.45 MeV C^+ ions, the survival curve of R_1 strain was exponential, suggesting that the damages induced by direct action can not be repaired, namely that a repairable damage may be induced from indirect action under wet condition. On the other hand, the survival of cells irradiated with electron beams did not decrease in the same range of fluences.

(2) TEM Observation

In order to clarify this remarkable difference between ions and electrons, changes in cell structure after irradiation were observed by electron microscope.

(i) Cell nucleus

As shown in Fig.2(A), a stripe pattern of cell nucleus was commonly observed in unirradiated cell. However, when the cells were irradiated with C^+ ions as shown in Fig.2(B), the stripe pattern disappeared after irradiation with a fluence of $1.2 \times 10^9 / \text{cm}^2$ which corresponds to 24 hits/cell. On the other hand, He^+ ions did not cause so significant changes in nucleus

at the same fluence. At the hundred times of fluence, partially broken nucleus was observed a little. In the case of electrons, no structural changes in nucleus was observed at the same fluence, but at $7.8 \times 10^{13}/\text{cm}^2$ reduction of the staining density were observed.

(ii) Cellular granule

Cellular granules were also destroyed by ion irradiation, and consequently the size of granules became about half. The effect of irradiation on decrease of size was more significant in C^+ ions than in He^+ ions and electrons. In the case of C^+ ions, the granules linked together were partially observed. Furthermore, a linear mark like ion track was observed in cytoplasm of cells irradiated with C^+ ions.

The width of linear mark was about 2 or 3 nm. The linear mark was also observed in the cells irradiated with He^+ ions, but not so clearly. The mark was not observed at all in the unirradiated and electron-irradiated cells.

(iii) Cell envelope

Changes in cell envelope consisting of slime layer and cell wall were observed especially in slime layer from low fluence, and increased with increasing fluence. At a low fluence of $10^9/\text{cm}^2$, the electron density in staining increased in outermost slime layer, and decreased with increase in fluence. Then the structure of slime layer became rough at high fluence. However, there was no characteristic difference between ion beams and electron beams.

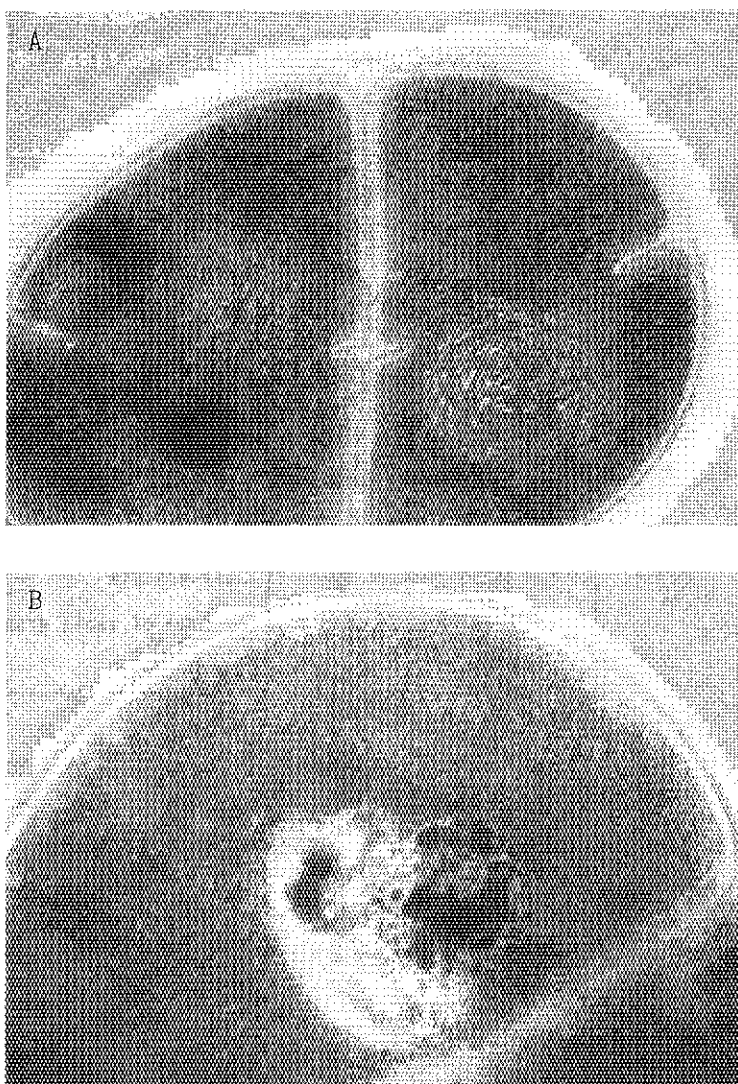


Fig.2 Thin Section of D. radiodurans R₁
A:unirradiated, B:irradiated with C^+ ions

Table 1 TEM Observation and Survival of Cells Irradiated with Ions and Electrons

Fluence (p/cm ²)	Survival (%)	Structure		
		Granule	Nucleus	
C ⁺	1.2 E09	90	Small granule, Granule chain	Damaged partially
	1.2 E10	40	do.	Increase of damage
	1.2 E11	<0.1	do.	Sash like structure
	2.5 E11	-	Decrease of large granule	do.
e ⁻	3.2 E12	100	NC*	NC
	2.3 E13	100	do.	do.
	5.4 E13	70	Small granule	Damaged partially
	7.8 E13	26	Increase of small granule	Rough structure
	1.3 E14	<0.1	Like necrosis	do.

NC* : not change

Table 1 summarizes the results of TEM observation and survival on the cells irradiated with C⁺ ions and electrons. It is clear that the effect of ion beams on the cells occurs particularly in the cellular nucleus and granules from low fluence. Therefore, the efficient lethal effect of ion beams appears to be due to the drastic destruction of nucleus and granules induced by radiation.

REFERENCES

- 1) A.W.Anderson, H.C.Nordan, R.F.Cain, G.Parrish and D.Duggan: Food Technol. 10 (1956)575.
- 2) S.Kitayama and A.Matsuyama: Biochem. Biophys. Res. Commun. 33(1968)418.
- 3) D.L. Dewey: Int. J. Radiat. Biol. 16(1969)583.
- 4) S.Kitayama, K.Igarashi, T.Karasawa and M.Matsuyama: Agri. Biol. Chem. 41(1977)2297.
- 5) M.Schafer and H.Bucker: GSI Scientific Report(1987) p.223.
- 6) H.Sunaga, K.Mizubishi, K.Yotsumoto, R.Tanaka and N.Tamura: JAERI-M Report 82-142(1982).

III ATOMIC PHYSICS, SOLID STATE PHYSICS
AND RADIATION EFFECTS IN MATERIALS

3.1 HIGH-RESOLUTION ZERO-DEGREE ELECTRON SPECTROSCOPY(II)

Ken-ichiro KOMAKI, Yasunori YAMAZAKI, Kenro KUROKI,
 Kiyoshi KAWATSURA,* Masao SATAKA,** Makoto IMAI,**
 Yohta NAKAI,** Hiroshi NARAMOTO,** Yasuyuki KANAI,**
 Tadashi KAMBARA,** Yohko AWAYA*** and Nikolaus STOLTERFOHT[†]

College of Arts and Sciences, University of Tokyo, ^{*}Faculty
 of Engineering and Design, Kyoto Institute of Technology,
^{**}Department of Physics, JAERI, ^{***}Institute of Physical and
 Chemical Research(RIKEN), [†]Hahn-Meitner Institute, Berlin,
 Federal Republic of Germany

Introduction

Energy spectra of electrons ejected in ion-atom collisions are known to be of great use in understanding of electronic structure of highly excited states and of collision processes in gaseous as well as solid targets. High resolution measurement of electrons emitted from projectile ions has been achieved with zero-degree electron spectroscopy.¹⁾

In the present work, we measure electrons emitted from the Rydberg states of 4-electron system, S^{12+} ions, via Coster-Kronig transitions and investigate the difference in angular momentum distribution of the states for He and carbon foil targets.

Experiment

The experimental arrangement is reported previously.²⁾ A beam of 64 MeV $^{32}S^{5+}$ ions were accelerated by the tandem accelerator at JAERI and were charge stripped by carbon foils ($10-30 \mu g/cm^2$). The fraction of S^{12+} ions was selected by a switching magnet and introduced to the collision chamber.

The targets were $2-30 \mu g/cm^2$ thick carbon foils and He gas with a pressure of $\sim 10^{-3}$ Torr and the cell length of 5cm. Electrons emitted in the forward direction were energy analyzed by the high-resolution zero-degree spectrometer.

Results and Discussion

Figures 1 and 2 show energy spectra of electrons emitted through 64-MeV $S^{12+} + He$ and $S^{12+} + carbon foil$ collisions, respectively. The

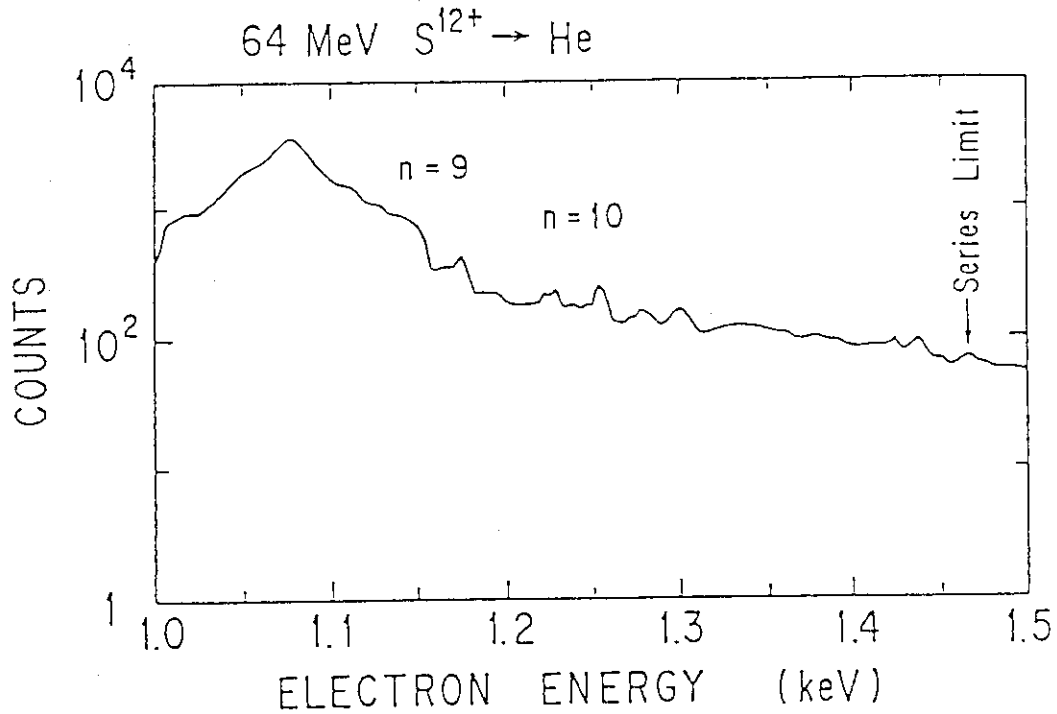


Fig. 1 Spectrum of electrons ejected at 0° in 64 MeV $S^{12+} + He$ collisions.

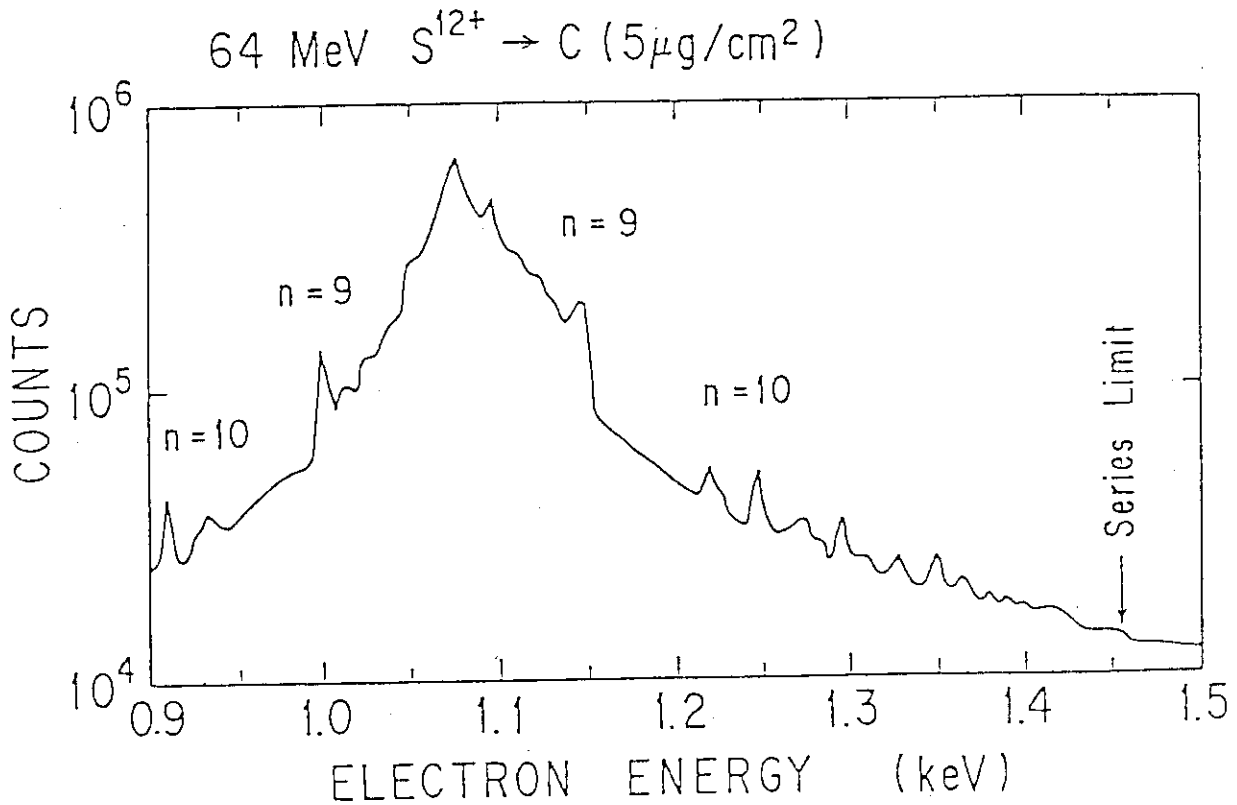


Fig. 2 Spectrum of electrons ejected at 0° in 64 MeV $S^{12+} + 5 \mu g/cm^2 C$ foil collisions.

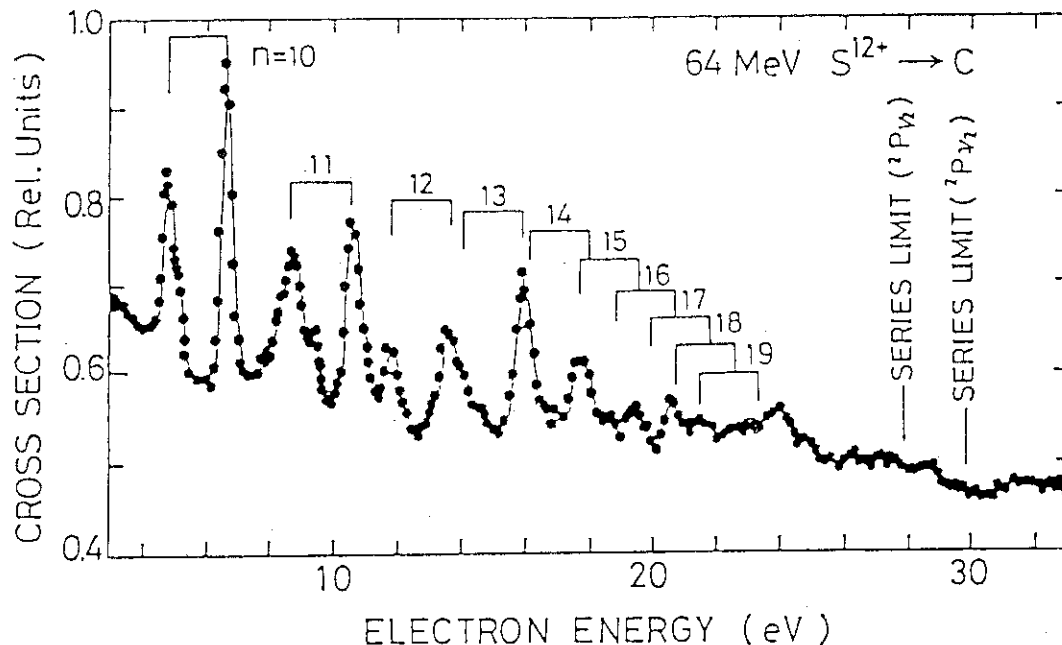


Fig. 3 Spectrum of electrons ejected at 0° in 64 MeV $S^{12+} + 5 \mu\text{g}/\text{cm}^2 \text{C}$ foil collisions. The energy refers to the projectile rest frame.

abscissas are electron energies in the laboratory frame. The dominant peak (cusp) at 1.09 keV is due to electron loss and/or capture to the continuum (ELC/ECC). Peaks on the low- and high-energy sides of the cusp originate from electrons in the same states emitted at 180° and 0° , respectively, in the projectile rest frame.

Converting the region of 1.2 to 1.5 keV of the spectrum in Fig. 2 into the projectile frame, one gets a series of peaks shown in Fig. 3. These peaks are attributed to the electrons emitted via the $1s^2 2p n l \rightarrow 1s^2 2s \epsilon l'$ Coster-Kronig transitions. As indicated in the figure, electron energies are in good agreement with the calculated ones.

$$E_{nQ} = \Delta E - Q^2 R_y / (n - \mu_Q)^2,$$

where n is the principal quantum number, Q the charge number of the atomic core seen by the Rydberg electron, μ_Q the quantum defect calculate by Theodosius et al.³⁾ and R_y the Rydberg energy (27.211 eV). Values of the energy difference ΔE of 2s and 2p orbitals were taken from the experimental transition energy of $S^{13+} 1s^2 2s - 1s^2 2p$ tabulated by Kelly⁴⁾ as 29.689 eV and 27.814 eV for $^2P_{3/2}$ and $^2P_{1/2}$ states, respectively. Higher intensities of the peaks for the solid target are due to contribution of metastable $1s^2 2s 2p$ state additionally populated in the target.

Transitions from the states with $n < 9$ for $^2P_{3/2}$ and $n < 10$ for $^2P_{1/2}$ states are energetically forbidden. Fig. 4(a) and (b) show the projectile

frame spectra of electrons through $1s^2 2p9\ell(^2P_{3/2})-1s^2 2p\epsilon\ell'$ transitions for gas(He) and solid(C foil) targets, respectively. Arrows in the figures show the theoretical energy values calculated for the angular momentum ℓ . The comparison of Fig.4(a) and (b) indicates a clear difference in the angular momentum distribution, i.e., the high- ℓ components are significantly enhanced for the solid target. A similar difference has been observed⁵⁾ in the case of 1.5-5.0 MeV C^{2+} ions emerging from solid and gas targets and was explained to be due to the multiple collisions in solid targets.⁶⁾

The dependence of the angular momentum distribution on the thickness of the solid target is currently investigated.

References

- 1) A. Itoh, T. Schneider, G. Schwietz, Z. Roller, H. Platten, G. Nolte, D. Schneider and N. Stolterfoht: J. Phys. B16(1983)3965.
- 2) K. Kawatsura, M. Sataka, H. Naramoto, Y. Nakai, Y. Yamazaki, K. Komaki, K. Kuroki, F. Fujimoto, Y. Kanai, T. Kambara, Y. Awaya and N. Stolterfoht: JAERI Tandem, Linac & V.d.G. Annual Report 1988, p.71.
- 3) C. D. Theodosius, M. Inokuti and S. T. Manson, At. Data Nucl. Data Tables 35(1986)473.
- 4) R. L. Kelly, ORNL-5922(1982).
- 5) Y. Yamazaki, N. Stolterfoht, P. D. Miller, H. F. Krause, P. L. Pepmiller, S. Datz, I. A. Sellin, A. Salin, P.D. Fainstein, R. Rivarola, J. P. Gradin, J. N. Scheurer, S. Andriamonje, D. Bertault and J. F. Chemin: Phys. Rev. Lett. 61(1988)2913.
- 6) J. Burgdorfer and C. Bottcher, Phys. Rev. Lett. 61(1988)2917.

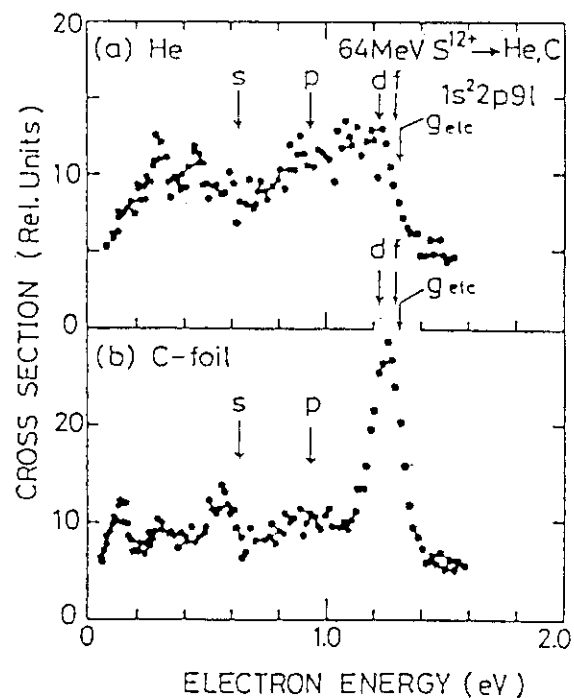


Fig. 4 Spectra of electrons from the $1s^2 2p9\ell(^2P_{3/2})$ state produced in collisions of 64 MeV S^{12+} on He(a) and C(b) targets.

3.2 RESPONSE OF SILICON SURFACE BARRIER DETECTOR TO HEAVY IONS

Ikuo KANNO

Department of Reactor Engineering, JAERI

Introduction

Silicon surface barrier detector (SSB) has been widely used for charged particle detections in a few decades. Some of the reasons of this popularity is their excellent proportionality of pulse height to the energy of incident particle, and rapid pulse rise time. In the measurement of heavy ions, the SSB loses its merits.

The pulse height induced by a heavy ion is lower to some extent comparing to the one induced by a light ion with the same kinetic energy. This phenomenon is called a pulse height defect. The pulse height defect has been considered separately as, (1) the energy loss in the entrance window, (2) the energy loss by the nuclear stopping, and (3) the energy loss attributed to other mechanisms.¹⁾ In these three defects, (1) and (2) are understood well and are estimated by calculations, however, the third defect which is called a residual defect, is not explained successfully and has been a theme of intensive studies.

The charge collection starts some nano seconds after the incident time of heavy ions. This phenomenon is called plasma delay. The plasma delay affects the time of flight of heavy ions. The author reported the models of plasma column formation and erosion.²⁾ In these models, the mechanism of plasma delay was explained, however, these models could not predict the plasma delays of charged particles because they had some constants to be determined by experiments. Comprehensive data of plasma delays of many kind of charged particles were required to determine the constants.

The purposes of this study are (1) to study the residual defect and (2) to obtain the data of the plasma delay.

Experimental

Experiments were performed at R-2 beam line of the Tandem Accelerator. ⁵⁸Ni ions of 140MeV and 203MeV in energy were scattered

by a gold foil ($100\mu\text{g}/\text{cm}^2$ in thickness) in 45 degree direction. In the flight path, two micro channel plate detectors (MCP1 and MCP2) and one SSB were placed. Scattered nickel ions and recoiled gold ions passed through carbon foils ($30\mu\text{g}/\text{cm}^2$ in thickness) which were mounted on the MCP housings and impinged on the SSB. The distance between MCP1 and MCP2 was 67.6cm, and the one between MCP2 and SSB was 29.3cm. For the study of resistivity dependence of the residual defect and the plasma delay, SSBs of $362\Omega\text{cm}$ and $2100\Omega\text{cm}$ in resistivity were employed. Both SSBs were made by ORTEC (F-series, effective area 300mm^2 , entrance gold window thickness $40\mu\text{g}/\text{cm}^2$). Data of the residual defect and the plasma delay were taken at ten bias voltages with each SSB. Schematic diagram of electronics circuit is shown in Fig.1.

Results and discussion

In Table 1, the incident energies of nickel and gold ions to SSBs E_0 are presented. The window losses Δ_w , the nuclear stopping losses Δ_n , energies spent to produce electron-hole pairs E and the lengths of the plasma column l are also shown.

Experimental results of residual defects are shown in Figs.2 and 3 for nickel and gold ions as a function of depletion layer thickness. Error bars indicate the full width at half maximum.

Recently, the author reported that the residual defect was explained quantitatively by an effect which was derived from the dielectric property of the plasma column³⁾, instead of recombinations of electrons and holes as has been considered¹⁾. The experimental results are under analysis with the model of dielectricity effect.

For the derivation of the plasma delay, the zero times of electronic circuits should be determined for each time of flight. The experimental time of flight consists of the (calculated) flight time of a charged particle, time retardation between the two electronic circuits and the time of plasma delay. The plasma delay should be vanished at the infinite field strength. The zero time would be determined by extrapolating the flight time as a function of inversed electric field strength $1/F$ to the value at $1/F=0$. In Fig.4, the time of flight of nickel ions between the MCP2 and SSB are shown. It might be difficult to determine the zero time by extrapolating the data. This difficulty is attributed to the rapid change of the plasma delay of nickel ions. The zero time must be determined by a charged par-

ticle with small plasma delay like alpha particle.

The author would like to express his acknowledgment to Drs. H.Ikezoe, Y.Nagame and T.Ohtsuki and the operating staff of Tandem Accelerator for their extensive help in the experiments.

References

- 1) B.D.Wilkins, M.J.Fluss, S.B.Kaufman, C.E.Gross, and E.P.Steinberg: Nucl. Instrum. & Methods 92 (1971) 381.
- 2) I.Kanno: Rev. Sci. Instrum. 58 (1987) 1926.
- 3) I.Kanno: Rev. Sci. Instrum., submitted.
- 4) H.W.Schmitt, W.M.Gibson, J.H.Neiler, F.J.Walter, and T.D.Thomas: Proceedings of the IAEA Conference on the Physics and Chemistry of Fission, Salzburg (International Atomic Energy Agency, Vienna, 1965).

Table 1 Incident particle energies, E_i , window losses, Δ_w , nuclear stopping losses, Δ_n , energies spent to produce electron-hole pairs, E_0 , and plasma column lengths, L .

Particle	E_i (MeV)	Δ_w (MeV)	Δ_n (MeV)	E_0 (MeV)	L (μm)
^{58}Ni	114.1	0.4	0.9	112.8	18.6
	167.1	0.6	0.9	165.6	25.5
^{197}Au	45.1	0.4	6.6	38.1	7.1
	66.4	0.5	7.1	58.8	9.1

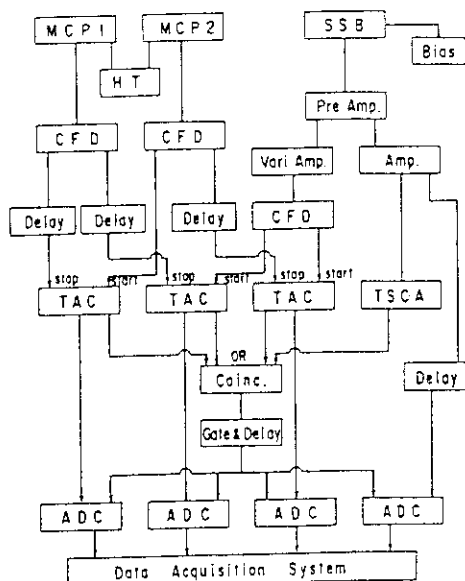


Fig.1 Schematic diagram of electronic circuit. MCP : micro channel plate detector, SSB : silicon surface barrier detector, HT : high voltage, CF D : constant fraction discriminator, Vari. Amp. : variable amplifier, Amp. : amplifier, TAC : time to amplitude converter, TSCA : timing single channel analyser, Coinc. : coincidence circuit, ADC : analog to digital converter.

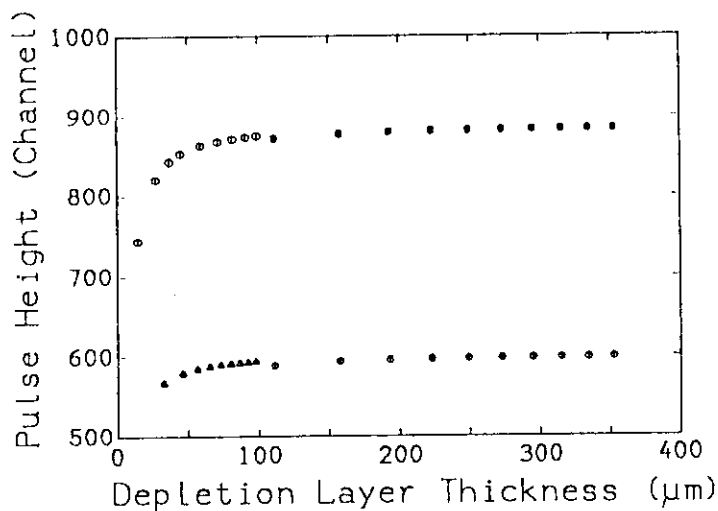


Fig.2 Experimental results of the residual defect for the nickel ions of 112.8MeV and 165.6MeV as a function of depletion layer thickness. The data taken at the depletion layer thickness less/greater than 100 μ m were measured by the SSB of 362 Ω cm/2100 Ω cm, respectively. Error bars show the full width at half maximum of the pulse heights.

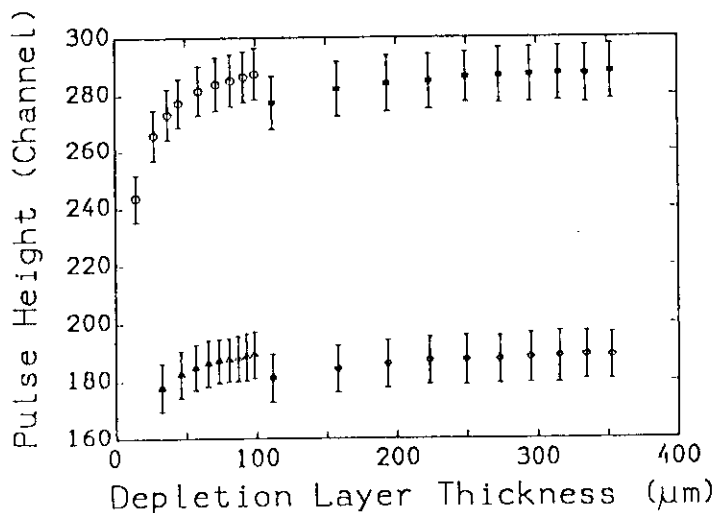


Fig.3 Same as in Fig.2, but for gold ions of 38.1MeV and 58.8MeV. Error bars show the full width at half maximum of the pulse heights.

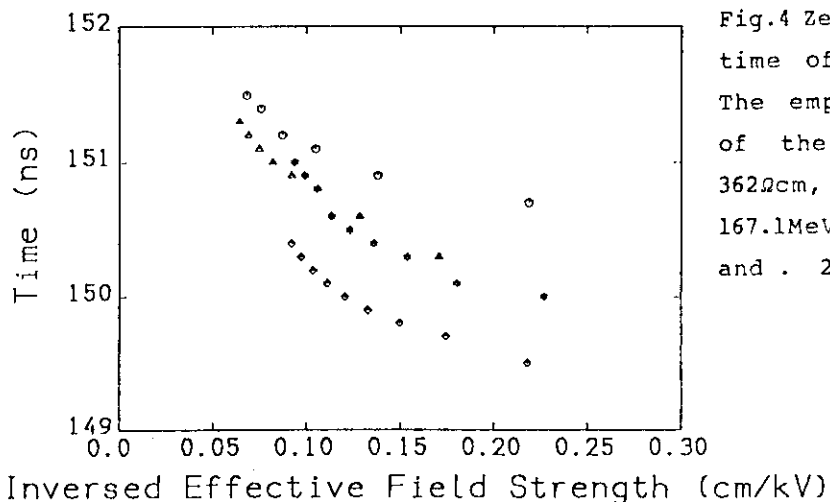


Fig.4 Zero time of the MCP2-SSB time of flight measurements. The employed SSB and energy of the nickel ion were . 362 Ω cm, 114.1MeV, . 362 Ω cm, 167.1MeV, . 2100 Ω cm, 114.1MeV, and . 2100 Ω cm, 167.1MeV.

3.3 PERTURBED ANGULAR CORRELATION MEASUREMENT USING Pd-100/Rh-100 NUCLEAR PROBES II

Hiroshi NARAMOTO, Yukio KAZUMATA, Masumi OHSIIMA,
Masao SATAKA, Yohta NAKAI, Sadae YAMAGUCHI*
and Shinji NAGATA*

Department of Physics, JAERI

*Institute for Materials Research, Tohoku University

1. Introduction

Surface analysis of materials has attracted the increasing interest because the modern functional materials are exposed to the various environments such as the radiations of energetic beams and chemically active substances for the fine processing. The ion beam analysis has been employed to obtain the depth-sensitive information¹⁾, and the results are the averaged ones in their nature. The structural change in the surface region is not in the thermal equilibrium, and there might exist the distribution of the microstructural configuration of the relevant atoms. Thus, the spectroscopic analysis is needed as the counter part of the ion beam analysis.

Among the methods of various spectroscopic analyses, Time Differential Angular Correlation(TDPAC) measurements are employed to perform the microstructural analysis as one of the surface sensitive methods in this study, and are shown some typical results in Be and some Nb samples.

2. Experimental procedure

In the present study, the $^{100}\text{Pd}/^{100}\text{Rh}$ nuclei were recoil-implanted into samples as the probe nuclei through the nuclear fusion reactions between incident 100 MeV ^{12}C ions and ^{93}Nb atoms in a thin foil target. In this measurement, is detected the perturbation experienced by probe nuclei through the interactions of nuclear spin at the intermediate level and the electric field gradient coming from the configuration of outer electrons. Figure 1 illustrates the process of recoil implantation using 100 MeV ^{12}C ions. In the present case, the nuclear reactions induced by heavy ions are employed, and the efficiency of recoil implantation amounts to 60 to 70%. The incident ^{12}C ions can be scanned laterally, and the uniform implantation is expected which is important for the material analysis.

Deuterium atoms in Nb were introduced using 5 keV ion gun, and the ion

beam analysis using the nuclear reactions of $D(^3\text{He}, \alpha)H$ assured the uniform distribution of deuterium atoms along the depth. A system for TDPAC measurements is described elsewhere²⁾.

3. Results and discussion

Figure 2 shows the TDPAC spectrum from Be foil recoil-implanted with $^{100}\text{Pd}/^{100}\text{Rh}$ nuclei, and $R(t)$ the asymmetry ratio is defined as $R(t) = 2((N(\pi, t) - N(\pi/2, t)) / (N(\pi, t) + N(\pi/2, t)))$. $R(t)$ describes the perturbed fraction normalized to the decay rate at each time. $R(t)$ curve was fitted with the perturbation function, which suggests the completely randomized electric field gradient resulting from the random distribution of micro-crystals. In addition, it is considered that the recoil-implanted probes occupy the unique sites, possibly the hexagonal lattice sites.

TDPAC measurements were also made in various kinds of Nb samples where the probe nuclei were introduced by the direct irradiation with 100 MeV ^{12}C ions. The spectra obtained are dependent of the sample preparation process even if in pure Nb samples. Figure 3 shows the spectrum from (100) single crystal, and it is hard to observe the effect of perturbation which is caused by breaking-down of the local symmetry of cubic Nb around the probes. Thus, it is concluded that the $^{100}\text{Pd}/^{100}\text{Rh}$ probe atoms occupy the substitutional sites without the influence of irradiation-induced defects. In the present case, it is reasonably estimated that the probe nuclei are introduced in the near surface region judging from the excitation function, and on the contrary, the most of lattice defects are produced around the projected range. In addition, it is known that the vacancies in Nb become unstable at around 100K³⁾. Thus, the probe atoms can not be decorated by the lattice defects.

Figure 4 shows the spectra taken at 7.4 K from two kinds of Nb thin foils, pure(top) and deuterium-implanted(bottom). In the case of foil sample, heavily perturbed spectra are observed even in a pure sample. This perturbation can not be attributed to the single frequency with simple gaussian distribution. The rolling process is considered to induce the various types of lattice imperfections resulting from the interactions between dislocations, which affects the complicated perturbation. The spectrum at the bottom is for Nb sample where deuterium atoms are dissolved interstitially. The main feature is not different from that in the pure sample even at the low temperature measurement. This result implies that the interaction of probe nuclei with deuterium atoms is very weak. It is needed to perform the

further experiment using crystalline sample dissolved with deuterium atoms.

References

- 1) For example: H. Naramoto, C. W. White, J. M. Williams, C. J. McIlargue, O. W. Holland, M. M. Abraham and B. R. Appleton, J. Appl. Phys. 54(1983) 183.
- 2) H. Naramoto, Y. Kazumata, M. Oshima, M. Sataka, K. Kawatsura, Y. Nakai, S. Yamaguchi, S. Nagata and Y. Fujino, JAERI TANDEM, LINAC & V.D.G. Annual Report 1988, p79.
- 3) H. Metzner, R. Sielemann, S. Klaumünzner, R. Butt and W. Semmler, Proc. of Yamada Conf. V on Point Defects and Defect Interactions in Metals, Kyoto, p224(1981).

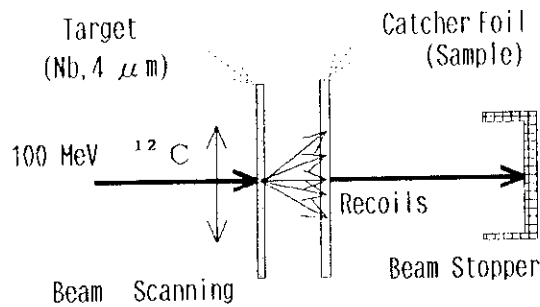


Fig. 1 Illustrative description of recoil implantation.

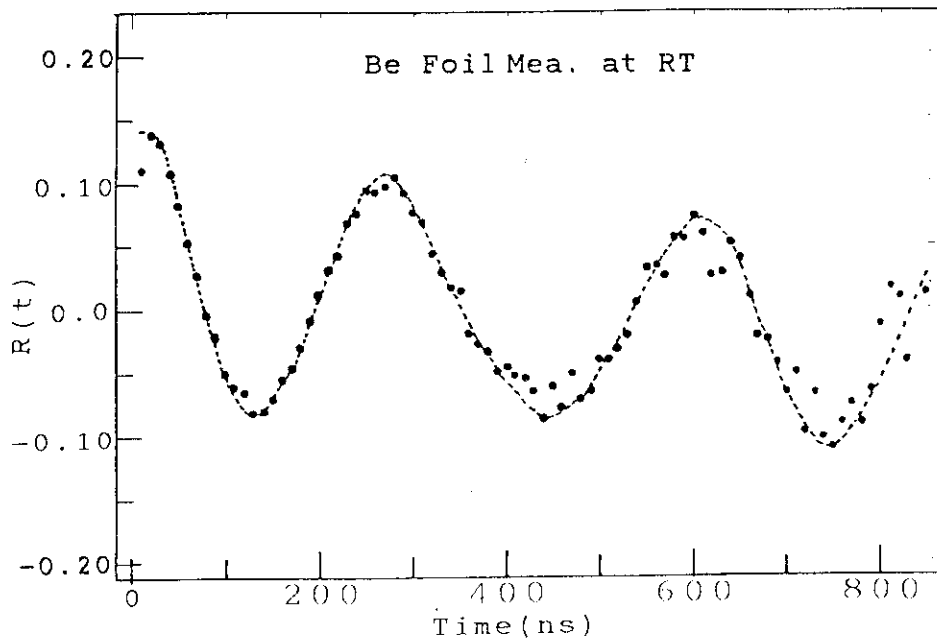


Fig. 2 Periodically perturbed $R(t)$ spectrum from $^{100}\text{Pd}/^{100}\text{Rh}$ probe nuclei in hexagonal Be sample.

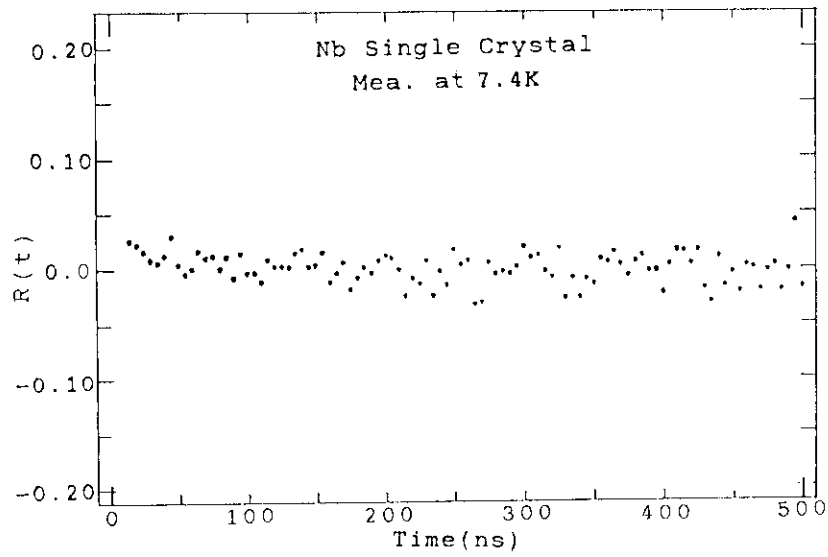


Fig. 3 R(t) spectrum of $^{100}\text{Pd}/^{100}\text{Rh}$ from a niobium single crystal.

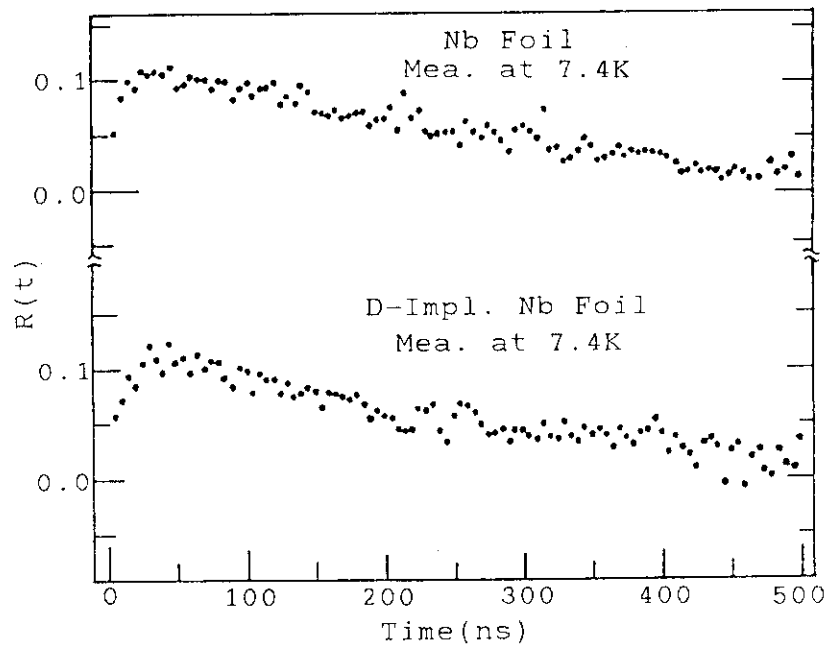


Fig. 4 R(t) spectra from rolled niobium foils, pure(top) and deuterium-implanted to about 7 %(bottom).

3.4 X-RAY DIFFRACTION ON CARBON ION-IRRADIATED DIAMOND

Hiroshi MAETA, Katsuji HARUNA^{*}, Kazutosi OHASHI^{*},
Takuro KOIKE^{**} AND Fumihisa ONO^{**}

Department of Physics, JAERI, ^{*} Faculty of Engineering,
Tamagawa University, ^{**} College of Liberal Arts and
Sciences, Okayama University

1. Introduction

Of interesting properties of diamond, such as high thermal conductivity, good thermal and chemical stability make it attractive for use in high temperature semiconductor device. Doping diamond, however, cannot be achieved by thermal diffusion due to the low diffusivity of impurities even at high temperature. Ion implantation is a prime candidate technique for doping, but the issues of annealing radiation damage, avoiding graphitization, and driving implanted species into substitution sites have not been completely resolved.

In order to resolve this process, the damage due to self-implantation with 100 MeV C ions was studied by means of x-ray diffraction, measurements of lattice parameters and diffraction profiles. We found a remarkable increase of integrated intensities of x-ray diffraction profiles on a synthetic diamond single crystal after ion-irradiation.

2. Experimental Procedures

The synthetic diamond single crystals used in this experiment were purchased of Sumitomo Denko Co.Ltd. The crystals are colored yellow because they contain 1-10 ppm of nitrogen. The crystal size is 3.5 x 3.5 x 0.3 mm³ and surfaces of the specimens were oriented parallel to the (100) plane. The specimens were irradiated with 100 MeV C⁺⁶ ion up to the fluences of 3.5 x 10¹⁵ ions/cm² at about liquid nitrogen temperature using TANDEM Accelerator. After the irradiation, the specimens were warmed up to room temperature.

Measurements of lattice parameters have been made by using the X-ray Bond method in which two counters were placed symmetrically. To attain the

highest observable accuracy, a finely focused K_{β} line from an iron target was used, together with the highest possible reflection angle corresponding to the (100) planes. In the present experiment the (400) reflection was observed, for which $2\theta = 160.01$. By using a fine slit of 0.2 mm in width, the Bragg reflections were measured at room temperature.

3. Results and Discussion

Figure 1 shows the relative change in lattice parameter before and after ion irradiations with the fluences of C^{6+} ions. With self ion irradiation of 48 keV C ions the center of the irradiated region became amorphous at a fluence of $4 \times 10^{16} \text{ cm}^{-2}$. In present work with the 100 MeV C^{6+} ion up to the fluences of $3.5 \times 10^{15} \text{ ions/cm}^2$, the projected range was $102 \mu\text{m}$. So, the damage was considered to be widely distributed.

Figure 2 shows the (400) diffraction peaks from the diamond specimens after irradiation with carbon ion up to $3.6 \times 10^{15} \text{ ions/cm}^2$. The integrated intensities did change with fluence, extremely after the ion irradiations, and the peaks were broadened. We measured the full width at half maximum (FWHM) of the diffraction profiles for the irradiated and unirradiated diamond specimens. The results were summarized in Table 1. The diffraction from pyrolytic graphite of ZXA grade which was measured at the same condition is also shown for comparison.

The lattice parameter increases and broadening of profiles for irradiated diamond are presumed to be due to the formation of point defects and growth of defect clusters into dislocation loops. It is thought that the interstitial in diamond is mobile well below room temperature and the vacancy becomes mobile at 500 C . Most of the radiation damage are present as interstitial dislocation loops and vacancies. The increases of integrated intensities is due to the extinction effects which are associated with the formation of the defects introduced by the irradiations. A more detailed analysis of the present results and a further experimental study are currently in progress.

References

- [1] R.S. Nelson, J.A. Hudson, D.J. Mazey, and R.C. Piller ; Proc Roy. Soc. Lond. A 386, 211 (1983).
- [2] S. Gorbalkin, R. Zuhr, J. Roth and H. Naramoto : to be published.

Table 1 Full width at a half maximum (FWHM) and integrated intensities of self ion irradiated diamond with 100 MeV C⁶⁺. The data of pyrolitiv graphite (ZYA grade) is shown for comparison.

Fluence (10 ¹⁵ ions /cm ²)	FWHM (degree)	Integrated intensity I / I ₀
unirradiated	0.17	1.0
0.68	0.20	4.2
2.4	0.23	4.9
3.6	0.23	5.8
Pyrolitic graphite	0.29	3.4

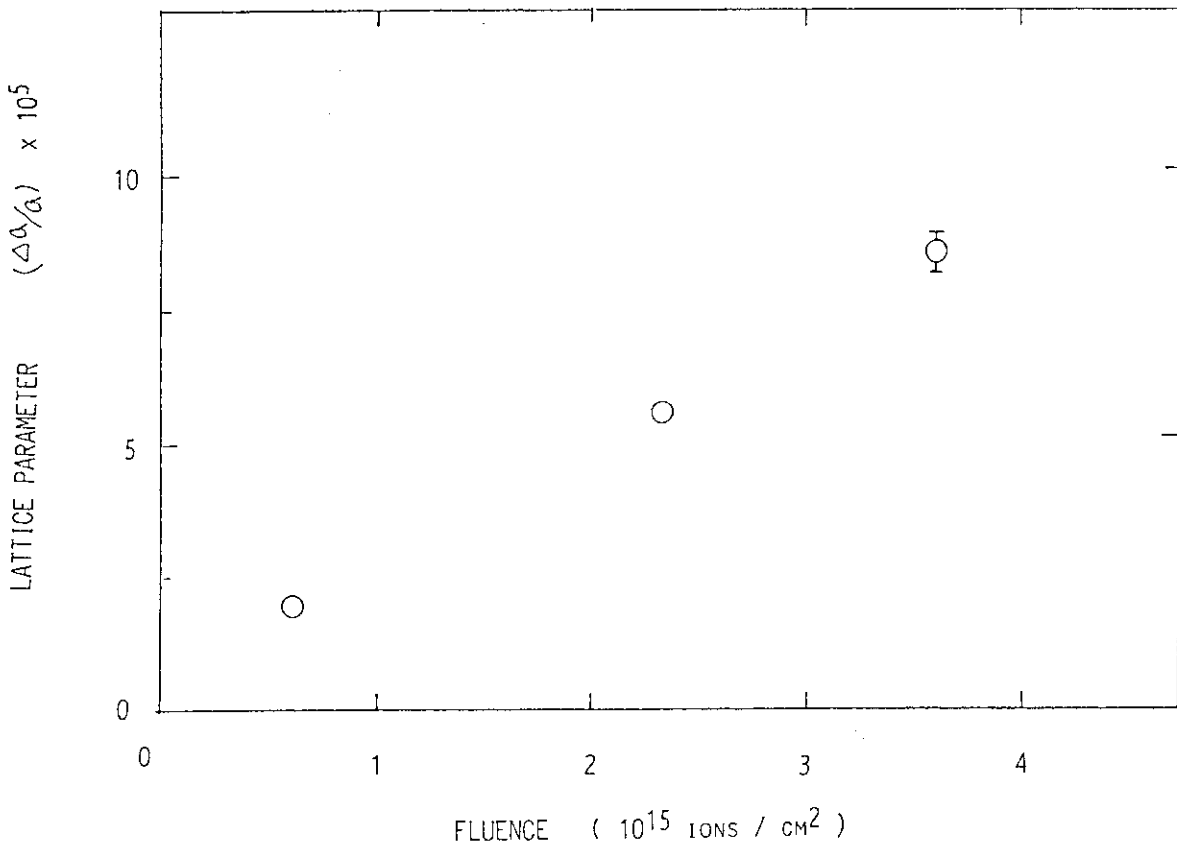


Fig. 1 The fractional increases of the lattice parameters of diamond with fluence of 100 MeV C⁶⁺ ions .

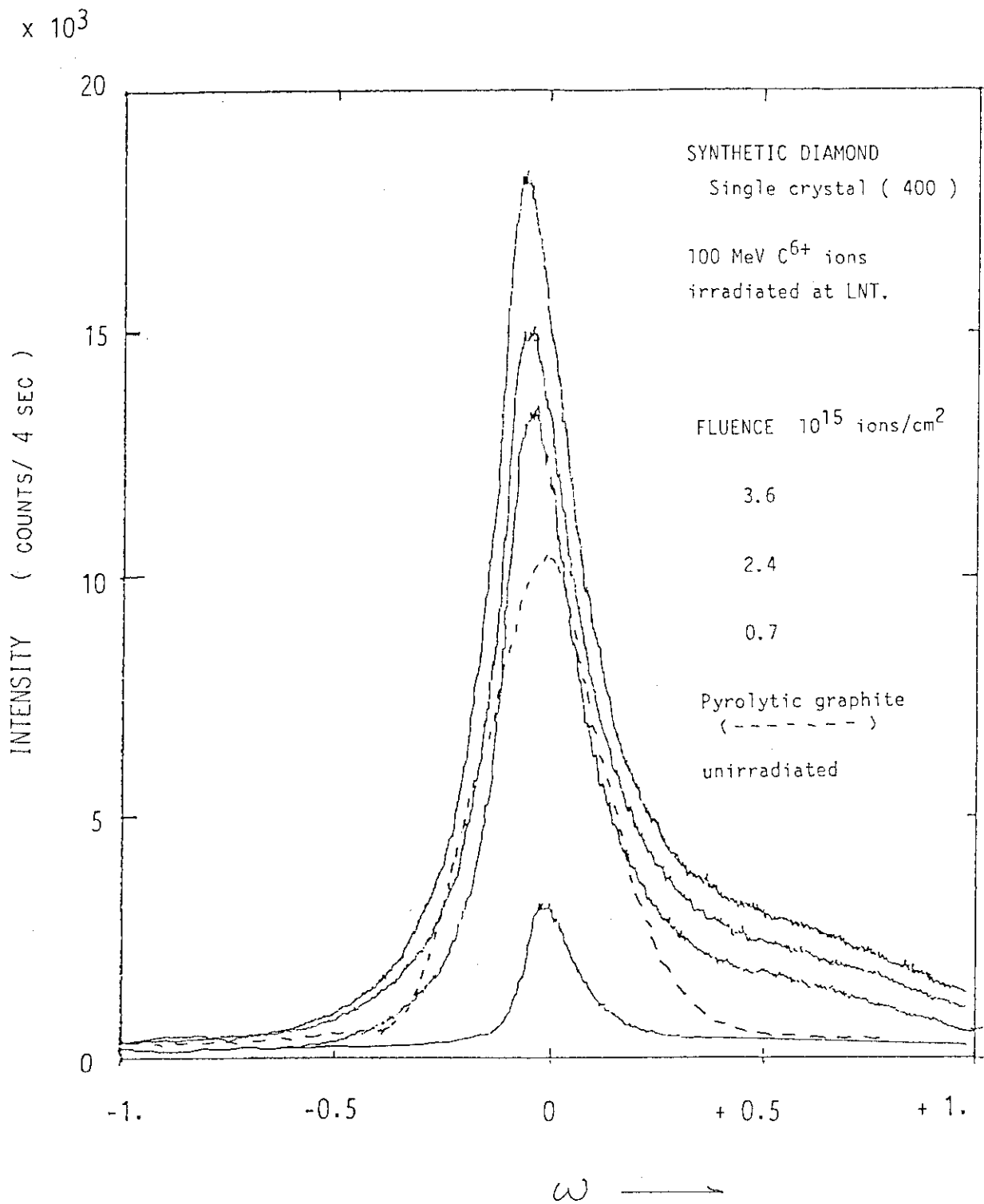


Fig. 2 The diamond (400) X-ray diffraction peak after 100 MeV C^{6+} ion irradiation (Fe radiation).

3.5 EFFECT OF ELECTRON-EXCITATION ON RADIATION DAMAGE IN
ION-IRRADIATED FCC METALS

Akihiro IWASE, Tadao IWATA, Takeshi NIHIRA*
and Shigemi SASAKI

Department of Physics, JAERI, * Faculty of Engineering,
Ibaraki University

In the previous papers¹⁻³⁾, we showed that the anomalous reduction of stage-I recovery and the extraordinarily large cross sections for the subthreshold recombination of stage-I defects were observed in Ni irradiated with high energy (~ 100 MeV) heavy ions. In Cu, however, the above phenomena could not be observed. We explained this difference between Ni and Cu as due to the electron-excitation by high energy ions and electron-phonon interaction. In this report, we show the experimental results of the thermal annealing in other typical FCC metals (Pt, Al and Ag).

Figures 1, 2 and 3 show the amount of the stage-I recovery in Pt, Al and Ag, respectively, as a function of the PKA (primary knock on atom) median energy $T_{1/2}$. As can be seen in Fig. 1, the amount of the stage-I recovery in Pt irradiated with ~ 100 MeV heavy ions is greatly reduced as compared with the case of low energy (~ 1 MeV) ion irradiations. On the contrary, in Ag irradiated with ~ 100 MeV heavy ions, the dependence of the amount of the stage-I recovery on $T_{1/2}$ is the same as in the case of low energy ion irradiation. In Al, the reduction of the amount of the stage-I recovery is observed for high energy ion irradiations, but is not so large as in Pt. According to the lattice thermal conductivity measurements⁴⁾, the electron-phonon interaction is strong in Pt and Ni, and is weak in Cu and Ag. The electron-phonon interaction strength in Al is smaller than in Ni and Pt, but is larger than in Cu and Ag. The present result and the previous result¹⁾ show that the amount of the reduction of stage-I recovery for high energy heavy ion irradiations becomes larger with increasing the strength of the electron-phonon interaction in target metal. This result supports our explanation that the lattice agitations induced by the energy

transferred from the excited electron to lattice through the electron-phonon interaction cause the annihilation of stage-I defects during the irradiation.

References

- 1) A. Iwase, S. Sasaki, T. Iwata and T. Nihira, Phys. Rev. Lett. 58 (1987) 2450.
- 2) T. Iwata and A. Iwase, Rad. Eff. 113 (1990) 135.
- 3) A. Iwase, T. Iwata, S. Sasaki and T. Nihira, J. Phys. Soc. Jpn. 59 (1990) 1451.
- 4) W. H. Butler and R. K. Williams, Phys. Rev. B18 (1978) 6483.

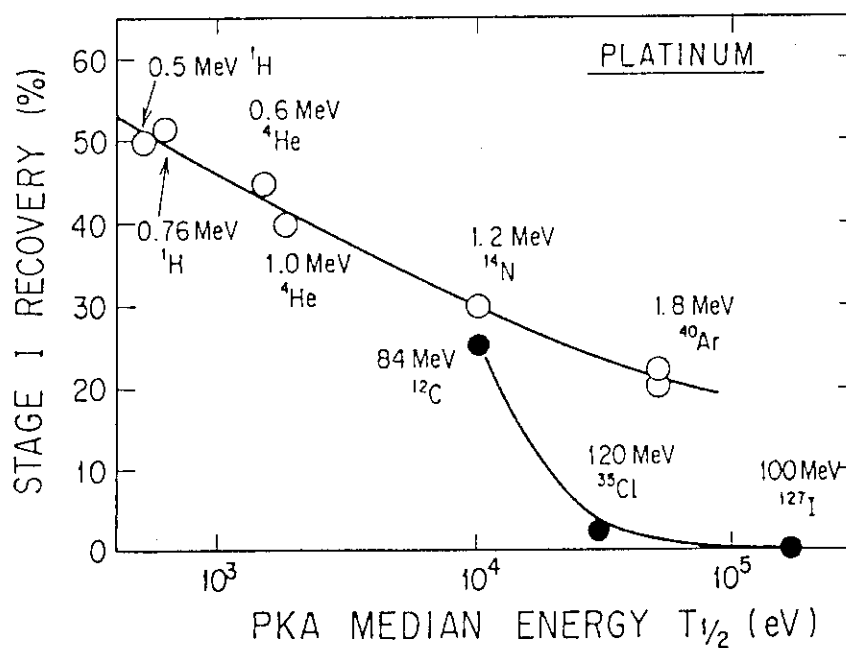


Fig.1

Amount of Stage-I recovery in Pt for low energy ion irradiation (open circles) and for high energy ion irradiation (solid circles).

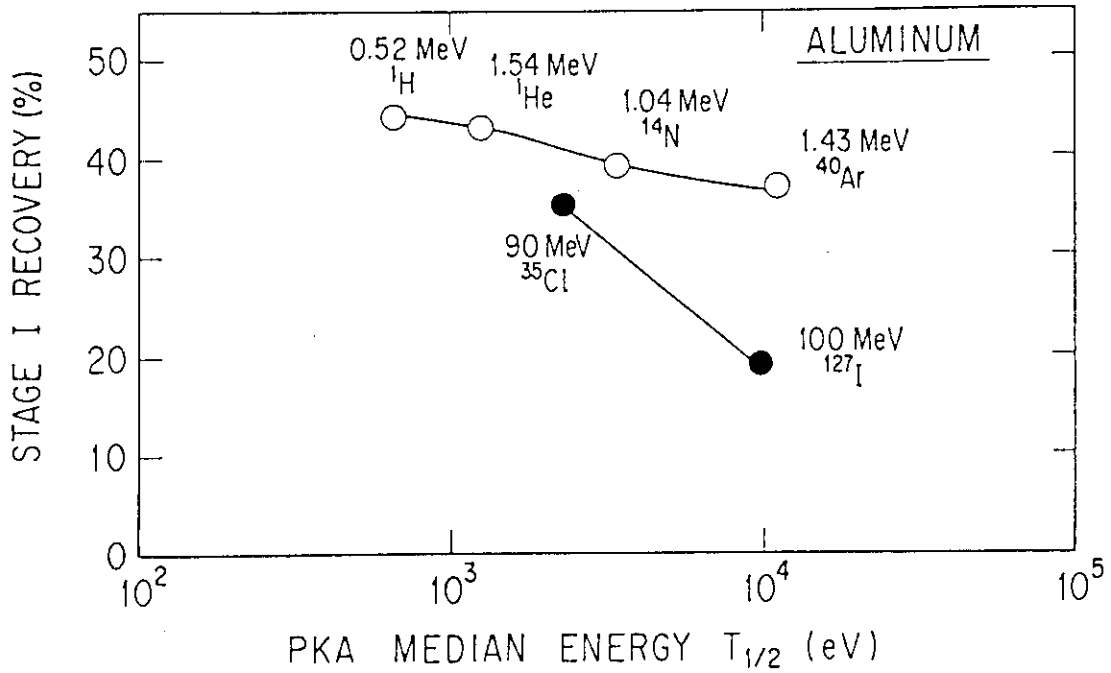


Fig.2

Amount of Stage-I recovery in Al for low energy ion irradiation (open circles) and for high energy ion irradiation (solid circles).

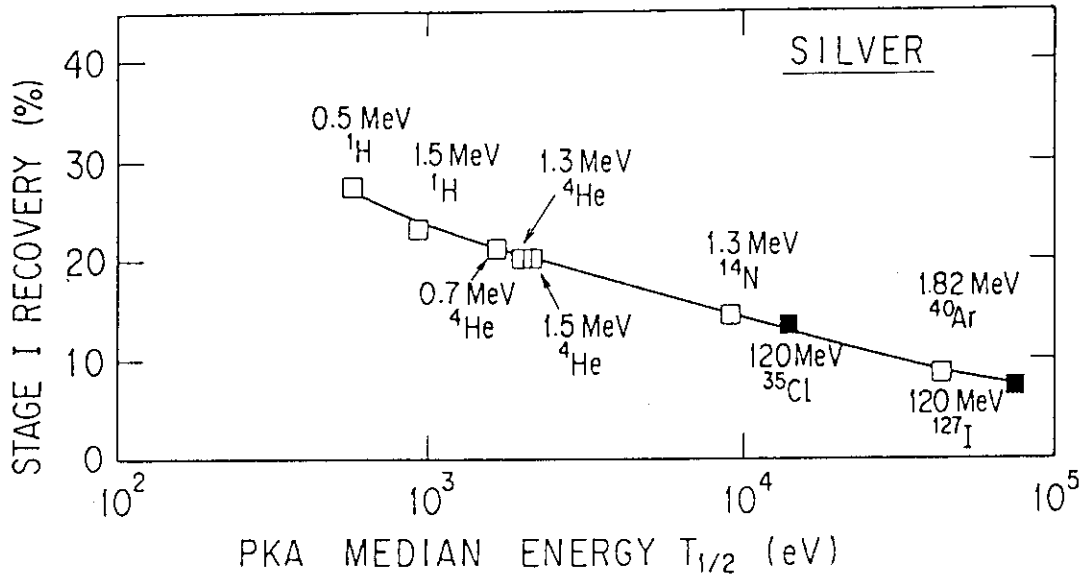


Fig.3

Amount of Stage-I recovery in Ag for low energy ion irradiation (open squares) and for high energy ion irradiation (solid squares).

3.6 CASCADES AND THEIR KINETIC BEHAVIOR IN ION-IRRADIATED COPPER

Ken-ichi FUKUMOTO, Hiroaki ABE, Toyokazu KOJIMA,
 Kazutoshi SHINOHARA, Masanori KUTSUWADA, Chiken KINOSHITA,
 Tadao IWATA*, Akihiro IWASE* and Yukio KAZUMATA*

Department of Nuclear Engineering, Kyushu University,

*Department of Physics, JAERI

Introduction

When crystals are irradiated with fast neutrons, the kinetic energy of neutrons is transferred to primary knock-on atoms (PKA). PKA are ions consisting of constituent elements and have wide variety of kinetic energy (E_p). The high energy PKA produce "cascades" in which high concentration of point defects are localized. Therefore, in order to understand the radiation damage process of neutron irradiated materials, it is indispensable to get information about the structure of cascades and their kinetic behavior as a function of E_p . High energy ions also deposit E_p in accordance with the depth from the incident surface and produce corresponding cascades. The first objective of the present work is to establish a sectioning method for preparing TEM specimens which provides information about cascades as a function of the depth of target materials. The second objective is to get knowledge of the kinetic behavior of cascades during irradiation through TEM observation.

Experimental

In this work, Cu was used as specimens, because it shows clear contrasts corresponding to clusters through TEM observation.

(1) Bulk specimens of 99.998% Cu (2 x 2 x 20 mm) were prepared and one surface of the each specimen was subjected to 100 MeV I⁷⁺ irradiation to fluences of 3.4×10^{17} and 2.4×10^{19} ions/m² at room temperature using the TANDEM accelerator at JAERI. Irradiated specimens were electroplated with Cu until their diameter became 8 mm, and then, they were cut into disks using an acid cutter. The final thinning was made by electropolishing, and TEM observation was performed using JEM-200BS in HVEM Lab, Kyushu University.

(2) *In-situ* observation of microstructural evolution in Cu under dual-beam

irradiation was done at room temperature using a JEM-1000 high-voltage electron microscope (HVEM) on line with an ion accelerator at the HVEM Laboratory, Kyushu University¹⁾. Xe^+ ions of 30 keV and electrons of 250 or 1000 keV were simultaneously irradiated under fluxes of 1.1×10^{14} ions/m²s and $1.9 \times 10^{22} \sim 1.9 \times 10^{23}$ electrons/m²s.

Results and Discussion

(1) High energy ion-irradiation

Weak-beam electron micrographs were taken and show up tiny defect clusters (~ 5 nm) along the direction of ion beam of irradiated specimens. The volume density of defect clusters was measured, and it is shown in Fig. 1 as a function of the distance from the incident surface for a specimen irradiated to a low fluence of 3.4×10^{17} ions/m². The density of defect clusters increases with the increasing depth and reaches the maximum value at about 6.5 μm from the surface. The depth profiles of damage were calculated for 100 MeV I^{7+} irradiation through the TRIM code with 40 and 50 keV for the threshold energies of sub-cascades, and they are also shown in Fig.1. The calculated value through the TRIM code with about 50 keV for the threshold energy shows fairly good coincidence with experimental values. Fig.2 is the same as Fig.1, but for a specimen irradiated to a higher fluence of 2.4×10^{19} ions/m². In contrast to Fig.1, the density of defect clusters for a

high fluence hardly shows the dependence on the depth from the surface. It is attributed to the overlapping of defect clusters because of a too large fluence.

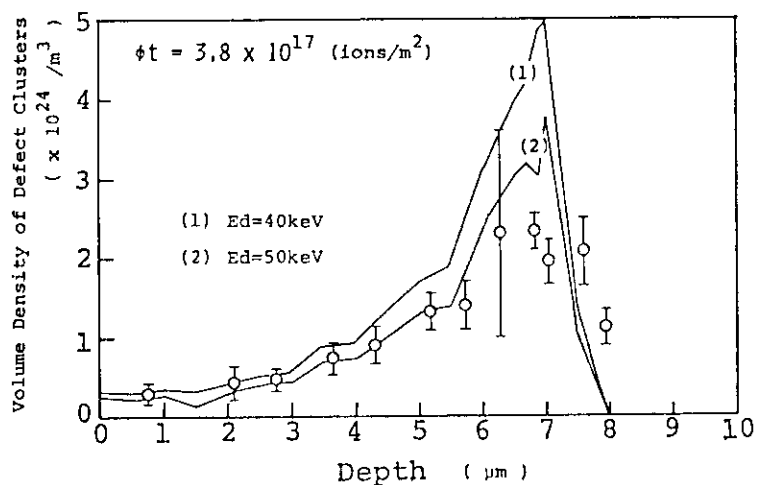


Fig. 1 The depth dependence of the volume density of defect clusters in Cu irradiated with 3.8×10^{17} 100-MeV I^{7+}/m^2 . Solid lines (1) and (2) are calculated through the TRIM code with 40 and 50 keV for the threshold energy of sub-cascades, respectively.

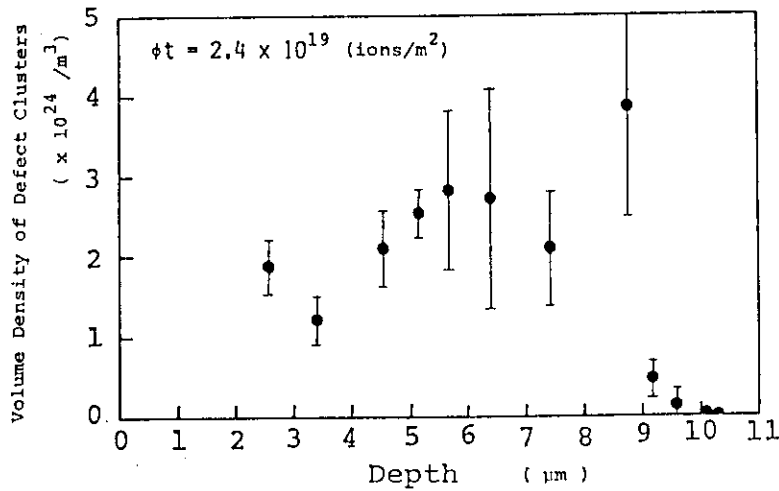


Fig. 2 Same as in Fig. 1, but for Cu irradiated with 2.4×10^{19} 100-MeV I^{7+}/m^2 .

(2) Low energy ion-irradiation

Fig.3 shows the irradiation time dependence of the area density of stacking fault tetrahedra (SFT) normalized against the production rate of cascades in Cu under the dual-beam irradiation. The density of SFT increases in proportion to irradiation time, t , in the beginning of irradiation and to $t^{1/2}$ in

the later stage under irradiation with 30 keV Xe ions and 250 keV electrons. Since 250 keV electrons induce a low concentration of Frenkel pairs, the accumulation process of SFT is primarily controlled by the interaction between the surface and cascades and that

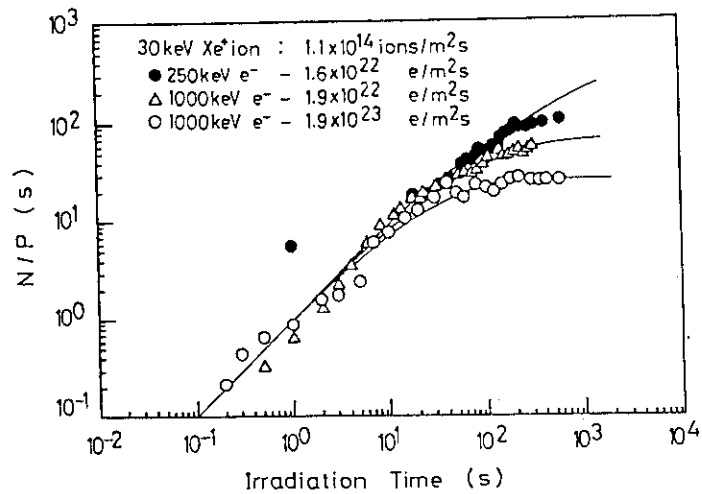


Fig. 3 Dependence of area density (N) of SFT in Cu on irradiation time under the dual-beam irradiation with 30 keV Xe^+ ions and 250 or 1000 keV electrons. Here, P is the production rate of cascades.

among cascades themselves. Irradiation with 1000 keV electrons, on the other hand, introduces a high concentration of Frenkel pairs, and suppresses the accumulation of SFT, making the density of SFT saturate earlier at the lower level. The level of the saturated density decreases with increasing the flux of 1000 keV electrons, because of the higher production rate of free interstitials which contribute to the annihilation of cascades.

Conclusions

- (1) The depth profile of the density of defect clusters is reproduced by TRIM code with 50 keV for the threshold energy of sub-cascades.
- (2) The dual-beam irradiation with 1000 keV electrons and 30 keV Xe⁺ ions suppresses the accumulation of cascades. The behavior of Frenkel pairs due to electron irradiation plays an important role in making cascades unstable.

Reference

- 1) K. Fukumoto, C. Kinoshita, H. Abe, K. Shinohara and M. Kutsuwada, to be published in J. Nucl. Mater..

3.7 EFFECTS OF He ION IRRADIATION ON CRITICAL CURRENT BEHAVIORS OF Bi-Sr-Ca-Cu-O FILMS

Takeo ARUGA, Saburo TAKAMURA*, Taiji HOSHIYA**
and Mamoru KOBIYAMA***

Department of Fuels and Materials Research, *Department
of Physics, **Oarai Research Establishment, JAERI,
***Faculty of Engineering, Ibaraki University

The current carrying capability of high Tc oxides is a major problem from the application point of view and from the fundamental understanding. The critical current density is given by the balance between the Lorentz force exerted on flux lines by the transport current and the pinning force. Although an irradiation induces the strong pinning centers, it degrades superconducting properties such as the transition temperature. Since above two mechanisms are responsible for the irradiation effects on high Tc superconductors, it is necessary to study changes in superconducting properties by the irradiations. In this report, we describe the effects of room-temperature He-ion irradiation on the critical current measured by an electrical resistance method in Bi-Sr-Ca-Cu-O films.

The details of the sample and the experimental methods in the present work were described in the previous papers 1-3). Magnetic field supplied was perpendicular to both the film surface and the current direction. The value of critical current was chosen to be the one at which the generated voltage between potential leads was 1V. The 400-keV He-ion irradiation was performed at room temperature. The temperature dependence of critical current was measured in a helium atmosphere after removing the sample from the irradiation chamber and the sample was again attached to the chamber for further irradiations.

The critical current I_c is plotted in Fig. 1 as a function of temperature under the magnetic field, for the sample irradiated to $2.0 \times 10^{17}/\text{m}^2$. The critical current under the zero magnetic field ($H=0$) decreases linearly with increasing temperature to 67 K and decreases very slightly by the irradiation to $2.0 \times 10^{17}/\text{m}^2$, where the defect concentration was about 60 ppm¹). Then, the critical temperature hardly

changes, whereas the resistivity in the normal state increases from $6 \times 10^{-6} \Omega \text{m}$ to $7 \times 10^{-6} \Omega \text{m}$ by the irradiation. However, under the magnetic field supplied up to 1.36 T, a slight increase in the critical current is discernible with increasing the dose up to $2.0 \times 10^{17} / \text{m}^2$, although the critical currents there are quite low and approaching zero. The result for the sample irradiated to a higher dose of $1.6 \times 10^{18} / \text{m}^2$ is given in Fig. 2. The critical temperature under $H=0$ decreases from 76 K to 58 K by the irradiation to $1.6 \times 10^{18} / \text{m}^2$, which induces the defect of 500 ppm in concentration. The critical current under $H=0$ and 0.68 T decreases by more than 50 % after the irradiation to $1.6 \times 10^{18} / \text{m}^2$. The critical current-temperature relation before irradiation under $H=0$ consists of major two linear regions by a change of slope at 65 K. The slope above 65 K is nearly equal to that of the linear portion of Fig. 1, whereas the slope below 65 K is less steep than that above 65 K. Since the polycrystalline sample is considered to consist of superconductors which are more or less weakly connected as an array of the weak links, the slope below 65 K seems to be due to the occurrence of weak links different from those in Fig. 1.

Using another sample, an attempt is made to find whether the pinning strength of flux lines can be obtained from critical current measurements after removing an applied magnetic field for the film ion-irradiated to $2.0 \times 10^{18} / \text{m}^2$. The magnetic field perpendicular to the film plane was supplied to 2.1 T at 70 K and the applied field was removed at 20 K. Measurement of the temperature dependence of critical current was performed with increasing the temperature. The temperature dependence of the critical current after removal of the applied magnetic field is compared in Fig. 3 with those measured without magnetic field, before and after the irradiations. The temperature dependence of the critical current after removal of the magnetic field before irradiation is nearly the same as that without magnetic field, showing that the pinning strength in the unirradiated sample is relatively weak. For the irradiated sample, the critical current after removal of the magnetic field is remarkably low compared with that without magnetic field. From the difference between the temperature dependences of the critical current after removal of the applied magnetic field and that without magnetic field for the irradiated sample, it is revealed that there is a certain distribution of pinning strength introduced in the

irradiated sample. Moreover, the temperature dependence of the critical current after annealing to 37 K is parallel to the curve without magnetic field during both decreasing and increasing temperatures. This result shows that the depinning of flux lines, which are pinned at the radiation-induced defects, takes place through thermally activated jumps. The definite enhancement of the critical current, however, can not be observed, as shown in Figs. 1 and 2, as long as the electrical resistance method is used. The degradation of superconducting properties in weak links by the irradiation seems to overwhelm the increase in pinning strength introduced by the irradiation.

References

- 1) T. Aruga, S. Takamura, T. Hoshiya and M. Kobiyama, Jpn. J. Appl. Phys. 28 (1989) L964.
- 2) S. Takamura, T. Hoshiya, T. Aruga and M. Kobiyama, Jpn. J. Appl. Phys. 28 (1989) L1395.
- 3) S. Takamura, T. Aruga and T. Hoshiya, Jpn. J. Appl. Phys. 28 (1989) L1118.

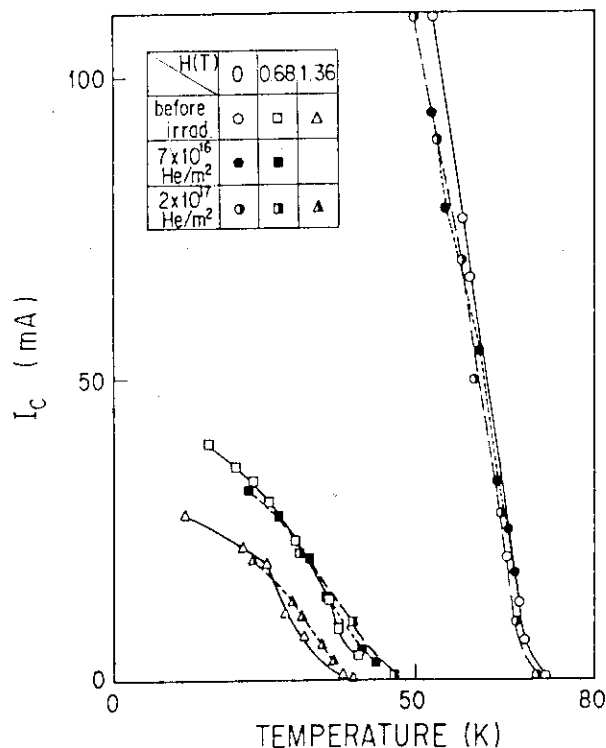


Fig. 1 Temperature dependence of critical current under magnetic field perpendicular to film plane before and after 400-keV He irradiations. The critical current of 100 mA corresponds to the current density of $5 \times 10^8 / \text{m}^2$.

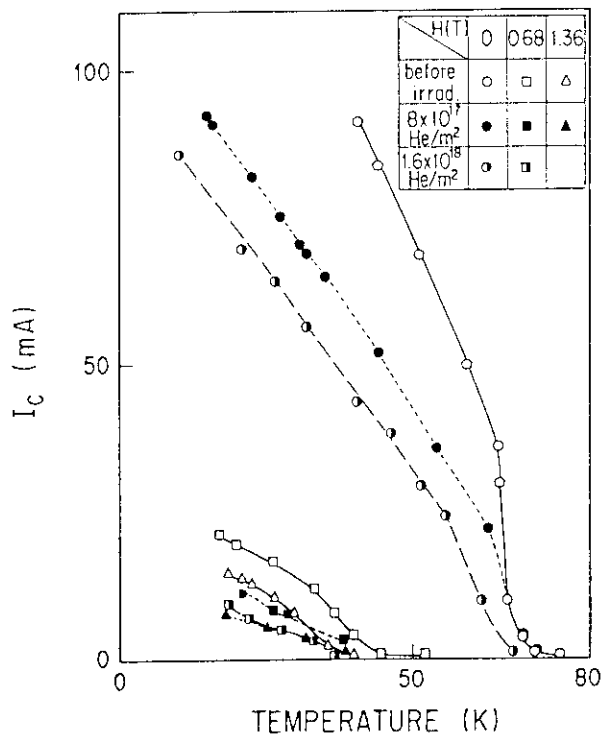


Fig. 2 Temperature dependence of critical current under magnetic field perpendicular to film plane for the sample irradiated to a higher dose.

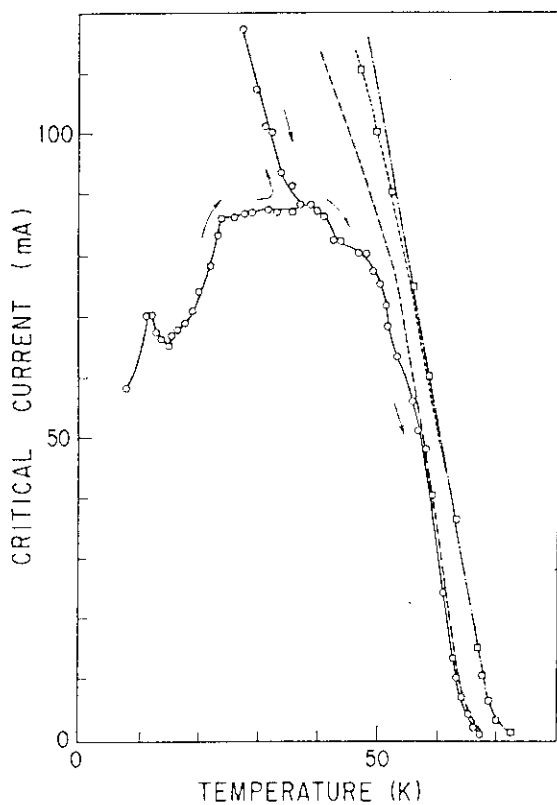


Fig. 3 The temperature dependence of critical current before and after 400-keV He ion irradiation to $2 \times 10^{18} / \text{m}^2$. The critical current before irradiation measured after removal of applied magnetic field ($--\square--$) and without field ($- \bullet -$). Similarly, the critical current after irradiation measured after removal of applied magnetic field ($- \circ -$) and without field ($---$). The order of measurements for the irradiated sample is shown by arrows.

3.8 EFFECT OF HIGH ENERGY ION IRRADIATION ON CURRENT-VOLTAGE CHARACTERISTICS IN OXIDE SUPERCONDUCTOR $\text{YBa}_2\text{Cu}_3\text{O}_{7-x}$.

Akihiro IWASE, Norio MASAKI, Tadao IWATA and
Takeshi NIHIRA*

Department of Physics, JAERI, *Faculty of Engineering,
Ibaraki University

One of the remarkable features of the oxide superconductor $\text{YBa}_2\text{Cu}_3\text{O}_{7-x}$ is the non-Ohmic current-voltage (I-V) relation near the superconducting transition temperature. This paper shows the effect of high energy ion irradiation on the non-Ohmic I-V characteristics in $\text{YBa}_2\text{Cu}_3\text{O}_{7-x}$.

The specimen used in the present experiment was carefully prepared from aqueous solutions of Y-, Ba- and Cu-nitrate in their appropriate ratio. The sheet-shaped specimen of $\sim 10 \times 1 \times 0.1 \text{ mm}^3$ was cut from the sintered disc for the electrical resistance measurement. The specimen was identified by its X-ray diffraction pattern as a single phase. Electrical resistance of the specimen was measured by a four-probe method with a measuring current of 0.1-10 mA. The irradiation was performed at 77.3 K with 120 MeV ^{16}O ions from the JAERI tandem accelerator. The projected range of the 120 MeV O ions in the specimen is about the same as the specimen thickness of 0.1mm. Then the unirradiated region hardly remains through the specimen. The I-V characteristics were measured also at 77.3 K for various oxygen ion fluences.

The experimental result is plotted logarithmically in Fig. 1. Figure 2 shows the same plot as in Fig.1, but only for $I < 2 \text{ mA}$. As can be seen in Fig. 2, for small current ($I < 2 \text{ mA}$), $\ln(V)$ varies linearly with $\ln(I)$ for various ion fluences, and the slope of the plot of $\ln(I) - \ln(V)$ decreases with increasing the ion fluence. This means that the voltage varies as a power of the current, i. e., $V \propto I^a$, and the exponent a is a function of the ion fluence, decreasing as ϕ is increased. Moreover, the straight line for each fluence can be extrapolated to the same point (I_0, V_0) . The linear relationship between $\ln(I)$ and $\ln(V)$ is, however, no longer

retained for larger current ($I > 2$ mA). Figure 1 shows that the gradient of $\ln(I)-\ln(V)$ curve decreases with the increase of the current for every ion fluence. In Fig. 3 is shown the plot of $\ln(V)$ against $\ln(\Phi)$ (i.e. the logarithm of the ion fluence) for various currents. As can be seen in Fig. 3, the linear relationship between $\ln(\Phi)$ and $\ln(V)$ exists for every measuring current. This means that the dependence of V on Φ also exhibits a power-law behavior, i.e. $V \propto \Phi^b$, and the exponent b decreases with the increase of I . For small current ($I < 2$ mA), each straight line can be extrapolated to the same point (Φ_0, V_0) . Here, it is worth noting that the value of V_0 in Fig. 3 is the same as that in Fig. 2. From the results mentioned above, the voltage V against the current I and the fluence Φ for $I < 2$ mA can be described by the following simple form:

$$\ln(V/V_0) = \alpha \ln(\Phi/\Phi_0) \times \ln(I/I_0) \quad \text{for } I < 2 \text{ mA}, \quad (1)$$

where, constants α , V_0 , I_0 and Φ_0 were determined from the experimental result as -1.06 , 7.9 mV, 7.7 mA and $4.8 \times 10^{15} \text{ cm}^{-2}$, respectively.

The power law behavior in the form of $V \propto I^a$ near T_c has been observed also in the ultra-thin (two dimensional) type II superconductors, and has been interpreted as due to the dissipative motion of thermally excited vortices which are unbound by the external current. Since oxide superconductor $\text{YBa}_2\text{Cu}_3\text{O}_{7-x}$ has a layered crystal structure, and can be considered approximately as two dimensional, the above mechanism has been used for the explanation of the power law behavior of the I - V characteristics in $\text{YBa}_2\text{Cu}_3\text{O}_{7-x}$. According to the above mechanism, voltage V varies as

$$V \propto I^{\frac{q}{2kT} + 1}, \quad (2)$$

when the production of free vortices is dominant as compared with the vortex trapping. Here, $q = (\pi n_s h^2 / 2m)^{1/2}$ is the effective vortex charge by analogy with the two dimensional coulomb gas, n_s is the areal superelectron density, and m is the electron mass. This corresponds to the large measuring current. On the other hand, when the vortex trapping rate

is much larger than the free vortices production rate (corresponding to the small current), voltage V varies as

$$V \propto I \frac{q^2}{kT} + 1 \quad (3)$$

Therefore, if the vortex pinning occurs, the slope of $\ln(I)$ - $\ln(V)$ plot should be changed from $q^2/kT + 1$ to $q^2/2kT + 1$ with increasing I . In the following, we discuss the experimental result using the above formula.

Figures 1 and 2 show that for small measuring current, the linear relationship exists between $\ln(I)$ and $\ln(V)$ and that the slope of the plot of $\ln(I)$ - $\ln(V)$ decreases with increasing the measuring current. Unfortunately we have not measured the I - V characteristics above $I=10\text{mA}$, and it is not evident whether the I - V characteristics fit another straight line on a log-log plot for large current. The change in the slope of $\ln(I)$ - $\ln(V)$ plot shown in Fig. 1, however, suggests that the vortex trapping occurs in the present experiment. By comparing eq. (3) with eq. (1), the following relation is obtained;

$$1 + q^2/kT = -1.06 \times \ln(\Phi/\Phi_0) \quad (4)$$

This relation shows that q^2 (or the areal superelectron density n_s) decreases linearly with increasing the logarithm of the ion fluence $\ln(\Phi)$. If the specimen is not homogeneous, but consists of a network of superconducting islands joined by weak links, and the change in the phase of order parameter occurs mainly at weak links (this situation is expected in the present specimen), q^2 provides the coupling energy of the neighboring two islands E_j . In this case, eq. (4) means that the weak links are damaged by the ion irradiation, and that the coupling energy decreases linearly with increasing $\ln(\Phi)$.

Therefore, we conclude that if the vortex pairs are thermally excited actually in the specimen, and q^2 or E_j decreases linearly with $\ln(\Phi)$, we can explain the dependence of the voltage on the current and the ion fluence. The existence of such excitation in $\text{YBa}_2\text{Cu}_3\text{O}_{7-x}$ is, however, not unequivocally proved now, and other explanations for the experimental result may be possible. In addition, the physical meaning of the values of the constants α , V_0 , I_0 and Φ_0 in eq. (1) remains unexplained. In this paper, first of all, it should be emphasized that the effect of high

energy ion irradiation on the I-V characteristics in $\text{YBa}_2\text{Cu}_3\text{O}_{7-x}$ was found to be described as a simple form of eq. (1).

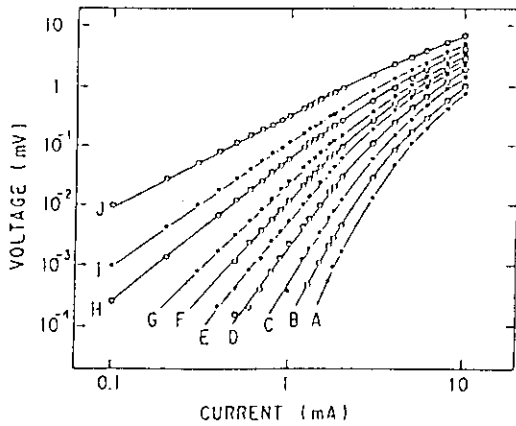


Fig.1 Voltage-current characteristics at 77.3 K for various ion-fluences, (A) before irradiation, (B) $2.96 \times 10^{13}/\text{cm}^2$, (C) $5.89 \times 10^{13}/\text{cm}^2$, (D) $9.89 \times 10^{13}/\text{cm}^2$, (E) $1.60 \times 10^{14}/\text{cm}^2$, (F) $2.14 \times 10^{14}/\text{cm}^2$, (G) $3.01 \times 10^{14}/\text{cm}^2$, (H) $5.00 \times 10^{14}/\text{cm}^2$, (I) $6.78 \times 10^{14}/\text{cm}^2$ and (J) $1.14 \times 10^{15}/\text{cm}^2$.

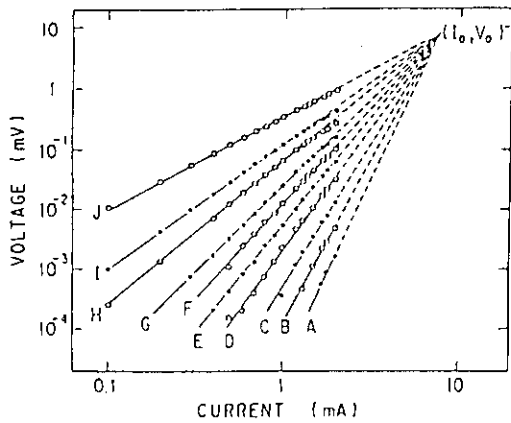


Fig. 2 Same as FIG. 2 except that the data are plotted only for $I < 2\text{mA}$.

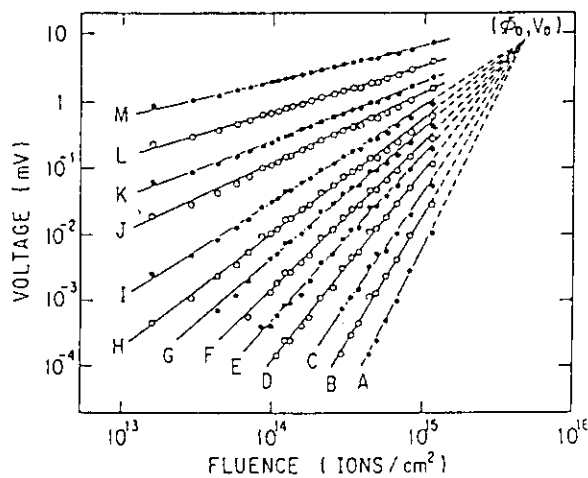


Fig. 3 Fluence dependence of voltage at 77.3 K for various measuring currents, (A) 0.1 mA, (B) 0.2 mA, (C) 0.3 mA, (D) 0.5 mA, (E) 0.7 mA, (F) 0.9 mA, (G) 1.2 mA, (H) 1.5 mA, (I) 2.0 mA, (J) 3.0mA, (K) 4.0 mA, (L) 6.0 mA, and (M) 10.0 mA.

3.9 ELECTRICAL AND STRUCTURAL PROPERTIES OF Li-ION IRRADIATED β -LiAl

Kazuo KURIYAMA, Naoyuki MINEO, Hiroyuki SUGAI*,
Hiroshi NARAMOTO**, Yukio KAZUMATA**, and
Haruhiko MOTOHASHI**

College of Engineering and Research Center of Ion Beam
Technology, Hosei University, *Department of Radioisotopes,
JAERI, **Department of Physics, JAERI

LiAl alloy is an useful material for solid-blanket of nuclear fusion.¹⁾ Electrical conductivity of β -LiAl below room temperature has been reported.²⁻⁴⁾ The important feature of the conduction mechanism for β -LiAl is governed by positive carriers(holes)^{5,6)} in the valence band. The electrical conductivity based on these holes is affected considerably by the defect structure⁷⁾ in β -LiAl(about 48-56at.% Li). The defect structure at room temperature consists of two types of defect: vacancies in the lithium sublattice (V_{Li}), and lithium antistructure atoms in the aluminium sublattice (Li_{Al}). The purposes of the present work are (i) to measure electrical resistivity of β -LiAl before and after Li-ion irradiation and (ii) to survey the modification of Li vacancies in Li-ion irradiated β -LiAl.

Samples were prepared by a resistance furnace melting of 99.9% lithium and 99.999% aluminum. The details of sample preparation have been previously described.^{8,9)} Ion irradiations were performed by a tandem accelerator at JAERI. 60 MeV- ${}^7Li^{3+}$ ion was used in this study. Samples were irradiated with Li-ions in a range $1.3 \times 10^{15} - 4.0 \times 10^{15} /cm^2$ at 140 K. The calculated range of Li-ions for β -LiAl was 0.56 mm for 60 MeV and 0.28 mm for 40 MeV as shown in Fig.1.

The electrical resistivity measurement was made using Van der Pauw technique.¹⁰⁾ The temperature-dependence electrical resistivity was measured at temperature range 90 - 300 K under vacuum of about 10^{-3} Torr. In order to evaluated the depth profiles of electrical properties, a few μm were removed from the irradiated side of the samples for each measurement. The polished surface was observed by an optical microscope. The crystal structure after irradiation was measured by X-ray diffractometer using Cu-K α radiation.

Figure 2 shows the typical electrical resistivities before and after irradiations. The resistivity data for the irradiated sample were measured after about 90 days

from irradiation. These irradiated samples revealed the aluminum precipitations as discussed later.

Figure 3 shows the photographs for as-irradiated surface(Fig.3(a)) and the polished surfaces. Figs.3(b) and (c) show the portions removed 40 μm and 400 μm from the surface, respectively. The metallic precipitations were observed obviously in the as-irradiated surface and the polished surface. The same species were also precipitated in the back surface as identified by X-ray diffraction. These precipitations were not observed after a week from irradiation.

Figure 4 shows the X-ray diffraction pattern of the irradiated surface. The diffraction lines corresponding to the Al(111) and Al(200) planes were observed. Therefore, the precipitations in the surface were identified with aluminum. The irradiated surface contains the $\alpha(\text{Al})$ and β phases.

Figure 5 shows a typical sheet resistance of the irradiated sample at room temperature as a function of the depth. The sheet resistance has a maximum near the range of Li-ions. The Li-ion irradiation is likely to influence the electrical properties, accompanied by the radiation damage.

In order to verify this hypothesis, the further detail study is required.

References

- 1) J.R. Powell, F.T. Miles, A. Aronson and W.E. Winsche; BNL-18236, Brookhaven National Laboratory (1973).
- 2) K.Kuriyama, T.Kamijoh, and T.Nozaki; Phys. Rev. B 22 (1980)470;
K.Kuriyama, S.Yanada, T.Nozaki, and T.Kamijoh; Phys.Rev.B 24 (1981)6158.
- 3) T.Asai, M.Hiratani, and S.Kawai; Solid State Commun. 48 (1983)173.
- 4) L.H.Hall, T.O.Brun, G. W. Crabtree, J.E. Robinson, S. Susman, and T.Tokuhiro; Solid State Commun. 48 (1983)547.
- 5) K.Kuriyama, T.Nozaki, and T.Kamijoh; Phys. Rev. B 26, (1982)2235.
- 6) M.Yahagi; Phys. Rev. B24 (1981)7401.
- 7) K.Kishio and J.O.Brittain; J. Phys. & Chem. Solids 40 (1979)993.
- 8) K.Kuriyama, S.Saito, and K.Iwamura; J.Phys. & Chem.Solids 40 (1979)457.
- 9) M.Yahagi; J.Cryst.Growth 49, (1980)396.
- 10) L.J.Van der Pauw; Philips Tech. Rev. 20, (1958)220.

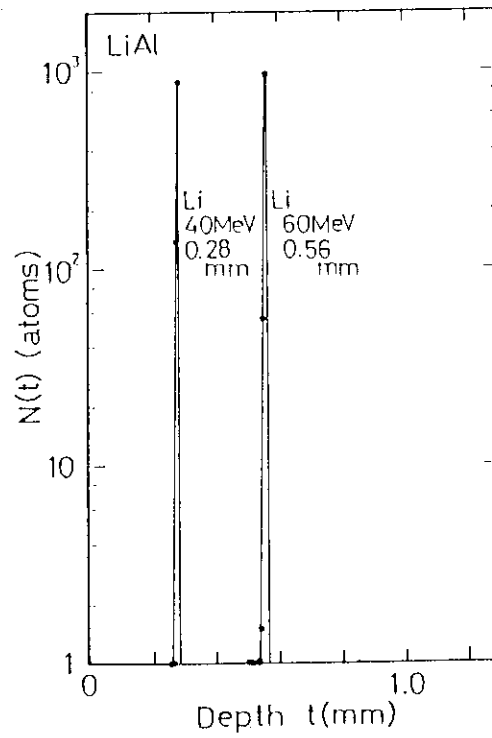


Fig.1 The calculated range of Li-ion in β -LiAl.

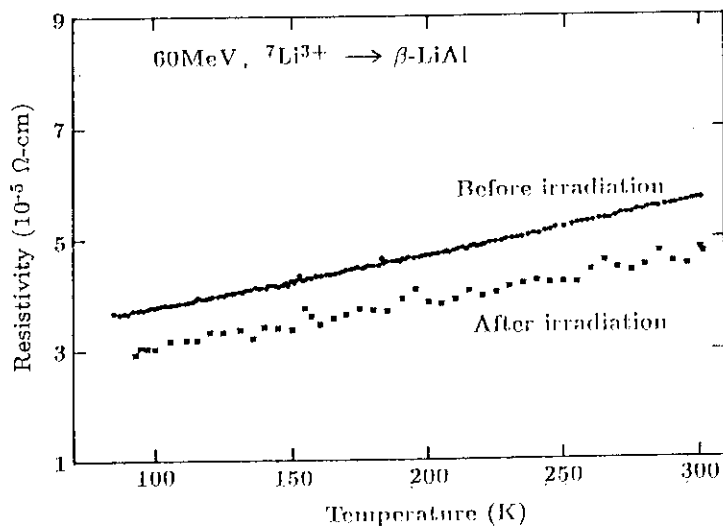
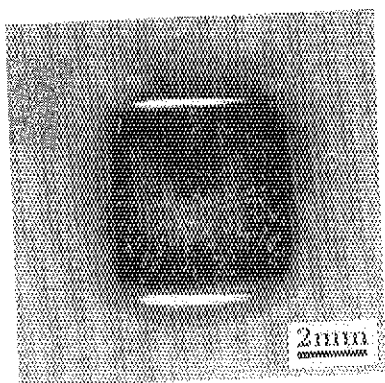
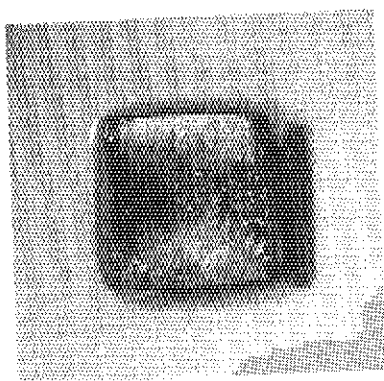


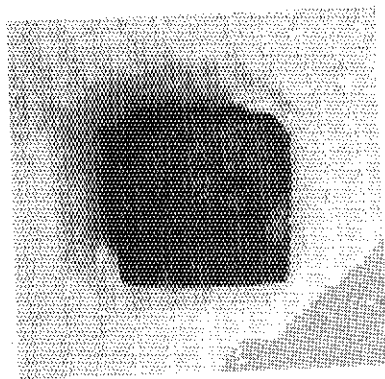
Fig.2 The typical electrical resistivities before and after Li-ion irradiations.



(a)



(b)



(c)

Fig.3 The photographs for (a) as-irradiated surface, (b) surface removed 40 μm , and (c) surface removed 400 μm .

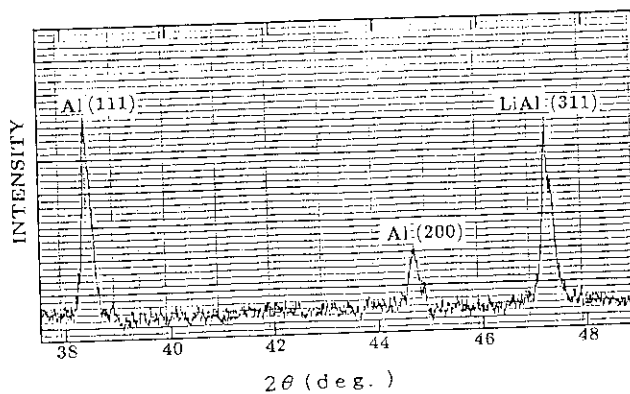


Fig.4 X-ray diffraction pattern of the irradiated surface.

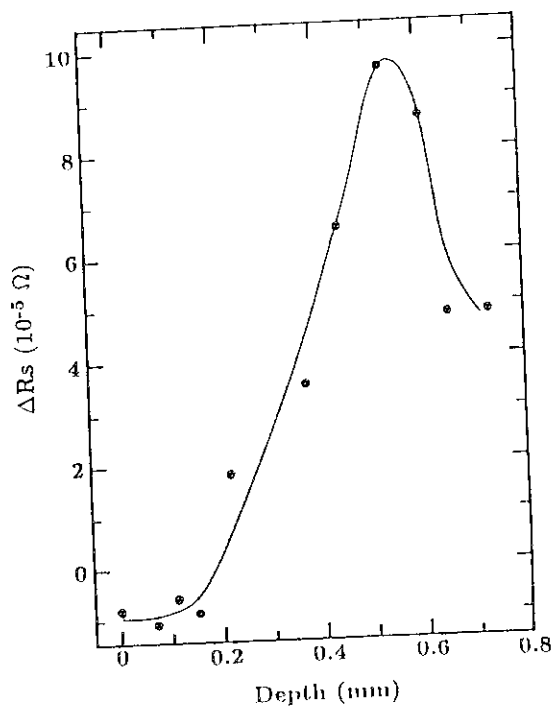


Fig.5 A typical sheet resistance of the irradiated sample at room temperature as a function of the depth.

3.10 IRRADIATION BEHAVIOR OF TRITIUM-BREEDING CERAMICS

Hisayuki MATSUI, Mikio HORIKI, Kenji NODA*, Yoshinobu ISHII*
and Hitoshi WATANABE*

Department of Nuclear Engineering, Nagoya University,

*Division of Material Development, JAERI

Introduction

In fusion technology (D-T fusion), tritium breeding blanket is one of the most important structural materials in the reactor. To this purpose, several kinds of ceramics including Li have been developed. From a view point of material characterizations, Li_2O has been considered to be a most desirable candidate for the blanket, thus being applied to FER. In an operation of the fusion reactor, all the structural materials are subjected in a strong radiation field; bombardment of fast (14 MeV) neutrons in the fusion reaction and other highly energetic particles, such as T (2.7 MeV) and He (2.1 MeV) produced in a ${}^6\text{Li}(n, \alpha){}^3\text{H}$ reaction. Therefore, an extended study of irradiation effects should be done on the blanket materials in order to verify the applicability in the fusion devices.

In the present study, we investigated effects of irradiation-induced defects on the electrical conductivity of some Li-based ceramics. In-situ conductivity measurements were done under irradiations by highly energetic self-ions (e.g., 120 MeV O^{7+} and 60 MeV Li^{3+} ions for Li_2O) at various temperatures. Many important informations concerning to defect structure and tritium diffusion were derived. In this paper, we report the results on irradiation behavior of Li_2O bombarded with 60 and 24 MeV lithium ions. On the irradiation behavior by 120 MeV O^{7+} ions, see previous reports^{1,2)}.

Experiments

Thin plates of single crystalline Li_2O were used for the electrical conductivity measurements. The specimens were irradiated by 24 and 60 MeV lithium (Li^{3+}) ions using the TANDEM accelerator at JAERI. In addition to post-irradiation measurements, in-situ measurements were also performed at various temperatures. The measurements of the conductivity (converted from the electric resistance) were carried out by the two-terminal ac method, employing the HP4194A Impedance Analyzer. A full automatic data collection

system was used in this measurement and a set of data of the resistance were compiled in a microcomputer. Details of the experimental procedures were reported in previous papers^{3,4}.

Results and Discussion

1. Post-Irradiation Measurement

In a normal way, one measures a particular physical property of a target material before and after irradiation and compares with them in order to investigate irradiation-induced effects. This procedure (so called "post-irradiation measurement") yields informations of a "steady-state" irradiation-induced defects which can survive after interrupting irradiation in an experimental condition.

Fig. 1 shows the changes of the "steady-state" conductivity of Li₂O irradiated by Li ions at various temperatures derived from the post-irradiation measurement. The conductivity decreased with Li ion fluence in temperature range between 453 and 573 K. Above 623 K, no significant change was observed. Whereas at 413 K (in 24 MeV Li ion irradiation in Fig. 1) the conductivity increased with ion fluence. In the case of 120 MeV O ion irradiation, the increased conductivity was seen below 440 K, while above that temperature a reduction of the conductivity was observed^{3,4}. Thus the irradiation effect on the conductivity of Li₂O was similar in Li and O ion irradiations. The decrease of the electrical conductivity could be explained by an introduction of F[•] centre which was a main irradiation-induced defect in Li₂O with particle bombard-

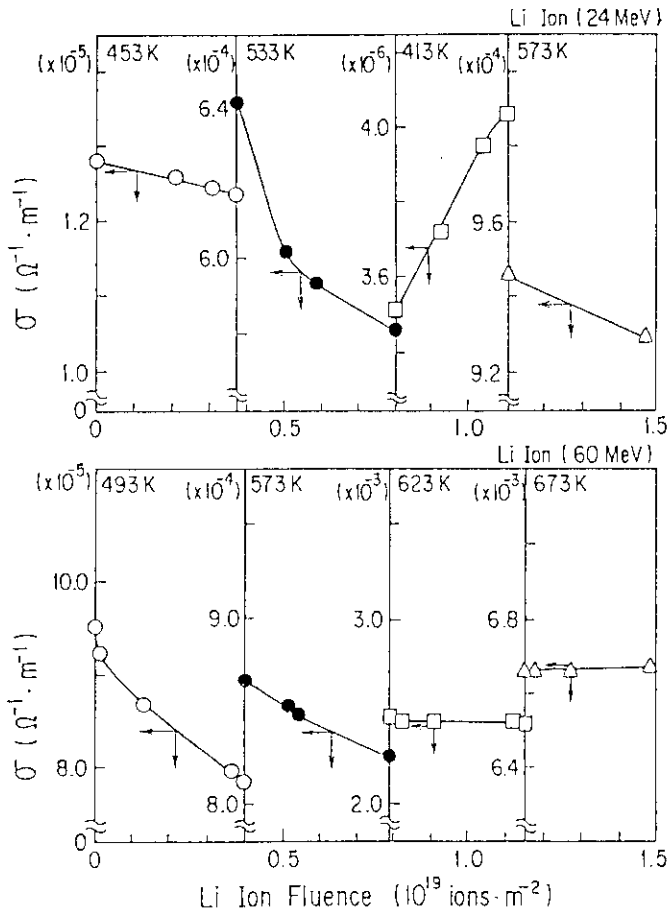


Fig.1 "Steady-state" conductivity of Li₂O irradiated by 24 and 60 MeV Li-ions

ment¹⁻⁴⁾. On the other hand, Li ion vacancies, which could be survive below 440 K, might be responsible to the increase of the conductivity. In conclusion, two types of defect, Li vacancies and F⁺ centre, respectively, in low and high temperature irradiation, were suggested to be majorly survived in Li₂O in the post-irradiation measurement.

2. In-Situ Measurement

As reported previously³⁾, a very rapid increase of the conductivity was found in an earlier stage of irradiation at any temperature. It was noticed here that the higher the ion intensity (ion flux or irradiation current), the bigger the increased conductivity. During irradiation, fresh defects are always supplied. It could be suggested that even the interstitial-type defects would be produced and survive. In addition, interactions of each induced defects might be expected. Hence, damage behavior should be very complicated in such a "transient" damage process. In order to investigate a detailed behavior of the increased conductivity, a special measurement procedure was applied. Instead of obtaining the half-circular of the impedance-resistance curve between 0.2 and 2000 kHz, we measured the resistance at a fixed frequency (e.g., 5 kHz). In this procedure, the resistance data could be compiled within every three seconds, although the values did not correspond to the real resistance, but a relative one.

In Fig. 2, we show schematically the change of "transient" conductivity of Li₂O bombarded by 60 MeV Li ions at a ion flux of 3.25×10^{14} ions/m² s (30 nA). Temperature of the specimen was kept at 493 K. When irradiation started, the conductivity increased abruptly and tended to saturate in about 5 min. After attaining the saturation, the conductivity began to decrease in the above case at 493 K, as

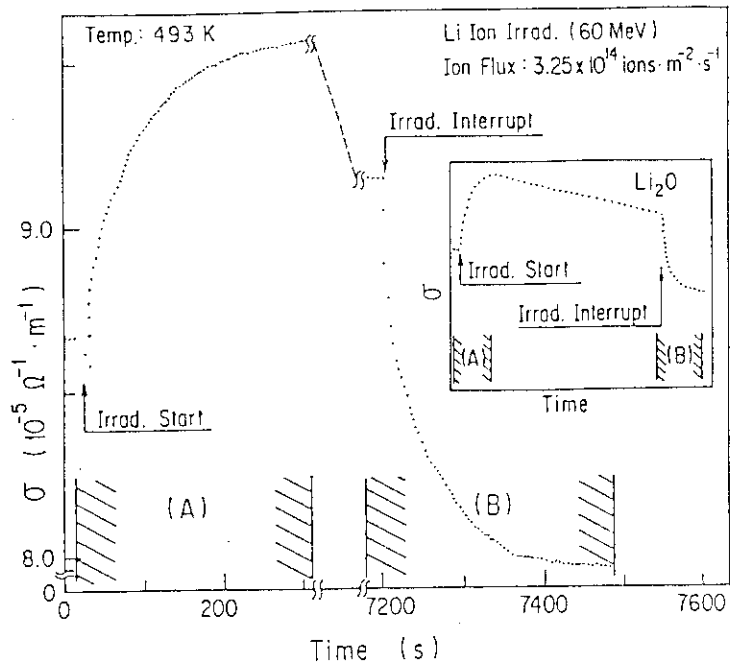


Fig.2 "Transient" conductivity of Li₂O in "in-beam" and "off-beam" conditions

represented in the inset of Fig. 2. The gradual decrease of the conductivity was found in the irradiations at 493, 573 and 623 K, while an inverse phenomenon (increase of the conductivity) was revealed in low temperature (403 and 413 K) irradiation runs. On the other hand, an abrupt decrease of the conductivity was found when the irradiation terminated. As a consequence, the final conductivity was increased totally after the irradiation, being consistent with the "steady-state measurement" as shown in Fig. 1.

Several ideas are proposed to interpret the abrupt increase at the irradiation start and the decrease at the irradiation termination of the conductivity.

1. Conductivity increase due to temperature rise by ion beam heating,
2. Enhanced diffusion of Li by excess defects under irradiation,
3. Increased conductivity by an electronic excitation process.

From an incremental increase of the measured conductivity from in-beam to off-beam measurements, one can roughly estimate the temperature increase. An estimated temperature rise was surprisingly high. For instance, a 100 K increase was calculated in an irradiation of Li_2O with 60 MeV Li ion flux of 3.25×10^{14} ions/ m^2s in a controlled specimen temperature at 543 K. Thus the specimen should be heated up to 643 K in this assumption. Such a high temperature rise could not explain the existence of F^+ centres which were confirmed by a followed recovery annealing, because the F^+ centre disappeared virtually up to 600 K.

In the present stage, no clear evidence on the electronic excitation process was observed. Therefore, an idea of an irradiation-enhanced phenomenon was most plausible. Because the Li mobility displays the conductivity in Li_2O , an enhanced diffusion of Li assisted by an excess of induced defects, probably in an athermal process, plays a major role to the abrupt increase of the conductivity. There must be a lot of unstable defects, such as Li interstitials and vacancies, in the beginning of the irradiation.

References

- 1) K.Noda, Y.Ishii, H.Ohno, H.Watanabe and H.Matsui: *Advances in Ceramics*, Vol. 25 (Am. Ceram. Soc., 1989) pp.155-164.
- 2) K.Noda, Y.Ishii, H.Matsui and H.Watanabe: *Rad. Effects* **97** (1986) 297.
- 3) K.Noda, Y.Ishii, H.Ohno, H.Watanabe and H.Matsui: *Adv. in Ceramics* (Am. Ceram. Soc., 1990) in print.
- 4) K.Noda, K.Uchida, T.Tanifuji and S.Nasu: *Phys. Rev.*, **B24** (1981) 3736.

3.11 IONIC CONDUCTIVITY OF Al-DOPED Li_4SiO_4 DURING AND AFTER IRRADIATION

Kenji NODA, Yoshinobu ISHII, Hisayuki MATSUI*,
Mikio HORIKI*, Masahiko OKUI*, Naomi OBATA*,
D. Vollath** and Hitoshi WATANABE

Department of Fuels and Materials Research, JAERI, *Faculty
of Engineering, Nagoya University, **Kernforschungszentrum
Karlsruhe GmbH, Institut für Material-und
Festkörperforschung III

1. Introduction

Lithium ceramics such as Li_2O and Li_4SiO_4 are candidates of tritium breeding materials for D-T fusion reactors. Ionic conductivity of the lithium ceramics is controlled by lattice defects including radiation-induced defects, solute atoms and impurities, and reflects diffusion of lithium ions. Furthermore, tritium diffusion in the lithium ceramics is considered to be related to lithium ion diffusion^{1,2)}. Recently, Al-doped Li_4SiO_4 ³⁾ and Mg-doped LiAlO_2 ⁴⁾ sintered pellets were made as advanced tritium breeding materials which were designed to improve the tritium release performance. In these materials, tritium diffusivity is increased through enhancement of lithium ion diffusion by introduction of lithium ion vacancies due to doping Al or Mg.

During operation of the fusion reactors, a huge number of defects will be introduced in these lithium ceramics by neutron irradiation. Such defects will affect transport phenomena such as tritium diffusion.

In the present study, irradiation effects on ionic conductivity of Al-doped Li_4SiO_4 during and after irradiation were investigated by in-situ experiments using lithium and oxygen ion irradiation, in order to obtain fundamental knowledge of radiation-induced defects and irradiation effects on transport of lithium and tritium.

2. Experimental

The specimens used were thin disks (8 to 9 mm in diameter, 1 mm in thickness) of $\text{Li}_{3.7}\text{Al}_{0.1}\text{SiO}_4$ sintered pellets which were fabricated from $\text{Li}_{3.7}\text{Al}_{0.1}\text{SiO}_4$ powder synthesized at KfK³⁾. The specimens were irradiated

at the prescribed temperatures in an irradiation chamber attached to a tandem accelerator at JAERI with lithium and oxygen ions. In-situ measurements of ionic conductivity were carried out at the prescribed temperatures with the two terminal AC method using a HP 4194 A impedance analyzer during and after irradiation.

3. Results and Discussion

Figure 1 shows the conductivity of $\text{Li}_{3.7}\text{Al}_{0.1}\text{SiO}_4$ in the post-irradiation condition versus ion fluence for 120 MeV oxygen and 60 MeV lithium ion irradiation. For the oxygen ion irradiation, the conductivity in the post-irradiation condition increased with the fluence at 383 and 413 K, while decreased slightly at 443 and 473 K. Similar irradiation effects in the post-irradiation condition were observed at 383 and 443 K for the lithium ion irradiation.

For Li_2O irradiated with 120 MeV oxygen and 24 or 60 MeV lithium ion irradiation, the conductivity in the post-irradiation condition increased with the fluence below 440 K, while it decreased with the fluence in the range 453 to 573 K^{5,6}). From the thermal recovery behavior of conductivity, the decrease in the range 453 to 573 K was attributed to introduction of F^+ centers, while the increase below 440 K was considered to arise from introduction of lithium ion vacancies or defects introducing the lithium ion vacancies⁶). Furthermore, the irradiation effects on the conductivity due to colloidal lithium metal centers which survived even at 673 K were considered to be negligibly small at the fluence up to 1.5×10^{19} ions. $\cdot\text{m}^{-2}$ ⁶).

On the analogy of irradiation effects on the ionic conductivity for Li_2O , above-mentioned two kinds of irradiation effects for $\text{Li}_{3.7}\text{Al}_{0.1}\text{SiO}_4$ suggest that existence of two types of radiation-induced defects.

Tritium migration in $\text{Li}_{3.7}\text{Al}_{0.1}\text{SiO}_4$ is assumed to be controlled by lithium ion diffusion. Thus, diffusivity of lithium ions and tritium in $\text{Li}_{3.7}\text{Al}_{0.1}\text{SiO}_4$ in the post-irradiation condition is considered to be increased with the fluence at 383 and 413 K, and decreased at 443 and 473 K.

The conductivity of $\text{Li}_{3.7}\text{Al}_{0.1}\text{SiO}_4$ during irradiation was larger than that before and after irradiation, and depended on the ion flux. Figure 2 shows the increments of conductivity between the post-irradiation condition and the during irradiation condition as a function of the flux for 120 MeV oxygen ion irradiation. The increments increased with the flux,

and the gradients of relationships between the increments and the flux changed with temperature. Essentially similar effects were observed for 60 MeV lithium ion irradiation.

For Li_2O , the ionic conductivity during irradiation also was larger than that before and after irradiation, and the increment of conductivity between the post-irradiation condition and the during irradiation condition increased with the flux⁶⁾. The increments of conductivity were considered to arise not only from the temperature rise due to beam heating but also from enhancement of lithium ion diffusion due to radiation-induced defects with relatively short lifetime by evaluating the increase of conductivity due to beam heating.

If enhancement of lithium ion diffusion during irradiation also contributes the increment of conductivity between the post-irradiation condition and the during irradiation condition for $\text{Li}_{3.7}\text{Al}_{0.1}\text{SiO}_4$ as well as beam heating, tritium diffusion in $\text{Li}_{3.7}\text{Al}_{0.1}\text{SiO}_4$ is considered to be enhanced during irradiation.

References

- 1) H. Ohno, S. Konishi, T. Nagasaki, T. Kurasawa, H. Katsuta and H. Watanabe: J. Nucl. Mater. 133-134 (1985) 1881.
- 2) K. Noda, Y. Ishii, H. Ohno, H. Watanabe and H. Matsui: Advances in Ceramics vol 25 "Fabrication and Properties of Lithium Ceramics" (American Ceramic Society, 1989) p. 155-164.
- 3) D. Vollath and H. Wedemeyer: Advances in Ceramics (American Ceramic Society), in press.
- 4) F. Botter, D. Cherquitte and C. Le Gressus: J. Nucl. Mater. 160 (1988) 260.
- 5) K. Noda, Y. Ishii, H. Matsui, H. Ohno, S. Hirano and H. Watanabe: J. Nucl. Mater. 155-157 (1988) 568.
- 6) K. Noda, Y. Ishii, H. Matsui, H. Ohno and H. Watanabe: J. Nucl. Mater., in press.

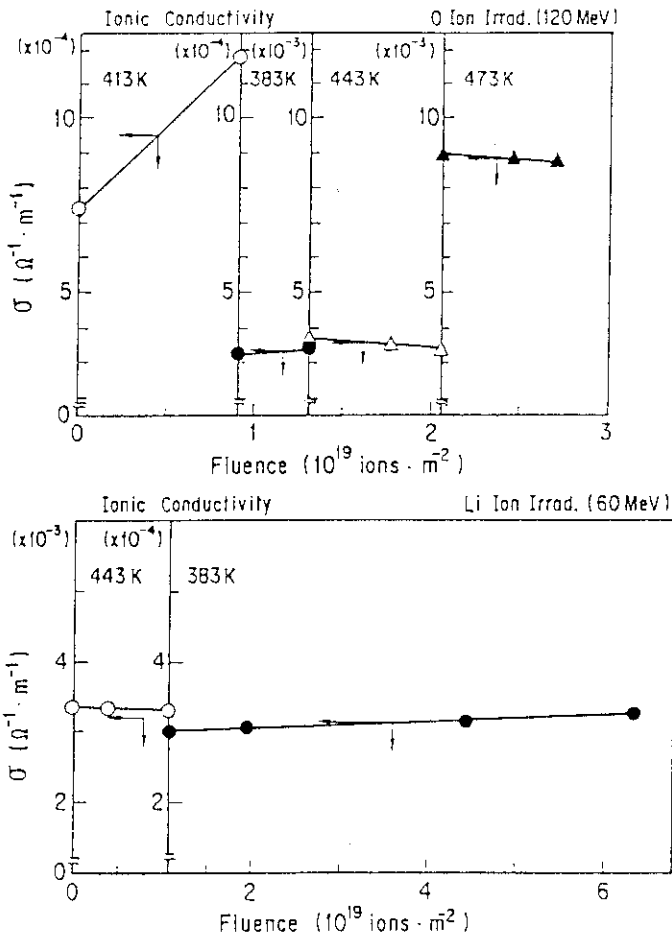


Fig.1 Ionic conductivity of $Li_{3.7}Al_{0.1}SiO_4$ in the post irradiation condition versus ion fluence for 120 MeV oxygen and 60 MeV lithium ion irradiation.

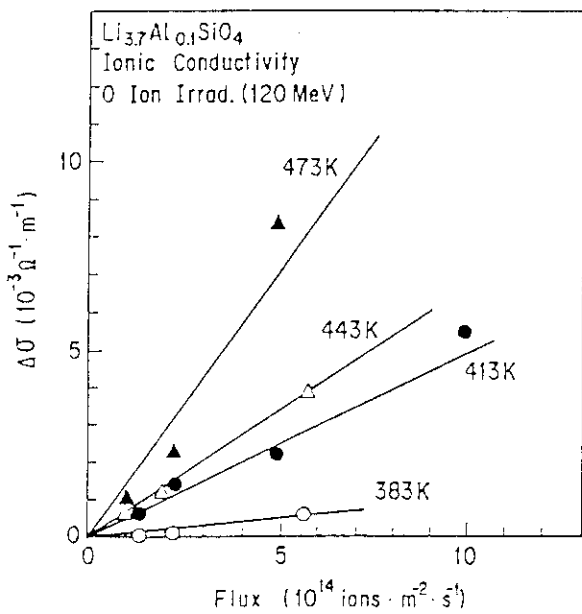


Fig.2 Increments of ionic conductivity of $Li_{3.7}Al_{0.1}SiO_4$ between the post irradiation condition and the during irradiation condition versus ion flux for 120 MeV oxygen ion irradiation.

3.12 A STUDY OF RADIATION DAMAGE IN Li_4SiO_4
BY ELECTRON MICROSCOPIC OBSERVATION

Kenji NODA, Yoshinobu ISHII, Kotaro KURODA*
Masakatsu SASAKI*, Hiroyasu SAKA* and Hitoshi WATANABE

Department of Fuels and Materials Research, JAERI, *Faculty
of Engineering, Nagoya University

Radiation damage is introduced in ceramic materials for nuclear energy systems during operation of the systems. The radiation damage induces degradation of dimensional stability and the functional performance. Researches of radiation damage are very important to develop new radiation-resistance ceramic materials for advanced nuclear energy systems including fusion reactors.

In the present study, radiation damage in Li_4SiO_4 which was a candidate of ceramic tritium breeding materials for D-T fusion reactors was investigated using a 200 kV transmission electron microscope (TEM).

After Li_4SiO_4 powder synthesized at KfK¹⁾ was pressed at hydrostatic pressure of $1.6 \times 10^3 \text{ kg cm}^{-2}$, Li_4SiO_4 sintered pellets were obtained by heating the compacted powder at 1353 K for 5 h. The pellets were cut into thin disks by a diamond cutter. The thin disks were lapped with emery papers, and then thin foil specimens for electron microscopic observation were made with ion-milling technique. The specimens were irradiated "in-situ" using the TEM by 200 kV electrons, and electron microscopic observation of microstructure change due to the irradiation was carried out.

For non-irradiated specimens, crystal grains in a diameter of several microns, which presented 2 types of electron diffraction patterns (i.e., spots and rings), were observed. This result shows that the Li_4SiO_4 specimens were composed of two phases, Li_4SiO_4 and another phase (Li_2SiO_3 or $\text{Li}_2\text{Si}_2\text{O}_5$).

There are large discrepancies among experimental data of thermal conductivity and mechanical properties for Li_4SiO_4 . Such discrepancies were supposed to arise from existence of the second phase such as Li_2SiO_3 ²⁾. The present result gave experimental evidence for the above-mentioned supposition.

Figure 1 shows electron micrographes of a region consisting of only

Li₄SiO₄ phase before and after irradiation together along a diffraction pattern for the irradiated region. White spotted contrasts such as voids appeared during the irradiation and the number of the contrasts increased with the fluence. (Fig. 1b, 1c) Also, diffraction rings were superimposed on the diffraction pattern of Li₄SiO₄ during the irradiation. (Fig. 1d) These suggest that decomposition of Li₄SiO₄ into Li₂SiO₃ or Li₂Si₂O₅ was taken place by displacement of lithium and oxygen atoms. (Li₄SiO₄ → Li₂SiO₃ + 2Li + O, 2Li₄SiO₄ → Li₂Si₂O₅ + 6Li + 3O)

Further 200 KV electron irradiation led to completed amorphization of the irradiated region, as shown in Fig. 2. The diffraction rings corresponding to the another phase were superimposed on the diffraction pattern of Li₄SiO₄ at $1.9 \times 10^{25} \text{ m}^{-2}$, and only hallow rings indicating amorphization were observed at $9.4 \times 10^{25} \text{ m}^{-2}$.

Decomposition of LiAlO₂ due to electron and oxygen ion irradiation was also observed^{3,4}). By the decomposition, LiAl₅O₈ was formed at electron fluence of $5.7 \times 10^{25} \text{ m}^{-2}$ and oxygen ion fluence of $1.3 \times 10^{21} \text{ ions} \cdot \text{m}^{-2}$. However, amorphization was hardly observed in the electron irradiation even at $9.4 \times 10^{25} \text{ m}^{-2}$. Consequently, irradiation resistance of Li₄SiO₄ seems to be smaller than LiAlO₂.

References

- 1) D. Vollath and H. Wedemeyer: J. Nucl. Mater. 141-143 (1986) 334.
- 2) W. Dienst: private communication.
- 3) M. H. Auvray-Gely, A. Dunlop and L. W. Hobbs: J. Nucl. Mater. 133-134 (1985) 230.
- 4) K. Noda, Y. Ishii, K. Kuroda, M. Sasaki, H. Saka and H. Watanabe: JAERI-M 89-119 (1989) p.105-107.

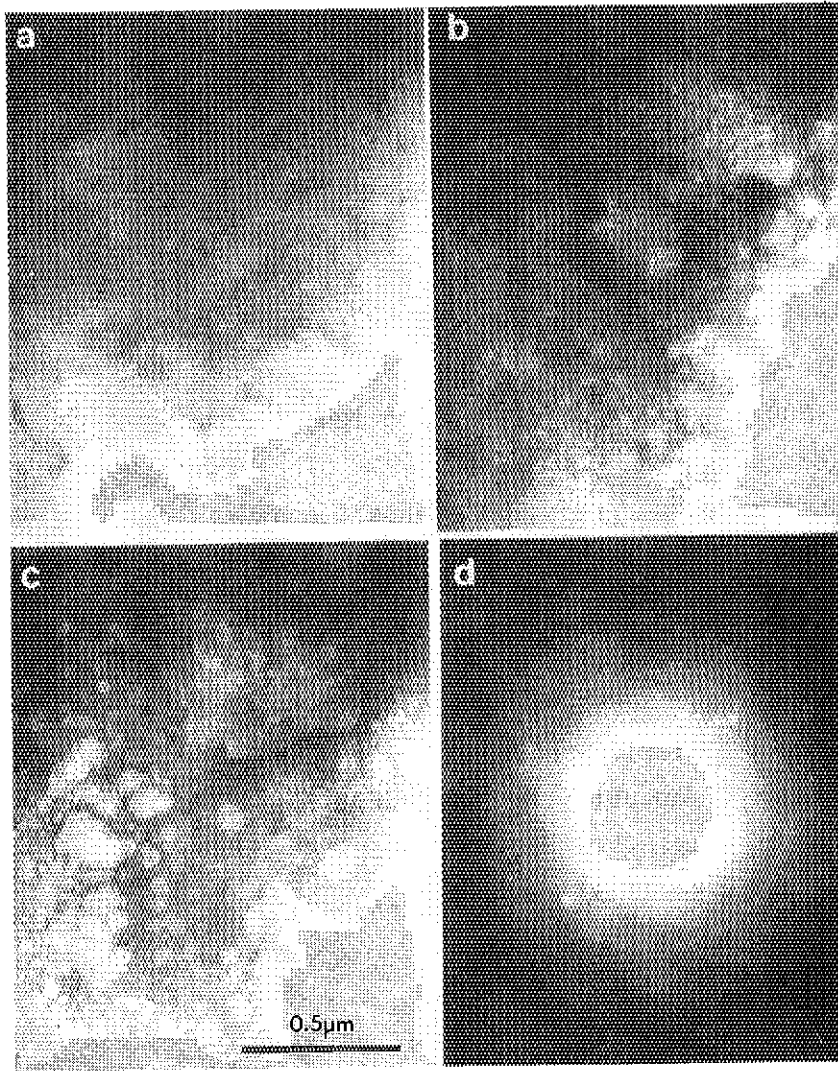


Fig.1 Electron micrographes of a region consisting of only Li_4SiO_4 phase before (a) and after 200 kV electron irradiation (b: $9.4 \times 10^{24} \text{ m}^{-2}$, c: $3.8 \times 10^{25} \text{ m}^{-2}$) together along a diffraction pattern for the irradiated region (d).

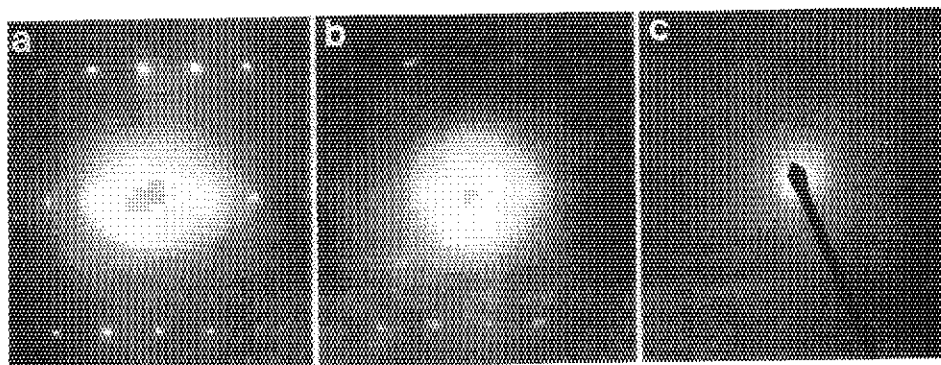


Fig.2 Electron diffraction patterns for irradiated regions. (a: before irradiation, b: $1.9 \times 10^{25} \text{ m}^{-2}$, c: $9.4 \times 10^{25} \text{ m}^{-2}$)

3.13 MICROSTRUCTURE AND MECHANICAL PROPERTIES OF α PARTICLE IRRADIATED STAINLESS STEELS

Kazuya MIYAHARA*, Shozo HAMADA, Akimichi HISHINUMA, Hideo
KAYANO** and Yuzo HOSOI*

Department of Fuels and Materials Research, JAERI *Faculty
of Engineering, Nagoya University, ** Institute for Materials
Research, Tohoku University,

1. Introduction

Ductility loss or brittle fracture of the first wall structural materials due to the helium generated by (n, α) reaction with fusion neutron, is considered to be one of the important problems to be solved. Recently, Mansur and Grossbeck reviewed the various aspects of the mechanical property changes induced by helium, and discussed the effects of helium level (He/dpa) and strain rate in tensile and creep tests on the ductility of irradiated structural materials¹⁾.

The present work is performed to investigate the effect of helium on the microstructure, mechanical property changes and fracture behaviors of helium-pre-injected stainless steel.

2. Experimental Procedure

The materials used in this work are the thin foils of type 316 (27.5 μm thick), 12Cr-15Mn (100 μm thick) austenitic stainless steels and 9Cr-2Mo ferritic steel (100 μm thick). These foils were solution-treated at 1373 K for 3.6 ks in vacuum and quenched into water. The foil of 12Cr-15Mn was annealed at 873K for 7.2 ks to stabilize carbides and the foil of 9Cr-2Mo was tempered at 1048 K for 21.6 ks after solution treatment. Disks with 3 mm diameter for transmission electron microscope (TEM) and very small specimens for tensile test (gauge width : 1.2 mm, gauge length : 5 mm, total length : 12.5 mm) were punched out of the foils after the above heat treatment, and then helium was injected to the disks and tensile specimens.

Helium was injected by 30 MeV α particle bombardment, by using a SF cyclotron for the Institute of Nuclear Study, the University of Tokyo and helium injection was performed so as to make an uniformly He-implanted region of

about 20 μm width around the midst of the specimen of each steel. The details of helium injection method are described in the proceedings in ICFRM-4²⁾. The average helium content and displacement damage in a He-deposited region were calculated to be about 2000 appm He and 0.4 dpa in type 316, about 500 appm He and 0.1 dpa in both 12Cr-15Mn and 9Cr-2Mo steels, respectively. The bombardment temperature was estimated to be about 773K²⁾.

After helium implantation, tensile tests (strain rate ; $1 \times 10^{-3}/\text{s}$) were performed at room temperature and 773 K in the atmosphere of argon gas, followed by scanning electron microscope (SEM) observation of the fracture surface of a tensile-tested specimen and by TEM observation of the He-deposited area.

3. Results and Discussions

3.1 Helium bubble formation and distribution

Fig.1 shows the helium bubbles formed in the grain interior and at the grain boundaries of type 316 as irradiated. A higher concentration and a larger size of helium bubbles were formed in general at the grain boundaries than in the grain interior.

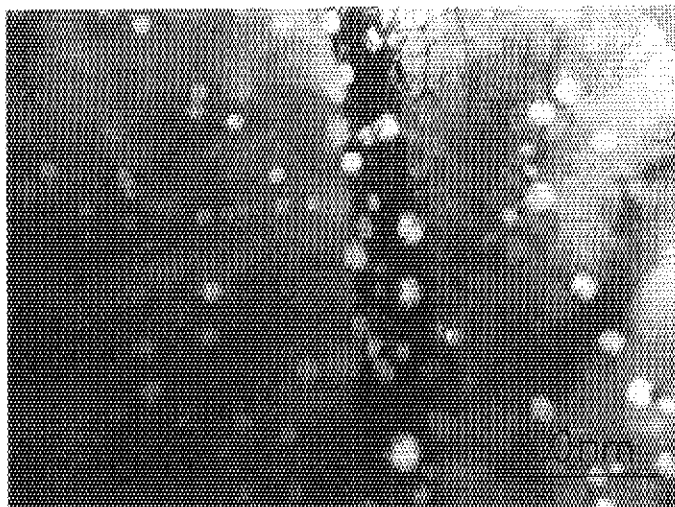


Fig.1 Helium bubbles in type 316 stainless steel implanted to 2000 appm He at ambient temperature.

The growth mechanism of helium bubble in the present experiment of type 316 was explained by "pressure driven model"³⁾, because the number of helium atoms measured by a beam current integrator coincided with that calculated from the number density and size distribution of helium bubbles with the assumption that helium gas is an ideal gas and that the internal gas pressure of helium bubbles is balancing with the ratio of surface tension/bubble radius⁴⁾.

The helium bubbles formed in the He-deposited area of both 12Cr-15Mn and 9Cr-2Mo steels. Number density and average diameter of bubbles are $2.9 \times 10^{20}/\text{m}^3$ and 42nm in 12Cr-15Mn and $4.6 \times 10^{19}/\text{m}^3$ and 72nm in 9Cr-2Mo, respec-

tively. It is interesting to note that the bubble formation behavior in 9Cr-2Mo of ferritic steel is in contrast to that in 12Cr-15Mn of austenitic steel; that is, a higher concentration and a smaller size of helium bubbles formed in 9Cr-2Mo than those in 12Cr-15Mn. It is also recognized that bubbles of larger size are formed at grain boundaries than in grain interior in 9Cr-2Mo as observed in type 316.

3.2 Tensile test

The He-implanted type 316 showed an increase in strength (0.2% proof strength and ultimate tensile strength) and a decrease in ductility comparing with the non-implanted specimens at room temperature and 773 K. In contrast to that, the He-implanted 12Cr-15Mn and 9Cr-2Mo steels showed a decrease in strength and an increase in ductility at 773 K, although the effect of He-implantation on strength was not clearly found at room temperature.

3.3 Fracture behavior

Fig.2 shows a scanning electron micrograph of fracture surface of type 316 after tensile testing. Transgranular fracture was a main fracture mode at room temperature and 773 K in the He-deposited region and in the non-implanted specimen of type 316. It is noted that intergranular fracture also was sometimes observed in the He-deposited region at room temperature as shown in Fig.2(a).

12Cr-15Mn steel partially fractured by an intergranular mode at room temperature, on the other hand, by transgranular-ductile mode at 773 K, whether a specimen was He-implanted or not. Accordingly, the effect of He-implantation on the fracture was not recognized at the level of 500 appm He.

9Cr-2Mo steel showed transgranular-ductile fracture at the level of helium of 500 appm at room temperature and 773 K.

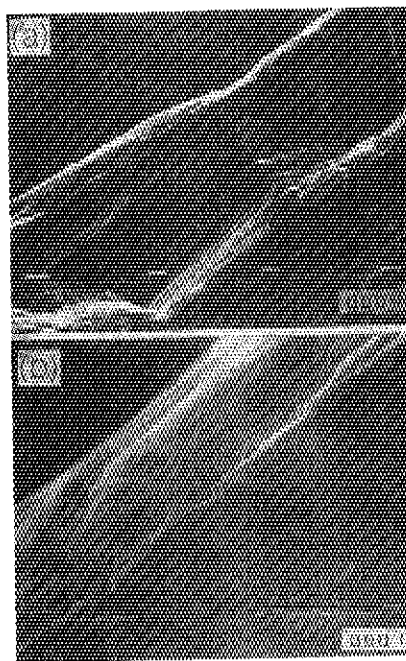


Fig.2 Fracture surface of He-implanted type 316
(a) Intergranular fracture at room temperature
(b) Transgranular fracture at 773 K

This mode of fracture is much different from intergranular fracture of so-

called He embrittlement.

In the present work, fracture of three kinds of steels proceeded by the transgranular-ductile mode in tensile tests at 773 K. This fracture is much different from the result of Yamamoto et al⁵⁾ that Ti-modified 316 steel (JPCA) fractured by a typical intergranular-brittle fracture at a post He-implantation creep test at 923 K on the level of 50 appm He. There could be many reasons for this difference of fracture mode. But, since big difference between tensile and creep tests is strain rate, it is considered to be very important to investigate the effect of strain rate on the helium embrittlement, as suggested by Mansur and Grossbeck¹⁾. The present authors found that 12Cr-15Mn tensile tested at 873 K showed typical intergranular fracture⁶⁾. Accordingly, testing temperature is considered to be also an important factor to determine fracture modes of He-implanted materials.

4. Summaries

The summaries are as follows;

- (1) It was generally observed that larger size of helium bubbles were formed at grain boundaries than in grain interiors in a type 316 and 9Cr-2Mo steels.
- (2) He-implantation increased the strength of type 316 at room and elevated temperature, but caused the decrease of the strength of 12Cr-15Mn austenitic steel and 9Cr-2Mo ferritic steel at elevated temperature.
- (3) The implanted specimens to 500-2000 appm He of type 316, 12Cr-15Mn and 9Cr-2Mo steels showed transgranular-ductile fracture at elevated temperature.

References

- (1) L.K.Mansur and M.L.Grossbeck, J.Nucl.Mater., 155-157(1988)148
- (2) K.Miyahara, Y.Sakamoto, S.Hamada and Y.Hosoi, to be published in the Proc. of 4th Intern. Conf. on Fusion Reactor Materials (Dec.1989)in Kyoto
- (3) H.Ullmaier : Radiat.Eff.,78(1983)1
- (4) K.Miyahara, Y.Sakamoto, H.Kayano and Hosoi, Tetsu to Hagane, 6(1990)158
- (5) N.Yamamoto, H.Shiraishi, H.Kamitsubo, I.Kohno, T.Shikata and A.Hishinuma, J.Nucl.Mater., 133&134(1985)493
- (6) K.Miyahara, Y.Sakamoto, S.Hamada, H.Kayano and Y.Hosoi, unpublished work

3.14 RADIATION EFFECT OF AUSTENITIC STAINLESS STEELS

Mititaka TERASAWA, Tohru MITAMURA, Kiyoshi KAWATSURA⁺,
 Eiichi YAGI⁺⁺, Hajime IWASAKI, Keiji KOTERAZAWA
 Masao SATAKA⁺⁺⁺, Makoto IMAI⁺⁺⁺ and Yohta NAKAI⁺⁺⁺

Himeji Institute of Technology, Himeji, + Kyoto Institute
 of Technology, Kyoto, ++ The Institute of Physical and
 Chemical Research, Wako, +++ JAERI

Ion channeling experiments were performed for single crystal austenitic stainless steels, SUS310S and SUS304, and also pure nickel with P implanted. Using He⁺ ions from a Van de Graaf or a Tandetron accelerator, induced K X-rays and Rutherford backscattered (RBS) He ions were measured in order to investigate locations of alloying and impurity atoms in the austenitic stainless steels. From the values of $2\psi_{1/2}$ and χ_{\min} obtained from the K X-ray angular scanning measurements, it is suggested that some of P atoms are located at the octahedral site in the face-centered cubic (FCC) structure and most of S and Si atoms at the lattice site.

1. Introduction

Radiation-induced segregation, which is one of the most stimulating phenomena in recent nuclear reactor material research, has been studied by several investigators. In austenitic stainless steels, alloying and impurity elements have been known to show an enhanced change in their concentration at the grain boundaries and it may affect the mechanical properties of the stainless steels. The purposes of the present experiments are to study 1) the locations of the major and the minor elements in austenitic stainless steels, and 2) the displacements of the elements during He⁺ ion irradiations. In order to observe these points more clearly, phosphorus implanted single crystal pure nickel were also investigated.

2. Experiments

Austenitic stainless steels, SUS310S and SUS304, were employed as target materials. Specimens with <100>, <110> or <111> axis were cut from single crystal rods which were prepared by the Bridgeman method. Single crystal pure nickel with the <110> axis was implanted by phosphorus ions up to an

amount of $1 \times 10^{15}/\text{cm}^2$ using a Cockcroft-Walton accelerator.

He^+ ions with an energy of 1.7 MeV from a Van de Graaf accelerator were used as an analytical probe and an irradiation projectile. Irradiations by He^+ ions were carried out at a room temperature. Measurements of He ion induced K X-rays and RBS He ions were carried out using Si(Li) detectors and surface barrier solid state detectors, respectively.

3. Results and discussions

Fig.1 shows the dip curves of He^+ ion induced K X-ray yields in the cases of the SUS310S $\langle 110 \rangle$ specimen. The minor alloying element, Si, has a similar shape to that of the major alloying elements, Cr+Fe+Ni. The dip curve

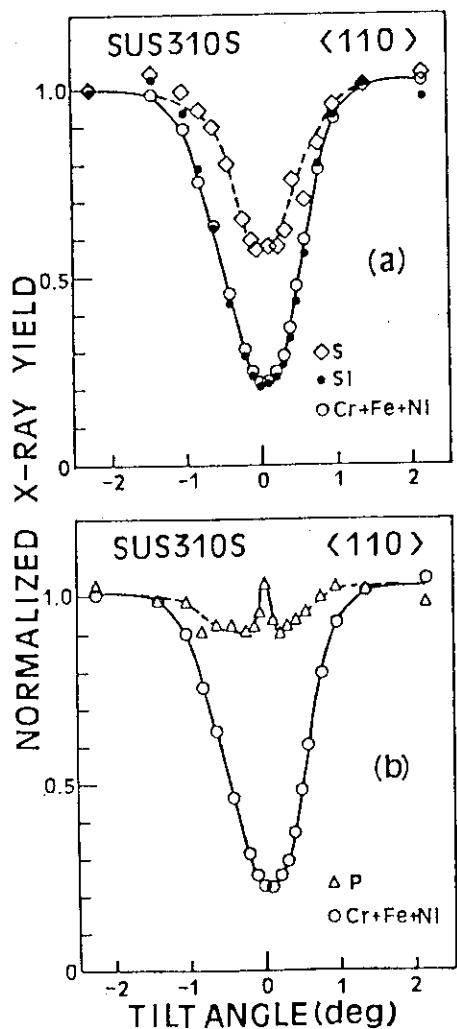


Fig.1 Angular scans of (a)Si,S and (b)P K X-ray yields across the $\langle 110 \rangle$ axis of SUS310S, compared with those of host the alloy elements.

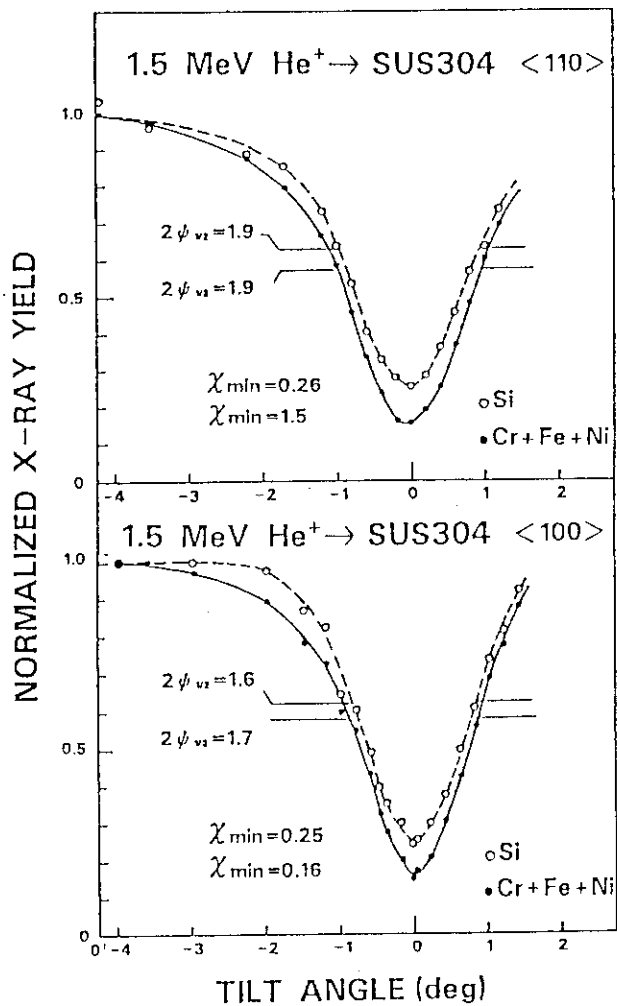


Fig.2 Angular scans of X-ray yields across (upper) the $\langle 110 \rangle$ and (lower) the $\langle 100 \rangle$ axis of SUS304.

of S atom shows a shallower dip. On the other hand, K X-ray yield of the P atom increases at the bottom of the dip curve only in the $\langle 110 \rangle$ angular scan. The same result was obtained in the case of the P implanted pure nickel specimen with the $\langle 110 \rangle$ axis as shown Fig.3. Fig.2 shows the K X-ray yields of Si and S in the case of the SUS304 specimen. The dip curves of Si and S are similar to that of the major alloying elements, Cr+Fe+Ni, although they are a little shallower in both the $\langle 100 \rangle$ and the $\langle 110 \rangle$ specimens.

Fig.4 shows the variations of χ_{\min} values as a function of the dpa during He^+ ion irradiations in the case of the SUS310S specimen. In this diagram, the parameter χ_{\min} of P was used for convenience the value of the peak yield divided by the yield in the random direction. P K X-ray yield only decreases

as the dpa increases, while K X-ray yields of the other elements increase, especially larger increase are seen in the cases of Si and Ni.

From the fact that the Si and S dip curves are similar to that of the major alloying elements, Cr+Fe+Ni, it is suggested that most of the Si atoms locate at the lattice site, namely substitutional site in the FCC structure of the austenitic stainless steel, and the S atoms also locate at or near the lattice site. On the other hand, the shallow dip of P K X-ray yield indicates that larger part of the impurity P atoms have a tendency to locate at the interstitial site, and especially, from the existence of the peak at the bottom of the dip curves of the $\langle 110 \rangle$ axis specimen, it maybe considered that the P atoms locate at the octahedral site of the FCC structure. This is also shown in the case of the single crystal pure nickel.

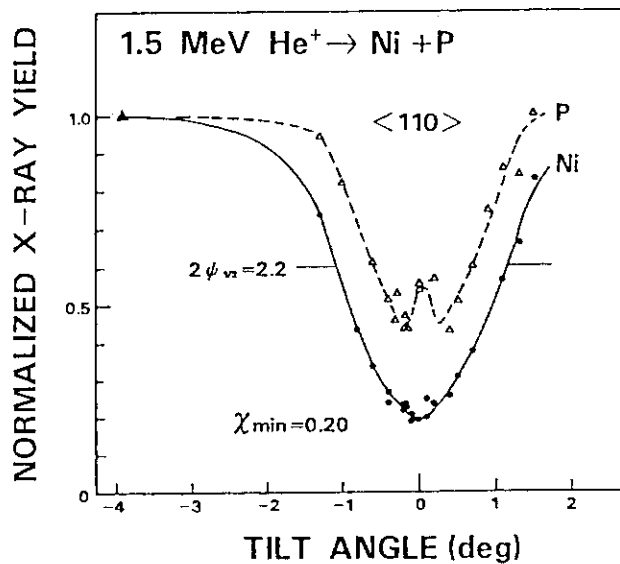


Fig.3 Angular scans of X-ray yields across the $\langle 110 \rangle$ axis of Ni implanted with P.

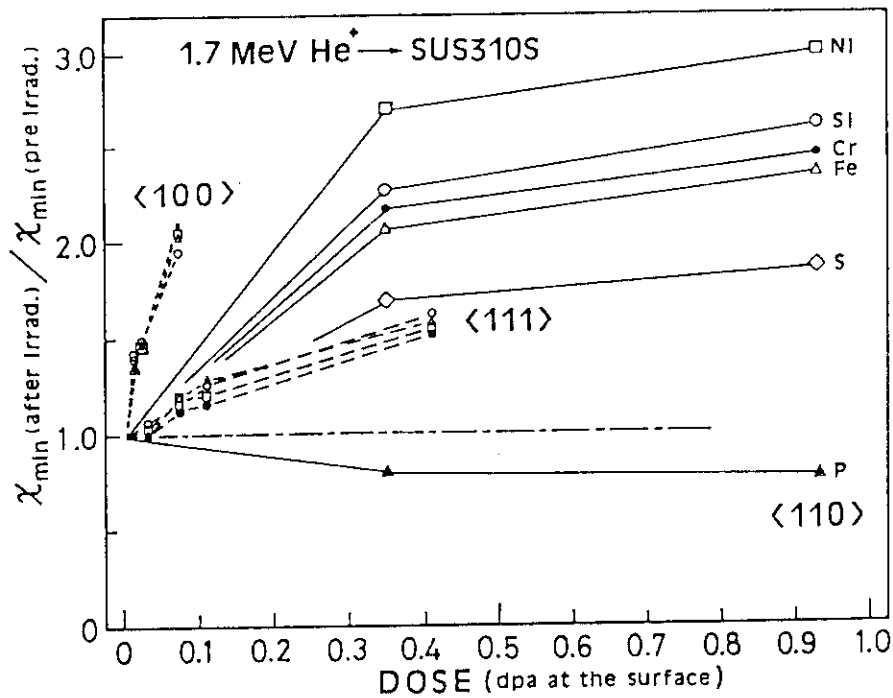


Fig.4 Variations of χ_{\min} as a function of He irradiation dose, dpa, for the <100>, <110> and <111> aligned channeling in SUS310S.

The larger increases of K X-ray yields of Ni and Si during He^+ ion irradiations might be the facts corresponding to the indication, reported by Fukuya et al.^{1,2)}, that these atoms show prominent radiation induced segregations. The decrease of P K X-ray yield during He^+ ion irradiation may suggest that the formation of a mixed dumbbell consisted of displaced Ni and interstitial P atom occurs.

References

- 1) K.Fukuya, S.Nakahigashi and M.Terasawa, Scripta Metal. 19(1985)959.
- 2) K.Fukuya, S.Nakahigashi, S.Ozaki, M.Terasawa and S.Shima, in: Environmental Degradation of Materials in Nuclear Power Systems - Water Reactors, eds. D.J.Theus and J.R.Weeks (The Metallurgical Society. 1988)

IV NUCLEAR CHEMISTRY

4.1 MEASUREMENT OF BETA-RAY MAXIMUM ENERGY WITH AN HPGE DETECTOR

Akihiko OSA*, Shin-ichi ICHIKAWA, Hideki IIMURA,
Masahide MIYACHI*, Michihiro SHIBATA*, Hiroshi YAMAMOTO*,
Kiyoshi KAWADE* and Yoichi KAWASE**

Department of Chemistry, JAERI, *Department of Nuclear
Engineering, Nagoya University and **Research Reactor
Institute, Kyoto University

A high purity germanium (HPGe) detector has recently been used for measurements of beta-ray maximum energies of short-lived nuclei far from the beta stability line.^{1),2),3)} In the present work, the energy dependence of response functions is studied by measuring monoenergetic positrons with an HPGe detector. Using the response functions, beta-decay energies of neutron deficient Cs nuclides are determined.

A double focusing beta-ray spectrometer at Kyoto University research Reactor Institute (KURRI)⁴⁾ was used to provide monoenergetic positrons from sources of ^{68}Ge - ^{68}Ga and $^{34\text{m}}\text{Cl}$. The sources of $^{34\text{m}}\text{Cl}$ were produced by the bremsstrahlung irradiation of polyvinylidene chloride at KURRI-LINAC⁵⁾. The HPGe detector used in this study has a 0.05mm thick Be-window, and the detector dimension is 16 mm in diameter and 10 mm in thickness. We obtained response functions in energy range from 0.8 to 3.8 MeV. Examples of the observed response functions are presented in Fig. 1. Response functions consist of four parts, namely, a full energy peak, the escape of bremsstrahlung photons, the escape of back and side scattering of positrons from the surface of detector and the summation of annihilation photons. The observed ratios of each part to the total counts were fitted by the method of least squares as a function of the incident positron energy.

For the evaluation of the present method for beta-ray maximum energy determination, beta-rays of ^{62}Cu , ^{68}Ga and ^{91}Mo with precisely known Q_{EC} -values were measured. The experimental spectra were deconvoluted with the above-mentioned response functions to obtain the true beta-ray spectra. Figure 2 shows a Fermi-Kurie plot for ^{68}Ga . The least-squares fit gave an endpoint energy of 1892 keV with a statistical error of 7 keV. The same analyses were carried out for ^{62}Cu and ^{91}Mo . It is found from the results

that Q_{EC} -values can be determined with systematic errors less than 30 keV with the present method.

The Q_{EC} -values of short-lived neutron-deficient nuclides of $^{121-124}, ^{126}\text{Cs}$ have been measured. These isotopes were produced by bombarding a 4.1 mg/cm^2 thick Mo foil with a $5.1 \text{ MeV/u } ^{32}\text{S}$ beam from the JAERI tandem accelerator. The reaction products ionized with a high temperature surface ion source were mass-separated and implanted into an aluminum-coated Mylar tape. The radioactive source was transported periodically to a detection port. Singles beta-ray and beta-gamma coincidence spectra were measured. Energy-calibration of the detector for beta-ray measurement was made up to 6 MeV with gamma-rays of ^{56}Co and prompt gamma-rays in the thermal neutron capture of Fe. Thermal neutrons were generated by a ^{252}Cf neutron source. The experimental results obtained in this study are summarized in Table 1.

References

- 1) D.M.Rehfield and R.B.Moore : Nucl.Instrum. & Methods 157 (1978) 365.
- 2) R.Decker, K.D.Wunsch, H.Wollnik, G.Jung, E.Koglin and G.Siegert : Nucl.Instrum. & Methods 192 (1982) 261.
- 3) V.R.Bom and P.C.Coops : Nucl.Instrum. & Methods 228 (1985) 387.
- 4) H.Yamamoto, K.Takumi and H.Ikegami: Nucl.Instrum. & Methods 68 (1968) 253.
- 5) KURRI Linac Lab. (Ed.), "Report of the Present Status and Products with KURRI-Linac", (in Japanese) (1988)

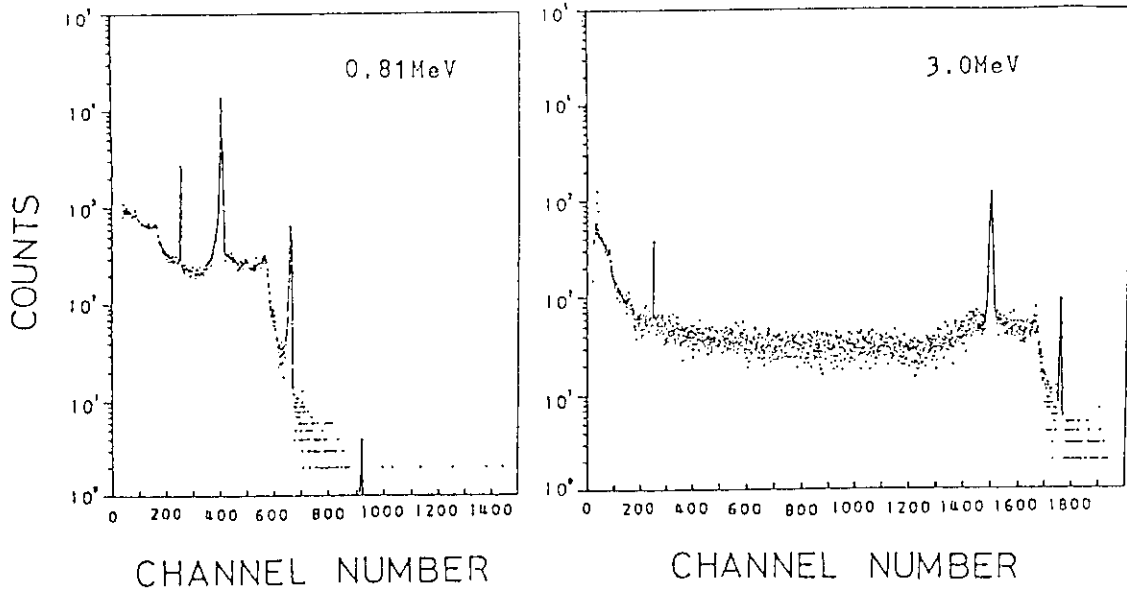


Fig. 1 Experimentally determined response functions of an HPGe detector for monoenergetic positrons of 0.81 and 3.0 MeV.

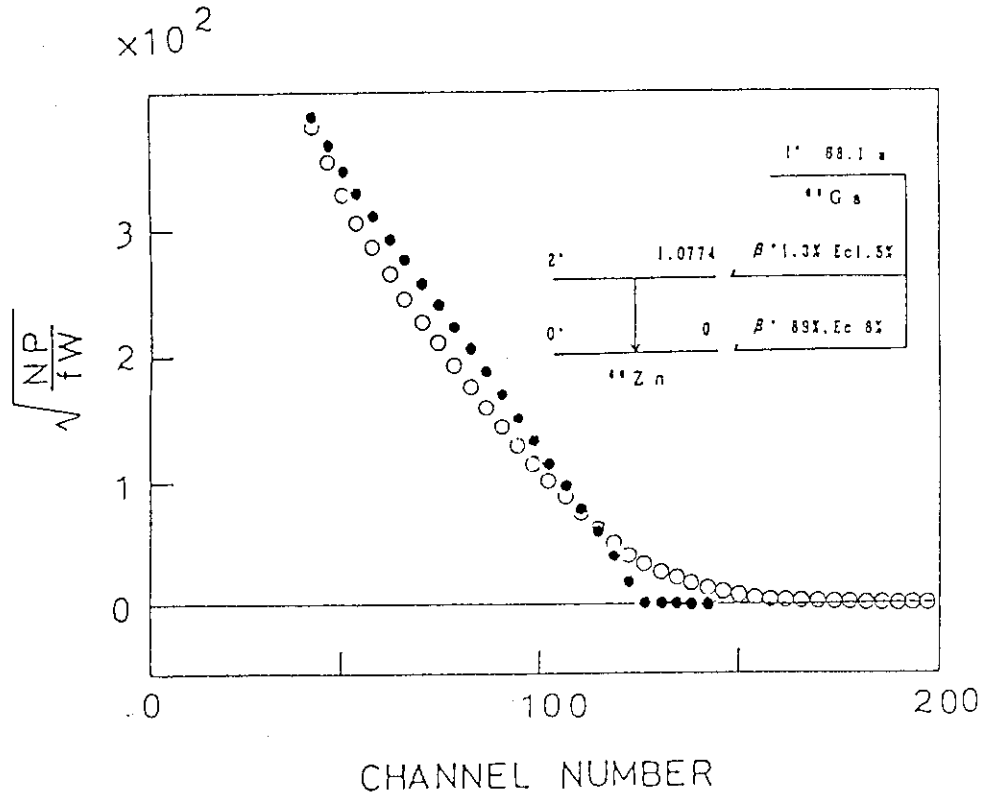


Fig. 2 Fermi-Kurie plots of singles beta-ray spectrum of ^{68}Ga obtained with an HPGe detector. Closed circles are corrected by using experimental response functions. Open circles are not corrected.

Table 1 Endpoint energies and Q_{EC} -values obtained in the present work.

Nuclide	Half life (sec)	Gated gamma-ray (keV)	End point energy (MeV)	Q_{EC} -value (MeV)	Evaluated Q_{EC} -value ^{a)} (MeV)
^{62}Cu	9.74min	-	2.943 ± 0.018	3.965 ± 0.018	3.949 ± 0.005
^{68}Ga	68.1min	-	1.892 ± 0.007	2.914 ± 0.007	2.9211 ± 0.0012
^{91}Mo	15.49min	-	3.428 ± 0.034	4.450 ± 0.034	4.438 ± 0.013
$^{121\text{m}}\text{Cs}$	121sec	179.4	4.22 ± 0.17	5.42 ± 0.12	$5.399\pm 0.020^{\text{b)}$
		459.8	3.93 ± 0.16		
$^{122\text{g}}\text{Cs}$	21sec	331.1	5.77 ± 0.58	7.12 ± 0.58	7.36 ± 0.41
$^{123\text{g}}\text{Cs}$	365sec	97.4	3.07 ± 0.19	4.24 ± 0.17	4.21 ± 0.05
		596.4	2.82 ± 0.38		
^{124}Cs	30.8sec	-	4.92 ± 0.10	5.95 ± 0.10	5.940 ± 0.094
		353.9	4.62 ± 0.41		
^{126}Cs	98.4sec	-	3.86 ± 0.04	4.88 ± 0.04	4.829 ± 0.024
		388.6	3.32 ± 0.29		

a) A.H.Wapstra and G.Audi : Nucl.Phys.A 432 (1985) 1.

b) Q_{EC} -value of $^{121\text{g}}\text{Cs}$

4.2 MEASUREMENT OF HOLD-UP TIMES OF A THERMAL ION SOURCE FOR METALLIC AND MONOXIDE IONS OF La AND Ce

Shin-ichi ICHIKAWA, Toshiaki SEKINE,* Hideki HIMURA
and Masumi OSHIMA**

Department of Chemistry, *Department of Radioisotopes, and
**Department of Physics, JAERI

Introduction

The isotope separator connected on-line to the JAERI tandem accelerator has been used for the study of unstable nuclei in the rare-earth region. So far the new isotope ^{121}La has been identified¹⁾ and the decay of neutron deficient La and Pr isotopes has been studied. For ionization of rare earths, a thermal ion source has been used. Its performance was reported previously, in particular for element selective mass separation using monoxide ion formation.²⁾ It is important for an isotope separator on-line that the time interval between production of a radioisotope and its deposition on a material for radioactivity measurement is kept as short as possible. The time of flight of an ion inside a mass separator is much less than 0.1 ms and can be neglected compared with the hold-up time in the ion source. Hold-up times of a thermal ion source were reported by Karnaukhov *et al.*³⁾ for Cs and Ba ions, which are obtained in high yields as mass-separated ion beams. Recently, Kirchner^{4,5)} studied hold-up times of FEBIAD-type ion sources. His results indicate that hold-up times for many elements are governed by sticking times to the cavity wall, and suggest a possibility that a thermal ion source has longer hold-up times for ions of La and Ce than for neighboring elements in the periodic table.

The present paper describes the experimental results of hold-up times of a thermal ion source for La and Ce ions as well as for LaO^+ and CeO^+ ions. As to ions of Cs, Ba, Pr and Nd, measurement was carried out for comparison.

Experimental

We measured the intensity of a mass-separated beam before and after the accelerator beam stopped. It was confirmed that the intensity of a mass-separated beam decreases exponentially after the accelerator beam is switched off and the production of the nuclide of interest stops.³⁾ Resultingly, a delay half-time after switch off of the accelerator beam was obtained; the value $T_{1/2}^{\text{del}}/\ln 2$ should be considered a hold-up time in the ion source. Strictly speaking, this kind of experiment is possible on the condition that

$$1. T_{1/2}(\text{nuclear decay}) \gg T_{1/2}^{\text{del}}$$

and

2. The precursor of the nuclide of interest is not produced.

These conditions, however, are difficult to fulfill in heavy-ion induced reactions. When the condition 1 was not applicable, Eq. (1) was used for correction of nuclear decay.

$$1/T_{1/2}^{\text{del}}(\text{corrected}) = 1/T_{1/2}^{\text{del}}(\text{observed}) - 1/T_{1/2}(\text{nuclear decay}) \quad (1)$$

The condition 2 was relaxed into either condition

$$(A) \sigma\eta(\text{the nuclide of interest}) \gg \sigma\eta(\text{precursor})$$

or

$$(B) \sigma\eta(\text{the nuclide of interest}) \simeq \sigma\eta(\text{precursor});$$

$$T_{1/2}(\text{the nuclide of interest}) \ll T_{1/2}^{\text{del}}(\text{precursor}),$$

where σ and η denote the formation cross section and ionization efficiency of the nuclide of interest or its precursor. The condition B was not known before experiment, but confirmed after experiment. Table 1 lists reaction systems used in this study. For each nuclide to be detected, the condition A or B is indicated at the last column.

Table 1 Reaction systems and measured radionuclides

Projectile Nuclide	Energy (MeV/u)	Target		Reaction channel	Measured radionuclide			Remark
		Nuclide	Thickness (mg/cm ²)		Nuclide	Half-life	Detected radiation	
³⁵ Cl	4.8	⁹² Mo	3.0	(HI,3p3n)	¹²¹ Ba	30 s	X-ray	(A)
				(HI,4p2n)	^{121m,g} Cs	2.0/2.3 m	X-ray	(B)
³² S	4.7	^{nat} Mo	4.0	(HI,1pxn)	¹²⁵ La	54 s	X/γ-ray	(A)
³⁵ Cl	4.8	^{nat} Mo	4.0	(HI,1pxn)	¹²⁶ Ce	50 s	X-ray	(A)
³⁵ Cl	5.4	¹⁰³ Rh	1.8	(HI,2p4n)	¹³² Nd	1.75 m	γ-ray	(A)
				(HI,3p3n)	¹³² Pr	1.6 m	γ-ray	(B)

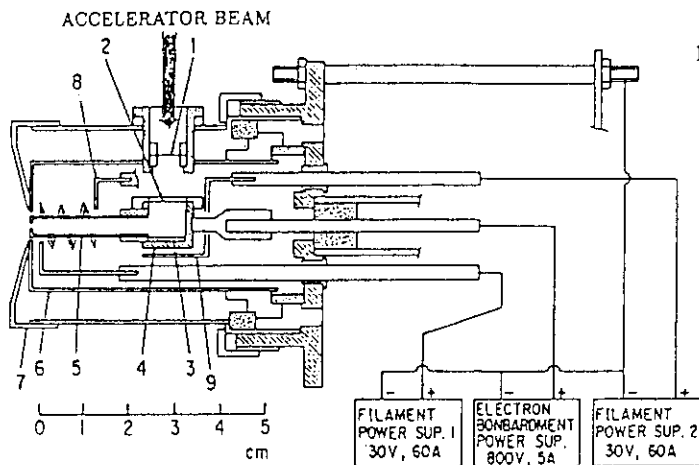


Fig. 1 Thermal ion source and its power supply scheme used for the measurement of release speeds; (1) target (thin window foil), (2) thin window foil (target), (3) catcher foil, (4) vaporizer (Ta), (5) ionizer (W; inner surface is covered by a thin Re foil), (6) inner heat shield (Ta), (7) outer heat shield (Mo), and (8) and (9) filament (W).

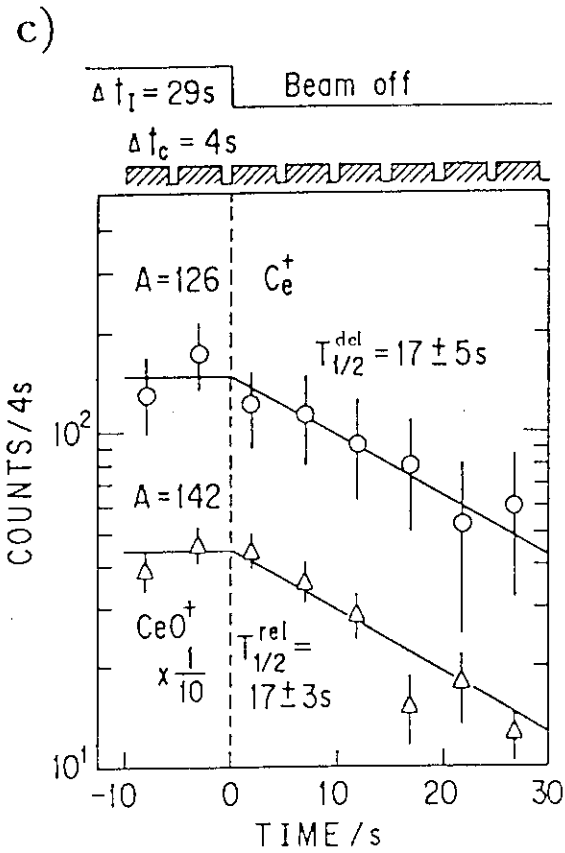
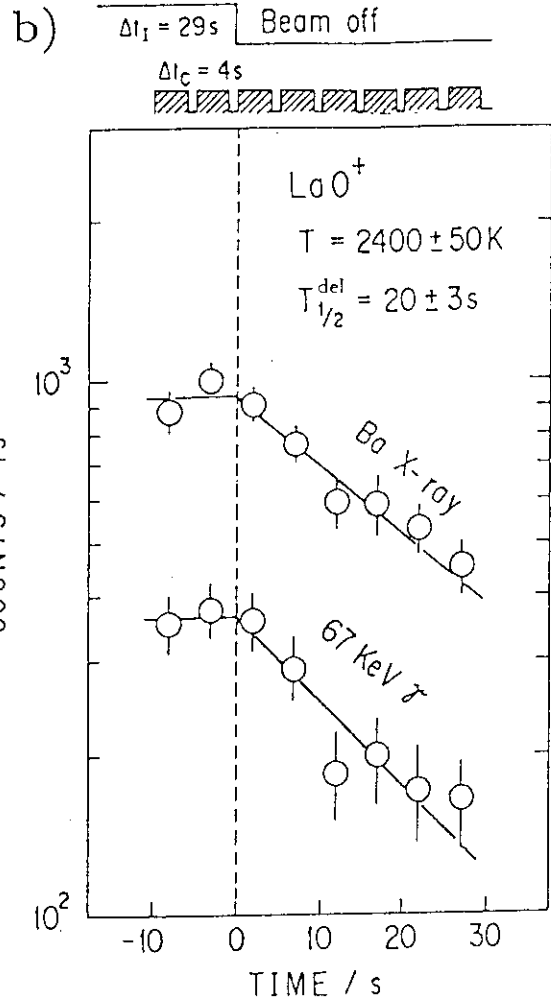
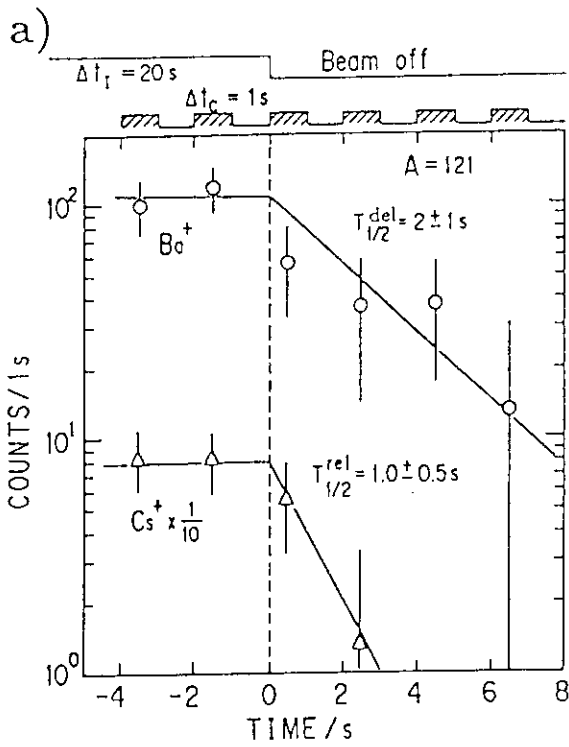


Fig. 2 Release profiles of the ions at an ion-source temperature of 2400 K: (a) $^{121}\text{Cs}^+$ and $^{121}\text{Ba}^+$, (b) $^{123}\text{LaO}^+$, (c) $^{126}\text{Ce}^+$ and $^{126}\text{CeO}^+$.

The structure of the thermal ion source used in this experiment was shown in Fig. 1. The target foil was working as a window of the ion-source cavity. The products recoiling from the target were caught by a 0.1 mm-thick Ta foil. The vaporizer with the catcher foil and the ionizer holding inside a 0.05 mm-thick Re foil were heated at a temperature of 2400, 2500 or 2600 K. The temperature of the ion source was measured with an optical pyrometer.

In an experiment, the accelerator beam irradiated the target during a period Δt_I . The accelerator beam was switched on and off by using a movable Faraday cup. Before and after the accelerator beam stopped, the mass-separated beam was collected during a period Δt_C at an Al coated Mylar tape and transferred, within a length of time Δt_T , to a detection port equipped with a HPGe detector. A γ - and/or X-ray spectrum was measured during the same period with Δt_C . The length of time Δt_T was set at 1 s, while the lengths of time Δt_I and Δt_C were changed according to the length of $T_{1/2}^{\text{del}}$ observed in a preliminary experiment. In a cycle, radioactivity measurement (and collection of the radioactivity) was repeated eight times; it was done two or three times before the accelerator beam stopped. A series of the procedures were controlled by a microcomputer. Events were accumulated by repeating the cycle several hundreds times.

Results and Discussion

Figure 2 shows the profiles of mass-separated beam intensities for $^{121}\text{Cs}^+$, $^{121}\text{Ba}^+$, $^{125}\text{LaO}^+$, $^{126}\text{Ce}^+$ and $^{126}\text{CeO}^+$ at an ion-source temperature of 2400 K. Since the delay half-times observed for $^{125}\text{La}^+$, $^{125}\text{LaO}^+$, $^{126}\text{Ce}^+$ and $^{126}\text{CeO}^+$ were rather long, correction for nuclear decay was made by using Eq. (1). The delay half-times obtained in the present work are summarized in Table 2. One can note from Table 2 that

- 1) the hold-up times of the metallic and monoxide ions of both La and Ce are much longer than those of the others, and
- 2) no difference is observed between the metallic and monoxide ions of each of La and Ce at any ion-source temperature.

The above observations are discussed in the following.

Table 2 Delay half-times of a thermal ion source

Temperature (K)	Delay half-time (s)							
	Cs ⁺	Ba ⁺	La ⁺	LaO ⁺	Ce ⁺	CeO ⁺	Pr ⁺	Nd ⁺
2400±50	1±0.5	2±1		27±4	26±8	26±6		
2500±50				20±4				
2600±50			12±3	12±3			≤3	≤3

Table 3 Adsorption enthalpies of several elements for Ta and Re surfaces⁶⁾

Surface	Adsorption enthalpy (eV)					
	Cs [†]	Ba [†]	La	Ce	Pr	Nd
Ta	2.5	4.0	5.5(5.9 [†])	6.1	5.1	4.7
Re	3.4	3.7	6.0	6.1	5.2	4.5

[†]Calculated values taken from Ref. 7. The others are experimental values.

The hold-up time of an ion source consists of the times in two independent steps: the diffusion of an atom in the catcher to its surface and the subsequent effusion in the ionizing cavity until emission as an ion. In our discussion, the time for the diffusion process and the time in sticking to the cavity wall during the effusion process are considered. It is because, in the effusion process, the time of flight of atoms between collisions with the cavity wall is not long substantially,^{3,4)} and ions are rapidly extracted due to the action of the electric field in the vicinity the exit orifice.³⁾

The diffusion time of an atom is determined by its distribution in the catcher and by the diffusion coefficient at a given temperature. Since the reaction systems in our experiment had almost the same bombarding energy of 5 MeV/u, it is assumed that the distributions of atoms in the catcher did not differ substantially. The diffusion coefficients of atoms in a heated Ta foil were experimentally determined and reported by Beyer *et al.*⁶⁾ Since their results shows that rare-earth atoms diffuse more rapidly than Cs and Ba atoms, it is impossible to ascribe the observation 1) to the difference between diffusion times of atoms.

Sticking of atoms to the wall of the cavity has been studied experimentally by Kirchner^{4,5)} on the FEBIAD ion sources. The sticking time per collision, t_a , is given for a Ta surface by the expression⁵⁾

$$t_a[s] = 2.4 \times 10^{-15} \exp\left(\frac{11605\Delta H_a[\text{eV}]}{T[\text{K}]}\right), \quad (2)$$

where ΔH_a denotes the adsorption enthalpy. Adsorption enthalpies determined experimentally or semiempirically by Eicher *et al.*^{7,8)} are listed in Table 3 for the atoms from Cs to Nd on Ta and Re surfaces; both Ta and Re are construction materials of the ion-source cavity. If we take the semiempirical value of 5.9 eV as the adsorption enthalpy of La onto Ta, the adsorption enthalpies of La and Ce are large enough to explain the observation 1). For example, the sticking time per collision for a Ce atom is calculated from Eq. (2) to be 15 ms at a temperature of 2400 K for both Ta and Re surfaces. A maximum collision number of an atom n is estimated to be 800 from that $n \approx S_{\text{int.}}/S_{\text{exit}}$, where $S_{\text{int.}}$ is the area of the wall inside the cavity, and S_{exit} the area of the exit orifice. The resulting total sticking time $nt_a \approx 10$ s at the same order of magnitude with the experimental hold-up time.

In the previous paper,²⁾ we assumed that the monoxide MO is produced in the gas phase through the reaction $M + O \rightarrow MO$, following the evaporation of the neutral atom M from the surface of the catcher, and that the reverse reaction $MO \rightarrow M + O$ takes place:



The reaction (3) means that there should be MO and M in the cavity with a constant ratio of their numbers. Hence, it is reasonable to find the same hold-up time for MO^+ and M^+ ions.

References

- 1) T. Sekine, S. Ichikawa, M. Oshima, H. Iimura, Y. Ngame, K. Hata, N. Takahashi and A. Yokoyama, *Z. Phy.* **A331**, 105 (1989).
- 2) S. Ichikawa, T. Sekine, H. Iimura, M. Oshima and N. Takahashi, *Nucl. Instr. Meth.* **A274**, 256 (1989).
- 3) V. A. Karnaukhov, D. D. Bogdanov, A. V. Demyanov, G. I. Koval and L. A. Petrov, *Nucl. Instr. Meth.* **120**, 69 (1974).
- 4) R. Kirchner, GSI 87-1, p.259 (1987).
- 5) R. Kirchner, GSI 88-1, p.339 and p.341 (1988).
- 6) G.-J. Beyer, W-D Fromm and A. F. Novgordov, ZfK-309 (1976).
- 7) B. Eicher, ZfK-396 (1979).
- 8) H. Rossback and B. Eicher, ZfK-527 (1984).

4.3 TEST OF AN ION GUIDE METHOD FOR ISOTOPE SEPARATION ON LINE

Shin-ichi ICHIKAWA, Hideki IIMURA, Nobuo SHINOHARA,
Masumi OSHIMA*, Toshiaki SEKINE** and
Yuichi HATUKAWA**

Department of Chemistry, *Department of Physics,
**Department of Radioisotopes, JAERI

An ion-guide method for isotope separation on-line (abbreviated as IGISOL) was developed by Arje et al.¹⁾ on the basis of the He-jet technique. A principle working for IGISOL has been reported in previous publications^{2,3)}, in which the rapid separation of isotopes produced by light-ion induced reactions has been demonstrated^{4,5)}. However, reports on application of this method to heavy-ion induced reactions are scarce in literature⁶⁾.

An ion-guide system has been constructed at the JAERI-ISOL connected to a tandem accelerator. The purpose of the present work is to measure ion-guide efficiencies for short-lived isotopes produced by heavy-ion induced reactions.

The ion-guide system consists of an ion-guide chamber, a pumping system and a gas flow system. The ion-guide chamber is vacuum chamber having a target chamber inside as shown schematically in Fig. 1. The target chamber is vacuum isolated from the outside by means of two HAVAR foil windows of 2.2 μm thickness. The ion-guide chamber is connected to the tandem accelerator-beam line with a HAVAR foil window of 5 μm thickness. The ion-guide chamber is evacuated by the pumping system which is composed of a turbo-pump having a pumping speed of 1800 l/s and a rotary pump (120 m^3/h). The ion-guide system is insulated from the ground to be able to stand against high tension up to 50 kV.

The helium mass flow rate through an exit hole of the target chamber and the pressure inside the target chamber were measured. We confirmed that the maximum mass flow rate and pressure are 50 cm^3/s (STP) and 200 mbar, respectively. Geometrical conditions and typical ion guide parameters are summarized in Table 1.

The performance of the ion-guide system was tested by measuring intensities of mass-separated ions in off- and on-line experiments.

In an off line experiment, a pressure dependence of ion yield was measured for ^{217}At ($T_{1/2}=32.3$ msec) ions by using a ^{225}Ac source. The source was placed at the target position in the target chamber. In the alpha-decay of ^{221}Fr , the daughter of ^{225}Ac , ^{217}At , ions recoiled out from the source with a recoil energy around 0.4 keV/u. The alpha-ray associated with the decay of ^{217}At was detected with a surface barrier detector placed in front of the collection point of a tape transport system. In this measurement, the acceleration voltage of the ISOL was set at 40 kV. The results obtained for different sizes of the exit hole are shown in Fig. 2. In every case, a maximum yield is observed in the pressure range from 80 to 90 mbar. This result indicates that the ions stopped in a small volume around the exit hole are evacuated effectively as singly-charged ions. The average recoil range of ^{217}At ions in helium at a gas pressure of 85 mbar is found from calculation to be 6.5 mm. It is interesting that this value of the recoil range agrees well with the distance between the exit hole and the target position (see Table 1).

In an on-line experiment, isotopes of ^{207}Fr ($T_{1/2}=14.8$ s) and ^{208}Fr ($T_{1/2}=58.6$ s) were used for testing the overall efficiency of the IGISOL. These isotopes were produced by bombarding a 4.7 mg/cm² thick Au target with a 6.25 MeV/u ^{16}O beam, through (HI,xn) reactions. The alpha-ray was measured in the same way as in the off-line experiment.

The reaction products with a recoil energy around 30 keV/u were stopped in 200 mbar helium, evacuated through a 0.8 mm exit hole and injected in the separator through a 1.5mm skimmer hole. Amounts of 1500 atoms/puC for ^{208}Fr and 140 atoms/puC for ^{207}Fr were separated. Taking into account the beam intensity, the target thickness and the formation cross sections⁷⁾, the observed yields are estimated to be 0.15% for the primary production coming out of the target. This value is equivalent to a separation efficiency of 2% for the ions thermalized in the target chamber.

Table 1
The ion guide parameters

symbol	definition	parameter value
V_{tc}	volume of the target chamber	3.5 cm ³
ϕ_{ex}	diameter of the exit hole of the target chamber	0.8 mm
ϕ_{sk}	diameter of the skimmer hole	1.5 mm
X_{es}	distance between exit hole and skimmer hole	7.5 mm
X_{tc}	distance between exit hole and target	6.5 mm
P_{tc}	pressure inside the target chamber	20 kPa
P_{vc}	pressure inside the vacuum chamber	50 Pa
Q_{HE}	helium mass flow rate through the exit hole of the target chamber	50 cm ³ /s(STP)
V_{sk}	voltage applied on the skimmer relative to target chamber	-45V/mm

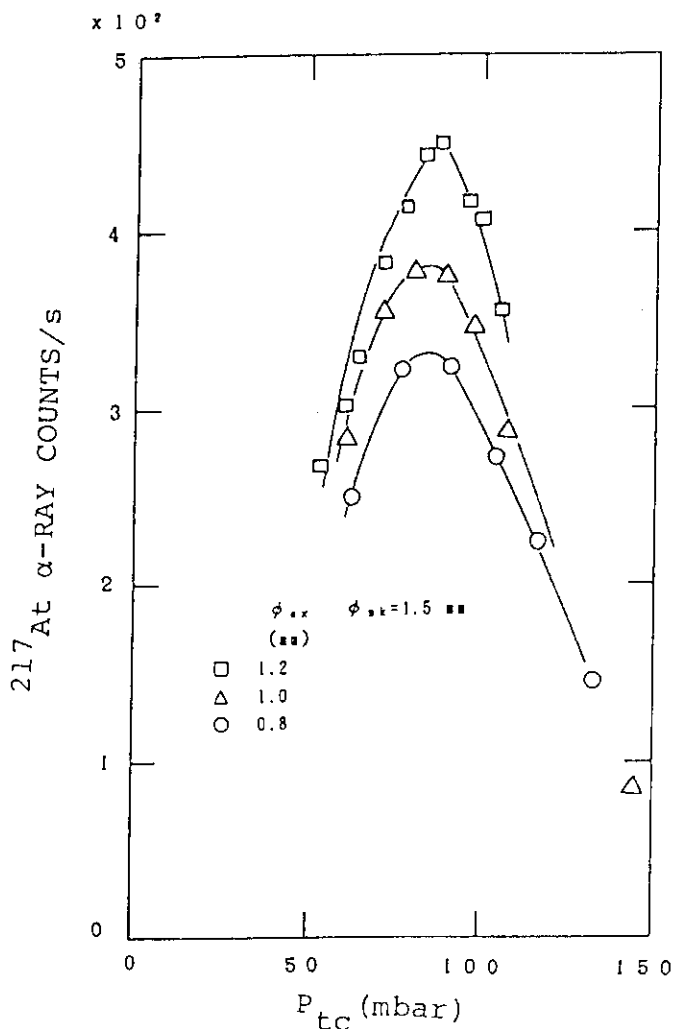


Fig. 2 Yields of ²¹⁷At vs the pressure P_{tc} inside the ion-guide target-chamber.

References

- 1) J.Arje, J.Aysto, J.Honkanen, K.Valli and A.Hautojarvi, Nucl. Instr. Meth. 186(1981)149.
- 2) J.Arje, J.Aysto, P.Taskinen, J.Honkanen and K.Valli, Nucl. Instr. Meth. B26(1987)384.
- 3) M.Yoshii, H.Hama, K.Taguchi, T.Ishimatsu, T.Shinozuka, M.Fujioka and J.Arji, Nucl. Instr. Meth. B26(1987)410.
- 4) J.Arje, J.Aysto, H.Hyvonen, P.Taskinen, V.Koponen, J.Honkanen A.Hautojarvi and K.Vierinen, Phy. Rev. Lett. 54(1985)99.
- 5) J.Aysto, J.Arje, V.Koponen, P.Taskinen, H.Hyvonen, A.Hautojarvi and K.Vierinen, Phys. Lett. 138B(1984)369.
- 6) K.Deneffe, B.Brijs, E.Coenen, J.Gentens, M.Huyse P. Va Duppen and D.Wouters, Nucl. Instr. Meth. B26(1987)399.
- 7) S.Baba, K.Hata, S.Ichikawa, T.Sekine, Y.Nagame, A.Yokoyama, M.Shoji, T.Saito, N.Takahashi, H.Baba and I.Fujiwara, Z.Phys. A331(1988)53.

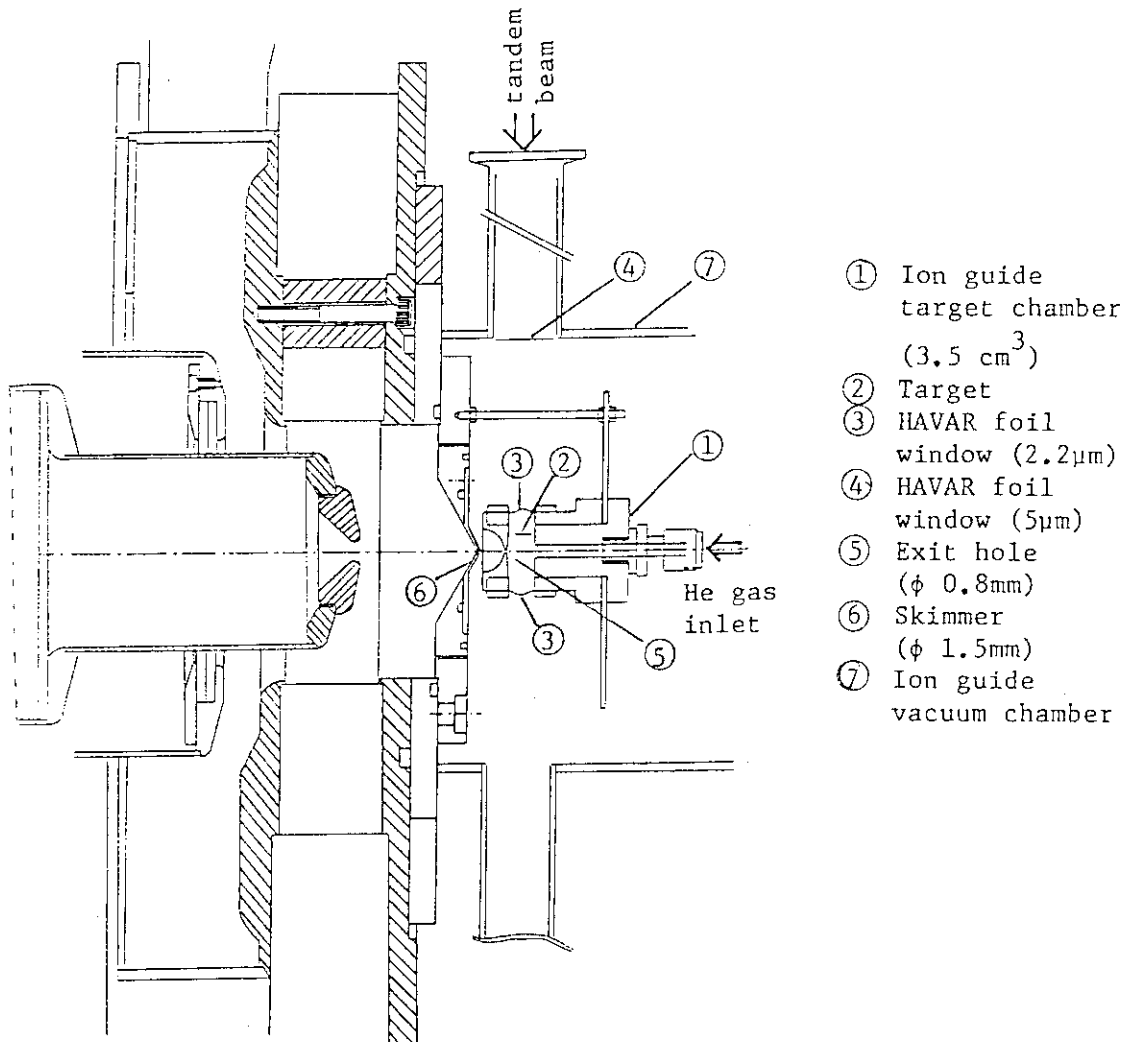


Fig. 1 Arrange of an ion-guide chamber and the extraction electrode of an isotope separator on-line.

4.4 A RESEARCH FOR THE PRODUCTION OF TRANSURANIUM ELEMENTS

Ichiro FUJIWARA, Seiichi SHIBATA^{*}, Hisaaki KUDO^{**},
 Kazuaki TSUKADA^{***}, Tsutomu OHTSUKI^{***}, Nobuo SHINOHARA^{****},
 Shin-ichi ICHIKAWA^{****}, Hideki IIMURA^{****}

School of Economics, Otemon Gakuin University,^{*} Institute
 for Nuclear Study, University of Tokyo,^{**} Department of
 Chemistry, Faculty of Science, Niigata University,
^{***} Department of Chemistry, Faculty of Science, Tokyo
 Metropolitan University,^{****} Department of Chemistry, JAERI

Introduction

Chemical properties of the heavy transuranium elements with atomic number greater than 100 are much interested in the point of an extended interpretation of the periodic table predicted from their atomic structures. Information on the nuclear data of the transuranium elements is also very important to understand their nuclear structures. However, the heavy elements cannot be synthesized through multi-neutron capture of nuclear fuel followed by successive beta-decays in a reactor. The only way to produce the heavy elements is the bombardment of a suitable transuranium element with ion beams from accelerator. The isotope of ^{250}Fm was produced in the $^{16}\text{O} + ^{238}\text{U}$ or $^{12}\text{C} + ^{242}\text{Pu}$ reaction by use of the JAERI Tandem accelerator by Shinohara et al.¹⁾ The elements with much larger atomic numbers ($Z=107, 108, 109$) were synthesized and investigated by Münzenberg et al.²⁾ However, not only the chemical properties but the nuclear structures have not been so much established in the region of such heavy elements.

Though the synthesis of the transuranium nuclides proceeds through the process of compound nucleus formation, the fission barrier of the compound nucleus with proton number greater than 100 is so low that almost all the compound nuclei turn out fission. Since neutron evaporation process of the compound nucleus competes with the fission in the every step of the successive neutron evaporations, the yield of the neutron evaporation residual becomes smaller as the neutron-evaporation multiplicity becomes greater. Therefore, the transuranium nuclides must be synthesized to form the compound nucleus with the excitation energy as low as possible, and simultaneously the projectile of the charged particles must overcome the

Coulomb barrier for the compound-nucleus formation reaction.

This report presents the recent results of the synthesis of mendelevium and lawrencium using the JAERI Tandem accelerator.

Experimental

Targets of ^{235}U , ^{244}Pu and ^{241}Am were prepared by electrodeposition from their organic solution. The thicknesses of the ^{235}U , ^{244}Pu and ^{241}Am targets were $800\ \mu\text{g}/\text{cm}^2$, $200\ \mu\text{g}/\text{cm}^2$ and $97\ \mu\text{g}/\text{cm}^2$, respectively, and the maximum intensity of the ^{12}C and ^{19}F beams was about $1\ \mu\text{A}$. Each target was located in a reaction chamber of He-jet rapid transportation system. The ^{235}U and ^{244}Pu targets were bombarded by ^{19}F beams with energy 101 and 103 MeV, respectively. The target of ^{241}Am was bombarded by ^{12}C beams with energy of 80.6 MeV. The recoiling transuranium nuclides produced in the particle evaporation reaction were caught by dioctyl Phthalate (DOP) aerosols, where the reaction chamber is small enough to eliminate fission fragments which have long recoiling ranges. The transuranium nuclides caught by the aerosols were transported rapidly through a capillary and collected on a surface of a stainless moving-tape through a skimmer. The DOP was removed from the collected sample by evaporation with heating in order to prepare a thin radiometric sample for alpha-ray spectrometry. The moving-tape system transferred the sample to a position of the first Si-surface-barrier detector and then to the next detector successively, and their alpha-ray spectra were measured. The duration of the collection and measurement was adjusted to the same as the half-life of the aimed transuranium nuclide. The cycle of collection, transfer and measurement was repeated several hundred times to accumulate the countings of the alpha-rays.

Results

The alpha-rays from ^{250}Md and ^{250}Fm , which were produced by the $^{235}\text{U}(^{19}\text{F},4n)^{250}\text{Md}$ reaction and the beta decay of ^{250}Md , were not detected in spite of sufficiently long duration of counting. The nuclides of ^{259}Lr and ^{255}Md expected to be produced by the $^{244}\text{Pu}(^{19}\text{F},4n)^{259}\text{Lr}$ and $^{244}\text{Pu}(^{19}\text{F},4n)^{255}\text{Md}$ reactions were not also detected. Nevertheless ^{249}Md and its beta-decay daughter ^{249}Fm were produced by the $^{241}\text{Am}(^{12}\text{C},4n)^{249}\text{Md}$ reaction and could be detected. Figure 1 shows the alpha-ray spectrum obtained by the continuous bombardment, collection and measurement during 2.3 hours.

In this figure, alpha-ray peaks of ^{250}Fm , $^{244,245,246}\text{Cf}$ and ^{242}Cm are also observed. Because the target thicknesses and the beam intensities were not so much different with each other, the cross sections of the $^{235}\text{U}(^{19}\text{F}, 4n)^{250}\text{Md}$, $^{244}\text{Pu}(^{19}\text{F}, 4n)^{259}\text{Lr}$ and $^{244}\text{Pu}(^{19}\text{F}, \alpha 4n)^{255}\text{Md}$ reactions are estimated to be less than 1 μb , whereas the cross section of the $^{241}\text{Am}(^{12}\text{C}, 4n)^{249}\text{Md}$ reaction seems to be much larger than those of the above ^{19}F -projectile reactions.

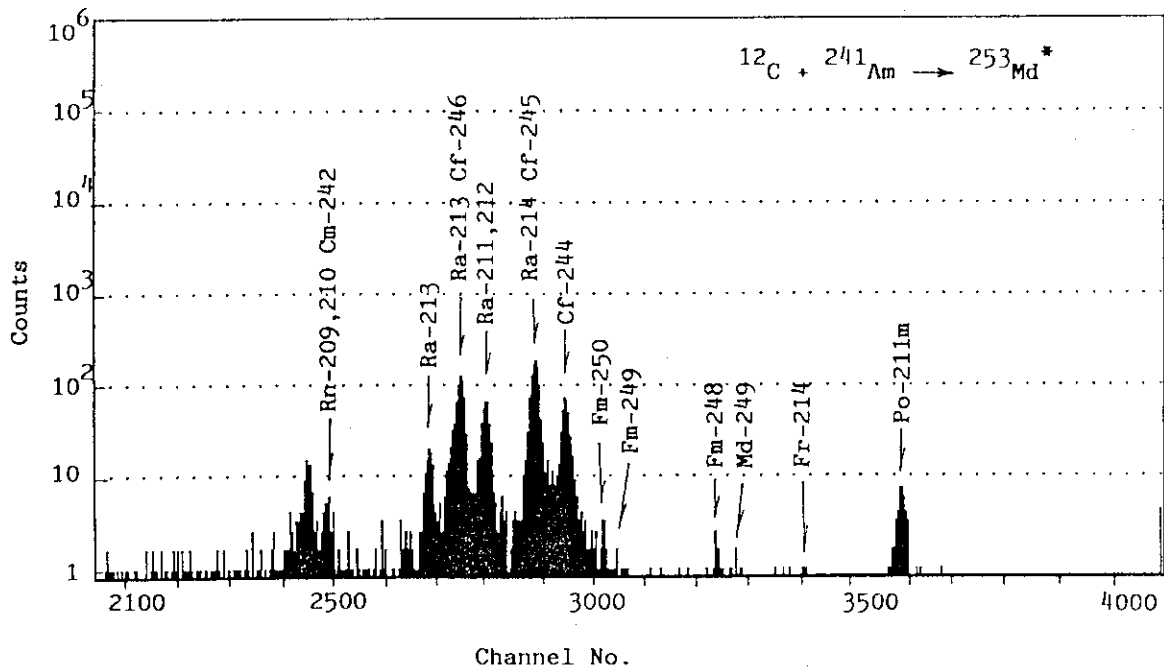


Fig. 1 Alpha-ray spectrum measured by means of a He-jet transportation and moving-tape system.

References

- 1) N. Shinohara, et al.: Phys. Rev. C34 (1986) 909.
- 2) G. Münzenberg, et al.: Z. Phys. A, 300 (1981) 107, 315 (1984) 145, 317 (1984) 235.

4.5 FISSION YIELDS OF RARE EARTH ELEMENTS
PRODUCED IN PROTON-INDUCED FISSION OF ^{244}Pu

Kazuaki TSUKADA, Keisuke SUEKI, Tsutomu OHTSUKI,
Takayuki KOBAYASHI, Ichiro NISHINAKA, Hiromichi NAKAHARA,
Nobuo SHINOHARA*, Shin-ichi ICHIKAWA*, Michio HOSHI* and
Yuichiro NAGAME**

Faculty of Science, Tokyo Metropolitan University, *Department
of Chemistry, **Department of Radioisotopes, JAERI.

Introduction

Detailed features of mass yield curves are necessary for the study of fission mechanism. However, in the rare earth region the mass distributions of fission products have scarcely been reported^{1,2)}, since many of the measurable nuclides have short half-lives. Recently, a computer-controlled rapid ion-exchange separation system has been developed³⁾, and we applied this system to the study of mass yields in the rare earth region. First, we have checked the separation method using a ^{252}Cf source and determined which nuclides could be determined by the present experimental setup. Next we studied the fission yields in the proton induced fission of ^{244}Pu .

System setup

The system is made up of three parts: (1) a gas jet transport system, (2) an ion-exchange separation system, and (3) a measurement system. All the steps through out the system are controlled by a personal computer with the BASIC interpreter. The collection of gas, dissolution, chemical separation, and source preparation would be completed within 8 min.

The fission products were adsorbed to KCl aerosol particles dispersed in such a gas as helium and argon in a chamber. The gas that carried fission products was transported to an injector, where the products were dissolved in a mixed solution of HCl and CH_3OH . The solution was fed into an ion-exchange column of 5 cm in length and 1.5 mm in inner diameter, with the pressure of nitrogen gas, through several tube pumps, 4 or 8 way-valves, and solenoid valves. The flow rates of the solution and eluents were controlled by changing the pressure of nitrogen gas (1-3 MPa) to normally about 0.5-1.5 ml/min. This system is shown in Fig.1. After the

ion-exchange separation, the effluents of the fractions of interest were heated to dryness and the γ -ray activities were measured.

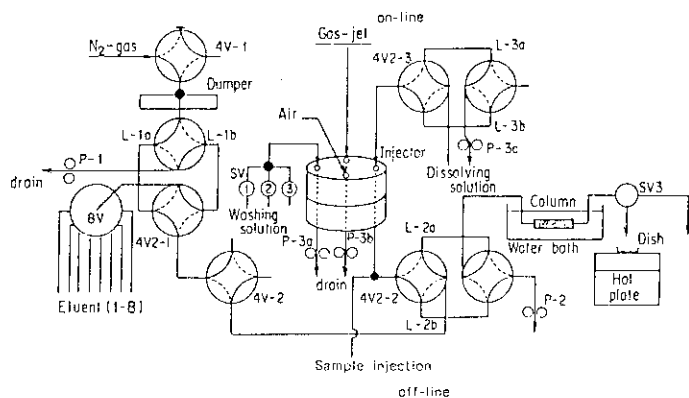


Fig.1 Automatic ion-exchange separation system with a gas-jet transport system;
 4V: 4-way valve,
 4VZ: dual 4-way valve,
 8V: 8-way valve,
 SV: solenoid valve,
 P-1,2: tube pump,
 P-3: triple tube pump,
 L: store loop for solution.

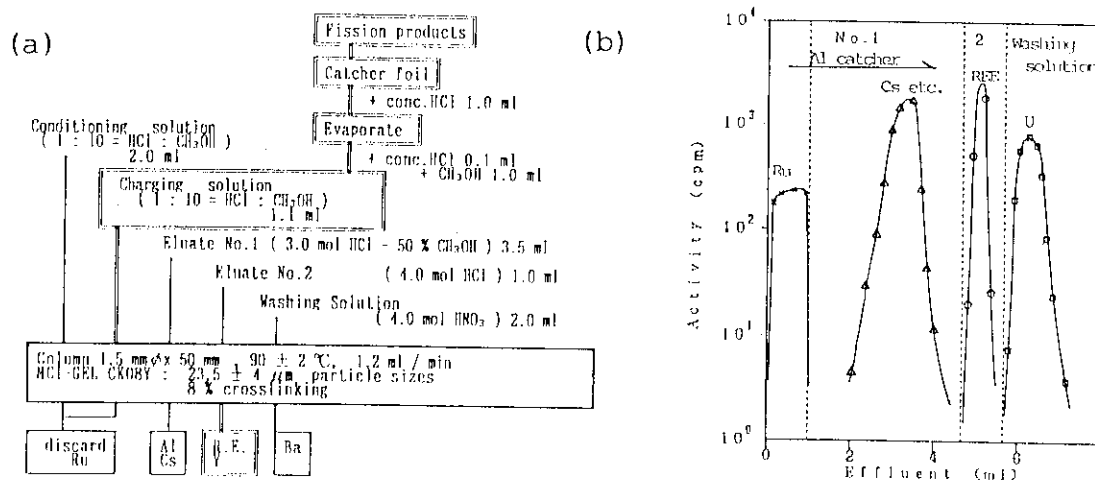


Fig.2 Rapid separation of rare earth elements produced by fission of actinides using the cation exchanger with HCl-CH₃OH mixed solution as eluents; (a) separation scheme for catcher foil method, (b) elution curve.

Experiment and results

Using a ²⁵²Cf source (2 mg), we checked the separation method and examined which nuclides could be investigated by the present setup and which γ -rays should be used for the determination of fission yields. The group separation for the rare earth elements was accomplished by cation exchanger⁴⁾. The resin was MCI-GEL CK08Y (Mitsubishi Chem. Ind. Co. Ltd.), with the resin size 24±4 μ m and crosslinking 8%. The separation procedure and elution curve are shown in Fig.2. The rare earth elements were eluted

in the second eluent, 4M HCl. The chemical yields were about 70%.

We have studied mass yield distributions of fragments in the proton energy range 11-16 MeV⁵⁾. In this experiment, the two supplementary methods, the gas-jet transport method and the catcher-foil method were used. Using a catcher foil, the whole procedure of dissolving the sample and the Al catcher foil, and the chemical separation of rare earths could be completed within 20 min, while with the direct gas-jet transport system, it was within 8 min. The efficiency of the gas-jet transportation, Ar(KCl), was about 60%. The cross section of each fission product was evaluated from the observed γ -ray intensities and those chemical yields and/or transport efficiencies cited above. The correction was also made, if necessary, for the charge distribution by assuming a Gaussian charge distribution with the most probable charge of the unchanged charge division model. The mass distribution obtained are shown in Fig.3.

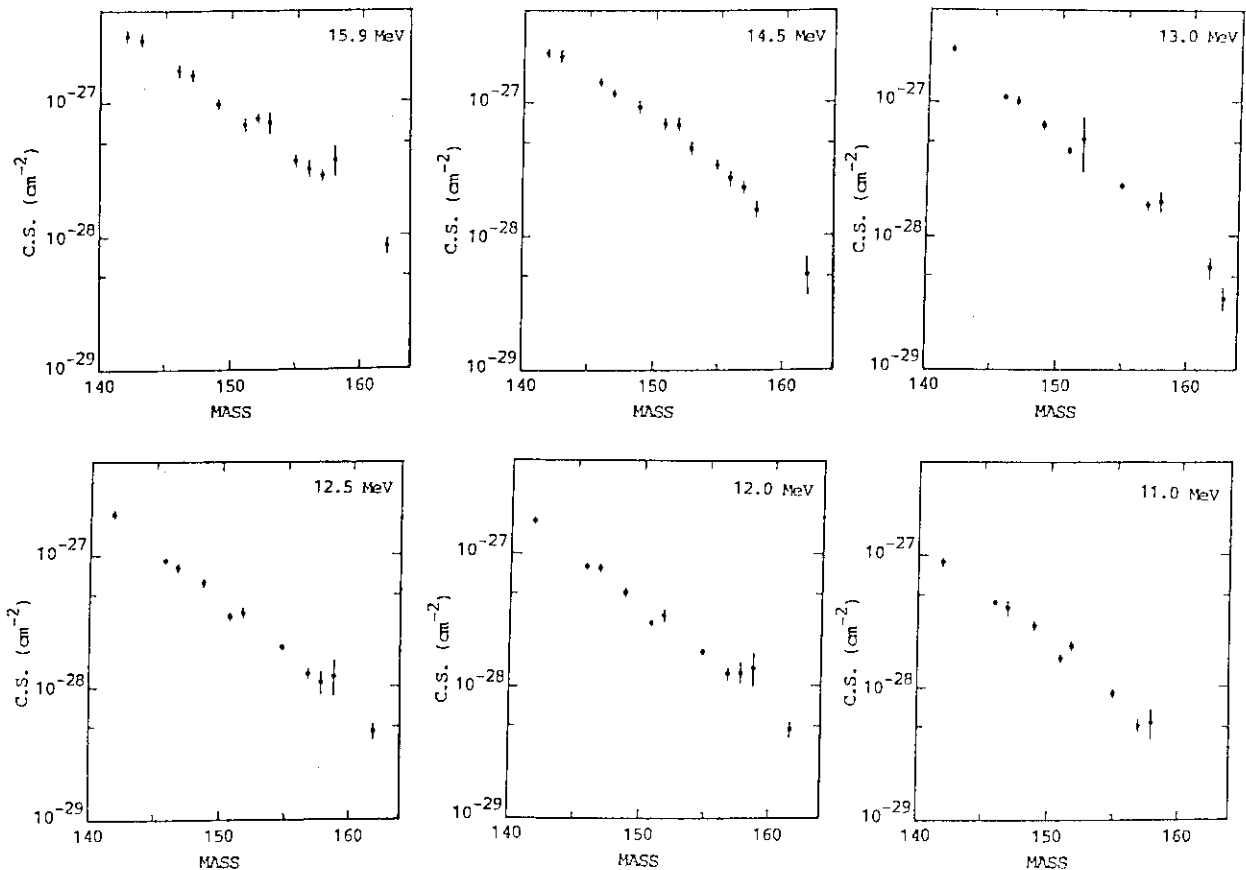


Fig.3 Mass yields distribution of fragments produced by 11-16 MeV proton induced fission of ^{244}Pu .

Summary

Using a computer controlled ion-exchange separation system, fission yields of short lived and low-yield nuclides in the rare earth region have been measured. The rare earth nuclides were completely separated as a group from other fission products within 8 min with the gas-jet transport method and within 20 min with the catcher foil method. Thus, we have established a method for measuring the mass distribution of the rare earth nuclides produced by fission of actinides. Next, we have applied this method to the proton-induced fission of ^{244}Pu , and the mass distributions have been obtained in the range of 11-16 MeV proton energy. This method is relatively easy, and applicable to the measurement of mass yields of rare earth products in other fission systems.

References

1. V. K. Rao, V. K. Bhargava, S. G. Marathe, S. M. Sahakundu and R. H. Iyer: Phys. Rev. C 19, 1372 (1979).
2. A. C. Wahl: Atom. Data and Nucl. Data Tables 39, 1 (1988).
3. K. Tsukada, T. Ohtsuki, K. Sueki, Y. Hatsukawa, H. Yoshikawa, K. Endo, H. Nakahara, N. Shinohara, S. Ichikawa, S. Usuda and M. Hoshi: Radiochim. Acta to be published.
4. S. Usuda: JAERI 1315 (1989).
5. T. Ohtsuki, Y. Hamajima, K. Sueki, H. Nakahara, Y. Nagame, N. Shinohara and H. Ikezoe: Phys. Rev. C 40, 2144 (1989).

4.6 MASS AND ENERGY DISTRIBUTION IN THE PROTON-INDUCED FISSION OF ^{232}Th

Tsutomu OHTSUKI, Yuichiro NAGAME*, Hiroshi IKEZOE**,
 Kazuaki TSUKADA, Ichiro NISHINAKA, Keisuke SUEKI,
 Ikuo KANNO***, Masaaki MAGARA****, Hiromichi NAKAHARA

Department of Chemistry, Tokyo Metropolitan University

*Department of Radioisotopes, **Department of Physics,

***Department of Reactor Engineering,

****Department of Chemistry, JAERI,

In recent years in the study of the fission phenomena, an attention has been given to the detailed structure of the mass and kinetic energy distributions and their relation with the structure of the potential energy surface of the deformed fissioning nucleus and/or that of a pair of product nuclei¹⁻⁴). We have investigated radiochemically detailed structures of mass yield distributions in the fission of actinides, and suggested the existence of the modal structure in the mass yield distribution⁵). In the present work, the structure of the kinetic energy distribution has been investigated in the fission of $^{232}\text{Th}+p$ by means of the double time-of-flight method used in coincidence mode.

The target of ^{232}Th was evaporated on a $10 \mu\text{g}/\text{cm}^2$ carbon foil and the thickness was estimated to be $45 \mu\text{g}/\text{cm}^2$. The beam of 13 MeV protons from the JAERI tandem accelerator was used for the bombardment. The beam current was about 500 nA. The measurement of velocities of fission fragments was made by a pair of time-of-flight (TOF) systems placed at 45° and -133.5° with respect to the beam direction in order to take into consideration the kinematical deviation. A micro-channel-plate (MCP) equipped with a carbon-foil gave start signals and a parallel plate avalanche counter (PPAC), stop signals. The flight paths were 88.4 cm and 75.0 cm. The flight time of each of a pair fragments in coincidence was accumulated event by event with an 8192 channels ADC and recorded in a host computer.

Altogether 1.5×10^5 fission events were accumulated in coincidence. The coincidence rate for pair of fission fragments was over 80 % with the present detection system. The velocity calibration was performed with a time calibrator and a ^{252}Cf source whose average velocities of the light and heavy fragments have been accurately measured by many groups⁶). The primary mass (before neutron emission) of a fission fragments was obtained from the ratio of the two velocities of the pair fragments with an assumption that no neutron was emitted from the compound nucleus prior to fission. The kinetic energy of fission fragments was calculated from the mass and velocity.

The primary mass distribution obtained from the velocity ratio is shown in fig.1. The shape is typically asymmetric and the bottom at the symmetric region is broad as expected. The average total kinetic energy distribution(TKE) was 167.2 MeV and this value was almost corresponding to the Viola's systematics⁷⁾. The average of the total kinetic energy $\langle TKE \rangle$ and the variance σ_{TKE} of the total kinetic energy distribution for each mass splitting are shown in figs.2 and 3. The $\langle TKE \rangle$ peaks at around mass 132. However, the peak of σ_{TKE} is shifted toward the inner side(peaking at 127-128). This fact suggests that the large σ_{TKE} could be caused by the existence of two kinds of energy distributions at around mass 126-132 as suggested by Britt et al.⁸⁾

In fig.4, the skewness of the total kinetic energy distribution for each mass split is shown as a function of the heavy fragment mass. It is found that the value takes a large negative value between fragment mass 132-145. It is interesting to note that this mass region coincides with the mass region where yields are largest. The skewness sharply increases beyond mass 145 and approaches to zero as the fragment mass is further increased. At present, we are still performing detailed analysis of the observed mass and kinetic energy distribution and the data presented in this report is preliminary.

References

- 1) V.V. Pashkevich, Nucl. Phys. **A169** (1971) 275.
- 2) M.G. Itkis et al. Sov. J. Nucl. Phys. **47** (1988) 765.
- 3) E.K. Hulet et al. Phys. Rev. Lett. **56** (1986) 313.
- 4) U. Brosa et al. Z. Phys. **A325** (1986) 241.
- 5) T. Ohtsuki et al. Phys. Rev. **C40** (1989) 2144.
- 6) J.S. Fraser et al. Can. J. Phys. **41** (1963) 2080.
- 7) V.E. Viola et al., Phys. Rev. C **31** (1985) 1550.
- 8) H.C. Britt et al. Phys. Rev. **129** (1963) 2239.

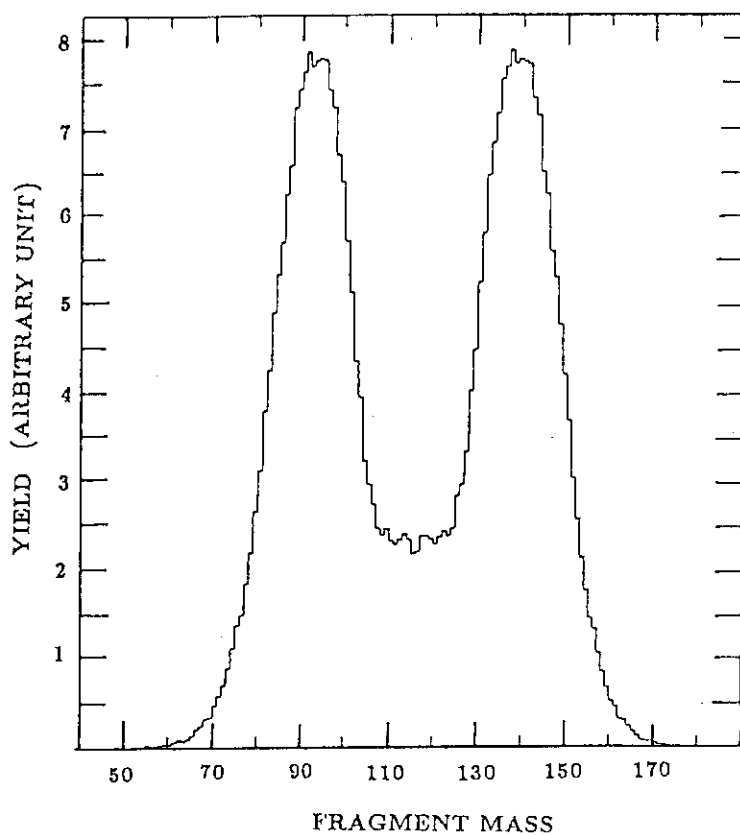


Fig.1 Mass yield curve of the $^{232}\text{Th}+p$ fission at $E_p=13.0$ MeV.

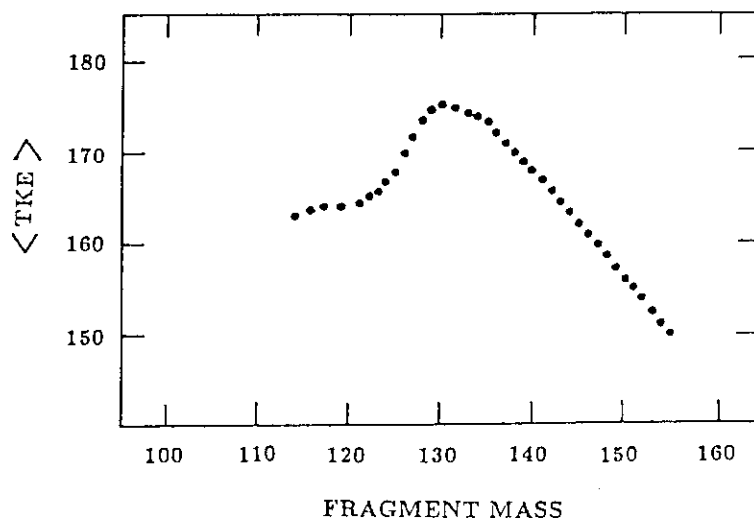


Fig.2 Average total kinetic energy distribution as a function of the fragment mass.

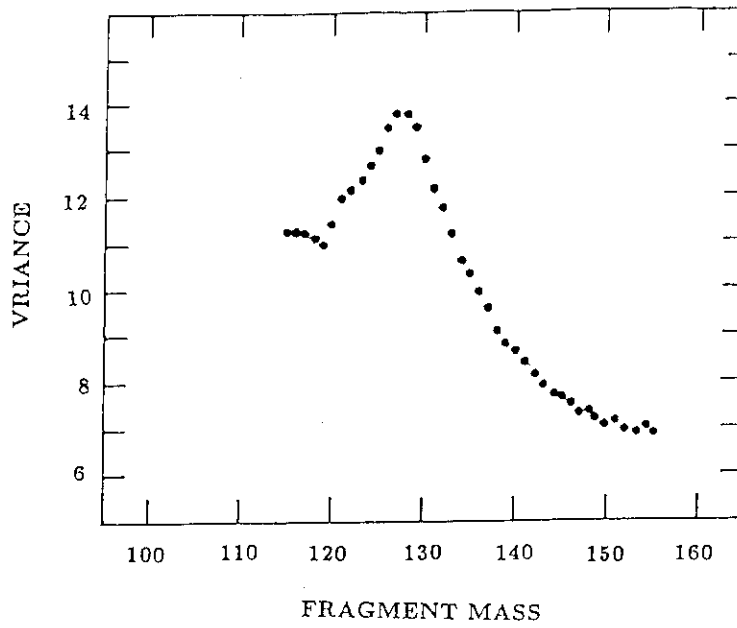


Fig.3 Variance of the kinetic energy distribution as a function of fragment mass.

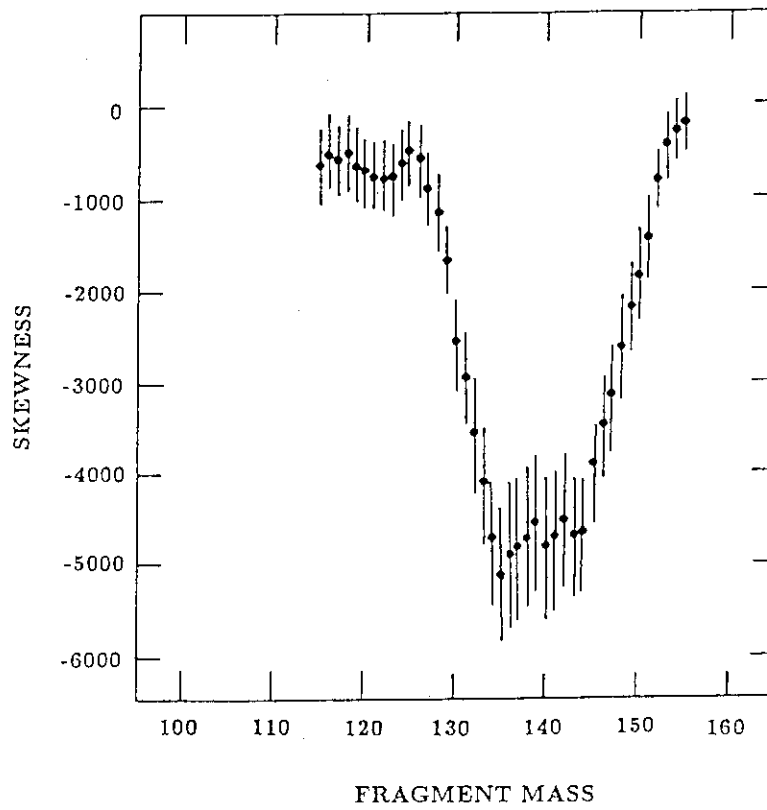


Fig.4. Skewness of the kinetic energy distribution of each fragment mass.

4.7 RUTHENIUM ISOTOPES PRODUCED IN THE PROTON-, ^{12}C - AND ^{19}F -INDUCED FISSIONS OF ACTINIDES

Nobuo SHINOHARA, Shin-ichi ICHIKAWA, Hideki IIMURA,
Kazuaki TSUKADA*, Tsutomu OHTSUKI*

Department of Chemistry, JAERI
* Tokyo Metropolitan University

The extensive studies have been undertaken by a radiochemical method on the fission of actinides induced by proton and heavier projectiles; the mass region 107-112 has been investigated by determining cumulative yields of some short-lived ruthenium isotopes in the proton-, ^{12}C - and ^{19}F -induced fissions of ^{232}Th , $^{233,235,238}\text{U}$, ^{237}Np and ^{244}Pu . Systematic study of these reactions could give insight into the reaction mechanisms involved.

All the ruthenium yields were determined by separating ruthenium from other fission products by rapid solvent extraction with SISAK.¹⁾ The ruthenium is isolated with a few seconds after the end of irradiation with ca. 80% chemical yield and high decontamination from other fission products. Figure 1 gives a gamma-ray spectrum of the ruthenium fraction after the separation in the $^{19}\text{F} + ^{238}\text{U}$ reaction system. The $^{107-112}\text{Ru}$ isotopes and their daughters are observed in the spectrum.

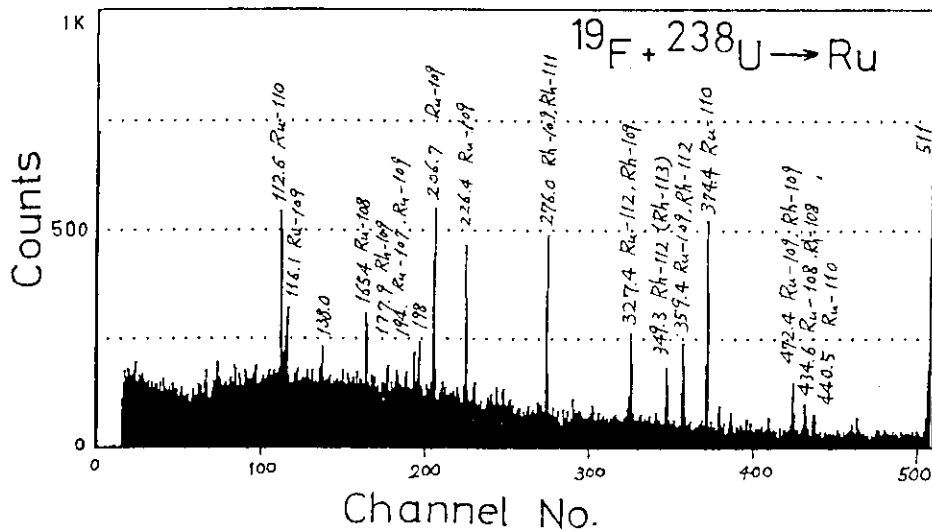


Fig. 1 Gamma-ray spectrum of the ruthenium fraction after the solvent extraction in the $^{19}\text{F} + ^{238}\text{U}$ system.

The reaction systems investigated in this work are shown in Table 1. To get information about the reaction mechanisms, the isotopic distributions of ruthenium in those reactions are being compared with each other and with those obtained in the neutron-induced fissions of the actinides.

Table 1 Reaction systems investigated in the present work.

reaction	fissioning nuclide
$p + {}^{238}\text{U}, {}^{237}\text{Np}, {}^{244}\text{Pu}$	${}^{239}\text{Np}, {}^{238}\text{Pu}, {}^{245}\text{Am}$
${}^{12}\text{C} + {}^{232}\text{Th}, {}^{233,235,238}\text{U},$ ${}^{237}\text{Np}, {}^{244}\text{Pu}$	${}^{244}\text{Cm}, {}^{245,247,250}\text{Cf},$ ${}^{249}\text{Es}, {}^{256}\text{Fm}$
${}^{19}\text{F} + {}^{235,238}\text{U}, {}^{237}\text{Np}, {}^{244}\text{Pu}$	${}^{254,257}\text{Md}, {}^{256}\text{No}, {}^{263}\text{Lr}$
spontaneous fission	${}^{252}\text{Cf}$

Reference

- 1) N. Shinohara, J. Alstad, S. Baba, I. Fujiwara, S. Ichikawa, H. Iimura, T. Ohtsuki, K. Tsukada, H. Umezawa: Proc. of Int. Symp. on Advanced Nuclear Energy Research, JAERI, Japan, pp.204 (1989).

4.8 SYMMETRIC MASS DIVISION OF ^{105}Ag FORMED IN THE REACTIONS $^{37}\text{Cl} + ^{68}\text{Zn}$ AND $^{16}\text{O} + ^{89}\text{Y}$

Yuichiro NAGAME, Hiroshi IKEZOE*, Tsutomu OHTSUKI**,
Kentaro HATA and Kazumi IDENO*

Department of Radioisotopes, *Department of Physics, JAERI,
**Department of Chemistry, Tokyo Metropolitan University

In the previous paper ¹⁾, we have observed a binary symmetric mass division in the $^{37}\text{Cl} + ^{68}\text{Zn}$ reaction and analyzed this process in terms of the angular momentum (l)-dependent ridge point model ²⁾. To elucidate further the characteristics of the symmetric mass division at high angular momentum in the region of relatively light mass nuclei, we measured mass, angular and total kinetic energy distributions in the ^{37}Cl induced reaction on ^{68}Zn and the ^{16}O induced reaction on ^{89}Y .

The experiment was carried out at the JAERI tandem accelerator using beams of ^{37}Cl with energies of 160 and 177 MeV and ^{16}O with 140 MeV to bombard self-supporting targets of ^{68}Zn (755 $\mu\text{g}/\text{cm}^2$ thick and 99.34% enrichment) and ^{89}Y (433 $\mu\text{g}/\text{cm}^2$ thick), respectively. The mass distribution of products was measured with a time-of-flight (TOF) telescope. The start detector was composed of a carbon foil (30 $\mu\text{g}/\text{cm}^2$ thick) and a microchannel plate ³⁾. The stop and energy signals were delivered with a 250 $\mu\text{g}/\text{cm}^2$ thick Si surface barrier detector located about 65 cm from the start detector.

Typical examples of the mass distribution in the center-of-mass system (c.m.) are displayed in fig. 1. The experimental mass distributions are corrected for neutron evaporation from fragments with an assumption that the excitation energy is shared between the fragments in proportion to their masses ³⁾. To avoid the contaminants from projectile-like products, the mass distributions were cut off below $A \sim 50$ in the $^{37}\text{Cl} + ^{68}\text{Zn}$ system. In the $^{16}\text{O} + ^{89}\text{Y}$ system in fig. 1(c), one can clearly see a peak of the symmetric mass division, while the components of projectile- and target-like products are seen in the mass regions of $A \lesssim 40$ and $A \gtrsim 65$, respectively. The dashed lines are least squares fit to the data by a Gaussian function having the center at $\frac{1}{2}A_{CN}$.

The angular distributions of the symmetric mass division products were essentially flat in $d\sigma/d\theta_{cm}$, as expected from the fission products of a compound nucleus or the decay products of a long-lived dinuclear system.

In fig. 2, the mean total kinetic energies $\langle TKE \rangle$ and the variances σ_{TKE} , obtained by assuming a Gaussian function of the total kinetic energy distributions for the symmetric mass division are plotted as a function of the scattering angle. To cancel out the effect of the nuclear temperature T_S at the saddle point, the experimental σ_{TKE}^{exp} values are reduced to the variance for $T_S = 1.6$ MeV at $l = l_{max}$ ¹⁾, where l_{max} is the maximum angular momentum for fusion taken from the prediction of the Bass model ⁴⁾.

As shown in fig. 2, $\langle TKE \rangle$ and σ_{TKE} are practically independent of the scattering angle. No significant dependence on the corresponding angular momentum was observed in $\langle TKE \rangle$ and σ_{TKE} in the studied l region. The solid line corresponds to $\langle TKE \rangle$ expected from the empirical formula of Viola et al. ⁵⁾ for the total kinetic energy of fission. The observed $\langle TKE \rangle$ is about 9 MeV larger than that predicted by this systematics ⁵⁾.

The dashed line is a σ_{TKE} value predicted from the liquid drop model of Nix ⁶⁾ for 1.6 MeV of the saddle point temperature at $l = 0\hbar$. The experimental variances are considerably larger than the calculated ones. Although the effect of l on σ_{TKE} has not yet been fully accounted for in a quantitative manner, the observed broad width would be interpreted as a contribution of some dynamical effects including l to the symmetric mass division process.

In the following, we discuss the relationship between the width of the symmetric mass distribution and the l -dependent potential energy surfaces. The variances σ_A^{exp} of the mass distributions (dashed lines in fig. 1) measured at a nuclear temperature $T_S(l)$ are normalized to a value corresponding to $T_S(l_{max}) = 1.6$ MeV ¹⁾.

In the inset of fig. 3 are shown calculated potential energy surfaces at the ridge point for different l on the decay of ^{105}Ag as a function of the mass asymmetry. Assuming that the shape of the mass distribution depends only on that of the static potential energy, the width of the corresponding mass distribution is expected to become narrower as the angular momentum increases ^{2,7)}. The solid and dashed lines are the σ_A values calculated on the basis of the ridge point static potential energy surfaces for the systems $^{37}\text{Cl} + ^{68}\text{Zn}$ and $^{16}\text{O} + ^{89}\text{Y}$, respectively.

As shown in fig. 3, the σ_A values are found independent of l_{max} in the l region studied and the deviation of the experimental variances from the calculated ones increases with l_{max} . The constancy of σ_A as a function of l is inconsistent with the feature predicted by the ridge point model.

With respect to the above discussion, Faber pointed out that the stiffness of the potential energy associated with the mass asymmetry degree of freedom at the saddle point is expected to decrease with l ⁸⁾; the mass distribution would become wider than that predicted by the static potential surface with l . The observed trend of σ_A shown in fig. 3 would be explained by this consideration.

In conclusion, the observed broad widths of the mass and TKE distributions cannot be accounted for within the liquid drop model. This result would be explained by some dynamical effects including l at the ridge point. A mechanism that the stiffness of the potential energy surface at the ridge point would be constant or decrease with l is needed. More complete and systematic studies in a wider range of angular momentum are needed for the better understanding of this feature.

References

- 1) Y. Nagame et al., Nucl. Phys. **A510** (1990) 518.

- 2) L.G. Moretto, Nucl. Phys. **A247** (1975) 211.
- 3) H. Ikezoe et al., Z. Phys. A **330** (1988) 289.
- 4) R. Bass, Phys. Rev. Lett. **39** (1977) 265.
- 5) V.E. Viola et al., Phys. Rev. C **31** (1985) 1550.
- 6) J.R. Nix, Nucl. Phys. **A130** (1969) 241.
- 7) L.G. Moretto and R.P. Schmitt, Phys. Rev. C **21** (1980) 204.
- 8) M.E. Faber, Phys. Rev. C **24** (1981) 1047.

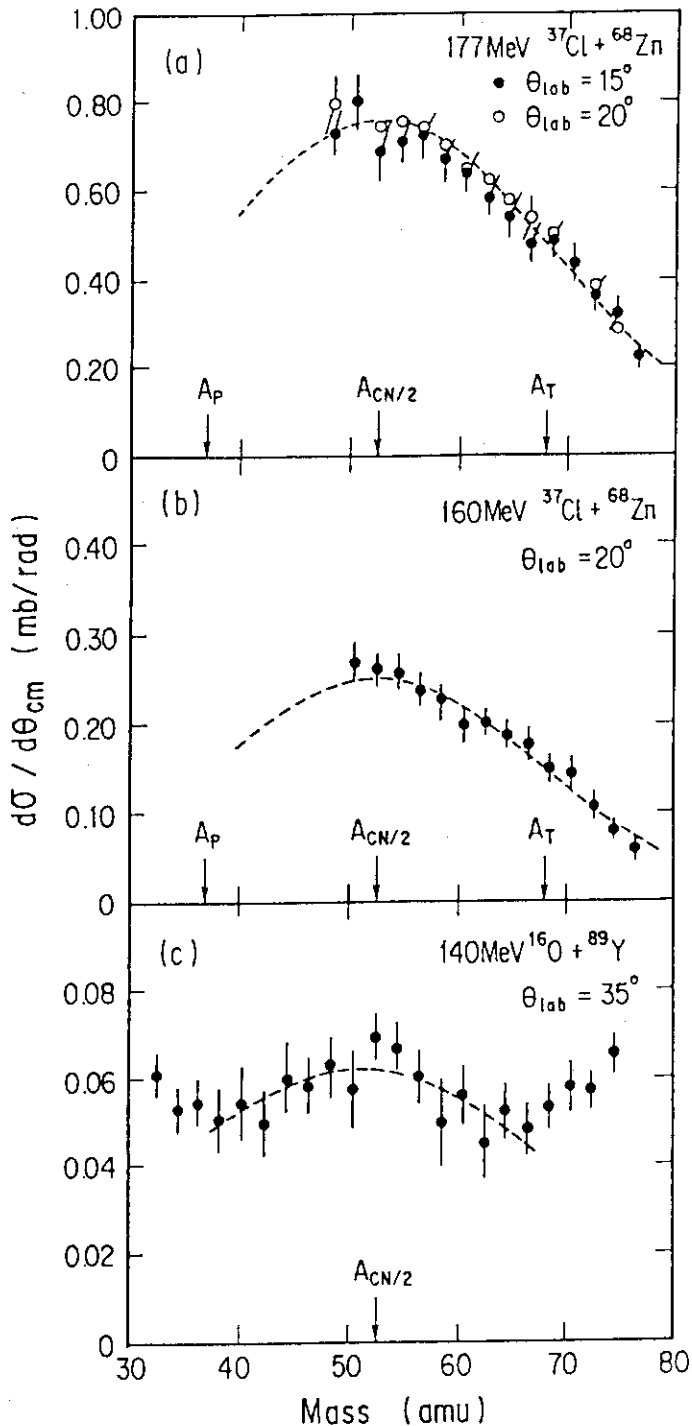


Fig.1 Typical fragment mass distributions for the reactions: (a) 177 MeV $^{37}\text{Cl} + ^{68}\text{Zn}$, (b) 160 MeV $^{37}\text{Cl} + ^{68}\text{Zn}$ and (c) 140 MeV $^{16}\text{O} + ^{89}\text{Y}$. The Symbols A_P , A_T and A_{CN} correspond to the mass numbers of the projectile, target and compound nucleus, respectively. The dashed lines are least squares fit by a Gaussian function.

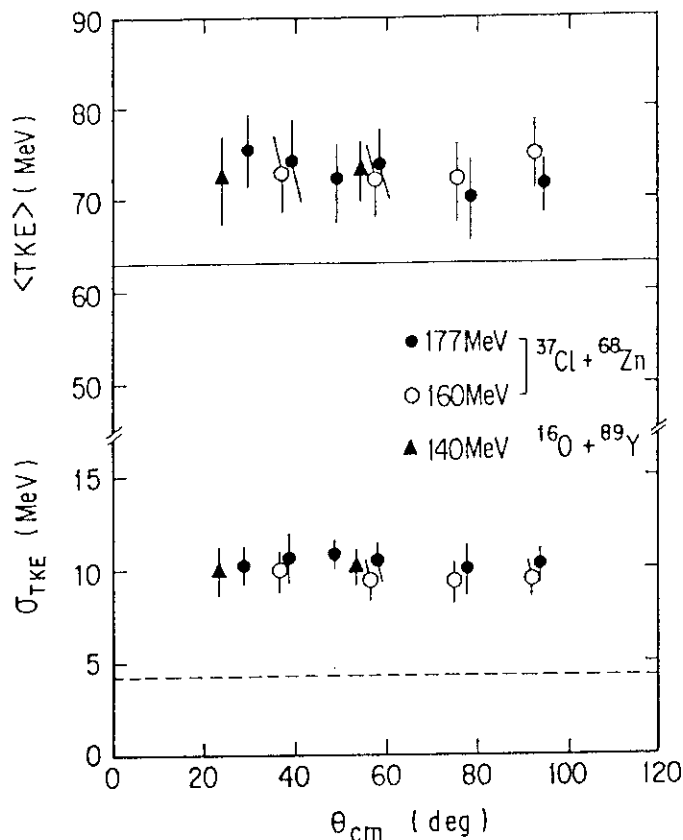


Fig.2 Mean total kinetic energy $\langle TKE \rangle$ and variance of the total kinetic energy distributions as a function of the scattering angle. The solid line corresponds to $\langle TKE \rangle$ expected from the empirical formula of Viola et al. The dashed line shows a σ_{TKE} value predicted by Nix at the saddle point temperature 1.6 MeV.

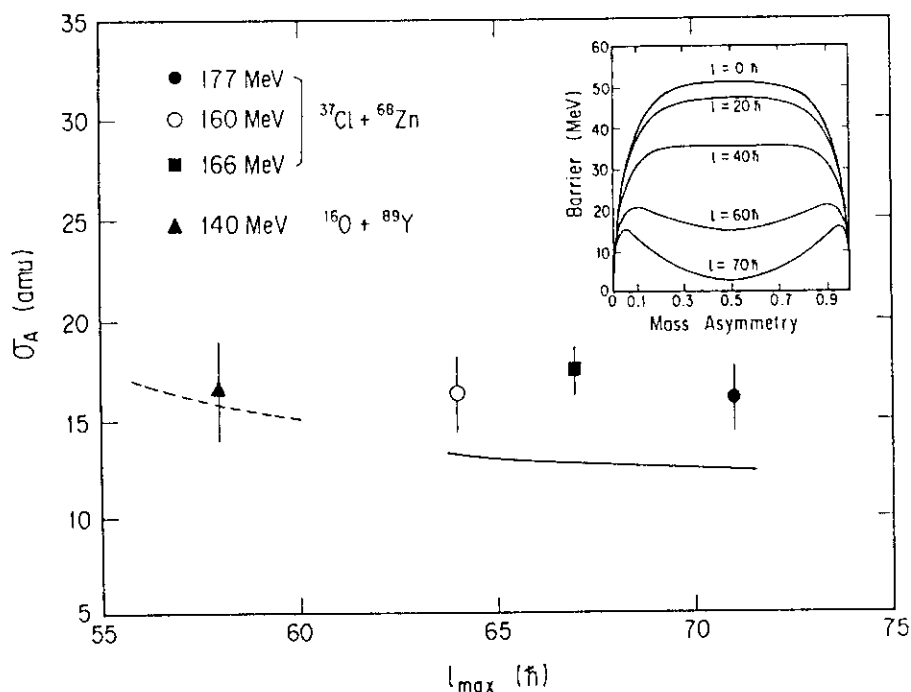


Fig.3 Variances of the mass distributions for the symmetric mass division as a function of l_{max} . The internal excitation energy of the composite system is normalized to an excitation energy corresponding to $T_S(l_{max}) = 1.6$ MeV. The value for the 166 MeV $^{37}\text{Cl} + ^{68}\text{Zn}$ reaction (open circle) is taken from ref. 1). The solid and dashed lines are the variances predicted from the statistical model calculation based on the ridge point model for the $^{37}\text{Cl} + ^{68}\text{Zn}$ and $^{16}\text{O} + ^{89}\text{Y}$, respectively. In the inset, potential energy surfaces at the saddle point for different l values on the decay of the ^{105}Ag compound nucleus as a function of the mass asymmetry are depicted.

V NUCLEAR PHYSICS

5.1 TRANSFER REACTIONS FOR $^{16}\text{O} + ^{144,152}\text{Sm}$ NEAR THE COULOMB BARRIER

Yasuharu SUGIYAMA, Yoshiaki TOMITA, Hiroshi IKEZOE, Kazumi IDENO,
Noriyoshi KATO*, Tsuyoshi SUGIMITSU* and Hiroshi FUJITA**

Department of Physics, JAERI, * Department of Physics, Kyushu University,
** Daiichi College of Pharmaceutical Sciences

Considerable experimental and theoretical attention has centered on the study of transfer reactions with heavy ions around the Coulomb barrier. The main features of transfer reactions has been understood within the frame work of the DWBA or the semi-classical models. The transfer probability of one- and two-nucleon transfer reactions at large distances, where the overlap of the two nuclei is very small, is described by a tunneling process. The semi-classical model¹⁾ predicts that the transfer probability defined as $P = d\sigma/d\sigma_{\text{Ruth}}$ should be given at large distance by the expression

$$P \approx \exp(-\alpha D) \sin(\theta_{\text{cm}}/2) \quad (1)$$

where D is the distance of closest approach,

$$D = \frac{Z_1 Z_2 e^2}{2E_{\text{cm}}} [1 + 1/\sin(\theta_{\text{cm}}/2)], \quad (2)$$

and $d\sigma_{\text{Ruth}}$ is the Rutherford cross section, $d\sigma$ the corresponding transfer cross section and α the so called slope parameter given by

$$\alpha = 2(2\mu E_{\text{B}})^{1/2}/\hbar. \quad (3)$$

Here E_{B} is the effective mean binding energy and μ the reduced mass of the transferred particle. One expects from eq.(3) that the one- and two-nucleon transfer slope parameter α are related by $\alpha_2 \approx 2\alpha_1$.

For a variety of heavy-ion reactions the data exhibit an exponential dependence on

the distance of closest approach as given in eq.(1). The one- and two-neutron transfer slope parameters obey eq.(3) when both collision partners are spherical²⁾, whereas a large departure from the expected behavior is observed for two-neutron transfer reactions with heavy ions in which at least one of the collision partners is deformed³⁾. So-called slope anomaly of $\alpha_2 \approx \alpha_1$ has been observed in two-neutron transfer reactions for many deformed systems. Recently it has been observed in the systems of $^{58}\text{Ni} + ^A\text{Sm}$ that one-neutron transfer reactions on the deformed Sm targets has small slope parameter than expected⁴⁾.

In order to clarify the origin of the slope anomaly we carried out experiments of transfer reactions for the $^{16}\text{O} + ^{144,152}\text{Sm}$ systems near the Coulomb barrier. The ^{16}O beam energies were 72 MeV and 60 MeV with typical beam intensities of 500nA. The energy spectra were measured with an energy resolution of 200 keV by using the heavy-ion spectrograph "ENMA"⁵⁾. The mass number, atomic number, Q-value and atomic charge state q of a reaction product were determined unambiguously from a measurement of the total energy E , energy loss δE and momentum P . Six nuclei ^{17}O , ^{18}O , ^{15}N , ^{12}C , ^{13}C and ^{14}C were observed in addition to elastically scattered ^{16}O . Other reaction products could not be identified because of their small yields.

Transfer probabilities of $P/\sin(\theta_{\text{cm}}/2)$ are shown as a function of the distance of closest approach D for the reactions leading to ^{17}O , ^{18}O , ^{15}N and ^{14}C in Fig.1. At large distances the data show an exponential behavior which is characteristic of a tunneling process, while the deviations observed at the short distances may be related to the onset of absorption processes. The solid lines are results from DWBA or semi-classical model calculations. The slopes of one-nucleon transfers reactions leading to ^{17}O and ^{15}N are well accounted for by these calculations. The slopes of the two-nucleon transfer reactions $^{152}\text{Sm}(^{16}\text{O}, ^{18}\text{O})$ at $E=60\text{MeV}$ and $^{144}\text{Sm}(^{16}\text{O}, ^{14}\text{C})$ at $E=72\text{MeV}$ are also explained well by the calculations. On the other hand the slope parameters of two-nucleon transfer reactions on ^{152}Sm target leading to ^{18}O and ^{14}C deviate strongly from the values of eq.(3) at $E=72\text{MeV}$. The dashed lines are for guiding the eyes.

In summary the transfer probabilities of one-nucleon transfer reactions leading to ^{17}O and ^{15}N at large distances are explained well by both DWBA and semi-classical model calculations. The slope anomaly is not observed in the one-nucleon transfer reactions on the deformed ^{152}Sm target. The slope of the two-nucleon transfer probability for $^{144}\text{Sm}(^{16}\text{O}, ^{14}\text{C})$ is explained by the calculations. On the other hand the slope parameters of two-nucleon transfer probabilities leading to ^{18}O and ^{14}C on the deformed ^{152}Sm target depends on the incident energies. The slope at $E=60\text{ MeV}$ is accounted for well by both DWBA and semi-classical model calculations, while at $E=72\text{ MeV}$ the slopes

deviate considerably from the calculations at large distances

References

- 1) G.Briet and E.M.Ebel: Phys. Rev. 103 (1956) 679.
- 2) W. von Oertzen et al.: Z. Phys. A313 (1983) 189.
- 3) S.Juutinen et al.: Phys. Lett. B192 (1987) 307.
- 4) R.R.Betts : Heavy-Ion Reaction Dynamics in Tandem Energy Region (Universal Academy Press, Tokyo 1988) pp.63-72.
- 5) Y.Sugiyama et al.: Nucl. Instrum. & Methods in Physics Research A281 (1989) 512.

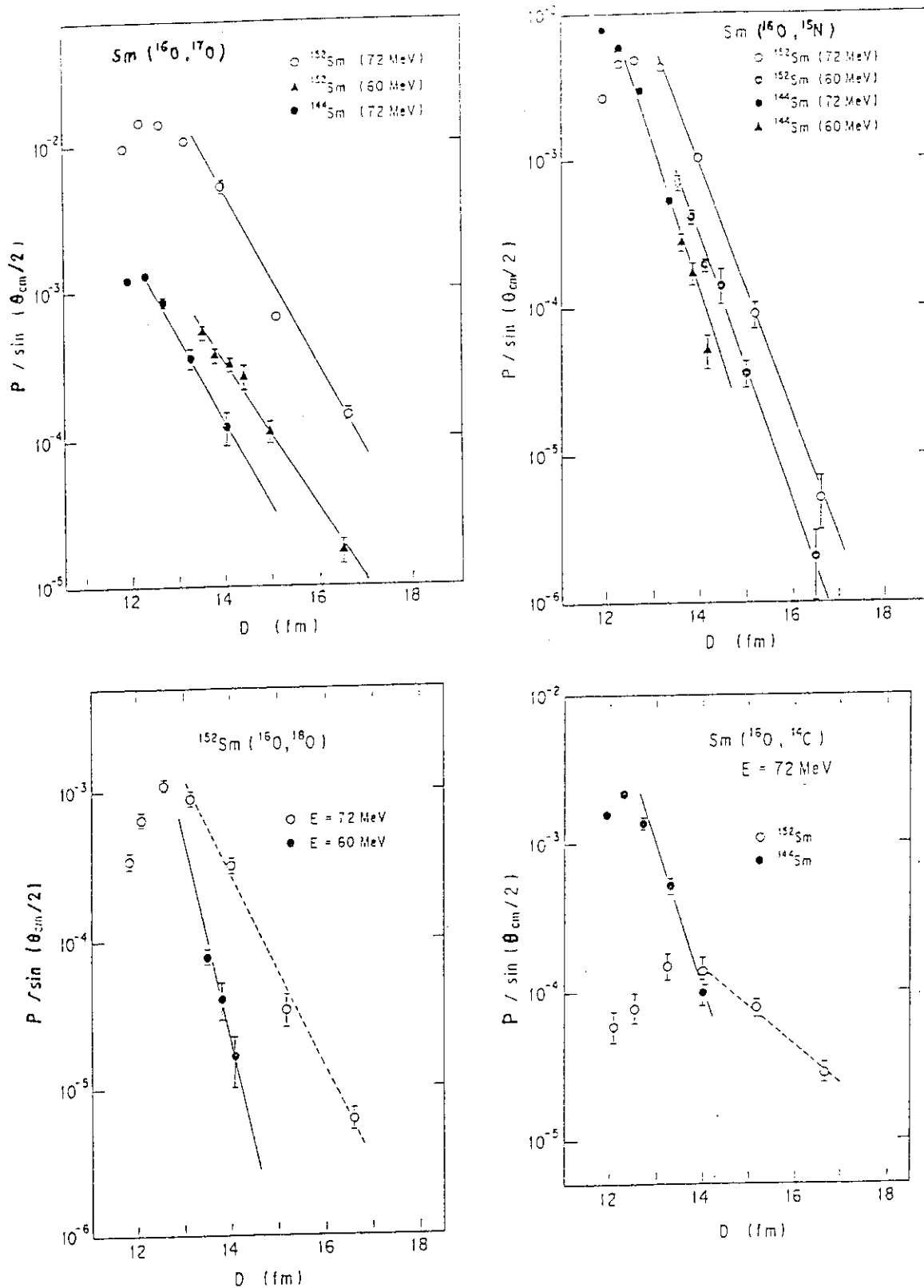


Fig. 1 Transfer probabilities of $P/\sin(\theta_{cm}/2)$ as a function of the distance of closest approach D for the one- and two- nucleon transfer reactions. The solid lines are results from DWBA or semi-classical model calculations. The dashed lines are for guiding the eyes.

5.2 INELASTIC SCATTERING OF ^{19}F ON ^{28}Si

Hiroshi FUJITA, Norihisa KATO*, Tsuyoshi SUGIMITSU*,
 Yoshinori FUNATSU*, Takumi OKAMOTO*, Shunji NIIYA*, Yasuharu
 SUGIYAMA**, Hiroshi IKEZOE**, Yoshiaki TOMITA**, Kazumi
 IDENO**, Shigeru KUBONO***

Daiichi College of Pharm. Sci., *Department of Physics,
 Kyushu University, **Department of Physics, JAERI, ***INS

Inelastic scattering of heavy ions on even-mass nuclei has been studied extensively. However, few studies of inelastic scattering of heavy ions on odd-mass nuclei have been done because of problems with experimental energy resolution. Previously we have studied elastic and inelastic scattering for $^{19}\text{F}+^{12}\text{C}$, ^{16}O systems and found that the structure of ^{19}F , lower positive parity states of which have a cluster structure of $t+^{16}\text{O}$ configuration, affects markedly the phase relation of the angular distributions of the elastic and inelastic scattering cross sections¹⁾.

In the present work, we studied the elastic and inelastic scattering for $^{19}\text{F}+^{28}\text{Si}$ system. This system is interesting because a strong spin-orbit force was suggested to explain the triton transfer reactions. The experiment was performed by using 120 and 155MeV ^{19}F beams from the JAERI tandem accelerator. The ejectiles were analyzed by using the heavy ion magnetic spectrograph "ENMA". The angular distributions of the inelastic scattering to the $1/2^+$ (g.s.), $5/2^+$ (0.197MeV) and $3/2^+$ (1.554MeV) states in

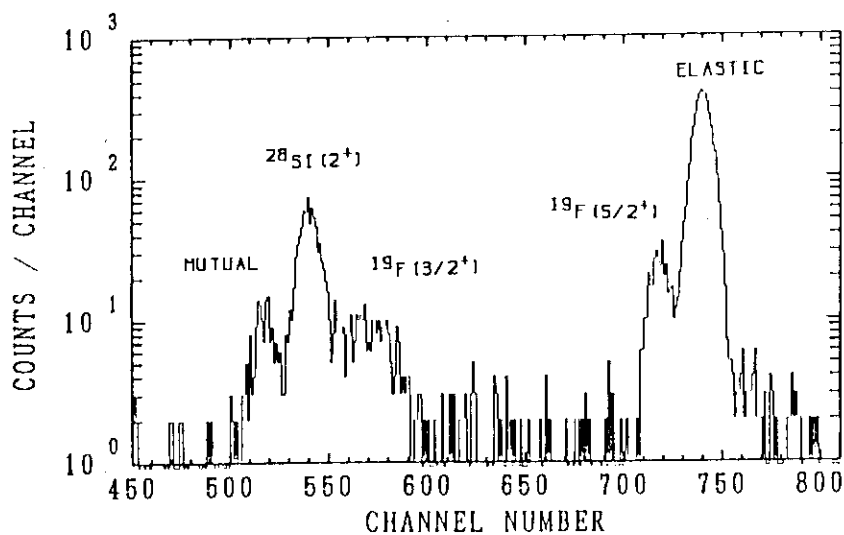


Fig.1 ^{19}F
 spectrum from
 the scattering
 of ^{19}F on ^{28}Si
 at $E_{\text{I}}=120\text{MeV}$ and
 $16\text{deg}(\text{lab})$.

^{19}F , the $2^+(1.780\text{MeV})$ state in ^{28}Si and the mutually excited ($5/2^+, 2^+$) state in both nuclei were obtained. For the measurement at the bombarding energy of 120MeV , a $12\mu\text{g}/\text{cm}^2$ ^{28}Si target (on $10\mu\text{g}/\text{cm}^2$ C backing) was used and the energy spectra with good energy resolution were obtained. A typical spectrum is shown in fig.1. However, at the bombarding energy of 155MeV , the peaks of the mutually excited state were not resolved sufficiently from the peaks of the 2^+ state in ^{28}Si because a $30\mu\text{g}/\text{cm}^2$ ^{28}Si target (on $10\mu\text{g}/\text{cm}^2$ C backing) was used.

Fig.2 shows the angular distributions of the inelastic scattering to the $5/2^+$ state in ^{19}F , the 2^+ state in ^{28}Si and the mutually excited state.

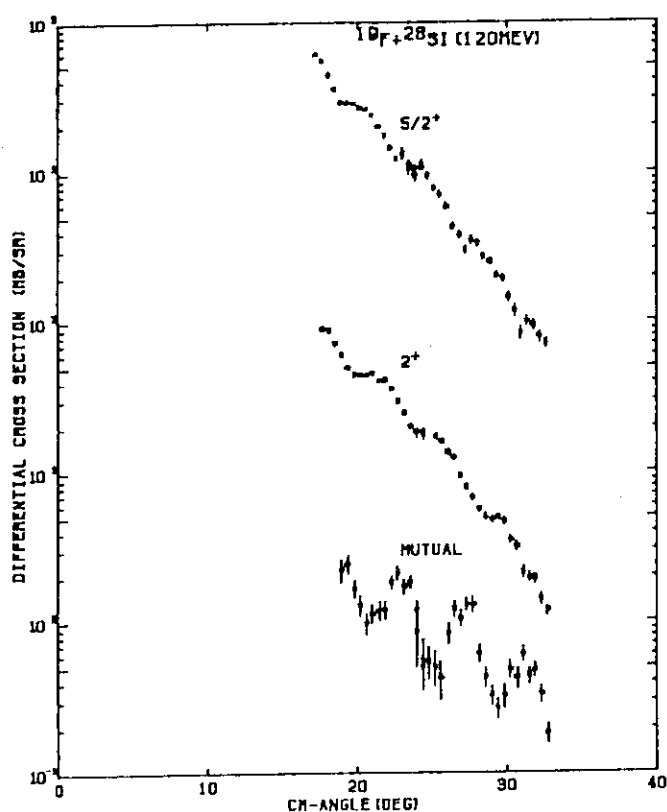


Fig.2 The angular distributions of the inelastic scattering to the $5/2^+$ state in ^{19}F , the 2^+ state in ^{28}Si and the mutually excited state

Oscillatory structures appear in each angular distribution. Preliminary results of the DWBA and CC calculations reproduce well the experimental result in the 2^+ state of ^{28}Si . For the $5/2^+$ state in ^{19}F , preliminary results reproduce also fairly well and the pronounced shift such as observed for $^{19}\text{F}+^{12}\text{C}$, ^{16}O systems was not observed between the calculated angular distribution and experimental one. Further analysis, e.g. the CC calculation including the mutual excitation, is in progress.

Reference

- 1) H. Fujita, N. Kato, T. Sugimitsu and Y. Sugiyama, Proceeding of the Heavy-Ion Reaction Dynamics in Tandem Energy Region, 1988, Hitachi, eds. by Y. Sugiyama et al. (Universal Academy Press, 1989) p.157.

5.3 MEASUREMENT OF ${}^8\text{Be}_{\text{g.s.}}$ - α DECAYS FROM ${}^{12}\text{C}$ NUCLEI
IN THE ${}^{16}\text{O} + {}^{60}\text{Ni}$ REACTION AT 90 MEV

Kazumi IDENO, Yoshiaki TOMITA, Yasuharu SUGIYAMA,
Hiroshi IKEZOE, Susumu HANASHIMA and Yuichiro NAGAME*

Department of Physics, *Department of Radioisotopes, JAERI

For the ${}^{12}\text{C}$ levels above the threshold of 3α decays, alpha decays via ${}^8\text{Be}$ nuclei occupy an important part¹⁻³⁾. In the heavy ion reactions, owing to the difficulties of direct measurement of 3α correlations, experimental information about the 3α decays is not sufficient. Our present concern is to study the effect of multi-nucleon transfer reactions on the excitation of the ${}^{12}\text{C}$ levels which are expected to be the clustering states of ${}^8\text{Be}_{\text{g.s.}}$ - α nuclei⁴⁻⁶⁾. For this purpose we chose the ${}^{16}\text{O} + {}^{60}\text{Ni}$ reaction at 90 MeV. We have constructed a detection system for the correlation measurement of closely-spaced three α particles emitted from ${}^{12}\text{C}$ nuclei; we modified our ${}^8\text{Be}$ detection system⁷⁾ and incorporated into a gas chamber four units which were comprised of drift chambers and large-area solid state detectors. Each of these units works independently as a 2-dimensional position-sensitive detector. Any combination of two neighboring units can identify 2α particles from a ${}^8\text{Be}_{\text{g.s.}}$ nucleus and one of the other units can detect an α particle in coincidence. From the space-energy correlation between the ${}^8\text{Be}$ and α particles, we can identify the ${}^{12}\text{C}$ excited levels. Using this system, we observed the ${}^8\text{Be}_{\text{g.s.}}$ - α decays from the ${}^{12}\text{C}$ levels in the ${}^{16}\text{O} + {}^{60}\text{Ni}$ reaction. The detecting angle was set around $\theta_{\text{lab}} = 30$ degrees. Fig. 1 shows a plot of relative energy between the ${}^8\text{Be}_{\text{g.s.}}$ and α particles. The detecting system covered a relative angle of about 20 degrees between the ${}^8\text{Be}_{\text{g.s.}}$ and α particles. Considering the observed average energy of α particles, the counting efficiency decreases rapidly above the ${}^{12}\text{C}$ excitation energy of 9 MeV. This is the reason that only one dominant peak at the 7.65 MeV level was observed. To extend the observation to higher excitations, it is necessary to cover a wider relative angle between α particles.

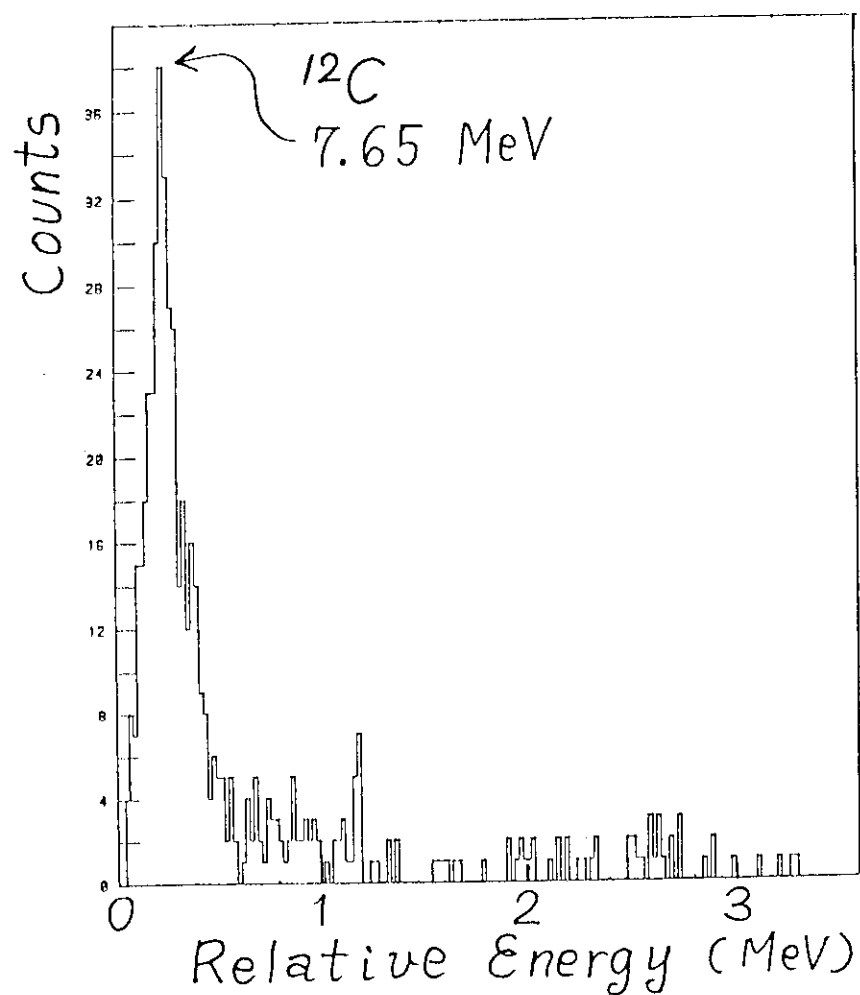


Fig. 1 Relative energy between ${}^8\text{Be}_{\text{g.s.}}$ and α particles.

References

- 1) W. C. Olsen et al.: Nucl. Phys. 61 (1965) 625.
- 2) C. Jacquot et al.: Nucl. Phys. A201 (1973) 247.
- 3) B. Antolkovic et al.: Nucl. Phys. A394 (1983) 87.
- 4) H. Morinaga: Phys. Lett. 21 (1966) 78.
- 5) E. Uegaki et al.: Prog. Theor. Phys. 59 (1978) 1031.
- 6) M. Kamimura: Nucl. Phys. A351 (1981) 456.
- 7) K. Ideno et al.: JAERI-M 88-181 (1988) 146.

5.4 PRE-SCISSION ^4He MULTIPLICITY IN THE $^{19}\text{F} + ^{197}\text{Au}$ REACTION

Hiroshi IKEZOE, Naomoto SHIKAZONO, Yuichiro NAGAME, Yasuharu SUGIYAMA, Yoshiaki TOMITA, Kazumi IDENO, Akira IWAMOTO and Tsutomu OHTSUKI*

Department of Physics, JAERI, * Department of Chemistry,
Faculty of Science, Tokyo Metropolitan University

Pre- and post-scission ^4He particle multiplicities for the $^{19}\text{F} + ^{197}\text{Au}$ reaction have been measured in coincidence with fission fragments. The experiment was performed at the JAERI tandem accelerator. A self-supported ^{197}Au target of a thickness of 1.2 mg/cm^2 was bombarded with ^{19}F beams with beam energies from 92 to 161 MeV. The lowest bombarding energy was just above the Coulomb barrier for the $^{19}\text{F} + ^{197}\text{Au}$ system. Fission fragments were measured by two solid state detectors ($60 \mu\text{m}$, 400 mm^2), which were set up at $\theta_f = 105^\circ$ and 125° with respect to the beam, respectively. Light particles (^4He and protons) were measured by three sets of solid state detector telescopes ($30 \mu\text{m}$ and $2000 \mu\text{m}$) positioned at inplane ($\phi = 90^\circ$) and out-of-plane angles ($\phi = 30^\circ$ and 60°). These telescopes were set at inplane negative angles ($\theta_{\text{lab}} = -135^\circ$ and -145°).

The energy spectra of ^4He measured in coincidence with the fission fragments are shown in Fig. 1. The dashed and the dash-dotted lines represent the calculated energy spectra corresponding to the emissions from the compound nucleus (CE) and fission fragments (FE), respectively. The ^4He energy spectra from CE and FE were calculated by the statistical model code PACE2¹⁾. The transmission coefficients of ^4He for FE were calculated using the optical model potential²⁾. The ^4He energy spectrum for CE at each bombarding energy was calculated by assuming an effective emission barrier for ^4He , where the transmission coefficients of ^4He for CE were shifted toward lower energies by 2 MeV. The calculated spectra (CE and FE) were obtained by transforming the calculated center-of-mass kinetic energy spectra to the laboratory frame. The observed coincidence energy spectra of ^4He are well reproduced by the calculated two components (FE and CE).

The mean center-of-mass kinetic energies $\langle \epsilon \rangle$ for CE measured inplane are plotted as a function of excitation energy in Fig. 2. The observed $\langle \epsilon \rangle$ is well reproduced by the calculation (solid line), where the transmission coefficient for ^4He was shifted toward lower energies by 2 MeV. The dashed line shows the calculated result without shifting the transmission coefficient toward lower energies. From the present results we confirmed that the effective emission

barrier for ${}^4\text{He}$ was lower by 2 MeV than the corresponding absorption barrier.

The observed pre-scission and post-scission multiplicities of ${}^4\text{He}$ are listed in Table I as $M\alpha(\text{CE})$ and $M\alpha(\text{FE})$, respectively. The observed values of $M\alpha(\text{CE})$ were compared to the results of the statistical model calculation. It was found that the calculated $M\alpha(\text{CE})$ depended sensitively on the effective emission barrier of ${}^4\text{He}$ and the reduction of 2 MeV of the effective emission barrier was consistent with the data of $M\alpha(\text{CE})$.

References

- 1) A. Gavron, Phys. Rev. C21 (1980) 230
- 2) J. R. Huizenga and G. Igo, Nucl. Phys. 29 (1962) 462

Table I Pre- and post-scission multiplicities of ${}^4\text{He}$ as a function of the bombarding energy.

E_{lab} (MeV)	U (MeV)	$M\alpha(\text{CE})$	$M\alpha(\text{FE})$
92	43.4	0.014 ± 0.003	0.008 ± 0.002
99	50.0	0.019 ± 0.004	0.009 ± 0.002
101.8	52.3	0.017 ± 0.003	0.008 ± 0.002
106.1	56.2	0.025 ± 0.005	0.010 ± 0.002
108.9	58.8	0.021 ± 0.004	0.011 ± 0.002
114.2	63.6	0.026 ± 0.005	0.012 ± 0.002
118.9	67.9	0.026 ± 0.005	0.013 ± 0.003
124.9	73.4	0.035 ± 0.006	0.015 ± 0.003
131.0	78.9	0.047 ± 0.007	0.019 ± 0.003
137.0	84.4	0.054 ± 0.010	0.018 ± 0.004
143.0	89.9	0.066 ± 0.010	0.020 ± 0.004

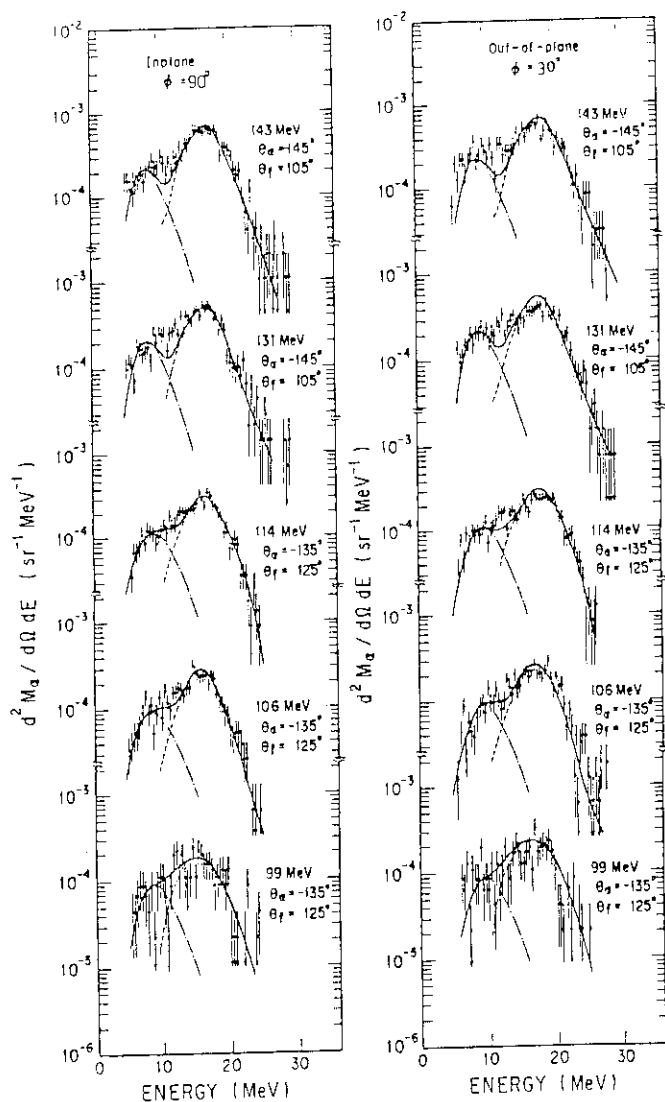


Fig.1 Energy spectra of ^4He in coincidence with the fission fragments at the various bombarding energies. The fission fragment and ^4He were detected at θ_f and θ_{lab} , respectively. The dashed and the dash-dotted lines represent the calculated spectra corresponding to the emission sources of CE and FE, respectively. The solid lines show the sum of the two components. The out-of-plane angle ϕ is defined as an angle between the normal to the reaction plane and the emission direction of ^4He .

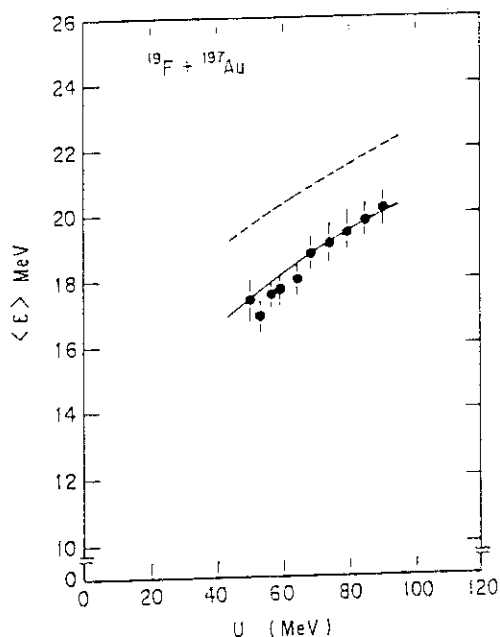


Fig.2 Mean center-of-mass kinetic energy of CE as a function of excitation energy U of the compound nucleus. The solid and the dashed lines indicate the calculated results by assuming the 2 MeV reduced barrier and the normal emission barrier for ^4He , respectively.

5.5 PRODUCTION MECHANISM OF FISSION-LIKE FRAGMENTS IN THE REACTIONS OF $^{37}\text{Cl}+^{64}\text{Ni}$, $E_{\text{Lab}}=170,186$ MeV

Yuehu PU, Sang Moo LEE, Sung Chang JEONG,
Hideaki FUJIWARA, Takeshi MIZOTA, Yasushi FUTAMI,
Takahide NAKAGAWA*, Yuichiro NAGAME**, and Hiroshi IKEZOE**

Department of Physics, University of Tsukuba, *RIKEN, **JAERI

Fission-like fragments have been observed in heavy ion collisions between ions of medium masses¹⁻⁵). The production mechanism of these fission-like fragments, which resemble fission fragments in both kinetic energies and angular distributions but exhibit a much wider mass distribution, still remain unresolved. In order to shed some light on this problem, we have performed an experiment on the $^{37}\text{Cl}+^{64}\text{Ni}$ system. We have chosen this system to compare the Z-distribution of fission-like fragments of this system with that of another similar system, $^{35}\text{Cl}+^{62}\text{Ni}$, which has been extensively studied by Bisplinghoff et al.¹⁻²). If a compound nucleus process is responsible for the broad Z-distributions observed by Bisplinghoff et al., there may be strong exit channel Q_{gg} effect on the final Z-distribution. Because decays toward symmetric channels from compound nucleus ^{101}Rh have deeper Q-values relative to asymmetric ones, a more symmetric Z-distribution for the $^{37}\text{Cl}+^{64}\text{Ni}$ system than Bisplinghoff's results²) could be expected⁷). A study of the present system also permits us to compare our data to those obtained with $^{12}\text{C}+^{89}\text{Y}$ system, at $E_{\text{lab}}=197$ MeV⁴), which forms the same compound nucleus.

The experiment was carried out by using JAERI's 20 MV Tandem Accelerator. A multi-window ionization chamber ($\Delta E(\text{gas})\text{-E}(\text{SSD})$) was used for the atomic number and angular distribution measurements of the fission-like fragments. A small gas counter telescope was also employed to measure the evaporation residues and elastic scattering at forward angles. Fig.1 shows an example of the 2-dimensional PI-E spectra ($\text{PI} \propto \text{AZ}^2$). Assuming a binary

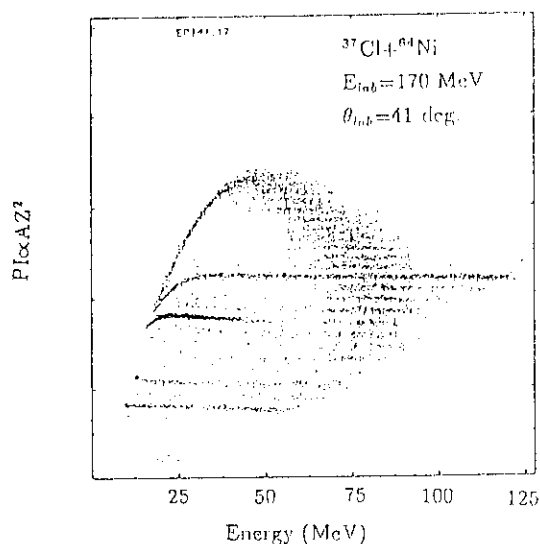


Fig.1 2-D spectrum of PI and total energy E, measured with gas counter.

process, we have calculated the mean experimental Q-values of each out-going channel and the result suggests a fully-damped mechanism. The angular distributions of these fully-damped fragments are found to have a $1/\sin\theta$ component, indicating a long life time of the intermediate composite system. The angular and energy integrated Z-distributions of fission-like fragments are shown in Fig.2 for both incident energies.

As can be seen in Fig.2, very broad Z-distributions have been obtained

which have nearly the same width as those obtained for $^{35}\text{Cl}+^{62}\text{Ni}$ system at almost the same incident energies. Therefore we conclude that the exit channel Q-values have no significant effects on the production of fission-like fragments in the reactions of Cl+Ni. In addition, a very narrow Z-distribution (FWHM \approx 6) have been observed with the system of $^{12}\text{C}+^{89}\text{Y}$ ⁴⁾ which can be explained by the symmetric fission of compound nucleus ^{101}Rh ⁶⁾. The different Z-distributions observed in the $^{37}\text{Cl}+^{64}\text{Ni}$ and $^{12}\text{C}+^{89}\text{Y}$ systems may be due either to dynamic effects involving the former system or/and to a difference in their angular momentum populations of the same compound nucleus. Therefore, further experimental study is necessary in order to find out which explanation is correct. If dynamic processes play a dominant role in the Cl+Ni system there may exist significant entrance channel effect on the Z-distribution, for instance, a study of Al+Ge system may show an even more asymmetric Z-distribution.

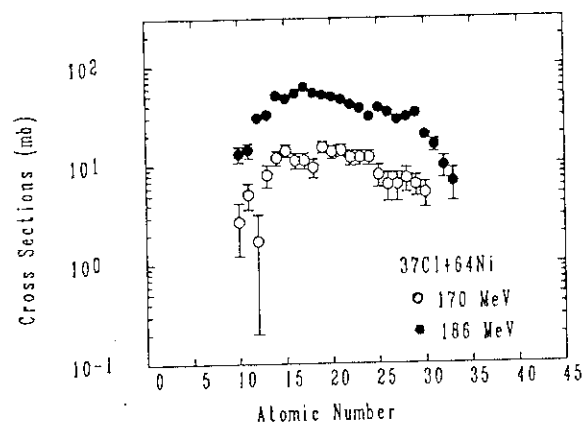


Fig.2 Angle and energy integrated Z-distributions of Fission-like fragments obtained at two lab energies.

References

- 1) B. Sikora et al.: Phys. Rev. C25(1982)1446.
- 2) J. Bisplinghoff et al.: Phys. Rev. C17(1978)177.
- 3) H. Oeschler et al.: Phys. Lett. B87(1979)193.
- 4) J.B. Natowitz et al.: Phys. Rev. C13(1976)171.
- 5) W. Yokota et al.: Z.Phys. A333(1989)379.
- 6) H. Oeschler and H. Freiesleben: Fusion-fission Type Collisions, Lecture Notes in Physics, 117(1980)113.
- 7) S.M. Lee, W. Yokota, and T. Matsuse: Proc. of the Symposium on "The Many Facets of Heavy-Ion Fusion Reactions"(Argonne 1986)p63.

5.6 A STUDY OF FISSION-LIKE REACTIONS WITH THE SYSTEM OF $^{28}\text{Si}+^{74}\text{Ge}$ AT $E_{lab}=176$ MeV

Yuehu PU, Sang Moo LEE, Sung Chang JEONG,
Hideaki FUJIWARA, Takeshi MIZOTA, Yasushi FUTAMI,
Takahide NAKAGAWA*, Yuichiro NAGAME**, and Hiroshi IKEZOE**

Department of Physics, University of Tsukuba, *RIKEN, **JAERI

As a continuation of the experimental study of $^{37}\text{Cl}+^{64}\text{Ni}$ system¹⁾, fission-like fragments²⁻⁴⁾ produced in the reactions of $^{28}\text{Si}+^{74}\text{Ge}$ at $E_{lab}=176$ MeV have been measured. The experiment was performed by using JAERI's 20 MV Tandem accelerator facility. The experimental set-up was identical to that employed in the previous $^{37}\text{Cl}+^{64}\text{Ni}$ experiment. A carbon backing $^{74}\text{GeO}_2$ ($400\mu\text{g}/\text{cm}^2$) target was bombarded with 176 MeV ^{28}Si beams. Gas counter telescopes were used to give the atomic number, energy, and angular information of the fission-like fragments. A run with a thick carbon target ($70\mu\text{g}/\text{cm}^2$) was also performed to check the behavior of reaction products from the carbon backing and oxygen contained in the target. Evaporation residues and elastic scattering were also measured.

From the accumulated data, angular distributions and energy distributions were deduced. The result indicates a dominant reaction mechanism with full damping of both kinetic energies and angular distributions. The integrated Z-distribution is presented in Fig.1 together with the previous result for $^{37}\text{Cl}+^{64}\text{Ni}$ system. The two reactions give quite similar Z-distributions but a concentration of yield around the projectile fragment is obvious in both cases. Therefore, we conclude that the productions of fission-like fragments in these two reactions are dominated by dynamic process with certain memory of the entrance channel retained despite the full relaxation in kinetic energy and angular distribution.

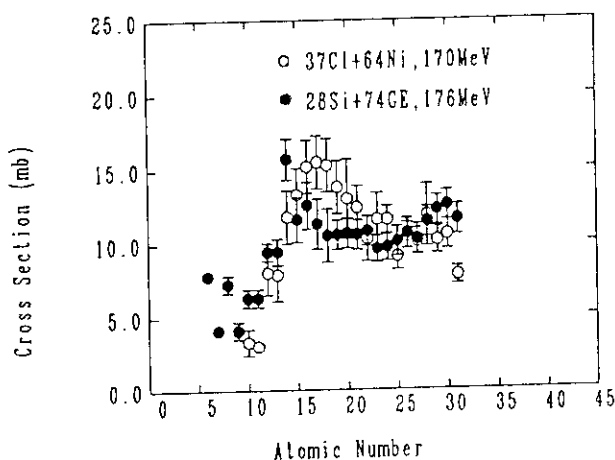


Fig.1 Z-distributions of fission-like fragments produced in reactions of two systems.

References

- 1) Y.H. Pu et al.: in this Annual Report.
- 2) B. Sikora et al.: Phys. Rev. C25(1982)1446.
- 3) H. Oeschler et al.: Phys. Lett. B87(1979)193.
- 4) H. Oeschler and H. Freiesleben: Fusion-fission Type Collisions,
Lecture Notes in Physics, 117(1980)113.

5.7 ROTATIONAL PERTURBATION IN THE $K=3/2^-$ BAND OF ^{155}Gd

Hideshige KUSAKARI*, Masumi OSHIMA, Masahiko SUGAWARA**,
 Shin-ichi ICHIKAWA***, Hideki IIMURA***, Takashi INAMURA****,
 Akira HASHIZUME****, Akiko UCHIKURA* and Ariyoshi TOMOTANI*

Department of Physics, JAERI, *Faculty of Education, Chiba
 University, **Chiba Institute of Technology, ***Department
 of Chemistry, JAERI, ****RIKEN

The ground-state rotational band of ^{155}Gd is based on the Nilsson orbit [521 3/2]. The signature dependence of $B(M1)$ in such a natural-parity band is very interesting, because it is expected to be different from that in unique-parity bands¹⁾. The neutron number of ^{155}Gd is 91, and the rotational band of this nucleus is expected to get strong effects of rotational perturbation. In the $K=3/2^-$ band of ^{155}Gd , members up to the $13/2^-$ 553 keV level were established²⁾.

In the present investigation the target nucleus ^{155}Gd was multiply Coulomb excited. This experiment was done using a beam of 250-MeV ^{58}Ni from the tandem accelerator at JAERI. The metallic ^{155}Gd foil was bombarded with this beam. In the gamma-gamma coincidence measurement, three anti-Compton spectrometers were used. Levels up to the one at 1322 keV were observed as shown in fig. 1. Angular distributions of gamma-rays were measured at seven angles between 0° and 90° to the beam direction. The angular distributions were fitted with Legendre polynomials. The derived coefficients A_2 and A_4 are presented in tables 1 and 2. Spin-parity assignments for observed transitions have been done as presented in Tables 1 and 2. Characteristic zigzag in the energy $E(I \rightarrow I-1)$ is seen in fig. 2. The $dI=1$ cascade transitions in the ground band of ^{155}Gd have large $M1$ components ($> 90\%$) as shown in Table 2. We can calculate the ratio of $B(M1; dI=1)/B(E2; dI=2)$ using the branching ratio and the mixing ratio. Lifetimes of the ground-band levels in ^{155}Gd were also measured by means of the recoil distance method. In order to get the absolute values of $B(M1)$ and $B(E2)$, analysis is in progress.

References

- 1) M. Matuzaki, Phys. Rev. C39 (1989) p.691
- 2) C.M. Lederer and V.S. Shirley, Table of Isotopes (7th ed.), 1978.

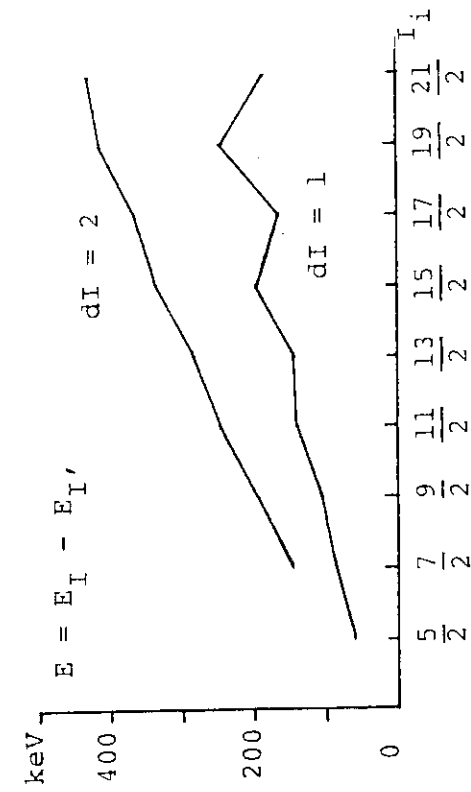


Fig. 2 The transition energies of $E_{dI=1}$ and $E_{dI=2}$ vs. spin values I_i in ^{155}Gd .

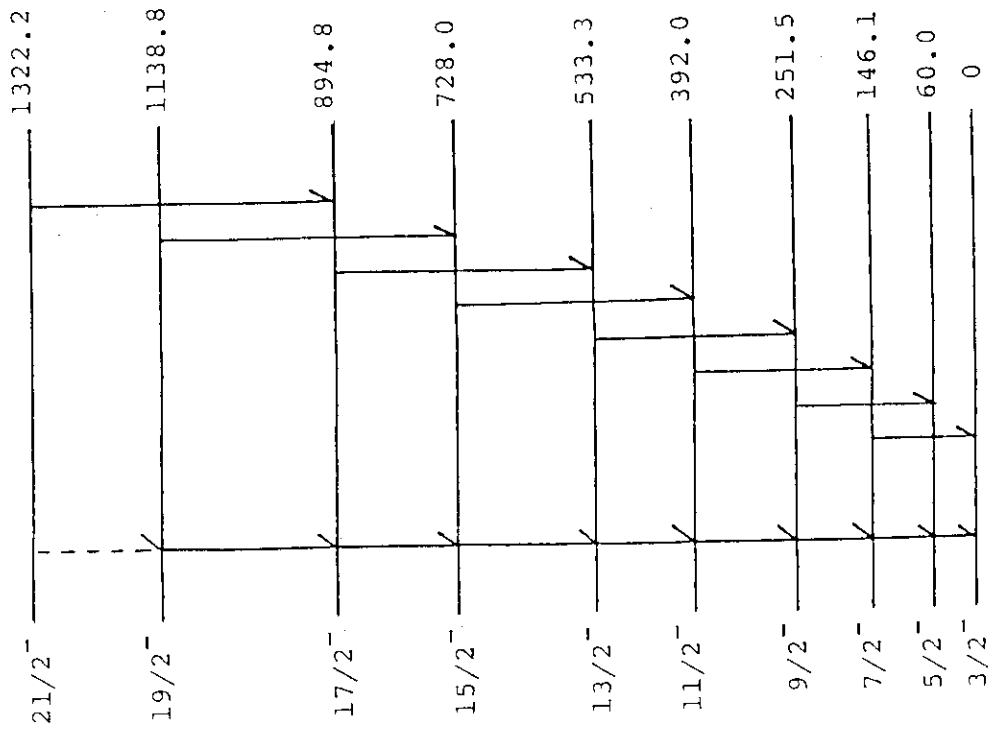


Fig. 1 The level scheme of ^{155}Gd . The $K=3/2^-$ band only is shown.

Table 1 Spin-parity assignments, relative intensities of γ -rays (I_G), coefficients of angular distributions (A_2 , A_4) and attenuation factors of alignment (α_2) for $dI=2$ transitions in ^{155}Gd . Errors are shown in parentheses.

E_G (keV)	$I_i \rightarrow I_f$	I_G	A_2	A_4	α_2
146.1(1)	$7/2^- \rightarrow 3/2^-$	1309(159)	0.007(22)	-0.005(27)	0.013(43)
191.5(2)	$9/2^- \rightarrow 5/2^-$	10000(108)	0.102(19)	-0.019(24)	0.214(41)
245.8(3)	$11/2^- \rightarrow 7/2^-$	8875(95)	0.125(19)	-0.010(24)	0.276(42)
281.8(3)	$13/2^- \rightarrow 9/2^-$	4512(78)	0.121(19)	-0.002(24)	0.274(43)
336.0(3)	$15/2^- \rightarrow 11/2^-$	2488(26)	0.108(19)	0.008(24)	0.251(44)
361.4(3)	$17/2^- \rightarrow 13/2^-$	1168(13)	0.114(20)	0.002(24)	0.271(46)
410.7(4)	$19/2^- \rightarrow 15/2^-$	398(6)	0.111(23)	-0.010(29)	0.269(56)
427.4(4)	$21/2^- \rightarrow 17/2^-$	155(4)	0.112(39)	0.027(49)	0.275(95)

Table 2 Spin-parity assignments, relative intensities of γ -rays (I_G), coefficients of angular distributions (A_2 , A_4) and mixing ratios (δ) for $dI=1$ transitions in ^{155}Gd .

E_G (keV)	$I_i \rightarrow I_f$	I_G	A_2	A_4	δ
60.0(1)	$5/2^- \rightarrow 3/2^-$		-0.099(55)	0.133(55)	0.18
86.1(1)	$7/2^- \rightarrow 5/2^-$	42334(766)	-0.044(33)	0.000(39)	0.10
105.4(2)	$9/2^- \rightarrow 7/2^-$	11704(173)	-0.160(27)	0.006(31)	-0.22
140.6(3)	$11/2^- \rightarrow 9/2^-$	4423(62)	-0.221(25)	-0.013(28)	-0.32
141.5(5)	$13/2^- \rightarrow 11/2^-$	1141(22)	-0.150(35)	-0.024(40)	-0.14
194.8(2)	$15/2^- \rightarrow 13/2^-$	753(9)	-0.164(20)	0.025(23)	-0.13
167.0(3)	$17/2^- \rightarrow 15/2^-$	131(7)	-0.313(93)	-0.008(114)	-0.6

5.8 LIFETIME MEASUREMENTS OF THE FIRST 2^+ STATES IN
 $^{124,126}\text{Ba}$

Masumi OSHIMA, Toshiaki SEKINE,^{*} Tsuneyasu MORIKAWA,^{*}
 Yuichi HATSUKAWA,^{*} Shin-ichi ICHIKAWA,^{**} Hideki
 IIMURA,^{**} and Michihiro SHIBATA^{***}

Department of Physics,^{*} Department of Radioisotopes,
^{**} Department of Chemistry, JAERI, and ^{***} Department of
 engineering, Nagoya University

The β - γ and γ - γ delayed coincidence technique has been most widely used in measuring lifetimes of nuclear excited states lying between ns and ms. If the lifetime is larger than the timing resolution of the system, the slope or convolution analysis become available which allows the most reliable determination of the lifetimes. Thus, good timing characteristics are essential in this technique. Recently discovered fast component^{1,2} in light emission in BaF_2 scintillators opened the possibility to access down to 10-ps lifetimes. At the neutron deficient side of nuclei many lifetimes have been measured by means of the recoil distance Doppler shift method by exploiting the large recoil velocity produced in heavy-ion induced fusion-evaporation reactions. The determination of lifetimes by this method, however, is not straightforward: it requires numerous and rather delicate corrections. This sometimes causes large uncertainty of the lifetimes, especially for long lifetimes (≈ 100 ps). The β - γ delayed coincidence technique will provide complementary data in this region of lifetimes.

We used plastic (Pilot-U) and BaF_2 scintillators for the detection of β and γ rays. The sizes of the plastic and BaF_2 are $2''\phi \times 2$ mm^t and $1''\phi \times 6$ mm^t, respectively. The scintillators are coupled to Hamamatsu H2431 and H3177 photomultiplier assemblies. We used Ortec 583 CFDD and Ortec 467 TPHC/SCA modules in the conventional fast timing setup. Typical timing resolution for gated prompt transitions was 130 ps FWHM at $E_\gamma = 1.3$ MeV using ^{60}Co radioactive source.

The on-line experiments were carried out at the JAERI tandem accelerator. The ^{nat}Mo target was bombarded with a 170-MeV ^{35}Cl beam. The ^{126}La and ^{124}La activities were mass-separated by the on-line isotope separator. Figure 1 shows the time spectra obtained from the β decay of the ^{126}La and ^{124}La . The slope of the

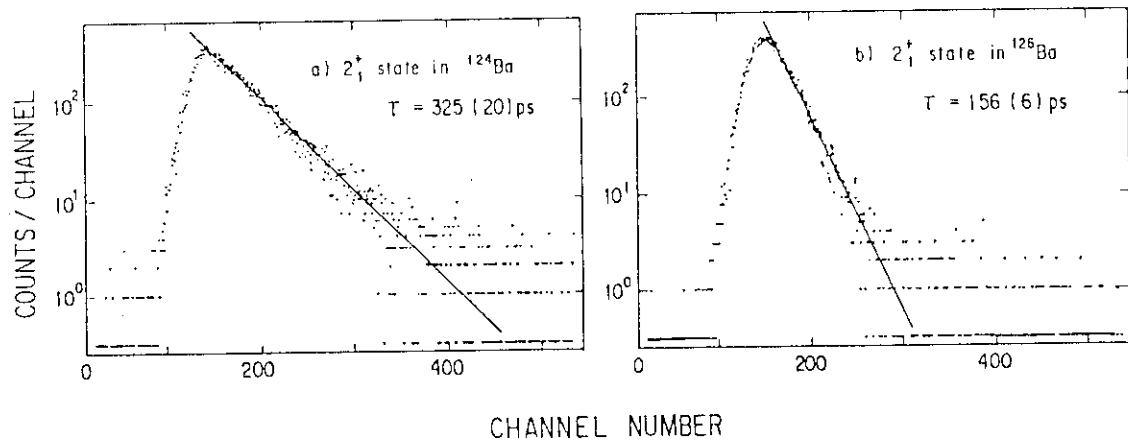


Fig. 1. Time spectra of (a) ^{124}Ba and (b) ^{126}Ba .

delayed side of the time distribution peak was analyzed by the least square fitting to give the lifetimes of $\tau = 325 \pm 20$ and 156 ± 6 ps for the first 2^+ states in ^{124}Ba and ^{126}Ba , respectively. The $B(E2; 0^+ \rightarrow 2^+)$ value of ^{124}Ba is deduced to be $1.26 \pm 0.08 e^2 b^2$. The $B(E2; 0^+ \rightarrow 2^+)$ value of ^{126}Ba is $1.53 \pm 0.06 e^2 b^2$, significantly smaller than the previously reported value, $1.84 \pm 0.20 e^2 b^2$ (Ref. 3.). An interesting result is that, while the excitation energy of the first 2^+ state decreases as going from ^{126}Ba to ^{124}Ba , indicating that ^{124}Ba has more collective character than ^{126}Ba does, the $B(E2)$ value for ^{124}Ba is smaller than for ^{126}Ba . We will pursue this intriguing problem with further analyses and systematic measurements of $B(E2)$ values in this mass region.

References:

- 1) M.Laval et al., Nucl. Instrum. Methods 206, 169 (1983).
- 2) M.Moszyzinski and H.Mach, Nucl. Instrum. Methods A277, 407 (1989).
- 3) G.Seiler et al., Phys. Lett. 80B, 345 (1979).

5.9 COULOMB EXCITATION OF THE UNSTABLE NUCLEUS ^{76}Kr

Masumi OSHIMA, Yasuyuki GONO^{*}, Hideshige KUSAKARI,^{**}
 Masahiko SUGAWARA^{***} and Ken MURAKAMI^{****}

Department of Physics, JAERI, ^{*}RIKEN, Wako-shi, Saitama 351-01,
^{**}Faculty of Education, Chiba University, Yayoi-cho, Chiba 260,
^{***}Chiba Institute of Technology, Shibazono, Narashino, Chiba 275, and
^{****}Tokyo Institute of Technology, Ookayama, Meguro-ku, Tokyo.

The Coulomb excitation (COULEX) is a powerful method for the nuclear structure study. One of the serious limitation of this method was that this technique could be applied only for the stable nuclei. However, the progress of the heavy-ion accelerators with respect to the beam energies and intensities opened the possibility to extend the application of this technique to the unstable nuclei. We have made a test experiment of COULEX of the unstable nucleus ^{76}Kr .

Since this was the first trial of this kind of experiment, we have chosen ^{76}Kr as the secondary beam to be used for COULEX so that the γ -ray yield could be estimated based on the known half-life (37 ps in Ref. 1) of the first excited 2^+ state of this nucleus. Experimental setup used is shown in Fig. 1. The secondary beam of ^{76}Kr was produced under the following conditions:

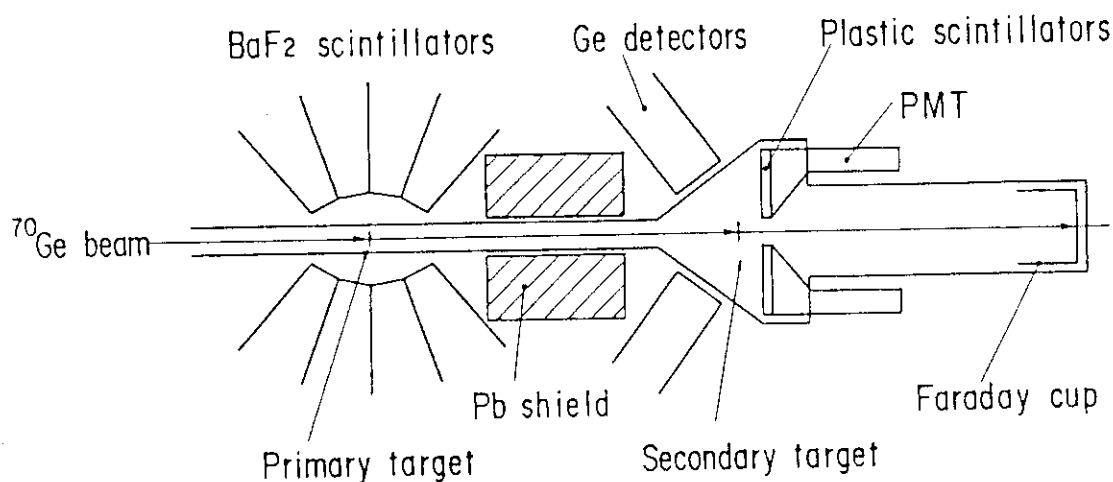


Fig. 1 Experimental setup of the secondary beam COULEX experiment.

- 1) The reaction used for the production of ^{76}Kr was $^9\text{Be}(^{70}\text{Ge}, 3n)^{76}\text{Kr}$.
- 2) The ^9Be target was a self-supporting metallic foil of 1 mg/cm^2 .
- 3) The 310-MeV ^{70}Ge beam was used which was delivered by the JAERI tandem accelerator.
- 4) The beam intensity used was 1 pA (6×10^9 particles/s).

With these conditions, the kinetic energy of the ^{76}Kr secondary beam was estimated to be 185 ± 21 MeV. The energy spread mostly stems from the energy loss of ^{76}Kr in the finite thickness of the ^9Be target. The secondary beam intensity was estimated to be about 10^5 s^{-1} using the reaction cross section of $\approx 300\text{ mb}$ which was obtained by the ALICE code calculation.

The enriched ^{208}Pb target of 2 mg/cm^2 was used for the COULEX of ^{76}Kr beam. The scattered ^{76}Kr were detected by the annular plastic scintillator of 0.2 mm thick which was divided to 4 sectors so that the Doppler shift of γ rays could be corrected depending on the scattered angles with respect to Ge detectors.

The primary target ^9Be was surrounded by 19 BaF_2 scintillators which detected primary γ rays from the reaction. The reaction products were selected by the time-of-flight (TOF) between the ^9Be target and the plastic scintillator. The distance between the target and the plastic scintillator was 56 cm. The γ rays from the

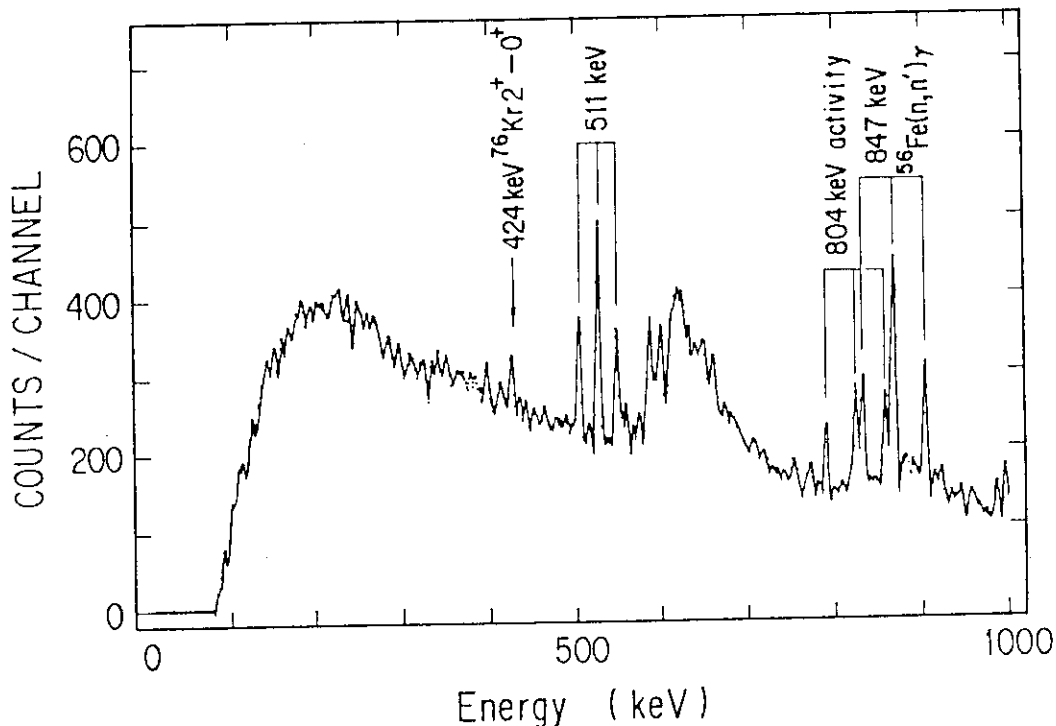


Fig. 2 The coincidence γ -ray spectrum of the secondary beam COULEX.

COULEX of ^{76}Kr beam were detected by four Ge's of 30 % efficiency in coincidence with the above mentioned TOF. These Ge's were shielded from the γ rays of the primary reactions by 20 cm thick lead which reduced the γ -ray background by factors 10^{-8} and 10^{-5} for 1 and 2 MeV γ rays.

Using this experimental setup, we could successfully observe the 424 keV γ ray which was the $2 \rightarrow 0$ transition of ^{76}Kr . The coincidence γ -ray spectrum is shown in Fig. 2. It was obtained after the Doppler-shift correction for three sets of angles between the Ge's and plastics. The background γ rays of 511, 804 and 847 keV resulted in three peaks in the Doppler-corrected spectrum, because they were not suffered Doppler shift. The corrected energy of 424 keV means that this peak really comes from the COULEX of ^{76}Kr , since the γ rays emitted from the primary reactions should be affected by the Doppler effect in the opposite direction. The γ -ray yield of this peak is consistent with the estimation made by using the known half-life of the 2^+ state of ^{76}Kr and the derived $B(E2; 0 \rightarrow 2)$ value of $0.56 e^2 b^2$.

Reference:

- 1) E. Nolte et al., Z. Phys. 268, 267 (1974).

5.10 SEARCH FOR A DOUBLE- γ VIBRATIONAL STATE IN ^{164}Dy

Masumi OSHIMA, Shin-ichi ICHIKAWA,^{*} Hideki IIMURA,^{*}
 Hideshige KUSAKARI,^{**} Masahiko SUGAWARA,^{***} Takashi
 INAMURA,^{****} and Akira HASHIZUME^{****}

Department of Physics,^{*} Department of Chemistry, JAERI,
^{**} Faculty of Education, Chiba University, Yayoi-cho, Chiba 260,
^{***} Chiba Institute of Technology, Shibazono, Narashino, Chiba 275,
 and ^{****} RIKEN, Wako-shi, Saitama 351-01

Whether double- γ vibrational states exist or not in deformed nuclei is currently one of the central problem for elucidating the collective excitation of nuclei.¹⁻⁴ Nevertheless, no definite evidence for the double- γ vibrational states in deformed nuclei have so far been provided experimentally. Because of this, we have searched for the double- γ vibrational states in ^{164}Dy by multiple Coulomb excitation.

^{164}Dy was multiply Coulomb-excited with beams of 76-MeV ^{16}O , 130-MeV ^{32}S , and 317-MeV ^{74}Ge obtained from the JAERI tandem accelerator. The target ^{164}Dy was a self-supporting metallic foil of 1.8 mg/cm² in thickness (95% isotopically enriched). Deexcitation γ rays were observed with seven Ge counters in coincidence with recoiled target atoms and scattered projectiles which were detected with four PPACs (Parallel Plate Avalanche Counter). The PPACs were placed symmetrically with respect to the beam, surrounding the target, so that they covered forward as well as backward angles. The size of PPAC was 10 cm \times 10 cm, and the distance between the center of the PPAC window and the target was 7 cm. The PPACs provided the position signals of detected particles. The observed γ -ray spectra were corrected for Doppler shifts kinematically by using the position signals.

We observed members of the ground-state rotational band up to 18^+ and of the γ band up to 10^+ . The transition from a possible double- γ vibrational state to the γ band is, however, not observed in the energy range of 750-1100 keV, which corresponds to the excitation energy of 2.0-2.5 times that of γ -band head.

Because the Coulomb-excitation cross section is simply proportional to the $B(E2)$ in first order, the upper limit of the unobserved γ -ray intensity gives the upper limit of the $B(E2; 4_{\gamma\gamma} \rightarrow 2_{\gamma})$ value. The estimation shows that $B(E2; 4_{\gamma\gamma} \rightarrow 2_{\gamma}) \leq 5 \text{ W.u.}$

The self-consistent collective-coordinates analysis done by Matsuo et al. predicted 9 W.u. for this value.¹ Also Yoshinaga et al. predicted 7 W.u. based on the interacting boson model.² It can be said that a double- γ vibrational state with more collectivity than the calculations does not exist in this energy region. A detailed experimental analysis is still under way.

References:

- [1] M.Matsuo and K.Matsuyanagi, Prog. Theor. Phys. 74, 1227 (1985); 76, 93 (1986); and 78, 591 (1987).
- [2] N.Yoshinaga, Y.Akiyama, and A.Arima; Phys. Rev. Lett., 56, 1116 (1986).
- [3] V.G.Soloviev: E4-87-795, Dubna (1987).
- [4] M.K.Jammari and R.Piepenbring, Nucl. Phys. A487, 77 (1988).

5.11 NS-ISOMERS IN NEIGHBOR NUCLEI OF ^{100}Sn

Tetsuro ISHII, Sombat GARNSOMSART^{*}, Mitsuhiro ISHII,
Yuichi SAITO, Mituo NAKAJIMA^{**} and Masao OGAWA^{**}

Department of Physics, JAERI, ^{*} Physics Department,
Srinakharinwirot Univ., Thailand, ^{**} Tokyo Institute of Technology,
Yokohama

The doubly magic nucleus ^{100}Sn , very interesting in nuclear structure study, is too far from the β -stability line to produce. We may, however, peep into its neighbor nuclei to see some aspects of the double shell closure. They have small seniority numbers at low excitation energy and large ones at high excitation energy. As a result, isomers of ns or so may be populated in those nuclei produced by heavy-ion reactions. In order to observe those isomers and their decays, we have constructed a "ns-isomer seeker", an improved shadow-bar apparatus, and have employed it in search of ^{100}Sn neighbors.

A schematic drawing of the ns-isomer seeker is shown in fig.1. The instrument consists of the target, the stopper foils, an endless chain supporting the foils and a tungsten shield of Ge detectors from prompt γ -rays from the target. The distance of the target to the stopper foils is typically 20mm, which corresponds to about 1.5ns' flight of fusion residues induced by a Ni beam. The chain is made of 44 pieces of stainless steel; each one is rectangular, 25mm \times 30mm. A stopper lead foil, 0.2mm thick, is attached every four pieces to the chain and 11 stoppers in total are periodically rotated in order to suppress the accumulation of long-lived activities. The Ge detectors have a 4cm or more thickness of tungsten along their sight lines to the target and have a direct view of the lead stopper just behind the target. The instrument suppresses the intensity of statistical transitions to one tenth and the accumulation of long-lived activities to one fifth at the detector position.

We have searched ns isomers in the reaction $^{46}\text{Ti}(225\text{MeV } ^{54}\text{Fe}, \text{xpyn})$ by taking γ - γ coincidences with three Ge detectors. The γ -rays have been observed from the isomers of ^{96}Pd , ^{95}Rh , ^{94}Ru , ^{93}Tc and ^{92}Mo with neutron number $N=50$; ^{96}Rh and ^{94}Tc with $N=51$; and ^{93}Ru and ^{91}Mo with $N=49$. Furthermore three new γ -ray sequences, as shown in fig.2, have been observed. One of them has been confirmed to come from ^{94}Rh by the separate experiments with the help of the Si-box and the systematics of the γ -rays from the Rh isotopes. The two others may be attributed to ^{96}Rh and ^{92}Tc .

In the reaction $^{48}\text{Ti}(230\text{MeV } ^{58}\text{Ni}, \text{xpyn})$, Code ALICE¹⁾ predicts the yield of 10 to 20mb for ^{104}Sn . No transition, however, has been found of ^{104}Sn . With the yields of

other isomers observed and the lifetime of the 6^+ state of ^{104}Sn estimated from those of $^{106,108}\text{Sn}^{2,3}$, the yield of ^{104}Sn is far less than 1mb. Code ALICE loses its validity of prediction for ^{104}Sn .

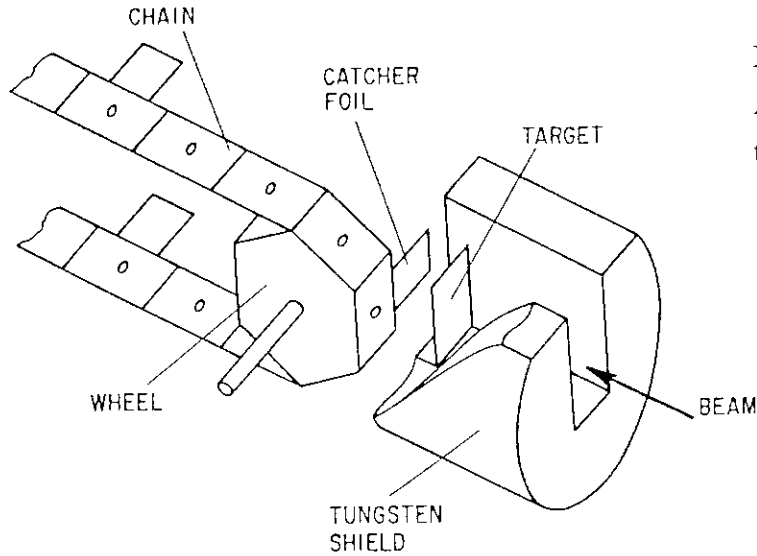


Fig.1
A schematic drawing of the ns-isomer seeker.

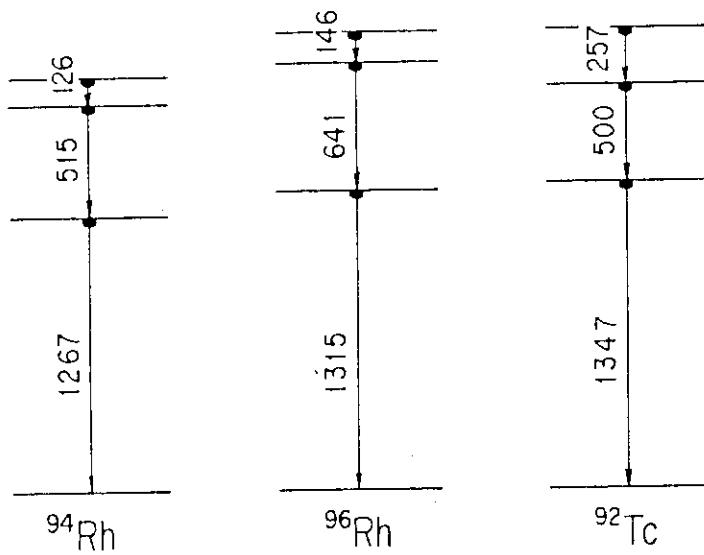


Fig.2
Level schemes of ^{94}Rh , ^{96}Rh and ^{92}Tc .
The transition energies are given in units of keV.

References

- 1) F. Plasil et al., Phys. Rev. C11(1975)508.
- 2) T. Ishii et al., JAERI-M 89-119(1989)165.
- 3) M. Hass et al., Nucl Phys. A410(1983)317.

5.12 EVAPORATION OF CHARGED PARTICLES FROM HIGHLY DEFORMED NUCLEUS

Akira IWAMOTO and Richard HERRMANN

Department of Physics, JAERI

The energy spectra of charged particles evaporated from the compound nucleus has presented us a challenging problem. The experimental data are shifted to lower energies compared to the standard statistical-model calculations.[1,2] Although there is a controversy if this shift is a real one or not[3], the recent experiment data in which the alpha particle is measured in coincident with the fission fragment[2] further confirm the necessity of the shift of emission barrier height relative to the barrier for the capture reaction. It is well known [4] that if the compound nucleus is deformed, the resulting emission-barrier height for the charged particle is reduced in the direction of the long axis.

To calculate such anomaly in the energy spectra of charged particle, we propose a new mechanism for the emission of particles. That is, in addition to the normal evaporation process, we calculate the evaporation process in which the residual nucleus stays in the fission-saddle-point configuration. We denote by $\Gamma^0(w)$ the emission width from the spherical compound nucleus with the excitation energy w and by $\Gamma^s(w)$, the emission width which leaves the residual nucleus in the fission-saddle-point shape. Because the saddle configuration is highly deformed, we can expect that these two channels are thought to be orthogonal and thus the total emission width $\Gamma(w)$ is written as

$$\Gamma(w) = \Gamma^0(w) + \Gamma^s(w). \quad (1)$$

Next task is to derive the expression for $\Gamma^s(w)$. The standard derivation which makes use of the inverse cross section is not helpful because we don't know the capture cross section to highly-deformed target. Instead, we adopt a new approach, the derivation of which, however, is lengthy and we will show only the final form,

$$\Gamma(w) = \frac{m \int d\vec{s} \int_{V(s)}^{w-E_{\text{def}}-Q} d\epsilon \epsilon \cdot (1 - \frac{V(s)}{\epsilon})}{4\pi^2 \hbar^2} \cdot \frac{Z(w^*)}{Z(w)}. \quad (2)$$

In this equation, m is the mass of the emitted particle, ϵ is its energy and $V(s)$ is the

barrier height which is a function of the position on the manifold of the emission barrier. Integration with respect to s is performed on this manifold and $Z(w)$ stands for the level density for the excitation energy w . The excitation energy w^* of the residue is given by

$$w^* = w - E_{\text{def}} - Q - \epsilon, \quad (3)$$

where E_{def} is the deformation energy which is identified to the fission barrier height in case of the emission from the saddle deformation and Q is the Q -value for the emission process. From this equation, we can define the emission width $\Gamma(w, \epsilon)$ for a fixed outgoing energy ϵ as

$$\Gamma(w, \epsilon) = \frac{\int d\vec{s} H\left(1 - \frac{V(s)}{\epsilon}\right) \epsilon \cdot \left(1 - \frac{V(s)}{\epsilon}\right) Z^*(w^*)}{4\pi^2 \hbar^2} \cdot \frac{1}{Z(w)}, \quad (4)$$

where $H(x)$ is the Heaviside function defined by

$$\begin{aligned} H(x) &= 1 \quad \text{for } x \geq 0, \\ &= 0 \quad \text{for } x < 0. \end{aligned} \quad (5)$$

For the spherical nuclei, eq.(4) reduces to the standard form of the emission width expression.

As an application of eqs.(1) and (4), we examine the pre-scission alpha particle emission from the fusion reaction $^{19}\text{F} + ^{197}\text{Au} \rightarrow ^{216}\text{Ra}$ [2]. In this reaction, the measured pre-scission alpha particle energy spectra show a deviation from the statistical-model calculation (PACE2) and there also exists very-low-energy component of alpha particles measured in between the pre-scission and the fragment emission peaks.

First we calculate the fission saddle point shape of ^{216}Ra and the shape is assumed to be equal to that of ^{212}Rn , the residue after the alpha particle emission from ^{216}Ra . The liquid-drop model [5] was used to calculate the energy of the deformed shape described by the two-center parameterization [6]. Saddle shape was searched by changing the four shape parameters simultaneously. After fixing the shape of the saddle, we calculate the potential energy for the alpha particle. Coulomb energy was calculated by assuming the sharp surface determined by the radius parameter $r_0 = 1.2049$ [5] and assuming constant density. Nuclear potential between alpha particle and ^{212}Rn was generated by the

proximity potential [7] by using the local curvatures of the saddle shape of ^{212}Rn .

Table 1 Fission saddle deformation and barrier heights for alpha particle emission.

Nucleus	Def	BH(0°)	BH(90°)	$\langle \text{BH} \rangle$	(BH) 0
^{186}Hg	0.368	13.56	23.20	22.21	23.37
^{216}Ra	0.465	17.47	25.72	24.56	25.29
^{256}Cf	0.605	21.80	27.95	26.67	27.22

In table 1, we show the typical barrier heights, that is, the barrier heights for long (BH(0°)) and short (BH(90°)) axes, the surface-averaged barrier height ($\langle \text{BH} \rangle$) and the barrier height for spherical residue ((BH) 0), for the saddle shape of ^{216}Ra together with those of two other systems. Also shown is the deformation Def of the saddle shape which is defined as the ratio of the radii of short and long axes. The surface-averaged barrier is calculated by averaging the barrier height with the weight of the area on the surface of the barrier top. A point of table 1 is that the reduction of the surface-averaged barrier height from the spherical nucleus is not so large but the minimum potential barrier is reduced so much.

Choosing the fusion reaction $^{19}\text{F} + ^{197}\text{Au} \rightarrow ^{216}\text{Ra}$ at incident energy of 137 MeV [2], we calculate the decay-width expression of eq.(4) as a simple approximation to the energy spectra. From PACE2 calculation, it turns out that the average angular momentum contributing to the alpha emission prior to the fission is about $35\hbar$ [2]. The corresponding fission barrier height calculated by the rotating-liquid-drop model with the rigid-body moment of inertia is about 4.5 MeV which is used for the value E_{def} in eq.(3). The excitation energy 84.4 MeV of the compound nucleus together with the ground state rotational energy of 5.4 MeV are used in eq.(3). The average transmission coefficient does not change much for $l=0$ and for $l=35\hbar$.

The pre-scission alpha energy spectrum calculated with the emission width eq.(1) is shown in Fig.1. This spectrum corresponds to the first-chance emission which is a predominant component of alpha spectrum in the statistical model calculation PACE2 [2]. There are two components, one from the spherical ground state which forms a peak at the right side and the new one from the saddle configuration which forms a broad peak on the

left. The total width is the sum of these two and is shown by the dotted line. We see that the new

peak from the saddle configuration gives a large contribution to the energy spectra at energies about 5 MeV below the main peak. In this case of $l=35\hbar$, the peak value for the new component is about 20 % of the one of main peak. For larger l values, this ratio increases because of the lowering of the fission barrier height. This new component might be the origin of the experimentally observed alphas whose energies are in between two peaks, one from the compound nucleus and the other from the fragments. The measured yields in this energy region are larger than those of the statistical-model calculation as are shown in Fig.6 of [2].

In summary, we pointed out a new mechanism of the particle emission which leaves the residual nucleus in the fission-saddle-point configuration. We derived a formula for the emission width of charged particles from highly deformed nucleus. Applying the model to the alpha emission from the compound nucleus, we obtained a new component of the energy spectra which might have been seen in the data.

References

- [1] N.G. Nicolis et al., Phys.Rev.C41 (1990) 2118.
- [2] H. Ikezoe et al., Phys.Rev.C (1990) in press.
- [3] J.R. Huizenga et al., Phys.Rev.C40 (1989) 668.
- [4] J.M. Alexander, D. Guerreau and L.C.Vaz, Z.Phys.A305 (1982) 313.
- [5] W.D. Myers and W.J. Swiatecki, Nucl.Phys.81 (1966) 1.
- [6] J. Maruhn and W. Greiner, Z. Phys.251 (1972) 431.
- [7] J. Blocki et al., Annals Physics 105 (1977) 427.

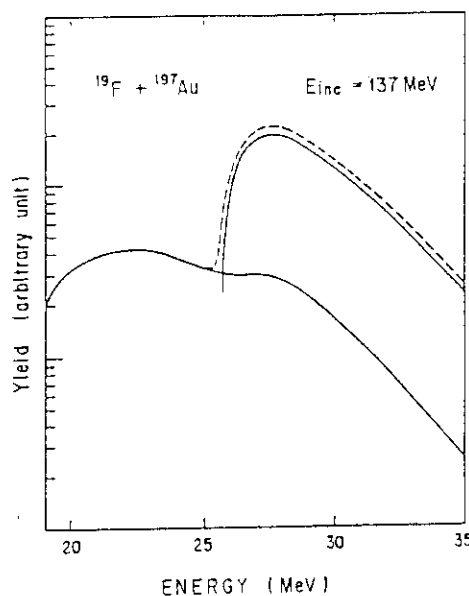


Fig.1
Energy spectrum of the first-chance pre-fission alpha particle.

5.13 SHAPE TRANSITION OF NUCLEI WITH MASS AROUND A=100

Michiaki SUGITA and Akito ARIMA*

Department of Physics, JAERI, *University of Tokyo

Introduction

Arseniev *et al.* ¹⁾ theoretically predicted the existence of a new region of deformed neutron-rich nuclei with $A \approx 100$, and Cheifetz *et al.* ²⁾ are the first to find some of them. Several theoretical and experimental studies have been done since [for example, see the review by Hamilton *et al.* ³⁾]. Figure 1 summarizes experimental excitation energies of the first $I^\pi=2^+$ states in nuclei around $A=100$ ⁴⁻⁶⁾. According to Sheline *et al.* ⁷⁾ the Zr isotopes ($Z=40$) behave like a "chameleon": Even though proton submagic, they change their nuclear shape in a peculiar way; the Zr isotopes with $N=50$ to 58 have a spherical shape but the one with $N=60$ is deformed. A similar trend can be found in the Sr isotopes ($Z=38$). On the other hand, the shape transition becomes moderate as the proton number exceeds $Z=40$: the first 2^+ excitation energy of the Ru isotopes ($Z=44$) decreases smoothly with N at $N \approx 60$. Even in this limited region of the nuclear mass, the shape transition strongly depends on the proton number.

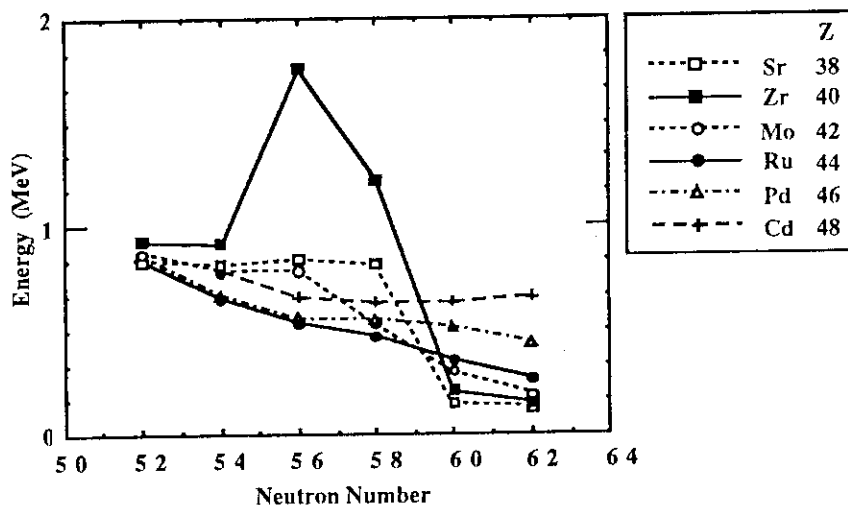


Fig. 1 The systematics of the first 2^+ states observed in nuclei with $A \approx 100$. The excitation energies are expressed in units of MeV.

The hamiltonian

The hamiltonian is composed of three terms:

$$\hat{H} = \hat{H}_\pi + \hat{H}_\nu + \hat{H}_{\pi\nu}, \quad (1)$$

where the first and second terms (\hat{H}_τ) express hamiltonians for identical particles ($\tau = \pi, \nu$), and $\hat{H}_{\pi\nu}$ stands for a proton-neutron interaction. We assume that the residual interaction

consists of the pairing plus quadrupole force. Respective terms in the hamiltonian \hat{H} are given by

$$\hat{H}_\tau = \hat{\varepsilon}_\tau - G_\tau \hat{P}_\tau^\dagger \hat{P}_\tau \quad (2)$$

and

$$\hat{H}_{\pi\nu} = -\chi_{\pi\nu} \hat{Q}_\pi \cdot \hat{Q}_\nu. \quad (3)$$

In Eq. (2), $\hat{\varepsilon}_\tau$ is the spherical single-particle energy operator.

Energy surface

Instead of solving the Schrödinger equation, we rely on the variational principle. First we introduce the following one-body deformed hamiltonian (\hat{h}_τ) in the respective intrinsic frames for π and ν :

$$\hat{h}_\tau(D_\tau, \Delta_\tau, \lambda_\tau) = \hat{\varepsilon}_\tau - \lambda_\tau \hat{n}_\tau - \Delta_\tau (\hat{P}_\tau + \hat{P}_\tau^\dagger) - D_\tau \hat{Q}_{0\tau}. \quad (4)$$

The parameter D_τ expresses the magnitude of nuclear deformation of τ nucleons and is connected to the conventional distortion parameter δ_τ by the relation: $D_\tau = \hbar\omega \delta_\tau$. The parameters Δ_τ and λ_τ are the pairing gap and the chemical potential, respectively, to be determined by the conventional BCS condition, so that Δ_τ and λ_τ are given as a function of D_τ . We take D_π and D_ν as variational parameters and express a trial function for the whole system as follows:

$$|D_\pi, D_\nu\rangle = |D_\pi\rangle |D_\nu\rangle = |D_\pi, \Delta_\pi(D_\pi), \lambda_\pi(D_\pi)\rangle |D_\nu, \Delta_\nu(D_\nu), \lambda_\nu(D_\nu)\rangle. \quad (5)$$

Thus we obtain the potential energy surface $E(D_\pi, D_\nu)$ as the expectation value of the hamiltonian \hat{H} with respect to the trial function $|D_\pi, D_\nu\rangle$.

Calculations

The energy curves have been calculated with the reasonable values for the parameters in the hamiltonian \hat{H} [See Ref. 8]. The spherical single-particle orbits involved are two adjacent harmonic oscillator shells outside the closed core $^{60}\text{Ca}_{40}$. The quadrupole strength $\chi_{\pi\nu}$ in Eq. (3) can be determined on the assumption that the spherical and deformed minima of the energy surface $E(D_\pi, D_\nu)$ have almost the same energies for the nucleus ^{98}Sr .

For a fixed $D_\pi (\geq 0)$, the energy surface $E(D_\pi, D_\nu)$ is a function of D_ν and possesses a single minimum with respect to D_ν . We define the energy curve $\tilde{E}(D_\pi)$ by expressing this minimum energy as a function of D_π . The energy curves $\tilde{E}(D_\pi)$ for the Ru and Sr isotopes are shown in Figs. 2(a) and (b), respectively. The energy curves of the Sr isotopes with $N=60$ show two minima at $\delta_\pi=0$ and $\delta_\pi=0.35$. For $N \leq 58$ the deformed minimum has a higher energy than the spherical one. The deformed minimum goes down rapidly with N and reaches the lowest at $N=62$. By contrast, the Ru isotope with $N=58$ is deformed and the deformation at the minimum energy increases with N .

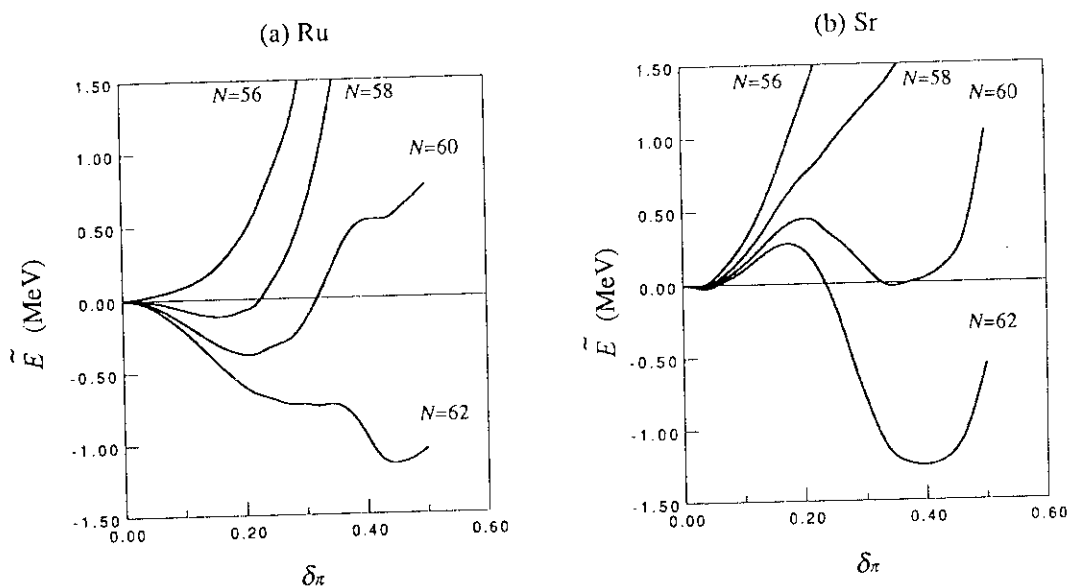


Fig. 2 Energy curves corresponding to *smooth* and *sharp* shape transitions. (a) *Smooth* shape transition in the Ru isotopes. The energy curves have been calculated for the Ru isotopes with $N=56$ to 62 . (b) *Sharp* shape transition in the Sr isotopes. The energy curves have been calculated for the Sr isotopes with $N=56$ to 62 .

“Self-consistency plot”

We will now consider the number of the stationary points on the energy surface $E(D_\pi, D_\nu)$ and their stabilities. See Ref. 8 for more information. The stationary points of $E(Q_\pi, Q_\nu)$ and their stabilities are then determined by the first and the second derivatives of $E(Q_\pi, Q_\nu)$ with respect to Q_τ . These derivatives are given by

$$\frac{\partial E(Q_\pi, Q_\nu)}{\partial Q_\pi} = D_\pi - \chi_{\pi\nu} Q_\nu, \quad (6)$$

$$\frac{\partial E(Q_\pi, Q_\nu)}{\partial Q_\nu} = D_\nu - \chi_{\pi\nu} Q_\pi, \quad (7)$$

$$\frac{\partial^2 E(Q_\pi, Q_\nu)}{\partial Q_\tau^2} = \frac{dD_\tau}{dQ_\tau}, \quad (8)$$

$$\frac{\partial^2 E(Q_\pi, Q_\nu)}{\partial Q_\pi \partial Q_\nu} = -\chi_{\pi\nu}. \quad (9)$$

Eqs. (6) and (7) express the requirement for points being stationary (i.e., $\frac{\partial E(Q_\pi, Q_\nu)}{\partial Q_\tau} = 0$) as

$$D_{\pi} = \chi_{\pi v} Q_v(D_v) \text{ and } D_v = \chi_{v\pi} Q_{\pi}(D_{\pi}) . \tag{10}$$

The stability of the stationary point depends on the sign of the following quantity S :

$$S = \frac{dD_{\pi}}{dQ_{\pi}} \frac{dD_v}{dQ_v} - (\chi_{\pi v})^2 . \tag{11}$$

If S is positive (negative), the stationary point is a local minimum (saddle). No local maximum appears [see Eqs. (8) and (9)].

In order to solve the simultaneous equations (10), we express them by curves in the $D_{\pi}-D_v$ plane with the abscissa D_{π} and the ordinate D_v as illustrated in the upper part of Fig. 3. The two curves corresponding to Eqs. (10) are denoted in the figure by N and P , respectively. Using a parametric representation, the coordinates of the points on the P and N curves are given by $(D_{\pi}, D_v) = (t, \chi_{\pi v} Q_{\pi}(t))$ and $(D_{\pi}, D_v) = (\chi_{v\pi} Q_v(s), s)$, respectively, where t and s are parameters.

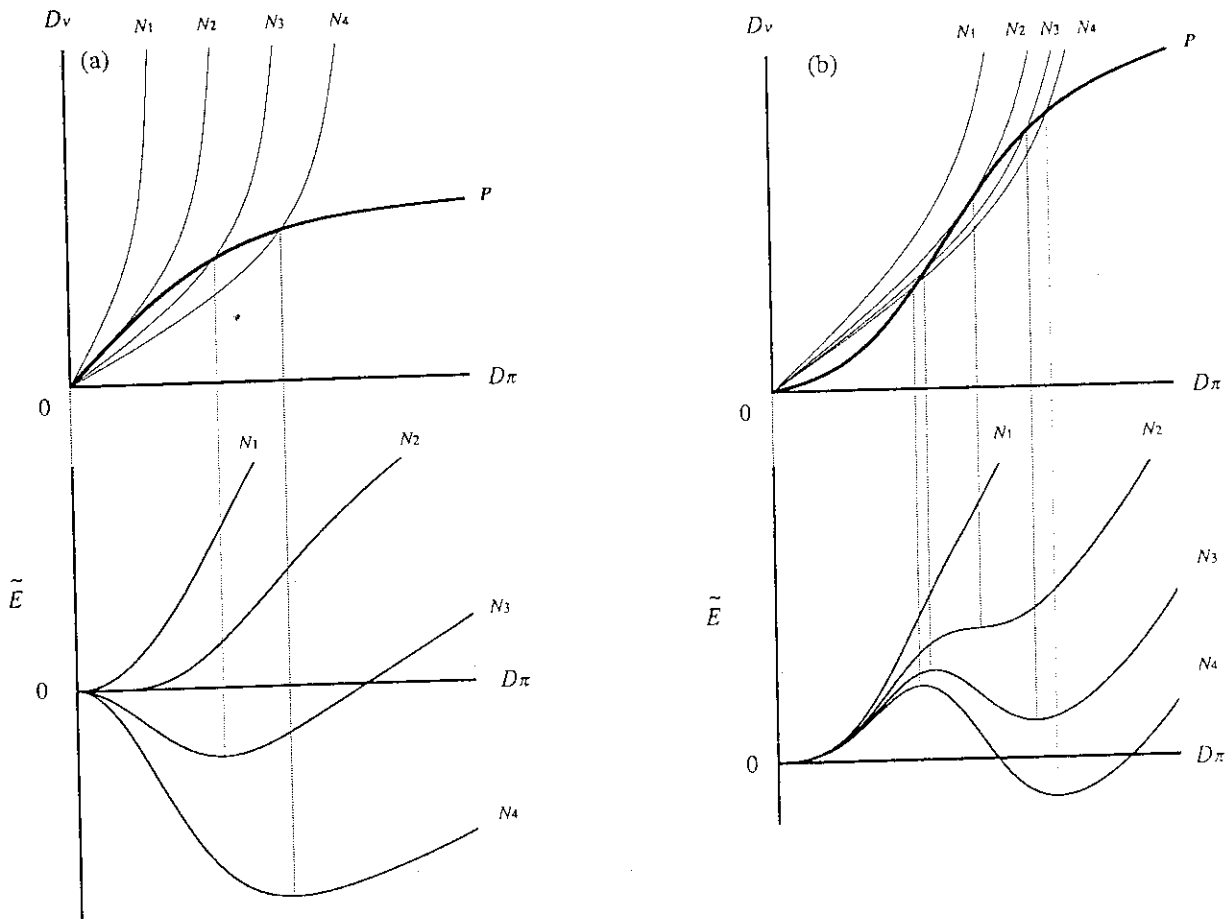


Fig. 3 Classification of the shape transitions based on the "self-consistency plots". See Ref. 8.
 (a) Type (a) corresponds to a smooth shape transition. The $Q_{\pi}(D_{\pi})$ and $Q_v(D_v)$ curves both have no inflection point and are upward convex as a function of D_{π} and D_v , respectively. At most two intersections occur. One of them always coincides with the origin.
 (b) Type (b) corresponds to a sharp shape transition. The $Q_{\pi}(D_{\pi})$ curve has an inflection point so that three intersections may occur.

Classification of types of shape transitions

Depending on how protons occupy the $0g_{9/2}$ orbital, the curves $Q_{\pi}(D_{\pi})$ for the protons in the nuclei around $Z=40$ can be divided into two types: Type (a): curves without any inflection point; Type (b): curves with an inflection point. The curves $Q_{\nu}(D_{\nu})$ for the neutrons always belong only to Type (a). Two types of "self-consistency plots" are schematically drawn in Fig. 3. In Fig. 3(a) both $Q_{\pi}(D_{\pi})$ and $Q_{\nu}(D_{\nu})$ have no inflection point and are upward convex as a function of D_{π} and D_{ν} , respectively. The self-consistency plots in Fig. 3(a) thus describe a *smooth* shape transition. In the case of the curve $Q_{\pi}(D_{\pi})$ with an inflection point, three intersections may appear in the self-consistency plot, as shown in Fig. 3(b). The self-consistency plots in Fig. 3(b) describe a *sharp* shape transition.

Summary

We have investigated the energy surfaces $E(D_{\pi}, D_{\nu})$ of the Sr and Ru isotopes with mass around $A=100$. We have introduced a "self-consistency plot" of the curves $Q_{\pi}(D_{\pi})$ and $Q_{\nu}(D_{\nu})$ and applied it to the classification of the shape transitions. It has turned out that the number of the intersections on the "self-consistency plot" determines the type of the shape transitions. Furthermore, the curves $Q_{\tau}(D_{\tau})$ directly reflect the microscopic nuclear structure in the individual isotopes.

The "self-consistency plot" of proton and neutron deformations has revealed that the differences in shape transition seen in the Sr and Ru isotopes are ascribed to the protons occupying the $0g_{9/2}$ orbitals.

References

- 1) D.A. Arseniev, A. Sobieczewski and V.G. Soloviev, Nucl. Phys. A139 (1969) 269
- 2) E. Cheifetz, R.C. Jared, S.G. Thompson and J.B. Wilhelmy, Phys. Rev. Lett. 25 (1970) 38
- 3) J.H. Hamilton, P.G. Hansen and E.F. Zganjar, Reports on Progress in Physics, 48 (1985) 631
- 4) C.M. Lederer and V.S. Shirley, in Table of isotopes, seventh edition (Wiley-Interscience, 1978)
- 5) F.K. Wohn, John C. Hill, R.F. Petry, H. Dejbakhsh, Z. Berant and R.L. Gill, Phys. Rev. Lett. 51 (1983) 873
- 6) S. Raman, C.H. Malarkey, W.T. Milner, C.W. Nestor, Jr., and P.H. Stelson, Atomic Data and Nuclear Data Tables 36 (1987) 1
- 7) R.K. Sheline, I. Ragnarsson and S.G. Nilsson, Phys. Lett. B41 (1972) 115
- 8) M. Sugita and A. Arima, to be published in Nucl. Phys. A (1990)

VI NEUTRON PHYSICS

6.1 NEUTRON CROSS SECTION MEASUREMENTS IN SEVERAL MEV REGION USING ${}^1\text{H}({}^{11}\text{B},n){}^{11}\text{C}$ NEUTRON SOURCE

Kazuo HASEGAWA^{*}, Motoharu MIZUMOTO^{*}, Masayoshi SUGIMOTO,
Yoshimaro YAMANOUTI, Yujiro IKEDA^{*}, Chikara KONNO^{*},
Tomohiko IWASAKI^{**}, Shigeo MATSUYAMA^{**}, Naohiro HIRAKAWA^{**},
Kazusuke SUGIYAMA^{**}, Masayuki IGASHIRA^{***}, Hideo KITAZAWA^{***}

Department of Physics, JAERI, ^{*}Department of Reactor Engineering, JAERI, ^{**}Faculty of Engineering, Tohoku University, ^{***}Research Laboratory for Nuclear Reactors, Tokyo Institute of Technology

Introduction

Fast neutron induced cross sections are requested for fusion reactor design calculation. The energy range of interest extends up to 16 MeV. There are, however, insufficient experimental data between 8 and 14 MeV because of lack of highly monoenergetic neutron sources. Monoenergetic neutron sources in this energy region are required to obtain experimental data with higher accuracy. To solve this situation, monoenergetic neutron source using ${}^1\text{H}({}^{11}\text{B},n){}^{11}\text{C}$ reaction was investigated and its properties have been measured¹⁾. By using this neutron source, neutron cross sections of gamma-ray production, activation and fission were measured at incident neutron energies from 11.5 to 13.0 MeV.

Neutron Source

Pulsed ${}^{11}\text{B}$ beam with a repetition rate of 4 MHz at bombardment energies of 62 to 68 MeV was provided by the JAERI Tandem Accelerator. Neutrons were produced in a 3 cm long 0.2 MPa pressurized H_2 gas target with a 5.1 mg/cm^2 Mo entrance window. Produced neutrons were measured by two sets of 5.1 cm dia. x 1.3 cm long NE213 liquid scintillation detectors located at 0 deg. and 29 deg., respectively. The efficiency of the NE213 detector was calculated by a computer program O5S²⁾. Activation method using standard ${}^{27}\text{Al}(n,\alpha){}^{24}\text{Na}$ reaction cross section was also employed to check an absolute neutron flux. Both results agreed within 5%. Energy spread of this neutron source was estimated to be 0.6 MeV FWHM.

Cross Section Measurements

Energy spectra of gamma-rays induced by fast neutrons were measured with a 7.6 cm dia. x 15.2 cm long NaI(Tl) detector surrounded by a 25.4 cm dia. x 25.4 cm long NaI(Tl) annular detector. These two detectors were operated in an anti-coincidence mode to reduce backgrounds. Gamma-ray pulse height spectra were unfolded with a computer program FERDOR³⁾. Sample had a cylindrical shape and was located at 9.8 cm from the neutron target. Table 1 lists measured samples and neutron energies including previous measurement⁴⁾ using D(d,n)³He neutron source. Measured results were compared with the experimental data obtained by white neutron source and with the evaluated values of JENDL-3 and ENDF/B-IV. An example of total gamma-ray production cross section of iron is shown in Fig. 1. Energy dependence of the earlier Oak Ridge white neutron source data were confirmed in the energy range from 8 to 13 MeV, but the absolute magnitudes of the present results are 30% lower than Chapman⁵⁾ and 20% higher than Dickens⁶⁾. Cross section for 0.96-MeV discrete gamma-ray in copper is shown in Fig. 2. Present results agreed well with Slaughter⁷⁾.

For the activation cross section measurements, samples were placed at the same position as the gamma-ray production cross section measurements. Target nuclei and reaction types are listed in Table 2. After irradiation, relative reaction rates were obtained from the gamma-ray counting using a Ge detector. Cross sections were deduced relative to the $^{197}\text{Au}(n,2n)^{196}\text{Au}$ reaction cross section as a standard. Fig. 3 shows $^{93}\text{Nb}(n,2n)^{92\text{m}}\text{Nb}$ cross section as a function of neutron energy.

Fission cross section of Np-237 at a neutron energy of 12 MeV was measured by a fission chamber coupled with a proton-recoil counter telescope⁸⁾ and preliminary data were obtained. Detail analyses are now in progress.

References

- 1) S. Chiba et al.: Nucl. Instr. and Meth. A281 (1989) 581
- 2) R. E. Textor et al.: O5S, ORNL-4160 (1968)
- 3) L. Harris Jr. et al.: FERDOR, GA-9882 (1970)
- 4) M. Mizumoto et al.: Proc. Int. Conf. on Nucl. Data for Sci. and Tech., (Mito,1988) pp197-200
- 5) G. T. Chapman et al.: ORNL-TM-5416 (1976)
- 6) J. K. Dickens et al.: ORNL-4798 (1972)

- 7) G. G. Slaughter et al.: Nucl. Sci. Eng. 84 (1983) 395
 8) T. Iwasaki et al.: Proc. Int. Conf. on Nucl. Data for Sci. and Tech.,
 (Mito, 1988) pp87-90

Table 1 (n, γ) Reaction Cross Section Measurements

element	size (mm)	weight (g)	D(d, n) ³ He		¹ H(¹¹ B, n) ¹¹ C		
			7.8MeV 90°	10.0MeV 90°	11.5MeV 90°	125°	13.0MeV 90°
C	φ 30x30	38.14	○	○	○	○	○
O(H ₂ O)	φ 32x40	30.47	○	○	○		
Al	φ 30x30	57.68	○	○	○	○	○
Si	φ 30x30	49.51	○	○	○	○	○
Si	φ 20x30	21.97		○			
Fe	φ 30x30	166.3	○	○	○	○	○
Ni	φ 20x30	83.79			○		○
Cu	φ 20x30	83.98			○	○	○
Pb	φ 30x30	243.2	○	○	○	○	
Pb	φ 20x30	108.6		○			○
Bi	φ 30x30	210.6	○	○	○		○

Table 2 Activation Cross Sections at 12.0 and 13.0 MeV

Reaction	Reaction Rate Ratio to ¹⁹⁷ Au(n, 2n) ¹⁹⁶ Au		Cross Section(mb)*	
	1855 mb at 12.0 MeV	2045 mb at 13.2 MeV	at 12.0 MeV	at 13.2 MeV
²⁷ Al(n, α) ²⁴ Na	0.069(3.0)	0.065(4.0)	128 +-4	131.9+-6
¹⁹⁷ Au(n, 2n) ¹⁹⁶ Au	1.00	1.00	1855	2045
⁹³ Nb(n, 2n) ^{92m} Nb	0.189(3.2)	0.226(4.3)	351+-10	462.2+-18
⁴⁷ Ti(n, p) ⁴⁷ Sc	0.88(6.7)	-----	163+-10	-----
⁴⁸ Ti(n, p) ⁴⁸ Sc	0.244(3.6)	-----	45.2+-2	-----
¹¹⁵ In(n, n') ^{115m} In	0.118(3.6)	0.056(3.9)	219+-8	115+-5
⁹⁰ Zr(n, 2n) ⁸⁹ Zr	-----	0.155(4.5)	-----	315+-15

* Cross sections were obtained relative to the ¹⁹⁷Au(n, 2n)¹⁹⁶Au Reaction.

Note#1: No correction for contributions from the low energy neutrons was performed. It must be done after neutron spectrum data are available.

Note#2: Uncertainties in the neutron spectrum are included in errors.

Fig. 1 Total gamma-ray production cross section for iron

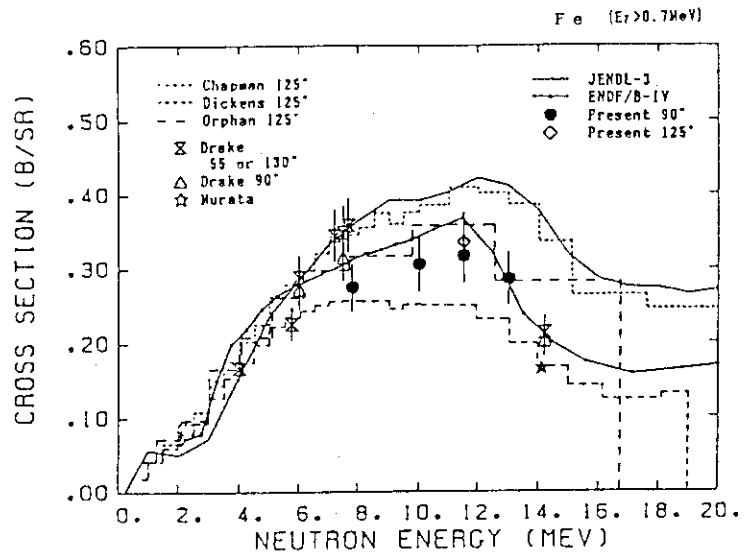


Fig. 2 Cross section for the production of the 0.96-MeV gamma-rays in copper

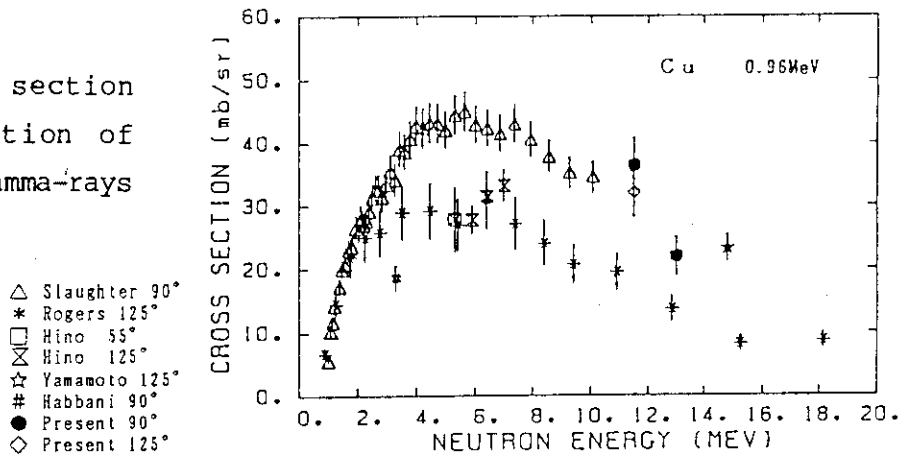
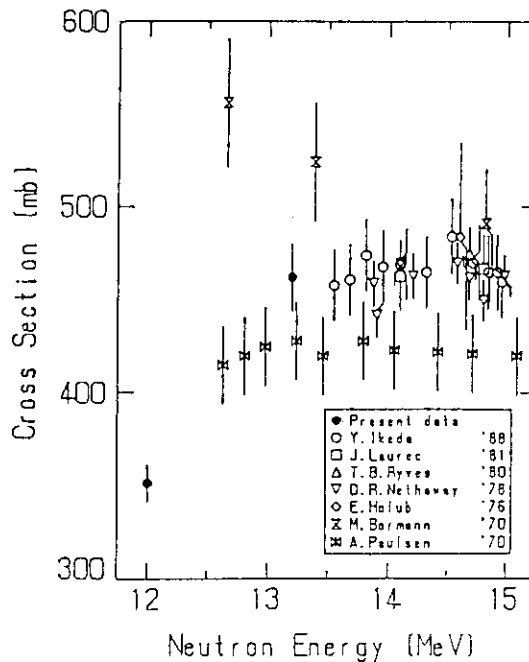


Fig. 3 Cross section for $^{93}\text{Nb}(n,2n)^{92\text{m}}\text{Nb}$ reaction



6.2 SCATTERING OF 18.5 MeV NEUTRONS FROM ^{52}Cr

Yoshimaro YAMANOUTI, Masayoshi SUGIMOTO, Motoharu MIZUMOTO,
Yukinobu WATANABE* and Yoshihisa WAKUTA*

Department of Physics, JAERI, *Department of Nuclear
Engineering, Kyushu University

Neutron scattering has been shown to give direct information about the nucleon-nucleus optical potential and the mechanism for the excitation of low-lying nuclear states. For the neutron scattering on ^{52}Cr in the energy range above 10 MeV, elastic and inelastic scattering from natural chromium has been measured at 14 MeV^{1,2)}. In this work differential cross sections for elastic and inelastic scattering of neutrons on ^{52}Cr were measured at 18.5 MeV in order to study the reaction mechanism in the energy region around 20 MeV, since Oak Ridge National Laboratory kindly accepted our request to borrow the separated isotope of ^{52}Cr converted to metal from oxide. The data were analyzed by the optical model and the coupled-channel (CC) theory, and compared with proton scattering in the framework of the Lane model.

The measurements were performed with the pulsed beam time-of-flight method. A pulsed beam of deuterons with a repetition rate of 2MHz and a burst of about 2 nsec was provided by the JAERI tandem electrostatic accelerator. Neutrons were generated by the $^2\text{H}(d,n)^3\text{He}$ reaction. The neutron detector is a 20 cm in diam by 35 cm thick NE213 liquid scintillator viewed by RCA 8854 photomultiplier tubes at the front and rear scintillator faces. Scattered neutrons were detected by an array of these four scintillator detectors. Five pieces of 99.74% enriched metal pellets with total weight of 46.49 g were used as the ^{52}Cr scattering sample.

Fig.1 shows a neutron time-of-flight spectrum taken at 90°. The experimental yields were calculated by fitting the peaks of interest with the code PEAKS. The relative efficiency of the neutron detector was determined by measuring the angular distribution of neutrons from the $^1\text{H}(n,n)^1\text{H}$ reaction. The experimental yields were normalized to the known n-p scattering cross section by measuring neutrons from a 1.2 cm in diam by 4 cm long polyethylene scatterer. The resulting differential cross sections

were corrected for the dead time in the time-to-amplitude converters and ADCs in the data acquisition system. Corrections for multiple scattering and flux attenuation in the sample were also taken into account. These corrections were made by means of the Monte Carlo code MULT1.

Differential cross sections were obtained for the elastic scattering and inelastic scattering to the excited states at 1.434 MeV (2^+) and 4.563 MeV (3^-). The differential cross sections were measured in the angular range from 20° to 140° in 10° -steps. The experimental cross sections are shown in figs.2 and 3 together with theoretical curves.

The data were analyzed by the phenomenological optical model with the standard form. The compound nuclear contribution estimated by the Hauser Feshbach formalism is small compared with the experimental cross sections at this incident energy. The microscopic JLM optical potential³⁾ also reproduced the elastic angular distribution.

The CC calculations based on the vibrational model were performed with the code ECIS79 and JUPITOR1. In the calculation the 2^+ (1.434 MeV) and 3^- (4.563 MeV) states were treated as the quadrupole one phonon state and the octupole one phonon state, respectively. The optical potential parameters except the spin orbit term, and the deformation parameter were adjusted to get the best fit to the experimental cross sections for the elastic and inelastic scattering. As shown in figs.2 and 3 the CC calculation gives good fit to the experimental cross sections.

An optical potential obtained in the proton scattering⁴⁾ was transformed into a neutron potential in the Lane model. With this transformed neutron potential and the same deformation parameter obtained in the analysis of the proton scattering CC calculations were carried out to examine its ability to predict the present neutron cross sections. The CC result reveals that the transformed potential and the proton deformation parameter reproduce the present neutron cross sections for the elastic and inelastic scattering.

References

- 1) P.H.Stelson et al: Nucl.Phys. 68 (1965) 97
- 2) G.Winkler et al: Proc.Int.Conf. Knoxville, 1979, P150
- 3) J.P.Jeukenne, A.Lejeune and C.Mahaux: Phys.Rev. C16 (1977) 80
- 4) E.Fabrici et al: Phys.Rev. C21 (1980) 844

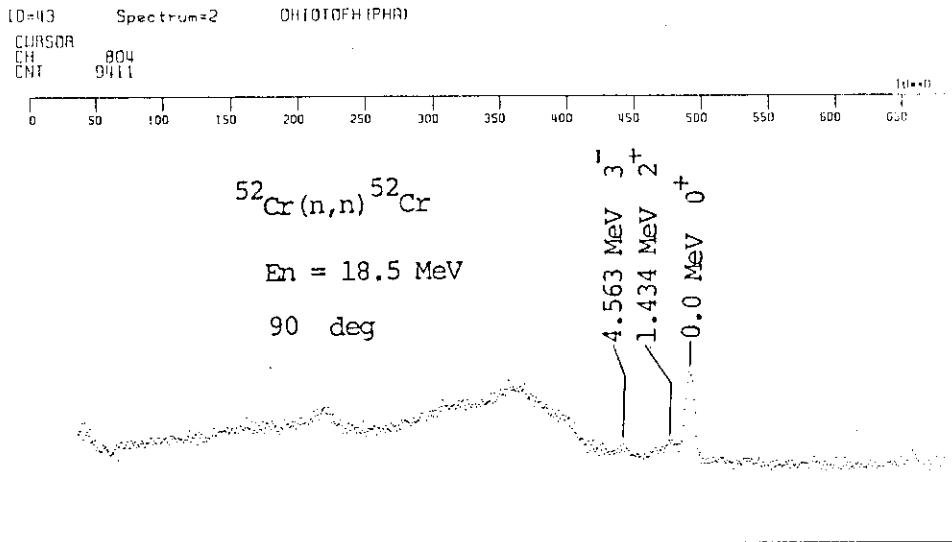


Fig.1 A time-of-flight spectrum of elastic and inelastic scattering of 18.5 MeV neutrons from ^{52}Cr at 90°

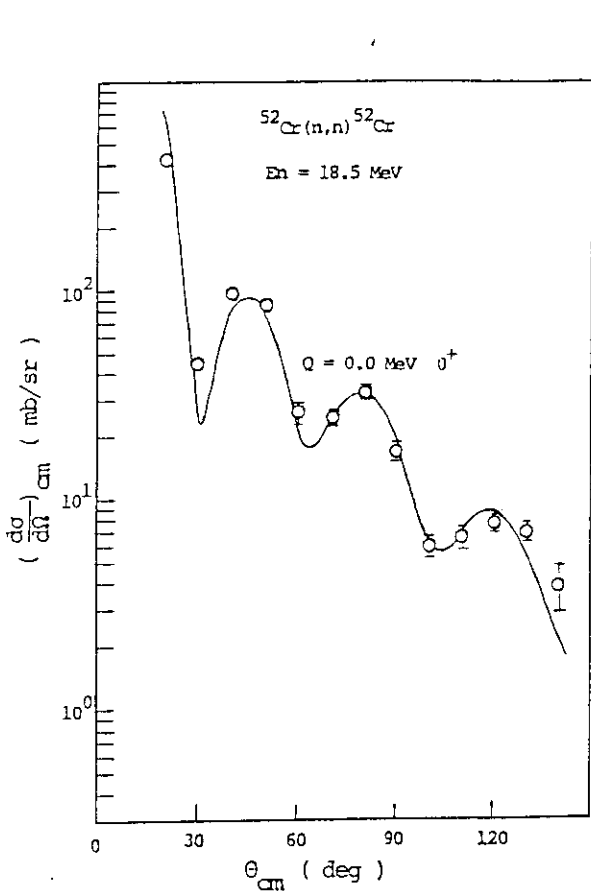


Fig.2 Experimental elastic cross section (open circles) and CC prediction based on the vibrational model (solid line)

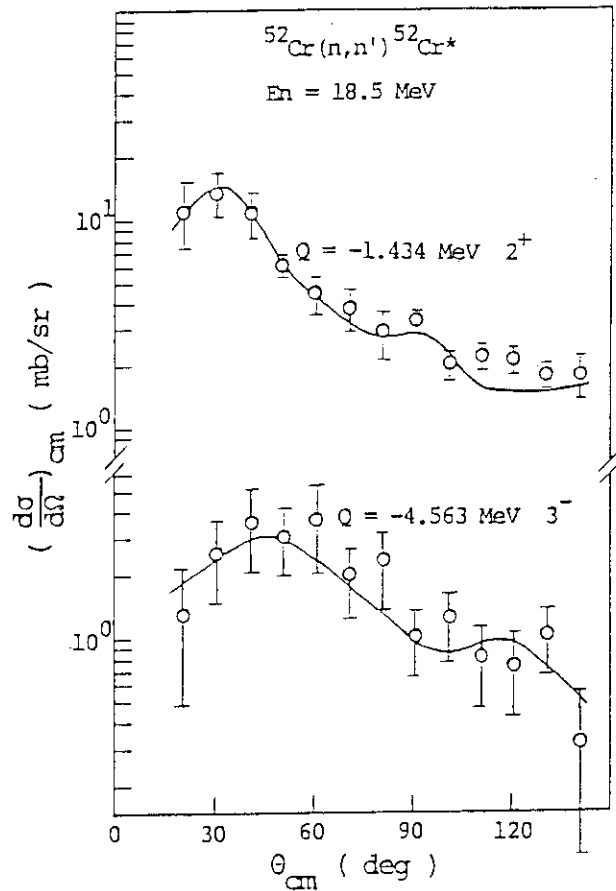


Fig.3 Experimental inelastic cross sections (open circles) and CC predictions based on the vibrational model (solid lines)

VII PUBLICATIONS

Journal/Proceedings

1. Aruga, T., Takamura, S., Hoshiya, T. and Kobiyama, M.
Effects of He Ion Irradiation on Superconductivity of Bi-Sr-Ca-Cu-O Films
Jpn. J. Appl. Phys. 28 (1989) L964.
V
2. Chiba, S., Mizumoto, M., Hasegawa, K., Yamanouti, Y., Sugimoto, M.,
Watanabe, Y. and Drosig, M.
The $^1\text{H}(^{11}\text{B},n)^{11}\text{C}$ Reaction as a Practical Low Background Monoenergetic
Neutron Source in the 10MeV Region
Nucl. Instrum. & Methods A281 (1989) 581
T
3. Hoshiya, T., Takamura, S., Aruga, T. and Kobiyama, M.
Annealing Effects on Transition Temperature of Superconducting
Bi-Sr-Ca-Cu-O Films after Ion Irradiation
Jpn. J. Appl. Phys. 28 (1989) L1352.
V
4. Ichikawa, S., Sekine, T., Iimura, H. and Oshima, M.
Measurement of Release Speeds of La and Ce from a Thermal Ion Source
Proc. of the 2nd Specialist Research Meeting on Studies of Nuclear
Chemistry and Nuclear Physics at Research Reactor, Kumatori, Jan.
17-18 (1990), p.21.
T
5. Ikezoe, H., Shikazono, N., Nagame, Y., Sugiyama, Y., Tomita, Y.,
Ideno, K., Iwamoto, A., and Ohtsuki, T.
Pre-Scission ^4He Multiplicity in the $^{19}\text{F} + ^{197}\text{Au}$ Reaction
Phys. Rev. C in press
T

6. Ikezoe, H., Shikazono, N., Nagame, Y., Sugiyama, Y., Tomita, Y., Ideno, K., Nakahara, H., Ohtsuki, T., Kobayashi, T. and Sueki, K.
Light Charged Particle Emissions in Fission
Proceedings of 50 Years with Nuclear Fission, April 25-28, (1989) p721
T
7. Ito, Y., Takamura, S., Sueoka, O., Kanazawa, I., Hirose, M. Mashiko, K.
Improvement of Beam Quality of the Intense Slow Positron Beam - Electron
Linac of JAERI -
Proc. 14th Linear Accelerator Meeting in Japan, (Nara, Sept. 7-9, 1989)
8. Ito, Y., Hirose, M., Sueoka, O., Kanazawa, I., Takamura, S., Okada, S.
Production of Intense Slow Positron Beam using an Electron Linac
2nd Int. Symp. on Advanced Nuclear Energy Research, Mito (Jan. 24-26 1990)
9. Iwamoto, A. and Takigawa, N
Anomalous Enhancement of the Subbarrier Fusion Cross Section
Phys. Lett. 219 (1989) 176.
10. Iwamoto, A. and Zukeiran, A
Report on the Int. Conf. on 50 Years Research in Nuclear Fission
J. Atomic Energy Society of Japan 31 (1989) 37
11. Iwamoto, A. and Takigawa, N.
Enhancement of the Subbarrier Fusion Reaction ... Anomalous Enhancement
in Ge + Ge system ... Butsuri 44 (1989) 674
12. Iwamoto, A.
Berlin Int. Conf. on 50 Years Research in Nuclear Fission
Nuclear Data News 34 (1989) 37
13. Iwamoto, A.
Fifty Years Research in Nuclear Fission
J. Atomic Energy Society of Japan 31 (1989) 1310

14. Iwase, A., Watanabe, M., Iwata, T., and Nihira, T.
Effect of 120 MeV ^{16}O Ion Irradiation at Liquid Nitrogen Temperature on
Superconducting Properties of Bi-Pb-Sr-Ca-Cu-O
Jpn. J. Appl. Phys. 28 (1989) L1939.
T
15. Iwase, A., Iwata, T., Sasaki, S. and Nihira, T.
Radiation Annealing in Nickel and Copper by 100 MeV Iodine Ions.
J. Phys. Soc. Jpn. 59 (1990) 1451.
T
16. Iwata, T. and Iwase, A.
Interaction of Energetic Neutrons and Charged Particles with Solids
Proceedings of International Symposium on Advanced Nuclear Research -
Near Future Chemistry in Nuclear Energy Fields - pp. 276-285. (1989)
T V
17. Iwata, T. and Iwase, A.
Damage Production and Annealing in Ion-Irradiated FCC Metals
Rad. Eff. 113 (1990) 135.
T V
18. Kanno, I.
A Model of Charge Collection in a Silicon Surface Barrier Detector
Rev. Sci. Instrum. 61, 129 (1990)
19. Kikuchi, A., Naramoto, H., Ozawa, K. and Kazumata, Y.
Damage Profiles in Alkali Halides Irradiated with High Energy Heavy Ions
Nucl. Instr. and Meth. B39 (1989) 724.
T
20. Kindo, T. and Iwamoto, A.
Methods for the Calculation of the Fission Half-Life in the Multi-
dimensional Space
Phys. Lett. 255 (1989) 203

21. Kumakura, M., Yoshida, M., Kohyama, H., Komaki, Y., Ishikawa, N., Sakurai, T., Furukawa, K. and Ohno, S.
Microhole Formation in Polymethyl Methacrylate Film by Heavy Ion Irradiation. Proceedings of 2nd International Symposium on ADVANCED NUCLEAR ENERGY RESEARCH, (Mito, 1990) p.674
T
22. Mitamura, T., Terasawa, M., Koterazawa, K., Iwaseki, H., Kawatsura, K. and Nakai, Y
Radiation effect study of single crystal austenitic stainless steel by ion channeling
Nucl. Instr. & Meth. B48 (1990) 470
V
23. Miyahara, K., Sakamoto, Y., Hamada, S. Kayano, H. and Hosoi, Y.
Microstructure and Mechanical Properties of α -Particle Irradiated Cr-Mn and the Other Stainless Steels
Proceedings of 4th Intern. Conf. on Fusion Reactor Materials (Dec. 1989), Kyoto
24. Mizumoto, M. and Sugimoto, M.
Influence of Water Absorption in a Sample for Neutron Capture Cross Section Measurement
Nucl. Instrum. & Methods, A282 (1989) 324
25. Mizumoto, M. and Nuclear Spallation Study Group I (Accelerator)
Development Plan of Basic Technology for High Intensity Proton Linear Accelerator
Proceedings of the 2nd International Symposium on Advanced Nuclear Energy Research - Evolution by Accelerators -
(Mito. 1990) p219
26. Mizumoto, M., Sugimoto, M., Okumura, Y., Shirakata, H., Nishida, T., Takada, H., Kanno, I., Yasuda, H., Nakahara, Y., Takizuka, T. and Kanako, Y.
Development Plan in JAERI for High Intensity Proton Linear Accelerator
Proceedings of the 1989 Seminar on Nuclear Data, JAERI-M 90-025 (1990) pp. 179-188

27. Nagame, Y., Ikezoe, H., Baba, S., Hata, K., Sekine, T., Ichikawa, S., Magra, M., Ideno, K., Yokoyama, A., Hatsukawa, Y. and Ohtsuki, T.
Statistical Emission of Complex Fragments Produced in the Reaction
 $^{37}\text{Cl} + ^{68}\text{Zn}$
Nucl. Phys. A510 (1990) 518
T
28. Nagame, Y., Sueki, K., Baba, S. and Nakahara, H.
Isomeric Yield Ratios in Proton-, ^3He -, and α -particle-induced
reactions on ^{197}Au
Phys. Rev. C41 (1990) 889
29. Nagata, S., Yamaguchi, S., Naramoto, H. and Kazumata, Y.
Lattice Location of Deuterium Implanted in TiC
Nucl. Instr. and Meth. B48 (1990) 231.
V
30. Nishida, T., Kanno, I., Nakahara, Y. and Takada, H.
Calculation of the Spallation Product Distribution in the Evaporation
Process
Advanced Neutron Sources 1988, p.771.
31. Nishida, T., Takada, H., Kanno, I. and Nakahara, Y.
Improvement of Spallation Reaction Codes NMTC/JAERI and NUCLEUS
Proc. 2nd Int. Symp. on Advanced Nuclear Energy Research, p.698.
32. Nishida, T., Takada, H., Kanno, I., Takizuka, T., Nakahara, Y.,
Mizumoto, M. and Kaneko, Y.
TRU Transmutation with High Energy Proton Beam
Proc. of the 1989 Seminar on Nuclear Data, p.343.
33. Noda, K., Ishii, Y., Kuroda, K., Sasaki, M., Saka, H. and Watanabe, H.
Electron Microscopic Observation of Lithium Aluminate Irradiated with
Oxygen Ions
JAERI-M 89-119, p.105-107.

V

34. Noda, K., Ishii, Y., Ohno, H., Watanabe, H. and Matsui, H.
Irradiation Defects and Ion Conductivity of Lithium Oxide
Advances in Ceramics vol. 25 "Fabrication and Properties of Lithium
Ceramics" (American Ceramic Society, 1989), p.155-164.
T
35. Noda, K., Ishii, Y., Matsui, H., Ohno, H. and Watanabe H.
A Study of Tritium Behavior in Lithium Oxide by Ion Conductivity
Measurements
Fusion Engineering and Design, 8 (1989) 329.
T
36. Noda, K., Ishii, Y., Matsui, H., Horiki, M., Nakaya, K., Nezaki, K.,
Obata, N. and Watanabe, H.
Ion Conductivity of Lithium Oxide Irradiated with Oxygen and Lithium
Ions
JAERI-M 89-119, p.93-96.
T
37. Noda, K.
Radiation Damage and Irradiation Effects in Solid Breeders
J. Nucl. Mater., in press.
T
38. Noda, K., Ishii, Y., Matsui, H., Ohno, H. and Watanabe, H.
Electrical Conductivity of Lithium Oxide under and after Irradiation
J. Nucl. Mater., in press.
T
39. Ohtsuki, T., Hamajima, Y., Sueki, K., Nakahara, H., Nagame, Y.,
Shinohara, N. and Ikezoe, H.
Systematic Analysis of Mass Yield Curves in Low-Energy Fission of
Actinides Phys. Rev. C40 (1989) 2144
T

40. Ohtsuki, T., Sueki, K., Hamajima, Y., Nakahara, H., Nagame, Y. and Ikezoe, H.
 Systematic Study of Mass Yield Curves in Low Energy Fission of Actinides
 Proceedings of 50 Years with Fission, ed. by J.W. Behrens and A.D. Carlson, (American Nuclear Society Inc., Maryland), p.750.
 T
41. Osa, A., Miyachi, M., Shibata, M., Yamamoto, H., Kawade, K., Kawase, Y., Ruan, J-Z., Ichikawa, S. and Iimura, H.
 Measurement of Beta-ray Maximum Energy with an HPGe Detector
 Proceedings of The 2nd International Symposium on Advanced Nuclear Energy Reseach (Jan. 24-26, 1990, Mito) pp.731-735.
 T
42. Oshima, M
 Search for Double- γ Vibrational States in Deformed Nuclei
 RCNP Report P-108 (1989) p.105
 T
43. Oshima, M
 Coulomb Excitation of Stable and Unstable Nuclei
 JAERI-M Report 90-072 (1990) p.55
 T
44. Oshima, M., Matsuzaki, M., Ichikawa, S., Iimura, H., Kusakari, H., Inamura, T., Hashizume, A. and Sugawara, M.
 Electromagnetic Transition Probabilities in the Natural-Parity Rotational Bands of ^{173}Yb
 Rhys. Rev. C40 (1989) 2084
 T
45. Oshima, M., Matsuzaki, M., Ichikawa, S., Iimura, H., Kusakari, H., Inamura, T., Hashizume, A. and Sugawara, M.
 Electromagnetic Transition Probabilities in the Natural-Parity Rotational Bands of ^{173}Yb
 RIKEN Accel. Progr. Rep. Vol.23 (1989) p.14
 T

46. Raman, S., Igashira, M., Dozono, Y., Kitazawa, H., Mizumoto, M. and Lynn, J.E.
Valence Capture Mechanism in Resonance Neutron Capture by ^{13}C
Phys. Rev. C41 (1990) 458
47. Sato, K., Funino, Y., Yamaguchi, S., Naramoto, H. and Ozawa, K.
Ion Channeling Studies of Carbon Irradiated TiC Single Crystals
Nucl. Instr. and Meth. B (1990) : Accepted for publication.
V
48. Sekine, T., Ichikawa, S., and Hatsukawa, Y.
Radioisotope Production with Combination of a Cyclotron and an Isotope Separator
Proc. of the 2nd Int. Sympo. on Advanced Nuclear Energy Research-Evolution by Accelerators -, Mito, Jan. 24-26 (1990), p.520.
T
49. Shinohara, N., Alstad, J., Baba, S., Fujiwara, I., Ichikawa, S., Iimura, H., Ohtsuki, T., Tsukada, K. and Umezawa, H.
A Study of Short-lived Ruthenium Isotopes produced in the Spontaneous Fission of ^{252}Cf using SISAK
Proc. of International Symposium on Advanced Nuclear Energy Research, (Feb. 15-16, 1989, Oarai, Japan) pp.204-205 (1989)
T
50. Sugita, M., Otsuka, T. and Gelberg, A.
Davydov-Filippov Limit of the IBM
Nucl. Phys. A493 (1989) 350
51. Sugiyama, Y., Tomita, Y., Ikezoe, H., Takekoshi, E., Ideno, K. and Shikazono, N.
Performance of the heavy-ion magnetic spectrograph ENMA on the kinematic correction
Nucl. Instru. & Methods in Physics Research A281 (1989) 512
T

52. Takada, H., Takizuka, T., Kanno, I., Ogawa, T., Nishida, T. and Kaneko, Y.
 A Conceptual Study of Actinide Transmutation System with Proton Accelerator (1) Target Neutronics Calculation
 Proc. of 2nd Int. Symp. on Advanced Nuclear Energy Research, p.375.
53. Takamura, S., Aruga, T. and Hoshiya, T.
 Pinning Strength of Bi-Sr-Ca-Cu-O Superconductor after Ion Irradiation
 Jpn. J. Appl. Phys. 28 (1989) L1118.
 V
54. Takamura, S., Hoshiya, T., Aruga, T. and Kobiyama, M.
 Ion Irradiation Effects on Critical Current of Superconducting Bi-Sr-Ca-Cu-O Films
 Jpn. J. Appl. Phys. 28 (1989) L1395.
 V
55. Takeuchi, S., Ishii, T. and Ikezoe, H.
 Niobium Superconducting Quarter-Wave Resonators as a Heavy Ion Accelerating Structure
 Nucl. Instrum. and Methods A281 (1989) 426.
56. Takeuchi, S., Ishii, T., Ikezoe, H. and Tomita, Y.
 Development of the JAERI Tandem Superconducting Booster
 Nucl. Instrum. and Methods A287 (1990) 257.
57. Takeuchi, S.
 Status Report on JAERI Activities
 Proc. of the 4th Workshop on RF Superconductivity, Tsukuba (Aug. 14-18, 1989) p.151.
58. Takeuchi, S., Ishii, T. and Ikezoe, H.
 Progress in RF-Superconductivity for Heavy-Ion Acceleration at JAERI
 Proc. of the 4th Workshop on RF Superconductivity, Tsukuba (Aug. 14-18, 1989) p.469.

59. Takeuchi, S.
 JAERI Tandem Superconducting Booster
 Proc. of the 2nd International Sympo. on Advanced Nucl. Energy Research
 Mito (Jan. 24-26, 1990) p.357.
60. Takizuka, T., Kanno, I., Takada, H., Ogawa, T., Nishida, T. and
 Kaneko, Y.
 A Study on Incineration Target System
 Proc. of 5th Int. conf. of Emerging Nuclear Energy Systems, p.70.
61. Takizuka, T., Takada, H., Kanno, I., Ogawa, T., Nishida, T. and
 Kaneko, Y.
 A Conceptual Study of Actinide Transmutation System with proton
 Accelerator (2) Target Thermal Hydraulics
 Proc. of 2nd Int. Symp. on Advanced Nuclear Energy Research, p.381.
62. Tsukada, K., Ohtsuki, T., Sueki, K., Hatsukawa, Y., Yoshikawa, H.,
 Endo, K., Nakahara, H., Shinohara, N., Ichikawa, S., Usuda, S.
 and Hoshi, M.
 Development of a Computer-Controlled On-Line Rapid Ion-Exchange
 Separation System
 Radiochim. Acta to be published.
 T
63. Watanabe, H., Inaba, S., Kobayashi, Y., Kikuchi, M. and Obata, R.
 Effect of Ion Beams Irradiation on Radiation Resistant Bacterium,
 Deinococcus radiodurans
 Proceedings of The 2nd International Symposium on Advanced Nuclear
 Energy Research, Mito, pp.551-555 (1990).
 V
64. Watanabe, H.
 Ion Beam-Induced Damage of Bacterial Cell Structure
 Proceedings of Symposium on Advanced Radiation Research, Tokyo,
 pp.55-56 (1989)

65. Yanagida, K., Yokomizo, H., Harada, S., Yokoyama, M.,
Nagai, T., Mashiko, K., Ishizaki, Y. and Tayama, H.
Present status of JSR
Proceeding of the 7th Symposium on Accelerator Science and
Technology (1989) 4
L
66. Yamaguchi, S., Fujino, Y., Naramoto, H. and Ozawa, K.
Recovery of Carbon-Implanted Silicon and Germanium
Nucl. Instr. and Meth. B39 (1989) 409.
V
67. Yokomizo, H., Sasaki, S., Harami, T., Yanagida, K., Konishi, H.,
Mashiko, K., Kawarasaki, Y., Ohkubo, M., Harada, Y., Sasamoto, N.,
Ashida, K., Harada, S., Hashimoto, H., Iizuka, M., Kabasawa, M.,
Nakayama, K., Yamada, K. and Suzuki, Y.
Design of a small storage ring in JAERI
Proceeding of European Particle Accelerator Conference vol.1 (1989)
445
68. Yokomizo, H., Yanagida, K., Sasaki, S., Konishi, H., Mashiko, K.,
Ashida, K., Harada, S., Hashimoto, H., Iizuka, M., Kabasawa, M.,
Nakayama, K., Yamada, K. and Suzuki, Y.
Construction of compact electron storage ring JSR
Rev. Sci. Instrum. 60 (1989) 1724
69. Yokomizo, H., Harada, S., Yanagida, K., Yokoyama, M.,
Nagai, T. and Suzuki, Y.
JAERI storage ring JSR
Proceeding of the 2nd International Symposium on Advanced Nuclear
Energy Research (1990) 273
L

Contributions to Scientific and Technical Meetings.

1. Arima, A. and Sugita, M.
 Shape Transition of Nuclei with Mass Around A=100
 Symposium on the Occasion of the 40th Anniversary of the Nuclear Shell
 Model (ANL, May 25-27, 1989)

2. Endo T., Murakami H., Haruna, K. and Maeta H.
 Positron Annihilation in Boron Nitride
 Fall Meeting of Japan Physical Society in Kagoshima city (Oct. 3-6 1984)
 V

3. Furukawa, K., Ohno, S., Komaki, Y., Namba, H., Aoki, Y. and Hakai, Y.
 Ionization Measurement in a Gas Traversed by a Beam of High-Energy
 Heavy Ion
 The 32nd Discussion Meeting on Radiation Chemistry in Hiroshima (Oct. 19-
 20, 1989)

4. Harada, S., Yokomizo, H., Yanagida, K., Yokoyama, M., Nagai, T.,
 Mashiko, K., Ishizaki, Y., Tayama, H. Suzuki, H., Shimada, T.,
 Yamada, K., Hashimoto, H., Iizuka, M. and Suzuki, Y.
 An analysis of JSR
 Autumn meeting of the Physical Society of Japan in Miyazaki (Oct. 11-14
 1989)
 L

5. Hasegawa, K., Mizumoto, M., Yamanouti, Y., Chiba, S., Sugimoto, M.,
 Igashira, M., Kitazawa, H. and Uchiyama, T.
 Measurements of Gamma-Ray Production Cross Sections at $E_n=11.5$ MeV
 Using $^1_0\text{H}(^{11}_5\text{B},n)^{11}_6\text{C}$ Neutron Source
 Annual Meeting of Atomic Energy Society of Japan in Osaka
 (Apr. 4-6, 1989)
 T

6. Hirose, M., Ito, Y., Sueoka, O., Kanazawa, I., Takamura, S., Okada, S.
Production and Quality Improvement of Intense Slow Positron Beam Using
an 100 MeV Electron Linac
Spring Meeting of Japan Institute of Applied Physics, (March 28-31, 1990)

7. Hoshiya, T., Takamura, S., Aruga, T. and Kobiyama, M.
Thermally Activated Flux Motion in Bi-Sr-Ca-Cu-O Superconductors
Spring Meeting of Japan Society of Applied Physics in Saitama
(March 28-31, 1990)

8. Herrmann, R.
Collective Motion in the Riemannian Space
Symposium on Fission as an Open Non-Equilibrium System, in Kyoto
(Feb. 15-17, 1990)

9. Herrmann, R.
Super-Heavy Element
INS Symposium on Unstable Nuclei, in Tokyo (Feb. 20-22, 1990)

10. Herrmann, R.
Introduction of Spin to the Riemannian Space of Collective Model
Autumn Meeting of the Physical Society of Japan, in Miyazaki
(Oct. 11-14, 1989)

11. Ichikawa, S., Sekine, T., Iimura, H. and Oshima, M.
Measurement of Release Speeds of La and Ce from a Thermal Ion Source
The 33rd Symposium on Radiochemistry in Hiroshima (Oct. 4-6, 1989).
T

12. Ideno, K., Tomita, Y., Sugiyama, Y., Ikezoe, H., Hanashima, S. and
Nagame, Y.
2-dimensional Position-sensitive Detection System for ^8Be Nuclei
Autumn Meeting of Japan Physical Society in Miyazaki (Oct. 11-14)
T

13. Iimura, H. Ichikawa, S. Oshima, M. Sekine, T, Shinohara, N. Shibata, M. Osa, A. Kotani, K. Yamamoto, H. and Kawade, K.
Decay of ^{123}La
Autumn Meeting of the Physical Society of Japan in Miyazaki (Oct. 1989).
T

14. Ichikawa, S. Iimura, H. Oshima, M. Sekine, T and Shibata, M.
An Ion Guide Isotope Separator On-Line at JAERI
Autumn Meeting of the Physical Society of Japan in Miyazaki (Oct. 1989).
T

15. Ishii, T., Ishii, M., Garnsomsart, S., Saito, Y., Nakajima, M. and Ogawa, M.
Nuclear Structure of $^{103,105}\text{In}$
Autumn Meeting of the Physical Society of Japan in Miyazaki (Oct, 1989)
T

16. Iwamoto, A. and Herrmann, R.
On the Evaporation of Alpha Particles
INS Symposium on Heavy-Ion Reaction Mechanism, in Tokyo (March 23-24, 1990)

17. Iwamoto, A. and Kindo, T.
Fission as Multi-Dimensional Tunneling Process
Int. Conf. on Fifty Years Research in Nuclear Fission, in Berlin (Apr. 3-7, 1989)
Iwamoto, A.
Adiabatic Approximation in Nuclear Fission
Autumn Meeting of the Physical Society of Japan, in Miyazaki (Oct. 11-14, 1989)

18. Iwamoto, A.
Multi-Dimensional Penetration Problem in Nuclear Fission
Int. Seminar on Recent Advances in Physics, in Dahka (Jan. 15-19, 1990)

19. Iwamoto, A.
 Is It Possible to Detect the Transient Phenomena in the Alpha-Particle
 Emission Accompanying Nuclear Fission
 Symposium on Collective Motion and Non-Linear Dynamics, in Kyoto
 (Jan. 29-31, 1990)

20. Iwamoto, A. and Herrmann, R.
 Alpha-Particle Emission Accompanying Nuclear Fission
 Symposium on Fission as an Open Non-Equilibrium System, in Kyoto
 (Feb. 15-17, 1990)

21. Iwase, A., Iwata, T., Masaki, N., Watanabe, M. and Nihira, T.
 Ion Radiation Damage in Oxide Superconductors and La_2CuO_4 .
 Fall Meeting of Japan Physical Society in Kagoshima (October 6, 1989).
 T

22. Iwase, A., Masaki, N., Iwata, T. and Nihira, T.
 Effect of High Energy Ion Irradiation on Current-Voltage
 Characteristics in Oxide Superconductor $\text{YBa}_2\text{Cu}_3\text{O}_{7-x}$.
 Spring Meeting of Japan Physical Society in Osaka (March 30, 1990).
 T

23. Iwase, A., Iwata, T., Nihira, T. and Sasaki, S.
 Effect of Electron-Excitation on Ion radiation damage ion FCC Metals
 Fall Meeting of Japan Physical Society in Kagoshima (October 3, 1989)
 T V

24. Kanno, I., Takada, H., Takizuka, T., Ogawa, T., Nishida, T. and
 Kaneko, Y.
 A study on TRU Incineration System with Proton Accelerator
 Spring Meeting of Japan Atomic Energy Society (Osaka, April, 1989)

25. Kanno, I.
 A Model of Charge collection Process in a Silicon Surface Barrier
 Detector
 Fall Meeting of Japan Atomic Energy Society (Tokai, October, 1989)

26. Kanno, I.
 On the Charge Collection Process in a Silicon Surface Barrier
 Detector
 5th Workshop on Radiation Detectors and their Uses (Tsukuba, January,
 1990)
27. Kawatsura, K., Yamazaki, Y., Sataka, M., Kanai, Y., Komaki, K.,
 Naramoto, H., Kuroki, K., Kanbara, T., Awaya, Y., Nakai, Y. and
 Stolterfoht, N.
 Zero-Degree Electron Spectroscopy in Energetic Ion-Atom Collisions (II)
 Autumn Meeting of the Physical Society of Japan in Kagoshima (Oct. 3-6,
 1989)
 T
28. Kawatsura, K., Sataka, M., Komaki, K., Yamzaki, Y., Kanai, Y.,
 Naramoto, H., Kuroki, K., Kanbara, T., Awaya, Y., Nakai, Y. and
 Stolterfoht, N.
 Zero-Degree Electron Spectroscopy in Energetic Ion-Atom Collisions (III)
 Annual Meeting of the Physical Society of Japan in Toyonaka
 (Mar. 30-Apr.2 1990)
 T
29. Kobayashi, Y., Inaba, S., Kikuchi, M., Obata, R., Nakai, Y. and
 Watanabe, H.
 Effect of Ion Beam Irradiation on Radiation Resistant Bacterium,
 Deinococcus radiodurans
 Annual Meeting of Japan Society for Bioscience, Biotechnology and
 Agrochemistry in Fukuoka (Mar.30-Apr. 2, 1990)
 V
30. Kusakari, H., Oshima, M., Sugawara, M., Ono, Y., Inamura, T.,
 Hashizume, A., Minehara, E., Ichikawa, S. and Iimura, H.
 Coulomb Excitation of $^{155,157}\text{Gd}$
 Autumn Meeting of Japan Phys. Soc. in Miyazaki (October 11-14, 1989)
 T

31. Matsumura, K., Yasuda, H., Kanno, I., Takizuka, T., Ogawa, T.,
Nishina, K. and Kaneko, Y.
Conceptual Study of Very Small Reactor Power System with Coated
Particle Fuel (II) Core Study
Fall Meeting of Japan Atomic Energy Society (Tokai, October, 1989)

32. Mitamura, T., Terasawa, M., Kawatsura, K., Yagi, E., Koterazawa, K.,
Iwasaki, H. and Nakai, Y.
Fourth international conference on fusion reactor materials
December 4-8 (1989)
Radiation effect of austenitic stainless steel single crystal
V T

33. Mitamura, T., Terasawa, M., Kawatsura, K., Yagi, E., Iwasaki, H.,
Koterazawa, K. and Nakai, Y.
Ion-beam analysis of austenitic stainless steel single crystal
The 45th annual meeting of the Physical Society of Japan in Toyonaka
(Mar. 30 - Apr. 2, 1990)
V T

34. Miyahara, K., Sakamoto, Y., Hamada, S. Kayano, H. and Hosoi, Y.
Microstructure and Strength of α -Particle Irradiated Stainless Steels
Spring Meeting of Japan Institute of Metals in Yokohama (Apr. 4-6, 1989)

35. Miyahara, K., Sakamoto, Y., Hamada, S. Kayano, H. and Hosoi, Y.
Mechanical Properties of an α -Particle Irradiated Stainless Steels
Autumn Meeting of Japan Institute of Metals in Sapporo (Sep. 29-
Oct. 1, 1989)

36. Mizumoto, M., Yasuda, H., Nishida, T., Okumura, Y., Sugimoto, M.,
Chiba, S., Kanno, I., Takada, H., Nakashima, H. and Kaneko, Y.
The Development Plan of Basic Technology for High Intensity Proton
Linear Accelerator
14th Linac Conference (Nara, September, 1989)

37. Mizusaki, T., Otsuka, T. and Sugita, M.
SPDF Boson Model and the Actinide Nuclei
Spring Meeting of Physical Society of Japan in Osaka (Mar., 1990)

38. Nagame, Y., Ikezoe, H., Ohtsuki, T., Tsukada, K., Hatsukawa, Y., Baba, S., Sekine, T., Hata, K. and Ideno K.
Complex Fragment Emission in the Reactions $^{37}\text{Cl} + ^{68}\text{Zn}$ and $^{16}\text{O} + ^{89}\text{Y}$
The 33rd Symposium on Radiochemistry in Hiroshima (Oct. 4-6, 1989)
T
39. Nagame, Y., Ohtsuki, T., Ikezoe, H., Baba, S., Hata, K., Sekine, T. and Ideno K.
Complex Fragment Emission in the Reactions $^{37}\text{Cl} + ^{68}\text{Zn}$ and $^{16}\text{O} + ^{89}\text{Y}$
The 1989 International Chemical Congress of Pacific Basin Societies in Honolulu, Hawaii (Dec. 17-22, 1989)
T
40. Naramoto, H., Kazumata, Y., Oshima, M., Sataka, M., Yamaguchi, S., Ngata, S., Kawatsura, K. and Nakai, Y.
Perturbed Angular Measurement on Lattice Imperfections of Niobium Using $^{100}\text{Pd}/^{100}\text{Rh}$ I'
Spring Meeting of Physical Society of Japan in Osaka (Apr. 1, 1990).
T
41. Noda, K., Ishii, Y., Ohno, H., Watanabe, H. and Matsui, H
Irradiation Effects on Ion Conductivity of Lithium Oxide
2nd Int. Sym. on Fabrication and Properties of Lithium Ceramics in Indianapolis (Apr. 23-27, 1989)
T
42. Noda, K.
Radiation Damage and Irradiation Effects in Solid Breeders
4th Int. Conf. on Fusion Reactor Materials in Kyoto (Dec. 4-8, 1989)
T
43. Noda, K., Ishii, Y., Matsui, H., Ohno, H. and Watanabe, H.
Electrical Conductivity of Lithium Oxide under and after Irradiation
4th Int. Conf. on Fusion Reactor Materials in Kyoto (Dec. 4-8, 1989)
T

44. Noda, K., Ishii, Y., Matsui, H., Vollath, D. and Watanabe, H.
Irradiation Effects on Ionic Conductivity of $\text{Li}_{3.7}\text{Al}_{0.1}\text{SiO}_4$
Spring Meeting of Japan Atomic Energy Society in Tokyo (Apr. 2-4, 1990)
T
45. Ohtsuki, T., Nakahara, H., Nagame, Y., Tsukada, K., Shinohara, N.,
Baba, S., Sueki, K. and Ikezoe, H.
Symmetric and Asymmetric Mass Divisions in Low-energy Fission of
Actinides
The 1989 International Chemical Congress of Pacific Basin Societies
in Honolulu, Hawaii (Dec. 17-22, 1989)
T
46. Ohtsuki, T., Tsukada, K., Sueki, K., Nakahara, H., Nagame, Y., Ikezoe, H.,
Baba, S. and Hashimoto, K.
Measurement of Mass and Kinetic Energy Distributions of Fission Fragments
Produced in the Reaction $^{232}\text{Th} + p$
The 33rd Symposium on Radiochemistry in Hiroshima (Oct. 4-6, 1989)
T
47. Ono F., and Maeta H.
Migration of Self Interstitial Atoms in Fe
Fall Meeting of Japan Physical Society in Kagoshima city (Oct. 3-6 1984)
48. Oshima, M
Search for Double- γ Vibrational States in Deformed Nuclei
RCNP Symposium on Gamma Rays and Nuclear Structure (Osaka, August 31-
September 2, 1989)
T
49. Oshima, M., Ichikawa, S., Iimura, H., Minehara, E., Kusakari, H.,
Inamura, T., Hashizume, A., Sugawara, M. and Shibata, M.
Fast Timing Test with Pilot-U and BaF_2 scintillators
Autumn Meeting of Japan Phys. Soc. in Miyazaki (October 11-14, 1989)
T

50. Oshima, M
 Coulomb Excitation of Stable and Unstable Nuclei
 JAERI Seminar on Nuclear Physics and Atomic Physics at the JAERI
 Tandem-Booster Accelerator (Tokai, November 6-7, 1989)
 T
51. Shinohara, N.
 Radiochemical Investigation of Transuranium Nuclides produced by Heavy
 Ion Reaction
 International School-Seminar on Heavy Ion Physics, Dubna, USSR
 (Oct. 3-12, 1989)
 T
52. Sugimoto, M. and Kawarasaki, M.
 Design of the Control System for JAERI-FEL
 Proc. of the 14th Linear Accelerator Mtg. in Japan (Sep. 7-9, 1989)
53. Sugita, M.
 α Decay in the SPDF Boson Model
 1989 Nuclear Chemistry Gordon Conference
 Sugita, M.
 Octupole Deformation and the SPDF Boson Model
 Meeting on γ ray and Nuclear Structure at RCNP (Aug., 1989)
54. Sugiyama, Y.
 Quasielastic scattering of $^{28}\text{Si} + ^{58,64}\text{Ni}$ near the Coulomb barrier
 Seminar at Argonne National Laboratory (August 1989)
 T
55. Sugiyama, Y., Tomita, Y., Ikezoe, H., Ideno, K., Fujita, H.,
 Sugimitsu, T., Kato, N and Kubono, S.
 Coupled Reaction Channels Analysis for the Elastic Scattering of
 $^{28}\text{Si} + ^{58,64}\text{Ni}$ Autumn Meeting of Physical Society of Japan in Miyazaki
 (Oct. 11-14, 1989)
 T

56. Sugiyama, Y.
Contribution of Nucleon Transfer to Elastic Scattering of $^{28}\text{Si} + ^{58,64}\text{Ni}$
near the Coulomb Barrier
Riken Symposium in Wako (Oct. 6, 1989)
T
57. Sugiyama, Y.
Transfer Reaction for $^{16}\text{O} + ^{144,152}\text{Sm}$
INS Symposium in Tokyo (Mar. 23, 1990)
T
58. Takada, H., Kanno, I., Nishida, T. and Kaneko, Y.
A Study of the Incinerator by Proton Accelerator
Spring Meeting of Japan Atomic Energy Society (Osaka, April, 1989)
59. Takada, H., Kanno, I., Takizuka, T., Akahori, M., Nishida, T. and
Kaneko, T.
Conceptual Study of TRU Incineration System Driven by Proton
Accelerator (II)
Fall Meeting of Japan Atomic Energy Society (Tokai, October, 1989)
60. Takizuka, T., Kanno, I., Takada, H., Ogawa, T., Nishida, T. and
Kaneko, Y.
A Study on Incineration Target System
5th International Conference on Emerging Nuclear Energy Systems
(Karlsruhe, July, 1989)
61. Tsukada, K., Sueki, K., Ohtsuki, T., Kobayashi, T., Nishinaka, I.,
Nakahara, H., Shinohara, N., Ichikawa, S., Hoshi, M. and Nagame, Y.
Mass Yields of Rare Earth Elements in Fission of Actinides
The 33rd Symposium on Radiochemistry in Hiroshima (Oct. 4-6, 1989)
T

62. Tsukada, K., Sueki, K., Ohtsuki, T., Kobayashi, T., Nishinaka, I., Nakahara, H., Shinohara, N., Ichikawa, S. and Iimura, H.
Measurement of the Fission Yields of the Heavy Rare Earth Elements
Using an Automatic Chemical Separation System
The 1989 International Chemical Congress of Pacific Basin Soc
in Honolulu, Hawaii (Dec. 17-22, 1989)
T
63. Yamanouti, Y., Sugimoto, M., Mizumoto, M. and Watanabe, Y.
The ^{52}Cr (n,n) and (n,n') reactions I
Fall Meeting of the Physical Society of Japan in Miyazaki
(Oct. 13, 1989)
T
64. Yamanouti, Y., Sugimoto, M., Mizumoto, M. and Watanabe, Y.
The ^{52}Cr (n,n) and (n,n') reactions II
Spring Meeting of the Physical Society of Japan in Osaka
(Apr. 1, 1990)
T
65. Yanagida, K., Yokomizo, H., Harada, S., Yokoyama, M., Nagai, T.,
Mashiko, K., Ishizaki, Y., Tayama, H. Suzuki, H., Shimada, T.,
Yamada, K., Hashimoto, H., Iizuka, M. and Suzuki, Y.
Present status of JSR
Autumn meeting of the physical Society of Japan in Miyazaki (Oct.
11-14 1989)
L
66. Yasuda, H., Kanno, I., Takizuka, T., Ogawa, T., Matsumura, K.,
Nishina, K. and Kaneko, Y.
Conceptual Study of Very Small Reactor Power System with Coated
Particle Fuel (I) System Concept
Fall Meeting of Japan Atomic Energy Society (Tokai, October, 1989)

67. Yasuda, H., Kanno, I., Matusmura, K., Takizuka, T., Ogawa, T., Kaneko, K., Aoki, H. and Kaji, O.
Conceptual Study of Very Small Reactor with Coated Particle Fuel
7th Symposium on Space Nuclear Power Systems (Albuquerque, January, 1990)
68. Yasuda, H., Kanno, I., Matsumura, K., Takizuka, T., Ogawa, T., Kaneko, Y., Aoki, H. and Kaji, O.
Conceptual Study of a Very Small Reactor with Coated Particle Fuel (I), (II), (III)
9th Symposium on Space Energy (Sagamihara, February, 1990)
69. Yokoyama, M., Yokomizo, H., Yanagida, K., Harada, S., Nagai, T., Mashiko, K., Ishizaki, Y., Tayama, H. and Suzuki, Y.
Study of beam accumulation for JSR
Spring meeting of the Japan Society for Synchrotron Radiation Research in Osaka (April 26-28 1990)

L

VIII PERSONNEL AND COMMITTEES

(April 1988 - March 1989)

(1) Personnel

Department of Physics

Naomoto	Shikazono	Director
		Since November 1, 1989
		Deputy Director General
		Tokai Establishment
Mitsuhiko	Ishii	Deputy Director
Yoichi	Suto	Administrative
		Manager

Accelerators Division

Scientific Staff	Chiaki	Kobayashi [*]
	Shiro	Kikuchi
	Suehiro	Takeuchi
	Susumu	Hanashima
Technical Staff (Tandem, V.D.G)	Yutaka	Sato
	Tadashi	Yoshida ^{**}
	Susumu	Kanda
	Katsuzo	Horie
	Satoshi	Tajima
	Yoshihiro	Tsukihashi
	Shinichi	Abe
	Shuhei	Kanazawa
Technical Staff (Linac)	Katuo	Mashiko ^{**}
	Kiyoshi	Mizubishi
	Tokio	Shoji
	Nobuhiro	Ishizaki
	Hidekazu	Tayama

Nuclear Physics Laboratory

Scientific Staff	Akira	Iwamoto [*]
------------------	-------	----------------------

* Head

** Leader, Technical Staff

Nuclear Physics Laboratory (continued)

Scientific Staff	Yasuharu	Sugiyama
	Yoshiaki	Tomita
	Hiroshi	Ikezoe
	Masumi	Ohshima
	Kazumi	Ideno
	Tetsuro	Ishii
	Michiaki	Sugita

Linac Laboratory

Scientific Staff	Yuuki	Kawarasaki*
	Makio	Ohkubo
	Motoharu	Mizumoto
	Eisuke	Minehara
	Yoshimaro	Yamanouchi
	Masayoshi	Sugimoto
	Satoshi	Chiba
	Masayuki	Takabe
	Jyun	Sasabe
	Masaru	Sawamura

Solid State Physics Laboratory I

Scientific Staff	Yukio	Kazumata*
	Hiroshi	Naramoto
	Hiroshi	Tomimitsu

Solid State Physics Laboratory II

Scientific Staff	Tadao	Iwata*
	Saburo	Takamura
	Hiroshi	Maeta
	Akihiro	Iwase

* Head

Atomic and Molecular Physics Laboratory

Scientific Staff	Yohta	Nakai *
	Masao	Sataka
	Makoto	Imai

Synchrotron Radiation Research Laboratory

Scientific Staff	Yasuo	Suzuki *
	Hideaki	Yokomizo
	Taikan	Harami
	Shigemi	Sasaki
	Hiroyuki	Konishi
	Kenich	Yanagida

* Head

Department of Chemistry

Nuclear Chemistry Laboratory 1

Scientific Staff	Masakatus	Saeki [*]
	Yasuyuki	Aratono
	Mikio	Nakashima

Nuclear Chemistry Laboratory 2

Scientific Staff	Michio	Hoshi [*]
	Shin-ichi	Ichikawa
	Nobuo	Shinohara
	Hidenori	Iimura

Analytical Chemistry Laboratory

Scientific Staff	Yuji	Baba
	Toshio	Suzuki

Physical Chemistry Laboratory

Scientific Staff	Mutsuhide	Komaki
	Jiro	Ishikawa

Solid State Chemistry Laboratory

Scientific Staff	Teikichi	Sasaki [*]
	Shigemi	Furuno
	Takeshi	Soga

Laser Chemistry Laboratory

Scientific Staff	Shin-ichi	Ohno [*]
	Katsutoshi	Furukawa

* Head

Department of Radioisotopes

Isotope Research and Development Division

Scientific Staff	Hiromitsu	Matsuoka
	Kentaro	Hata
	Toshiaki	Sekine
	Yuichiro	Nagame
	Takami	Sorita
	Mishiroku	Izumo
	Hiroyuki	Sugai

Department of Fuels and Materials Research

Radiation Effects and Analysis Laboratory

Scientific Staff	Akimichi	Hishinumua *
	Takeo	Aruga
	Shozo	Hamada
	Tomotsugu	Sawai
	Katsumaro	Fukai

Material Processing and Qualification Laboratory

Scientific Staff	Hitoshi	Watanabe *
	Kenji	Noda
	Yoshinobu	Ishii

Department of Reactor Engineering

Scientific Staff	Ikuo	Kanno
------------------	------	-------

* Head

Department of Health Physics

Technical Staff	Shoji	Izawa *
	Kenji	Yamane
	Masamitsu	Kikuchi
	Akihiko	Kuramochi

* Chief, Radiation Control Division II

(2) Tandem Steering Committee

(Chairman)	Naomoto	Shikazono	(Deputy Director General, Tokai Research Establishment)
	Toru	Hiraoka	(Deputy Director, Department of Reactor Engineering)
	Tatuo	Kondo	(Director, Department of Fuels and Materials Research)
	Mitsuhiko	Ishii	(Deputy Director, Department of Physics)
	Enzo	Tachikawa	(Director, Department of Chemistry)
	Susumu	Shimamoto	(Director, Department of Thermonuclear Fusion Research)
	Hirokazu	Umezawa	(Director, Department of Radioisotopes)
(Secretary)	Chiaki	Kobayashi	(Head, Accelerators Division)
(Secretary)	Yoichi	Suto	(Administrative Manager, Department of Physics)

(3) Tandem Consultative Committee

(Chairman)	Takumi	Asaoka	(Director General, Tokai Research Establishment)
(Vice Charman)	Naomoto	Shikazono	(Deputy Director General, Tokai Research Establishment)
(Vice Chairman)	Mitsuhiko	Ishii	(Deputy Director, Department of Physics)
	Hiromichi	Kamitsubo	(Principal Scientist, Institute of Physical and Chemical Research)
	Koji	Nakai	(Professor, National Laboratory for High Energy Physics)
	Hiroyasu	Ejiri	(Professor, Osaka University)
	Shiori	Ishino	(Professor, University of Tokyo)
	Hiroyuki	Tawara	(Associate Professor, Institute of Plasma Physics, Nagoya University)
	Kohzoh	Masuda	(Professor, University of Tsukuba)
	Shiro	Iwata	(Professor, Kyoto University)
	Ichiro	Fujiwara	(Professor, Otemon Gakuin University)
	Kenji	Sumita	(Professor, Osaka University)
	Naohiro	Hirakawa	(Professor, Tohoku University)
	Hirosuke	Yagi	(Professor, University of Tsukuba)
	Syunpei	Morinobu	(Associate Professor, Research Center for Nuclear Physics Osaka University)
	Hiromichi	Nakahara	(Professor, Tokyo Metropolitan University)
	Sadaei	Yamaguchi	(Professor, The Research Institute for Iron, Steel and other Merals, Tohoku University)

	Hatsuo	Yamazaki	(Professor, Hokukaido University)
	Mamoru	Akiyama	(Professor, University of Tokyo)
	Yasuo	Ito	(Associate Professor, University of Tokyo)
(Secretary)	Chiaki	Kobayashi	(Head, Accelerators Division)
(Secretary)	Yoichi	Suto	(Adiministrative Manager, Department of Physics)
(Secretary)	Hirokazu	Umezawa	(Director, Department of Radioisotopes)
(Secretary)	Tadao	Iwata	(Head, Solid State Physics Laboratory II)
(Secretary)	Yohta	Nakai	(Head, Atomic and Molecular Physics Laboratory)

(4) Tandem Program Advisory Committee

(Chairman)	Mitsuhiko	Ishii	(Deputy Director, Department of Physics)
	Hirokazu	Umezawa	(Director, Department of Radioisotopes)
	Shoji	Izawa	(Chief, Radiation Control Group, Department of Health Physics)
	Hitoshi	Watanabe	(Head, Material Processing and Qualification Laboratory)
	Yohta	Nakai	(Head, Atomic and Molecular Physics Laboratory, Department of Physics)
	Yuuki	Kawarasaki	(Head, Linac Laboratory, Department of Physics)
	Akira	Iwamoto	(Head, Nuclear Physics Laboratory)
	Yukio	Kazumata	(Head, Solid State Physics Laboratory I)
(Secretary)	Chiaki	Kobayashi	(Head, Accelerators Division, Department of Physics)
(Secretany)	Shiro	Kikuchi	(Accelerators Division, Department of Physics)
(Secretany)	Tadashi	Yoshida	(Accelerators Division, Department of Physics)

IX CO-OPERATIVE RESEARCHES

Title	Contact person Organization
1. Gamma-Ray Spectroscopy in the Neighbour Nuclei of ^{100}Sn	Masao OGAWA Tokyo Institute of Technology
2. Study of Reaction Mechanism Induced by Heavy Ions	Toru NOMURA Institute for Nuclear Study, University of Tokyo
3. Study of Nuclear Interactions in Heavy-Ion Reaction	Takao NAKAJIMA Department of Physics, Kyushu University
4. Theoretical Investigation of Nuclear Fission and Heavy-Ion Fusion Reaction	Noboru TAKIGAWA Department of Physics, Tohoku University
5. Nuclear Structure Analysis Based on the Interacting Boson Model	Takaharu OTSUKA Department of Physics, University of Tokyo
6. Study of Nuclear Fission Induced by Heavy Ions	Sang Moo Lee Department of Physics, University of Tsukuba
7. Study of Higher-Order Effect in Nuclear Collective Motion through Coulomb Excitation	Hideshige KUSAKARI Faculty of Education, Chiba University
8. Nuclear Study by Fast Neutrons	Yoshihisa WAKUTA Department of Nuclear Engineering, Kyushu University
9. A Development of Collimated Neutron Source and Its Application to a Study of Neutron Reaction Cross Sections	Kazusuke SUGIYAMA Faculty of Engineering, Tohoku University
10. A Study of Fast-Neutron Induced Gamma-Ray Production Cross Sections	Hideo KITAZAWA Research Laboratory for Nuclear Reactors, Tokyo Institute of Technology
11. Basic Research on Free Electron Laser	Hirotada OHASHI Faculty of Engineering, University of Tokyo

- | | |
|---|---|
| 12. Irradiation Effect on Electrical Property of LiAl with Li and Other Heavy Ions. | Kazuo KURIYAMA
Research Center of Ion Beam Technology, Hosei University. |
| 13. Surface Analysis of Functional Materials with High Energy Ions. | Sadae YAMAGUCHI
Institute for Material Research, Tohoku University. |
| 14. Radiation Damage of Materials for Environment Resistance Devices. | Kazutoshi OHASHI
Faculty of Engineering, Tamagawa University. |
| 15. Study of Ion-Irradiation Damage in Metals by Magnetic Method | Fumihisa ONO
College of Liberal Arts and Science, Okayama University. |
| 16. Interaction Between Radiation Defects and Hydrogen Atoms in Metals. | Kohji YAMAKAWA
Faculty of Engineering, Hiroshima University. |
| 17. Study of the Defect Production in Heavy-Ion Irradiation to Metals. | Takeshi NIHIRA
Faculty of Engineering, Ibaraki University. |
| 18. Structure of Tracks and Cascades in Inorganic solids. | Chiken KINOSHITA
Faculty of Engineering, Kysushu University. |
| 19. Atomic Collision Research Using Highly Charged Ions. | Ken-ichiro KOMAKI
Institute of Physics, College of arts and Sciences, University of Tokyo. |
| 20. Ion-Beam Analysis of Fusion Reactor Materials. | Michitaka TERASAWA
Faculty of Engineering, Himeji Institute of Technology. |
| 21. Mass Division Processes in Fissions of Actinide Elements. | Hiromichi NAKAHARA
Faculty of Science, Tokyo Metropolitan University. |
| 22. A Research for the Production of Transuranium Elements. | Ichiro FUJIWARA
Faculty of Economy, Otomon Gakuin University. |
| 23. A Study of Irradiation Behavior of Ceramic Breeders. | Hisayuki MATSUI
Faculty of Engineering, Nagoya University. |